



Top_Fuel 2006

**2006 INTERNATIONAL MEETING
ON LWR FUEL PERFORMANCE**
"NUCLEAR FUEL: ADDRESSING THE FUTURE"

22-26 October 2006
Salamanca, Spain

Transactions

Organised by
European Nuclear Society (ENS)

In cooperation with
American Nuclear (ANS)
Society and Atomic Energy Society of Japan (AESJ)
International Atomic Energy Agency
Spanish Nuclear Society
Nuclear Energy Agency (NEA)



TABLE OF CONTENTS

Poster Session II

High Burnup

HIGH BURNUP FUEL (PELLET BURNUP 80 GWD/T) BEHAVIOR-FISSION GAS RELEASE, PELLET SWELLING, MICRO-STRUCTURE 5

Fuel Manufacturing

LEAN SIX SIGMA 12

AREVA NP FUEL MANUFACTURING INVESTS FOR THE FUTURE TO ENSURE SECURITY OF SUPPLY TO ITS CUSTOMERS 17

ZIRCONIUM PRODUCT MANUFACTURING WITHIN AREVA: A KEY ELEMENT FOR THE NUCLEAR FUEL SUPPLY CHAIN 22

Methods and Models

ANALYSIS OF ABNORMAL OPERATING OCCURRENCES FOR STA. MARIA DE GAROÑA WITH TRACG 26

TANOXOS: AN ANALYTICAL IRRADIATION PROGRAM AIMING AT UNDERSTANDING THE BEHAVIOUR OF VARIOUS DOPED UO₂ FUELS. 31

THE BENEFITS OF THE FUMEX-II PROJECT FOR EXTENDING THE VERIFICATION OF THE TRANSURANUS CODE 40

RECENT MODELLING FEATURES IN THE COPERNIC3 AREVA NP FUEL ROD PERFORMANCE CODE 45

UTILIZATION OF SIMTAB METHODOLOGY IN TRANSLATING THE KINETICS PARAMETERS FROM SIMULATE-3 TO RELAP5/PARCS FOR REA 3D-DYNAMIC ANALYSIS IN TRILLO NPP 50

CYRANO3: THE INDUSTRIAL PLEIADES FUEL PERFORMANCE CODE FOR EDF PWR STUDIES 57

ANALYTICAL AND EXPERIMENTAL STUDIES OF FRETTING-CORROSION AND VIBRATIONS OF FUEL ASSEMBLIES OF A VVER-1000 WATER COOLED AND WATER MODERATED POWER REACTOR 62

Fuel Performance

EFFECT OF MECHANICAL PROPERTIES OF SPACER GRID SPRINGS ON THE FRETTING WEAR OF A NUCLEAR FUEL ROD 77

EXPERIENCE ON FUEL INSPECTION SYSTEM 82

COMPARISON OF THE CODE PREDICTIONS WITH PIE DATA FOR WWER-1000 FUEL RODS, AND COMPARATIVE CALCULATIONS OF WWER AND PWR TYPE FUEL RODS 87

ENSURING FUEL ECONOMY AND SAFE BWR CONTROL ROD MOVEMENTS THROUGH BWR FUEL CHANNEL MEASUREMENT 92

RESULTS OF POST-IRRADIATION EXAMINATIONS (PIE) OF E110 CLADDINGS AND ALLOY UPGRADING FOR VVER 97



Fuel Strategies and Core Management	
DETERMINISTIC BWR CORE DESIGN	102
Spent Fuel Management	
LONG TIME STORAGE OF FAILED FUEL ROD	107
LOCA & RIA Issues	
EXPERIMENTAL DATABASE OF E110 CLADDING_OXIDISED IN HYDROGEN RICH STEA	112
FAILURE BEHAVIOR OF ZIRCONIUM CLADDING AFTER THE LOSS OF THE COOLANT ACCIDENT (LOCA)	117
HIGH POWER AND HIGH SPEED RAMPS IN THE OSIRIS REACTOR	122
WATERCARE™ PROGRAM OVERVIEW	127
PROPOSAL FOR A FUEL INTEGRITY EVALUATION SYSTEM UNDER A BWR POST-BT CONDITION	132
Advance in Fuel Design	
OUT-OF-PILE TESTS UNDER LOCA CONDITIONS FOR J-ALLOY™, HIGH CORROSION-RESISTANT ALLOY FOR PWR FUEL CLADDING TUBE	137
MANUFACTURING AND CHARACTERIZATIONS OF J-ALLOY™, HIGH CORROSION-RESISTANT ALLOY FOR PWR FUEL CLADDING TUBE	142



POSTER SESSION II

HIGH BURNUP FUEL (PELLET BURNUP 80 GWD/T) BEHAVIOR - FISSION GAS RELEASE, PELLET SWELLING, MICRO-STRUCTURE -

**JIN KAMIMURA, KOICHI OHIRA,
KAZUTOSHI OKUBO, NOBORU ITAGAKI**

*Nuclear Fuel Industries, Ltd
Fuel Engineering and Development Department (Tokai Works)
3135-41, Muramatsu, Tokai-Mura, Naka-Gun, Ibaraki-Ken, 319-1196 Japan*

AKIRA TAKAGI

*Tokyo Electric Power Company
Nuclear Power Engineering, Quality & Safety Management Department
1-3, Uchisaiwai-cho, 1-Chome, Chiyoda-Ku*

ABSTRACT

Fuel rods equipped with on-line instrumentations were irradiated up to pellet peak burnup 80 GWd/t in Halden Boiling Heavy Water Reactor (HBWR) and the fuel rod irradiation behavior data (centerline temperature and inner pressure of the fuel rods) were obtained^[1]. In this time, destructive examinations; rod puncturing tests, ceramo-graphic examinations and pellet density measurements, were performed for irradiated fuel rods. As the results of the ceramo-graphic examinations, heterogeneous structure with the grains surrounded by the fine pores were observed at relative radius $r/r_0=0.75$ and rim structure with a lot of fine pores and sub-divided grains were observed in the pellet periphery at $r/r_0>0.9$. Temperature increase due to the rim structure formation was estimated less than 10°C, and the effect of rim structure formation on fuel temperature was very small. As the results of density measurements, the swelling rate was increased in high burnup region, which shows similar tendency with the other studies. And as the results of the rod puncturing tests, fission gas release rate of the fuel rods were within the expected range of previously obtained results. On the other hand, estimated fission gas release histories showed that the gas release was occurred under lower temperature condition. However, the fission gas release in this region was small.

In this study, it was concluded that the high burnup fuel behavior such as pellet thermal conductivity, high burnup structure formation, fission gas release and pellet swelling were within the expected range.

1. Introduction

A lot of irradiation data up to high burnup region have been reported today, but for the development of ultra high burnup fuels, it is important to confirm the effects of the specific phenomena at high burnup region such as the formation of high burnup structure (rim structure) or the increase of fission gas release on fuel performance. In order to estimate the fuel rod performance at high burnup region, NFI in cooperation with Japanese BWR electric power companies has irradiated the fuel rods equipped with on-line instrumentations up to pellet peak burnup 80 GWd/t in HBWR and the fuel rod behavior data (centerline temperature and inner pressure of the fuel rods) under irradiation were obtained. Then destructive examinations; rod puncturing tests, ceramo-graphic examinations and pellet density measurements, were performed for irradiated fuel rods. This paper describes the results about high burnup structure formation, fission gas release and pellet swelling for the high burnup fuel and estimation of its effects on fuel performance at high burnup region.

2. Fuel design and Irradiation

The specification of fuel rods for irradiation is shown in Tab 1. Two UO₂ fuel rods equipped with on-line instrumentations were irradiated in this study in order to obtain the fuel rod behavior under irradiation. Both of them were instrumented with pressure transducer (PF) at lower end. And for one fuel rod, fuel centerline temperature is measured by expansion thermometers (ETs) inserted into the 1.8 mm diameter hole drilled into pellets through fuel stack length.

The fuel rods were irradiated at HBWR coolant conditions (235°C, 34 bar) up to target pellet peak burnup 80 GWd/t. The linear heat rates histories for each rod is shown in Fig 1. The irradiation power histories of the fuel rods in the HBWR were sufficiently high to envelope the irradiation power histories expected in commercial BWRs up to high burnup region.

Fuel type		UO ₂
Pellet diameter	(mm)	8.1
Pellet central hole	(mm)	1.8
Pellet density	(%TD)	97
Fuel rod diameter	(mm)	9.5
Cladding Material		Zry2
Active length	(mm)	400
He initial pressure	(MPa)	1

Tab 1: Irradiated fuel rod design

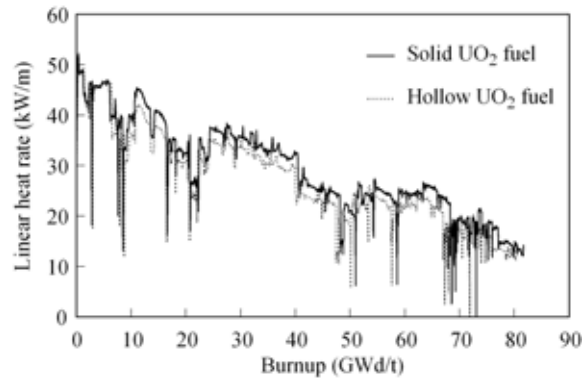


Fig 1. Irradiation power histories in Halden reactor

3. Experimental Results

Irradiated fuel rods were transported to Kjeller hot laboratories and performed post irradiation examinations. Optical microscopy images on ceramographic cross-sections of solid UO₂ fuels at different radial positions are shown in Fig 2. Sample was cut at near around peak burnup axial position, and etched after mechanical polishing. At radial positions $r/r_0 < 0.25$, formation of central void, columnar grains and equiaxed grains due to high power irradiation were observed (a). At radial positions inside $r/r_0 = 0.75$, precipitations of metal FPs in bright contrast and some intergranular gas bubbles were observed (b). From the overview of pellet cross-section, so-called dark ring were shown at radial positions $0.50 < r/r_0 < 0.75$, which indicated fission gas release were occurred inside from this region. Around radial position $r/r_0 = 0.75$, heterogeneous structure with the as-fabricated size grain surrounded by the fine pores, which was similar to that observed at the rim structure, were started to see (c). In the pellet periphery region at radial positions $r/r_0 > 0.90$, rim structure with a lot of fine pores and sub-divided grains were observed (d).

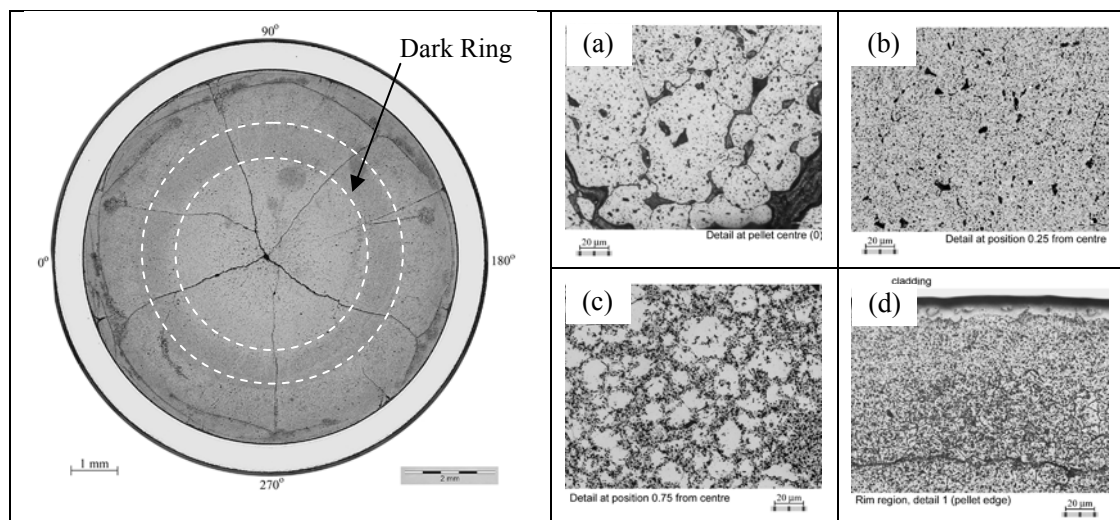


Fig 2. Ceramograph in radial direction from pellet center to pellet edge at positions; (a) $r/r_0=0$, (b) $r/r_0=0.25$, (c) $r/r_0=0.75$, (d) $r/r_0=1.0$, solid fuel in etched condition.

Fig 3 shows the radial distribution of grain size and number density of fine pores by image analysis of ceramographs. Grain size keeps as-fabricated grain size at intermediate zone of pellet cross-sections and decreases between $r/r_0=0.75$ and 0.90 due to formation of sub-divided grains. Number density of pores are almost flat up to $r/r_0=0.75$ and increases at pellet peripheral region.

Fig 4 shows the equivalent pore size distribution for each radial position. Pores less than $1\mu\text{m}$ are dominant at each radial positions, and number density of pores are increased clearly at pellet edge.

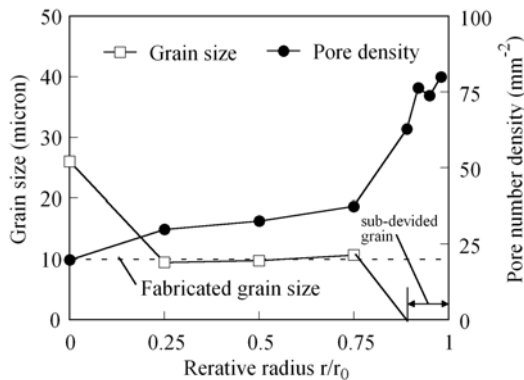


Fig 3. Radial distribution of grain size and number density of pores by image analysis

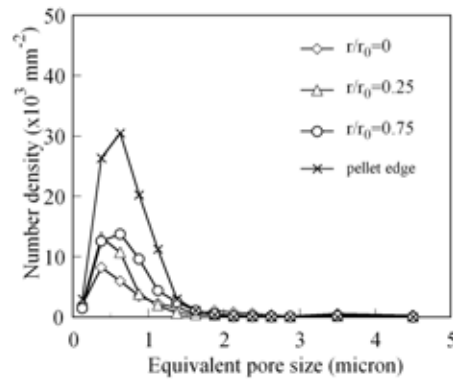


Fig 4. Pore size distribution at each radial position

It is well known that the increase of fine pores at rim structure causes the degradation of pellet thermal conductivity. NFI has developed a fuel performance analysis code to predict well higher burnup fuel rod irradiation behaviors, and this code is applied the pellet thermal conductivity model considered into the degradation of thermal conductivity with burnup and increase of pellet porosity in the rim region^{[1][2][3]}. The effect of rim structure on pellet center temperature evaluated by this model is shown in Fig 5. Temperature increase due to the degradation of thermal conductivity with rim structure formation was less than 10°C , which was quite small. Fig 6 shows the measurement and calculation of fuel centerline temperature for hollow UO_2 fuels. As shown in the figure, the thermal conductivity model developed by NFI could predict well a center temperature of the UO_2 pellet even in high burnup, which supported that the effect of rim structure formation on fuel temperature was very small.

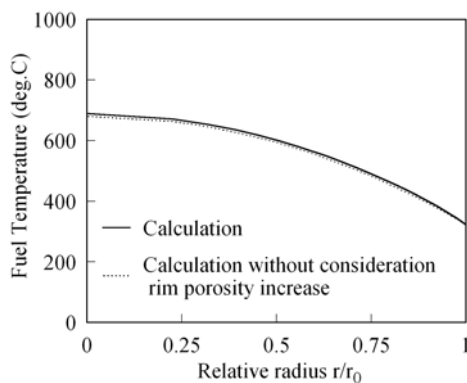


Fig 5. Influence of rim structure formation on fuel temperature, solid pellets at pellet burnup 80 GWd/t.

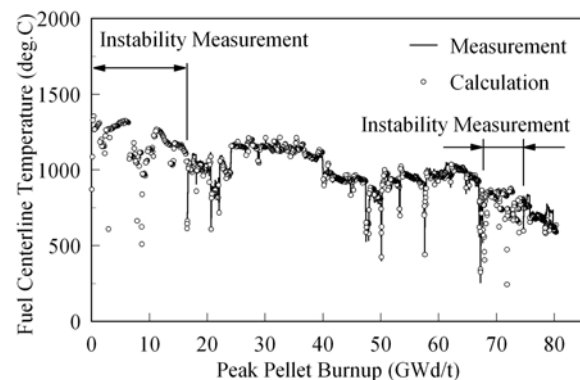


Fig 6. Fuel centerline temperature histories with hollow pellets

The correlation between pellet structure observed by ceramo-graphy and fuel temperature at several bunup is shown in Fig 7. Fuel temperature was estimated by NFI fuel performance code. Fuel center regions were experienced above 1600°C up to 27GWd/t , which caused the formation of pellet central void, columnar grains and equiaxed grains. At radial positions $0.5 < r/r_0 < 0.7$, it was observed the dark ring from overview, fuel temperature in this region was around 1000°C at 27GWd/t and 64GWd/t . At radial positions $0.75 < r/r_0 < 0.9$, it was observed partial formation of rim structure, fuel temperature

was between 700 and 1000 °C at 26GWd/t and less than 800 °C at the end of life. Then at radial position $r/r_0 > 0.9$, it was observed rim structure, fuel temperature was below 700°C through all the irradiation time. It is reported that the temperature threshold of the rim formation is around 1100°C by irradiation test of disk pellets at constant temperature [4], but in this study, temperature threshold of the rim formation was relatively lower. In case of a normal fuel rod irradiation, it is possible that the rim structure formation is effected by temperature change, radial temperature gradient, constraint condition and so on.

According to the change of grain size and number density of pores, rim width of this fuel was estimated about 500µm (1200 µm in case of including transient structure). This value was equivalent with the other data (Fig 8).

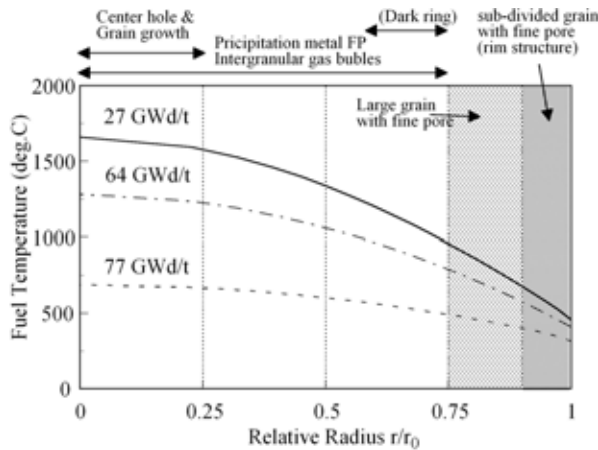


Fig 7. Relation between fuel temperature and observed pellet structure

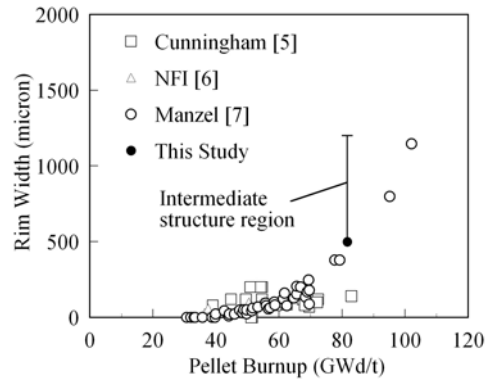


Fig 8. Burnup dependence of rim width estimated by ceramograph

Pellet density was measured by the buoyancy technique using xyrol. Test samples were cut from near ceramograph samples. The samples showed the chemical bonding at pellet peripheral, however, since the racking of pellet periphery for each fuel pieces was not seen, samples could be representative whole of a pellet with rim structure. Pellet densities were averaged for each sample.

Fig 9 shows the change of pellet density with pellet burnup. At high burnup region, it is reported that increase of swelling rate is occurred [7]. Decrease of pellet density in this study was larger than the expected value from typical swelling rate of 0.6 % per 10 GWd/t, and similar tendency to the other studies.

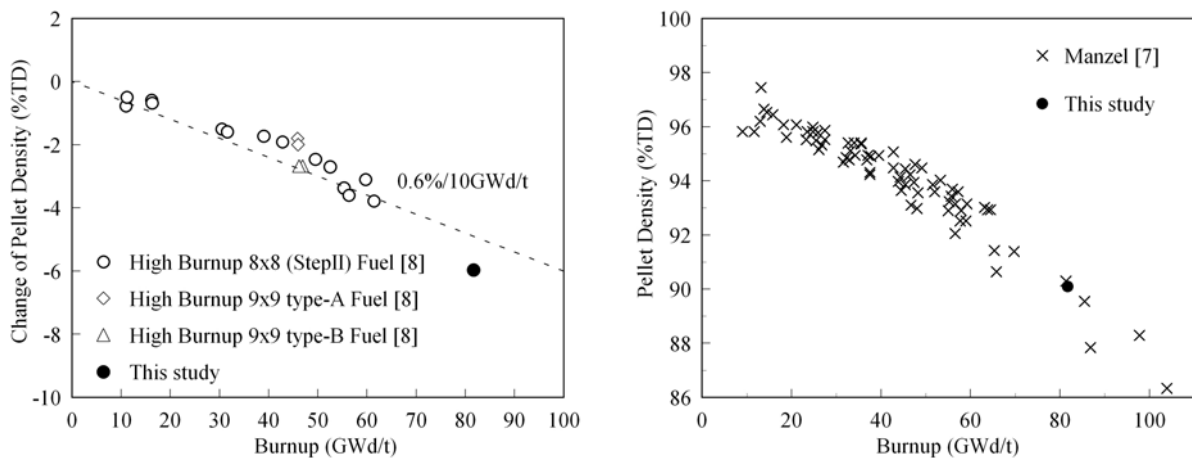


Fig 9. Pellet density as a function of pellet burnup

The fission gas release rate of solid UO_2 fuel by rod puncturing is shown in Fig 10. It is also compared with the recent measurement data of fuel rods on commercial reactor in the figure.

Fission gas release rate in this study was about 13%, which was relatively higher than the other data [8]. However, it is considered that fission gas release rate in this study is not anomaly because the fuel rods was experienced higher linear heat rate as shown in Fig 1 and axial peaking of 400mm segment rod is flat compared with commercial fuel rods.

Fig 11 shows rod inner pressure histories of solid UO_2 fuel under irradiation. In this figure, rod inner pressure at hot stand-by condition is represented, since rod inner pressure saturated at high burnup due to close to the limitations of PF instrumentation. Rod inner temperature at hot stand-by was about 5MPa, and it was supposed that rod pressure was about 6MPa at full-power under irradiation.

As rod inner pressure at EOL was well agreed with the measurement data by rod puncturing, it was confirmed that on-line data by instrumentations was correct.

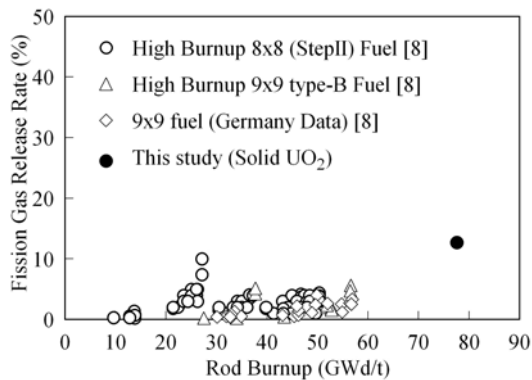


Fig 10. Relation between burnup and fission gas release rate of solid UO_2 fuel

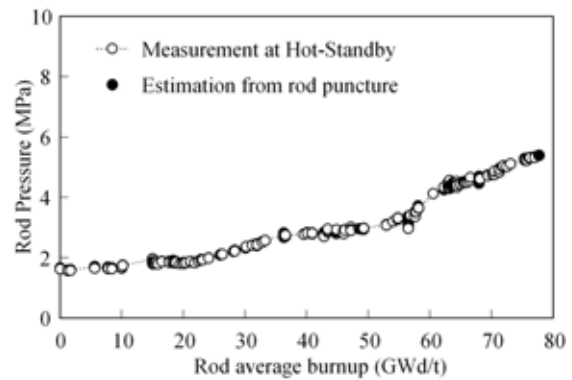


Fig 11. Rod inner pressure histories of solid fuel under hot-standby condition

Fission gas release histories estimated from the change of rod pressure data are shown in Fig 12. Remarkable increase of fission gas release rate was seen at the burnup between 25 and 35 GWd/t, 55 and 62 GWd/t respectively. Estimated fission gas release was well agreed with measurement data at EOL. Figure also shows estimated fuel centerline temperature of solid fuel rod. Fuel temperature was estimated by NFI fuel rod performance code. Vitanza threshold curve was well known as the correlation between fuel temperature and fission gas release [9]. As shown in the figure, fission gas release in this study was almost followed Vitanza threshold. However, at the burnup above 70GWd/t, fission gas release was slightly increased despite fuel centerline temperature was below the threshold. This result suggests that the fission gas release can be occurred in relatively lower temperature condition at high burnup. The increase of fission gas release rate in this region was estimated 2-3%.

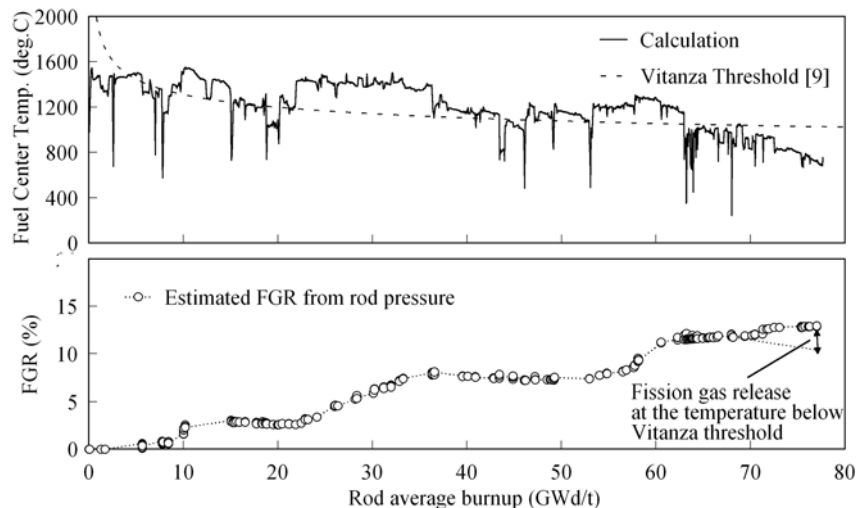


Fig 12. Estimated fission gas release histories

In the recent study, it is reported that fission gas release rate are increase at high burnup region over 50 to 60 GWd/t in spite of lower linear heat rate conditions^[7]. To explain of these phenomena, various models were proposed such as the tunnel effect due to the connection of accumulated intergranular gas bobbles or release from rim structure, and the data such as distribution of fission gas release in the pellet cross-section by EPMA and XRF techniques were obtained.

In the recent study, it is reported that the fine pores of rim structure keep the fission gas with high pressure and fission gas release from rim structure at pellet peripheral is very small.

Fig 13 shows the report of xenon concentration at pellet outer region (from $r/r_0=0.7$ to pellet edge) measured by XRF techniques^[10]. This result suggests that most amount of xenon contained fuel matrix was retained in pores of the rim structure due to the rim structure formation at bunup 75 GWd/t, and 20% of generated xenon is released to the rod free volume. Considering if the local fission gas release rate from rim region is about 20%, fission gas release from 500 μm rim region in this study was estimated less than 5% against the generated fission gas in the pellet cross-sections. On the other hand, it is reported that the increase of fission gas release at high burnup region is dominant from intermediate zone of pellet cross-sections ($0.4 < r/r_0 < 0.7$) as the results of EPMA measurements^[7]. Considering further increase of fission gas release from intermediate zone of pellet cross-sections in addition to the gas release from rim region, total fission gas release of fuel rod in this study is supposed to be higher than 5%. However, as it is mentioned before, the fission gas release in this study at burnup over 70GWd/t was estimated 2-3%. From the present data, the fission gas release in this region is not clear whether it was from rim region or intermediate region, but fission gas release in this study was relatively lower than the other data. In the future, SEM/EPMA will be performed and investigated the detailed fission gas release distribution in the pellet cross-sections.

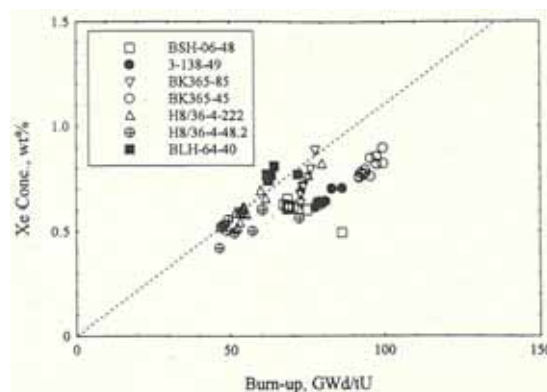


Fig 13. Local concentration of xenon by XRF technique as function of the local burnup^[10]

4. Conclusion

Fuel rods equipped with on-line instrumentations were irradiated up to pellet peak burnup 80 GWd/t in Halden reactor and destructive examinations, i.e. rod puncturing tests, ceramo-graphic examinations, pellet density measurements etc., were performed for irradiated fuel rods.

As the results of the ceramo-graphic examinations, heterogeneous structure with the grains surrounded by the fine pores were observed at relative radius $r/r_0=0.75$, and rim structure with a lot of fine pores and sub-divided grains were observed in the pellet periphery region at $r/r_0 > 0.9$. Rim structure was observed at pellet outer region of 500 μm , and fuel temperature in this region was below 700°C through the irradiation time.

Decrease of pellet density in this study was larger than expected value from typical swelling rate of 0.6 % per 10 GWd/t, and pellet swelling rate was increased at high burnup region.

Decrease of pellet density shows similar tendency to the other studies.

Fission gas release rate was relatively higher than the other data in the commercial reactors. However, it

is considered that fission gas release rate in this study is not anomaly since the fuel rods were experienced higher linear heat rate compared with fuel rods in commercial reactor.

Fission gas release histories in this study were almost followed Vitanza threshold. However, at the burnup above 70GWd/t, fission gas release was slightly increased despite fuel centerline temperature was below the threshold. This result suggests that the fission gas release can be occurred in relatively lower temperature condition at high burnup. The increase of fission gas release rate in this region was estimated 2-3%, which is relatively lower.

5. References

- [1] K.Ohira, et al., "Recent Experience and Development of BWR fuel at NFI", AESJ 2005 Water Reactor Fuel Performance Meeting, Kyoto, Japan, 2005.
- [2] M.Owaki, et al., "DEVELOPMENT OF A FUEL ROD THERMAL-MECHANICAL ANALYSIS CODE FOR HIGH BURNUP FUEL", IAEA Technical Committee Meeting on Nuclear Fuel Behavior Modelling at High Burnup and its Experimental Support, Windermere, UK, 2000.
- [3] N.IKATSU, et al., "Influence of RIM Effect on Fuel Center Temperature", IAEA Technical Committee Meeting on Fuel Chemistry and Pellet-Clad Interaction Related to High Burnup Fuel, Nyköping, Sweden, 1998.
- [4] M.Kinoshita, et al., "HIGH BURNUP RIM PROJECT:(III) Properties of Rim-Structured Fuel", ANS International Topical Meeting on Light Water Reactor Fuel Performance, Orlando, Florida, 2004.
- [5] M.E.Cunningham et al., "Development and characteristics of the rim region in high burnup UO₂ fuel pellets", Journal of Nuclear Materials, 188, pp.19-27, 1992.
- [6] N.Itagaki, et al., "Experience and Development of BWR Fuel Supplied by NFI", ANS International Topical Meeting on Light Water Reactor Fuel Performance, Park City, Utah, 2000.
- [7] R.Manzel, C.T.Walker, "HIGH BURNUP FUEL MICROSTRUCTURE AND ITS EFFECT ON FUEL ROD PERFORMANCE", ANS International Topical Meeting on Light Water Reactor Fuel Performance, Park City, Utah, 2000.
- [8] Y.Hirano, et al., "Irradiation Characteristics of BWR High Burnup 9x9 Lead Use Assemblies", AESJ 2005 Water Reactor Fuel Performance Meeting, Kyoto, Japan, 2005.
- [9] C.Vitanza, et al., "Analysis of Fission Gas Release Tests to High Burnup", ANS International Topical Meeting on Light Water Reactor Fuel Performance, Portland, Oregon, 1979.
- [10] M.Mogensen, et al., "Behavior of fission gas in the rim region of high burn-up UO₂ fuel pellets with particular reference to results from an XRF investigation", Journal of Nuclear Materials, 264, pp99-112, 1999.

6. Acknowledgements

This study was carried out as a joint research program with the following Japanese BWR utilities: Tokyo Electric Power Company, Tohoku Electric Power Company, Chubu Electric Power Company, Hokuriku Electric Power Company, Chugoku Electric Power Company and the Japan Atomic Power Company. The authors wish to thank all the personnel concerned from these organizations for their efforts and support.

LEAN SIX SIGMA

J. PORTER, A. LINGENFELTER

Global Nuclear Fuel

3901 Castle Hayne Road, Wilmington, NC 28402 – USA

ABSTRACT

Lean Six Sigma is a combination of a world renowned statistical improvement systems with a simple, common sense, “just try it” methodology approach to drive growth within GE. Six Sigma has been utilized within GE for well over a decade now, driving process improvements within our organization that impact our customer’s “critical to quality” needs. “It is the way we run our business”. Lean has been in practice within GE for years, however, it has just recently risen to new heights in order to simplify our manufacturing processes. Most recently we have begun to utilize Lean to streamline our “knowledge flow” or transactional processes throughout the business. Together these two methodologies are a powerful set of tools that will drive simplification, solutions to complex problems, and most importantly customer satisfaction. In GE Nuclear we have utilized Lean Six Sigma to drive change in manufacturing, engineering, sourcing, logistics, services, and are reaching to other key functions of the business such as IT and HR. In 2006 we expect to utilize Lean Six Sigma tools in every functional area of the business. In addition to the numerous projects that individuals are working on, the business has over 75 AWOs (Action Work Outs) planned for this year to drive Lean “thinking” into our processes.

Some examples of where Lean Six Sigma has impacted our business and benefited our customers are our World Class Ceramics shop, and our two Model Lines in Channels and Bundle Assembly. In 2005 the Ceramics team set a target to increase yields and thus productivity and throughput. The team developed a pareto of defects and closely monitored the reasons for these defects to focus on their elimination. The team was able to develop a method for timely defect recognition and reporting that ultimately led to defects being stopped earlier in the process. This resulted in an increase in yields from 88% to 93%. The two Model Lines are areas of continuous improvement utilizing all of the tools from Lean. To date, the Channels area has developed standard work practices and set standard Work in Process targets. This has resulted in a reduction of inventory and Lead Time of 48%. The Bundle Assembly area is also currently concentrating on standard and combination work, evaluation of Cycle Time vs. Takt Time, and manual and automated productivity increases. Because both areas are Model Lines, Kaizens “change for the better” will continue in order to bring our customers the best quality of product and the best value.

1. Introduction

The foundation of Lean Six Sigma is to look at products/services through the customer’s eyes and determine how improvements can eliminate “waste”. Lean Six Sigma follows a rigorous process of **DEFINE...MEASURE...ANALYZE...IMPROVE...CONTROL**. Through this process we identify the 7 types of waste.... Overproduction, Inventory, Extra Processing, Motion, Defects, Waiting, and Transportation. A team is formed to conduct an Action Work Out to implement improvements that will eliminate the waste. Because “Waste creates Waste” we must continuously Kaizen (change for the better) in order to simplify and streamline our processes. We excel to model the Toyota Production System (TPS) with the assistance of Shingijutsu consultants that teach us the Lean system. TPS consist of many different tools that, when used

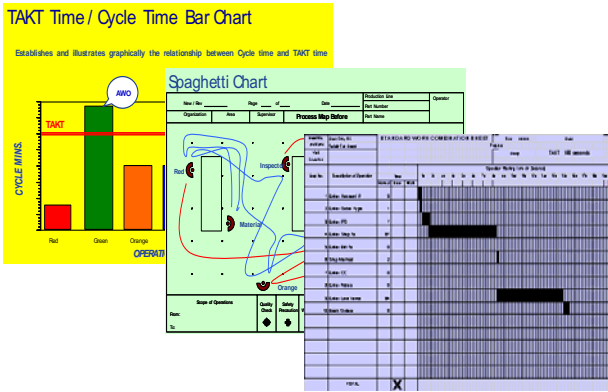
together, will minimize Lead Time, and Inventory, while maximizing productivity through “Flow”. “Flow” is the process by which we are able to implement Just in Time philosophies in order to meet our customer’s expectations when and only when they request the product or service.

2. The House of Toyota

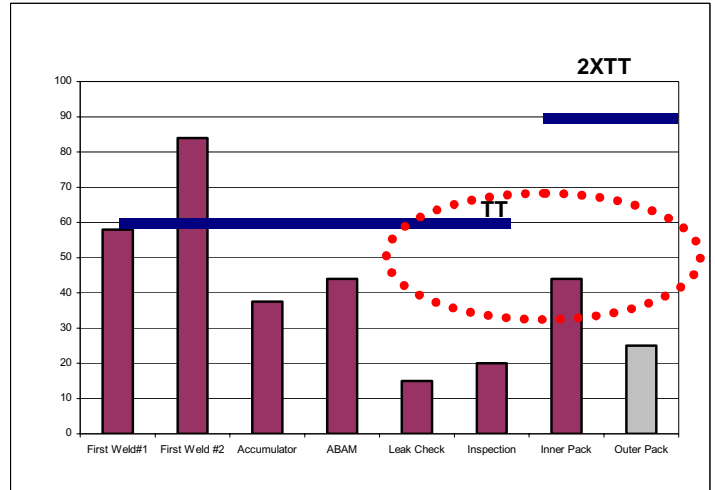
The House of Toyota consists of a foundation and two pillars. Combined these make up the Toyota Production System. The foundation rests on Customer First, Respect for Humanity, Simplification Philosophies, Elimination of Waste, and Hejunka (Level loading of the production processes). Viewing our processes through our customer helps us understand the difference between Value Add and Non-Value Add. Also, because most customers want the product/service when and only when it is right for them, we must implement Hejunka in order to minimize our cost and maximize output while maintaining customer satisfaction. The two pillars are identified as Just in Time and Jidoka. Lean manufacturing started through the identification of defects. Through detection methods, abnormalities are stopped at the point of origin and corrected prior to continuing to the next process. This concept is known as Jidoka. Today at Global Nuclear Fuels we have many examples of Jidoka (defect detection) throughout the factory. These consists of automated equipment that has built in “human intelligence” and will stop the machine when an abnormality is detected, and visual or audible indicators to notify the operators of a problem. GNF also has implemented several in process quality checks while assembling the fuel bundle to assure that not only are the correct parts used, but that they are positioned correctly and free of defects prior to proceeding. This enables early detection of a defect and minimizing man-hours, re-work, and the risk of not meeting our customer’s expectations. The final pillar is referred to as JIT or Just in Time. JIT consists of 3 elements; Takt Time Production, Single Piece Flow, and Pull. Takt Time is a mathematical calculation to determine the frequency at which we need to have 1 unit produced in order to satisfy our customer demand. Takt Time therefore is a ratio of customer unit demand and the amount of available time in the factory to produce these units. Once the Takt Time is calculated, effort is concentrated on equalizing all process steps and to meet Takt Time as close as possible. By implementing this philosophy we can “flow” parts one piece at a time, minimize the Work in Process (WIP), increase our productivity, and most importantly meet our customer demand. In many manufacturing processes this is not an easy task. In these instances the Lean solution is to implement “Pull”. A Pull system institutes methodology such that process steps are performed only when indicators put in place determine the need. Through this method single piece flow is still possible while keeping WIP to a minimum.

3. Standardization

One of the first and most crucial elements of Lean is to Standardize the process. In GNF we have worked tirelessly to implement Standard Work in our operations. Through standardization GNF has removed variability in our processes that allows us to improve our yields. In Bundle Assembly the 3 Tools of Standard Work shown below on the left, enabled the team to maximize productivity and output.

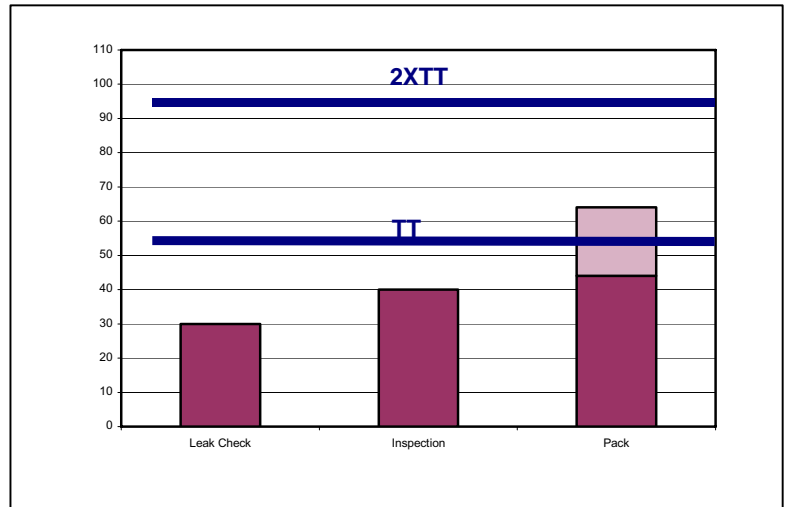


BEFORE



When all of the tasks in the shop were evaluated for cycle time vs. demand and available operator time, the shop was able to determine opportunities for improvements. Through the use of the Combination sheet the team was able to realize a 20% improvement in operator productivity, a 50% reduction in non-value added work, and a \$300K reduction in Work in Process.

AFTER

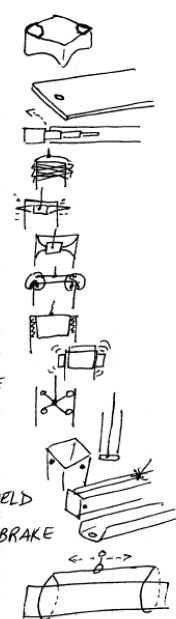


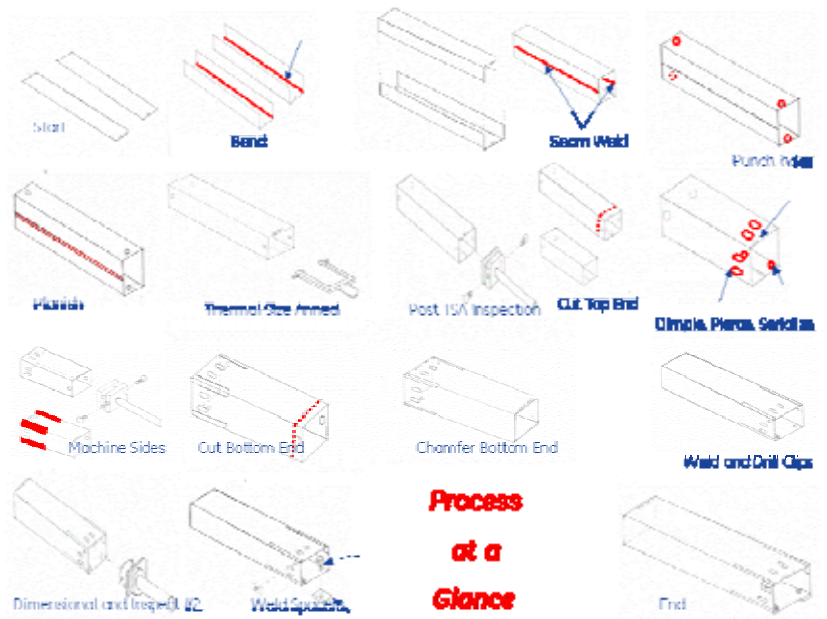
4. GNF's Model Lines

Global Nuclear Fuels currently has 2 Lean Model Lines, Fuel Bundle Assembly and Channel Fabrication. A Lean Model Line is an area in which all of the Tools of the Toyota Production System are applied over time. The Channels Model Line was started in January 2005 with 5S methodology in order to better organize the shop. The team then focused on Standard Work in Process by establishing lot sizes of 5 throughout most process steps...this is equivalent to the

Thermal Size Anneal furnace batch size. By implementation of SWIP the team was able to reduce inventory levels by 45% and ensure that the bottleneck process, TSA, continued to run at all times. Most recently the team performed a 3P (Production...Preparation...Process) AWO. The team utilized several Lean tools including 7 ways (below left), a Pugh matrix, and a Process at a Glance (below right) in the elimination of 2 process steps. Below you can see the team's ideas of lifting a Channel differently from today's methodology throughout the process. The team utilized the Pugh matrix to eliminate any safety concerns with the lifting methods and then actually went to the floor and built fixtures and experimented with new ways. In conclusion the team was able to realize a 50% reduction in cycle time on 2 process steps and a \$130K reduction in scrap material.

SEVEN WAYS

- 1) PUT CLIPS ON EARLIER
 - 2) STRIP VENDOR PUNCH HOLES
 - 3) TELESCOPING UP-ENDER
 - 4) CHINESE FINGER PRISON
 - 5) PIERCING GRAPPLE
 - 6) SUCTION GRAPPLE
 - 7) PLATE DOG GRAPPLE
 - 8) BOAT PLUG GRAPPLE
 - 9) MAGNETIC GRAPPLE
 - 10) TOGGLE CLAMP GRAPPLE
 - 11) BOTTOM PULL
 - 12) LIFT BY SPACER HOLES
 - 13) PUNCH HOLES AT SEAM WELD
 - 14) FORM IN HOLES AT PRESS BRAKE
 - 15) COFFEE CUP HANDLE
- 



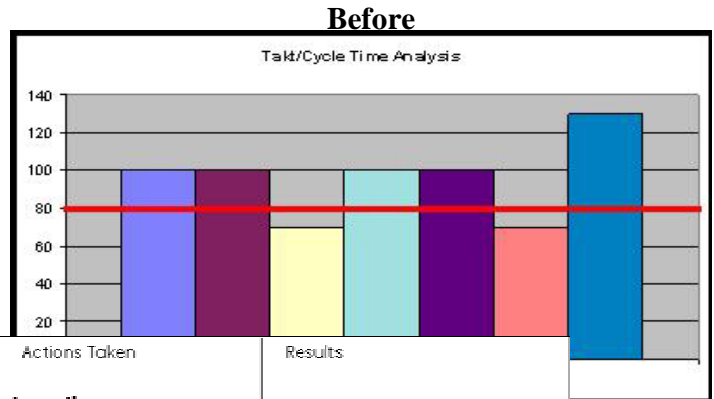
Currently the team is working on the analysis of the Takt Time vs. Cycle Time chart throughout the Channels process. Through level loading of the process steps and rearrangement of any necessary equipment, the team believes single piece flow is possible. The benefits of single piece flow consist of lower inventories, meeting the exact customer demand, higher yields, and maximizing use of all resources including both personnel and equipment.

5. Knowledge Flow

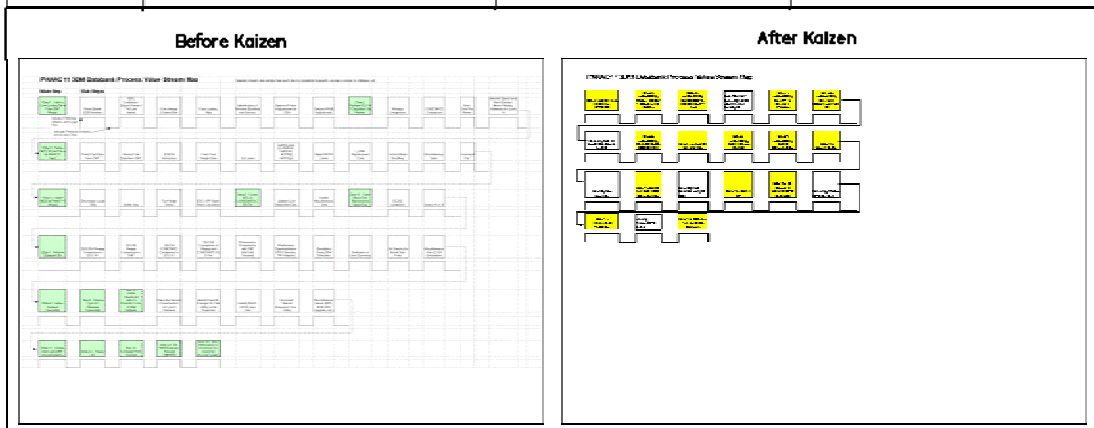
GNF in 2006 has started to realize the benefits of Lean Six Sigma in the non-traditional manufacturing areas. Functions like Finance, Sourcing, Engineering, IT, and HR can and have all realized the benefits of Lean. While waste is much more difficult to see in transactional flow, the Lean tools are applied in a similar manner. The Engineering team recently looked at simplifying the Fuel Databank process. Through the creation of the Value Stream Map, the team was able to determine the value added and non-value added steps. The team was able to eliminate 355 manual process steps by having the data automatically loaded, this was equal to 84% of the total

steps required. The team was also able to eliminate 11 of the 16 different software systems used for this process making the engineer's job much easier. This will result in a 70% reduction in the number of hours required to process the customer's request.

Value Stream Map



Operation	Problem	Actions Taken	Results
Databank Generation Process	<ul style="list-style-type: none"> • Non-Standardized Process • Many Manual Steps • Extensive Verification • Multiple Input Sources 	<ul style="list-style-type: none"> • Automation • Consolidate Input Location 	<ul style="list-style-type: none"> • Process Standardization • Automated Verification • Elimination of Manual Input <p>(355 steps eliminated)</p>



6. Summary

GNF is making great strides on our Lean Six Sigma journey. Through the help of the Shingijutsu consultants and the dedicated work of the employees we are realizing the tremendous benefits of Lean Manufacturing. Together the team continues to change the culture and drive simplification through AWOs and Lean philosophies. In 2006 alone, the team will conduct over 70 AWOs and invest 16,800+ man-hours implementing Lean improvements in order to improve our customer service.

7. References

1. *GE Lean 201/202 Lean Training* by Rick Guba, GE Transportation MBB, rev 03222006

AREVA NP FUEL MANUFACTURING INVESTS FOR THE FUTURE TO ENSURE SECURITY OF SUPPLY TO ITS CUSTOMERS

CHRISTIAN DELEVALLEE, ALAIN LACOSTE, JEAN-FRANCOIS

MARROT

AREVA, FBFC

Les Bérauds, BP1114

26104 Romans Cedex - France

HANS-UWE SIEBERT

AREVA, AREVA NP

Tour AREVA

92084 Paris la défense

France

ABSTRACT

FBFC's Romans plant, which belongs to the Fuel Manufacturing Business Unit (FMBU) of the AREVA NP Fuel Sector, has been manufacturing nuclear fuel since 1976. The cumulative production of FBFC is roughly 30 000tU, which amounts to about 62000 assemblies.

An investment of about 100 million euros over the 2004-2008 period will lead to the complete renewal of the production capability, while meeting the more stringent requirements in terms of safety, radiation protection and environment. The following key safety commitments are integrated into the design of equipment and buildings:

- Incorporation of the experience feedback from the past 10 years
- Personnel radiation exposure less than one quarter of the regulatory limits
- Reinforcement of the earthquake resistance of the buildings, improvement of their segmentation and fire protection,
- Ergonomic approach to workstations and credit taken for the human factor in plant operating processes,
- Automation of the safety functions
- Reduction of solid waste and both liquid and atmospheric releases.

The introduction of state-of-the-art technologies into a continuous production process has called for the re-definition of production organization and the adaptation of competency profiles, with the aim of guaranteeing their effectiveness.

In parallel to this renewal initiative, the governmental authorization was revised in March 2006 to raise the authorized capacity to 1800 tU for the Conversion Line and 1400tU for the Pelletizing/Assembling Line (formerly 1200 and 820 tU respectively).

This significant investment reinforces the long-term security of supply which the AREVA NP Fuel Sector offers to its customers.

1. Preparing the future with regular upgrading of the industrial tool

In a general context of increasing demand for nuclear energy supply, fuel assembly security of supply and reliability appear more than ever as key points for all players in the nuclear fuel activities.

Thanks to its worldwide integrated and customer-oriented organization and to its up to date industrial tool, the AREVA NP Fuel Sector ensures flexibility and a strong procurement security for the supply of fuel assemblies to its customers.

This program focuses on three progress areas:

- Develop the versatility of the production units and their flexibility,
- Strive for the best industrial practices within the various plants, and their general application.
- Modernize the facilities.

In this context, an investment of about 100 million euros over the 2004-2008 period will concern the manufacturing plant of Romans (France). It will lead to the complete renewal of its production capability, while meeting the more stringent requirements in terms of safety, radiation protection and environment fulfilling AREVA's commitment to Sustainable Development.

It aims to achieve three main objectives:

- Meet the most demanding standards in the fields of nuclear safety, radiation protection and environmental protection
- Reduce the manufacturing cycle time of the assemblies
- Introduce as far as necessary the latest technologies originating in the best industrial practices.

It will result in improvements in different aspects : personnel radiation exposure less than one quarter of the regulatory limits, reinforcement of the earthquake resistance of the buildings, improvement of their segmentation and fire protection, automation of the safety functions, reduction of solid waste and both liquid and atmospheric releases.

In parallel to this renewal initiative, the governmental authorization was revised in March 2006 to raise the authorized capacity to 1800 tU for the Conversion Line and 1400tU for the Pelletizing/Assembling Line (formerly 1200 and 820 tU respectively).



The Romans plant (France) produces UO_2 powder, pellets, fuel rods and fuel assemblies for PWRs. The plant is licensed to process uranium up to 5.0 wt% ^{235}U . In a separate shop, lower and upper tie plates are produced for PWR fuel assemblies.

Romans site is ISO 9001, ISO 14001 certified and achieved OHSAS 18001 certification.

The Romans factory, built in the first half of the seventies, has used 16000 tons of uranium to manufacture about 32000 fuel assemblies.

2. The Technology

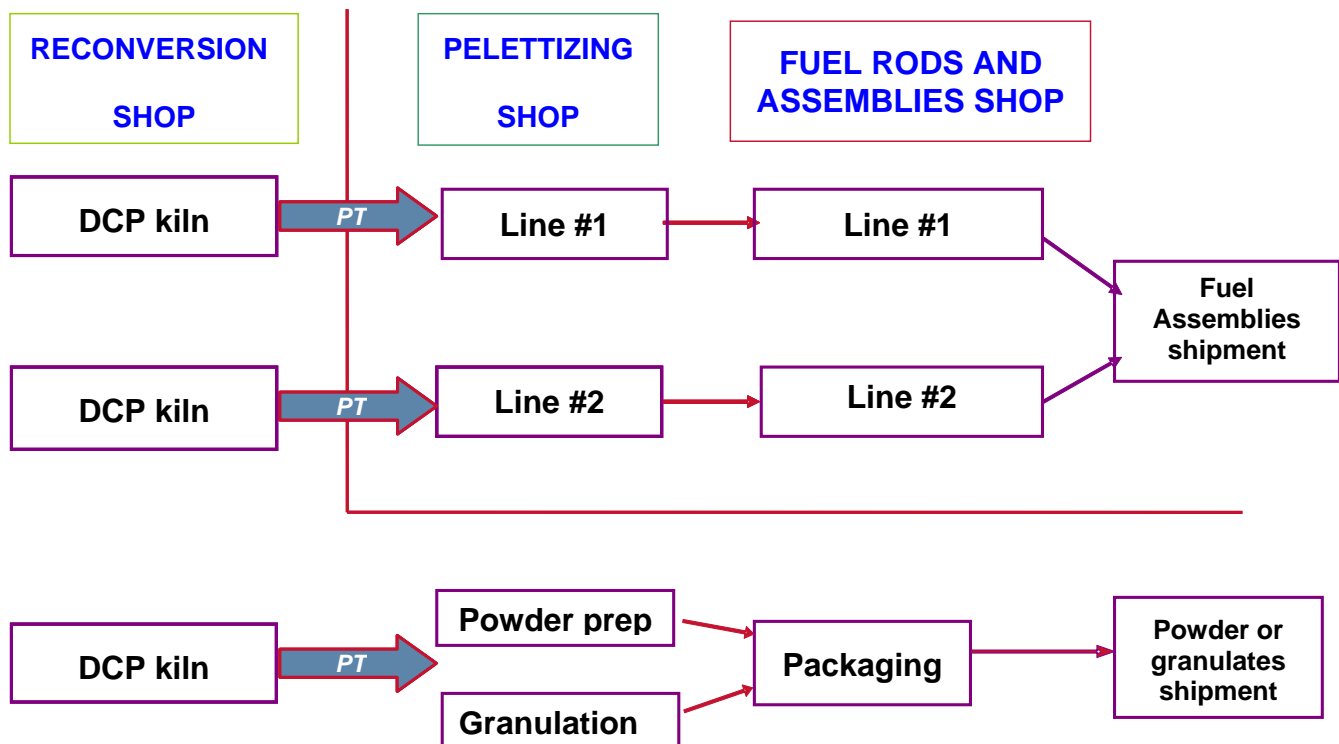
The introduction of the latest technologies particularly concerns instrumentation/control and supervision. It is accompanied by a review of the work and control stations.

These new technologies will enable, in particular :

- more extensive automation of the production lines and inspection operations ,
- fully computerized traceability with real-time compliance processing at each process step,
- general application of on-line statistical process control tools,
- maintainability studies and the development of predictive maintenance.

3. Reducing the manufacturing cycle

The reduction of the manufacturing cycle time will be obtained by putting the process on line, accompanied by the elimination or drastic reduction of intermediate stocks and the automation of the product transfers between work stations. As an illustration, all the powder movements will be by means of pneumatic transfers. This speed-up of flow is also achieved by cutting the number of equipment and setting up larger-capacity equipment (conversion kilns and pelletizing).



4. Safety, radiation protection and environment requirements

By building its "new" Romans plant, AREVA is giving itself the means to become a worldwide benchmark in terms of nuclear security and safety.

The whole project has been conceived to exceed the regulatory requirements in all areas. Our buildings, extensively reinforced, will meet the strictest earthquake standards. The radiological exposure of the employees will be four times less than the regulatory limits. The automation of the safety-important actions and the ergonomics of a centralized control room will significantly reduce the risk of human error. The improved confinement of all the facilities working with nuclear material will provide a further protective barrier.

Beyond these enhancements and thanks to the heavy involvement of the Romans teams in this project, the whole safety culture of the plant and of its personnel is moving forward.

The safety approach was conducted by systematically covering, for each equipment item, or part of the process, the potential risks as listed below:

- . Nuclear risks:
 - risk of disseminating radioactive materials
 - risk of exposure to ionizing radiation (external and internal exposure)
 - risk of criticality.

- . *Internally-generated non-nuclear risks:*
 - risk of fire
 - risk of explosion
 - chemical risk
 - handling-related risk
 - risk arising from loss of utilities
 - risk arising from human factors
 - ageing-related risk.
- . *Externally-generated non-nuclear risks*
 - Earthquake.

Then, for each of these risks, safety options were defined. The enforcement of these options is defined through safety standards. A few examples are given below.

Earthquake:

The selected options are:

- maintain sub-critical conditions
- maintain nuclear material confinement
- maintain hazardous chemical material confinement
- ensure there are no outbreaks of fire in the nuclear buildings.

This has led us to:

- . Recalculate the earthquake resistance of the buildings and strengthen many of them;
- . size the equipment items accordingly, depending on their function (from non-mixability to the retention of active functions) ;
- . set up earthquake detection systems and the associated automatic devices for isolating hazardous fluids and the power supply.

Chemical risk:

The selected options are:

- minimize the risk arising from UF₆ vaporization
- observe the personnel exposure limit value in the HF treatment station.

This has led us to:

- . Replace the ovens in the conversion workshop by autoclaves, which means putting an additional barrier between the UF₆ and the environment;
- . Install a new, more reliable and higher-performance vaporization room purification column; the scrubbing of gases with potassium is replaced by scrubbing with borated water.

Internal and external exposure:

The selected options are:

- internal plus external dose less than 5 mSv/year for the whole workforce
- no mask worn for routine manufacturing operations.

This has led us to:

- . Switch from a ventilation system providing air flow and direction at the openings to a ventilation system ensuring a negative pressure cascade
- . Segregate the building and process ventilation networks
- . Systematically provide a dual confinement:
 - first confinement between material and personnel
 - second confinement providing back-up to the first if it fails
- . Limit confinement breaks
- . Clean the equipment thoroughly
- . Develop a new type of dynamic confinement for powder container docking
- . Develop the networking of atmospheric contamination monitors
- . Develop a methodology for predicting internal and external doses.

Handling:

The selected options are:

- limit handling operations
- automate or diminish the risks for the remaining handling operations.

This led us to:

- . Use a guided trolley instead of a hoist for handling the UF₆ cylinders
- . Set up pneumatic transfers to limit the use of powder containers
- . Systematically load green and sintered pellets into boats and use self-guided trolleys to handle these boats.

Human factors

A particular effort was made to reduce the risk arising from human factors, by selecting in particular the option of eliminating any manual control which could lead to a safety risk upon single failure.

This led us to:

- . Automate safety-important actions (with independent sensors and wired logic)
- . Design the workstations with a human factors expert
- . Build a centralized control room.

Waste issue

Lastly, it should be noted that, as a by-product of this project, the Romans factory is conducting an aggressive policy of reducing the volume of waste production.

This made it possible in early April 2006 to shut down the incinerator, which would have been difficult to bring to the same safety level as the rest of the plant.

As a result, the gaseous release activity level of the plant will decrease from 6.1 % to 1.5 % of the limits authorized by the governmental decree of June 22nd 2000.

5. An upgraded and optimized industrial tool to the benefits of AREVA's customers

By end 2008, at the end of the renewal project, AREVA will have available at the Romans site a "new" plant within strengthened buildings.

A world-class plant, with high flexibility, extensively automated with a high safety level exceeding the most demanding standards.

This plant will be operated by highly reactive teams with renewed competencies, a plant ready to take up the challenges of the twenty years to come.

As a unique integrated fuel assembly manufacturer, setting high priority on security and environment and fully committed to Sustainable Development, AREVA establishes itself as a long-term reliable supplier, so contributing to a globally increased long term security of supply for all players in the nuclear fuel industry.

ZIRCONIUM PRODUCT MANUFACTURING WITHIN AREVA: A KEY ELEMENT FOR THE NUCLEAR FUEL SUPPLY CHAIN

J-P. GROS , R. DOUBLET

AREVA, CEZUS, a subsidiary of AREVA NP
Tour AREVA, 92084 Paris La Défense Cedex, France

ABSTRACT

Zirconium Business unit is a core component of AREVA to ensure the integrity of the nuclear fuel supply chain. Zr BU business philosophy is to master the entire zirconium process route from ore to final components including research and development of new alloys and technologies. We view it as the only means to obtain a safe supply of outstanding quality zirconium products. Preparing the future of Nuclear Energy is also a long term approach and win-win customer relationship and sustainable development are both strategic enablers. The past years have seen the complete amalgamation of all Zr units of the Areva group under one unified leadership, a complete rethinking of our organizational approach and implementation of a global QSE system. Zr BU is now a leading zirconium supplier well prepared to tackle challenges associated with a sharp growth in a economic context marked by the necessity of efficiency and risk prevention.

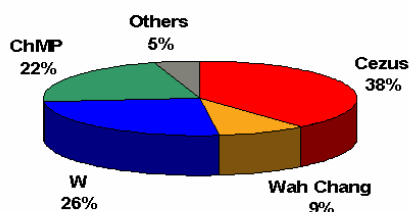
Introduction

In a general context of increasing energy shortage worldwide and of renewed interest for nuclear power plants as a reliable and greenhouse effects free energy supply source, nuclear fuel reliability and safety on one hand and potential to secure increased demand appear more than ever as key points for all players in the nuclear fuel activities to achieve the Nuclear Renaissance we are all now expecting and preparing for. This paper will present Zirconium activities within Areva, describes Zirconium specific manufacturing processes and develop our organizational approach for now and the future.

Zirconium activities within AREVA

Within the AREVA group, fuel assembly manufacturing industrial chain - including Zirconium product supply - has always been considered as a strategic issue and a core competency. AREVA NP Zirconium Business Unit is the world leader in Zirconium products manufacturing , with a completely integrated process route from zircon sand to finished products such as channel and spacer strips, endplug barstock, thimble and cladding tubes, bars and tube products.

Nuclear zirconium semi-products market shares by supplier (2005 figures in %, including Russia)



→ Cezus world leader

→ Three main suppliers nuclear integrated

BWR and PWR reactors.

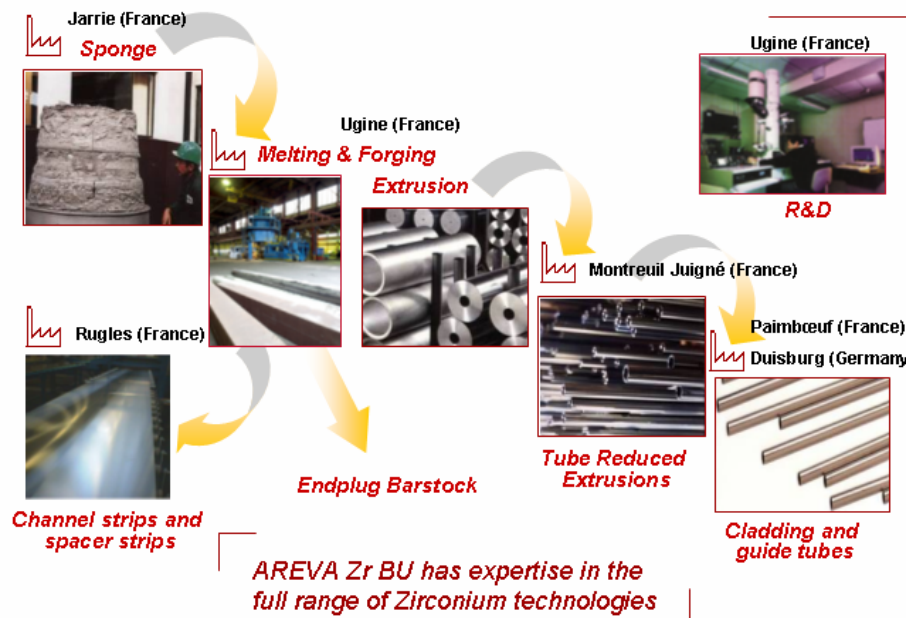
Zirconium manufacturing activities comprise Cezus in France with 5 facilities (Jarrie, UGINE, Rugles, Montreuil-Juigné and Paimboeuf) and ANF Duisburg in Germany with the largest combined capacity in the world for nuclear grade zirconium sponge, zirconium alloys semi-products and nuclear fuel tubings. We supply approximately 40% of all nuclear grade zirconium with respect to worldwide needs (including ex-USSR and India) and 30% of tubing market. Product range is specialized for

Zirconium manufacturing process

Our process starts with the import of premium grade zircon sands from Australia, South Africa and United States at our Jarrie plant near Grenoble. Jarrie plant processes zircon sands first in hafniated zirconium tetrachloride by carbochlorination, then separates Hf from Zr through its state of the art patented distillation in molten salts process before reducing low Hf Zirconium tetrachloride in zirconium sponge via the kroll reduction process. Hafnium tetrachloride is in parallel transformed into metal by electrolysis for the production of nuclear grade hafnium used in control rods and blades. Key elements of this plant are the use of the most efficient process worldwide from an environmental point of view and the largest sponge capacity (2200 tons of sponge annually). Bulk of sponge production is then shipped to Uginé plant while significant quantities are sold in the open market for both nuclear and aerospace applications.

Next step is Uginé, located near Albertville in the French Alps where raw material preparation, melting, forging and extrusion are performed. Output is above 5000 tons of zirconium alloys ingots – having in mind that triple Vacuum Arc Remelting is required to remove all impurities and ensure analytical homogeneity along the length of ingots while growing the weight of ingots up to 6,3 tons in order to facilitate forging steps. One key area of Uginé is also its important recycling activity with above 1000 tons of zirconium scraps produced internally and shipped back by customers reincorporated in the raw material supply chain. Average recycling ratio within our ingots is now consistently above 40% with complete analytical mastering. In the coming years a specific innovative approach is being implemented in order to find a way to recycle or dispose in an intelligent manner of all zirconium scraps and wastes within the whole of the Zr Business Unit and other units of the AREVA NP Fuel Sector. Recycled products which are not compatible with the quality standards of the nuclear activity are segregated and sold in the industrial market for applications such as alloying. Last but not least, Uginé plant also shelters our barstock workshop where endplugs bars are produced.

A fully integrated nuclear oriented supplier



Our normand factory, located at Rugles receives slabs from Uginé and manufactures all flat products in nuclear grade zirconium and hafnium: hot-rolled plates, square bars, channel strips and spacer strips for assembly components in PWR and BWR fuel.

Finally the mainstream plants with Montreuil-Juigné plant, near Angers, Paimboeuf factory, near Nantes and Duisburg factory near Düsseldorf manufacture cladding tubes and guides tubes. Paimboeuf and Duisburg mills have an amalgated capacity above 7000 km a year. Key manufacturing processes are pilgering, heat treatment and finishing operations (dimensional and visual inspection, eddy current and ultrasonic testing). Montreuil-Juigné is specialized in intermediate pilgering steps while Paimboeuf and Duisburg produce the final components. Guide tubes will serve as part of the PWR fuel assembly skeleton, while cladding tubes – along with endcaps machined from barstock – will serve for the fuel rods that contain uranium or mixed oxide pellets.

Zirconium Business Unit organization

The decision to organize all AREVA Zirconium activities under one single leadership has been guided by two cornerstones of the group's strategy (AREVA WAY):

- Customers satisfaction first and foremost. We always seek to build enduring win-win long term relationship promoting whenever possible partnership. Continuity in our strategy for more than 20 years is the best proof of this dedication.
- Sustainable Development: to ensure our long term future, a company must sell quality products and services in a profitable, safe and sustainable way. Under ever more stringent environmental regulations and in view of the Nuclear Renaissance to come this is what we think is the best way to adress the market.

In the past years – since 2000 - the amalgation of Cezus, Zircotube (Paimboeuf tubing plant) and ANF Duisburg has enhanced our product portfolio and expertise. In a very competitive global nuclear market, yet market by overcapacity, scale economies are key to profitability and investment. Gaining major status is our current answer to the current market climate and it guarantees our customers' long term supply.

To ensure optimum reactivity with customers, Zirconium activities have been organized into Product Lines. An Upstream Line – made up of Jarrie and Ugine plants, supplies its semi-finished products to the downstream product lines directly serving our customer base:

- Flat product line in Rugles
- Barstock product line in Ugine
- Tubing Line in Montreuil-Juigné, Paimboeuf and Duisburg.

More recently, to optimize its industrial organization and to enhance customer service (quality, supply chain and technical assistance), the Zirconium Business Unit has implemented widespread programs for deployment of a global integrated management of our tubing plants, multi-year cost reduction action plan and process optimization through accelerated best practice sharing.

In addition implementation of our common fuel components strategy leads to an upgraded product portfolio which will enhance in-reactor performance while at the same contribute to reinforce flexibility and quality. Zr BU research and development competencies and capabilities are key success factors in the design of future advanced zirconium alloys (next generation quaternary alloys but also continuously improved M5) as well as for state of the art mastering of manufacturing processes through modelization and 6-sigma initiative. Customer focus is promoted through the practice of regular customer surveys and specific training initiatives such as our new "Customer recognition program". Customer, Technology and Quality are at the heart of our vision.

As a key player in the nuclear industry, Zirconium Business Unit has set high priority on security and environment, fulfilling AREVA's commitment to Sustainable Development. All Zirconium manufacturing sites are now ISO 14001 certified while Jarrie and Duisburg already obtained their

OHSAS 18001 certification. Continued emphasis and investments in the mid to long term will maintain momentum on those programs. Special attention has been given and will continue to be given on energy, water and consumables savings, zirconium fire prevention, scrap and waste recycling.

A long term reliable supplier

We have already demonstrated in the past years that we were capable to invest heavily and successfully to develop our production capacities, develop state of the art equipments, reduce and prevent environmental hazards, recycle and treat scraps and wastes.

Next challenges for AREVA Zirconium Business Unit will be to adapt ourselves in order to be ready for the challenges to come when the Nuclear Renaissance will start to put additional pressure on our capacities. Preparing and shaping us for this future is an ambitious task which will encompass in the ten coming years regular review of our industrial capabilities worldwide, renew and develop our core competencies especially hiring new talents worldwide and paving the way with you for the introduction of advanced new products for a more efficient, safer and environmentally sound nuclear energy. Special attention is given to emerging countries such as India and China but also more traditional nuclear countries such as the United States because our expectation of growth in the long term (2020) with the Nuclear Renaissance will oblige us to prepare for the future additional capacities.

ANALYSIS OF ABNORMAL OPERATING OCCURRENCES FOR STA. MARIA DE GAROÑA WITH TRACG

JAVIER GARCÍA, JAVIER HACES

ENUSA

c/Santiago Rusiñol, 12, 28040 Madrid - SPAIN

JUAN CARLOS MANCHOBAS

NUCLENOR

Hernán Cortés, 26, 39003 Santander – SPAIN

JENS ANDERSEN, CHARLES HECK

GLOBAL NUCLEAR FUEL

P. O. Box 780, Wilmington NC 28402-0780, USA

ABSTRACT

Santa Maria de Garoña Nuclear Power Plant (NPP) is a BWR/3 Mark I containment unit owned by NUCLENOR and designed by General Electric (GE). Current reloads come with longer and more challenging cycles and require obtaining wider operating margins. The most important parameter is the Minimum Critical Power Ratio (MCPR).

TRACG is an advanced development by GE based on the TRAC-BF1 code, with several model improvements and new features. The main one is the Three-dimensional (3D) kinetics capability that makes possible to model a wide variety of events. The current application of this code includes not only Anticipated Operational Occurrences (AOO) but also Loss of Coolant Accidents (LOCA), Anticipated Transients without Scram (ATWS), Reactivity Insertion Accidents (RIA) and Stability Analyses.

The initial implementation will include only the AOO analysis. The code will be used to gain some margin in the MCPR, obtain better fuel cost and reducing reload batch sizes or enrichment requirements.

1. Introduction

With the application by ENUSA of GE's best estimate methodology based on the TRACG code, NUCLENOR seeks the main objective of improving the quality of the reload licensing analysis of its Garoña NPP. The new methodology represents a significant step forward in this direction, as it incorporates a powerful computational tool, an accurate model of the plant and its components, a thorough assessment of the uncertainties and biases of the model, and a systematic evaluation of the uncertainties of the results. The outcomes of this process are sound, reliable, and safe, but not unduly conservative, operational limits. In other words, a better reload licensing analysis. The TRACG methodology will be first applied in Garoña for the reload licensing of Cycle 25, with a startup date scheduled for late March 2007. It is worth noting that this application will be one of the first among GE's world reactor fleet, thus showing both the technical qualification and proactive attitude promoting safety culture of ENUSA and NUCLENOR companies.

2. C.N. Sta. Maria de Garoña

This plant is property of "Centrales Nucleares del Norte, NUCLENOR". This plant was connected to the Spanish electrical net on March 2nd of 1971. This plant is a typical GENE BWR/3 plant, has an electric output of 466 MWe. It is a low power density plant with 400 bundles. The vessel diameter is 4.78 m. with 97 control rods and 109 two stages steam separators.

3. Description of the TRACG Code

TRACG is a GE proprietary version of the Transient Reactor Analysis Code (TRAC). It is a best estimate code for analysis of boiling water reactor (BWR) transients ranging from simple AOO

transients and reactor stability to design basis LOCA, RIA and ATWS. TRACG is based on a multi-dimensional two-fluid model for the reactor thermal hydraulics and a 3D neutron kinetics model. The models are accurate and can be used to simulate a large variety of test and reactor configurations. These features allow for detailed, realistic simulation of a wide range of BWR phenomena.

TRACG has been extensively qualified against separate effects tests, component performance data, integral system effects tests and full-scale BWR plant data.

The application methodology of TRACG is based on a statistical process following the Code Scaling, Applicability and Uncertainty (CSAU) methodology [2] and NRC regulatory guides for the application of best estimate methodologies [3,4].

TRACG has several advantages over previous NRC-approved models [1]. The use of best estimate methods coupled with a statistically based estimate of the uncertainties in the critical safety parameters allows for reduced conservatism compared to the currently approved methods. The 3D kinetics model coupled with a multi-dimensional simulation of the core thermal hydraulics allows for a more realistic simulation of the transient power response for the reactor core. For reactor transients such as a pressurization event, the high power channels will experience a smaller decrease in void fraction than the average channel, and consequently the relative increase in power will be less for the high power channels than for the core as a whole. TRACG allows for a more direct implementation of licensing criteria. For reactor transients, the criterion that 99.9% of the fuel rods avoid boiling transition [1,5] has been directly implemented into the transient application methodology.

4. TRACG Applications Process

The proposed application of TRACG to BWR LOCA follows the CSAU methodology [2-4]. The CSAU methodology consists of the following major elements:

- Definition of plant and event (CSAU steps 1-3).
- Description of analysis code and code uncertainties (CSAU steps 4-10).
- Definition of plant parameters and uncertainties (CSAU step 11).
- Statistical process for determination of total uncertainty (CSAU steps 12-14).

These four elements are divided into 14 steps. These 14 steps are summarized in Table 1.

CSAU Step	Description
1	Scenario Specification
2	Nuclear Power Plant Selection
3	Phenomena Identification and Ranking
4	Frozen Code Version Selection
5	Code Documentation
6	Determination of Code Applicability
7	Establishment of Assessment Matrix
8	Nuclear Power Plant Nodalization Definition
9	Definition of Code and Experimental Accuracy
10	Determination of Effect of Scale
11	Determination of the Effect of Reactor Input Parameters and State
12	Performance of Nuclear Power Plant Sensitivity Calculations
13	Determination of Combined Bias and Uncertainty
14	Determination of Total Uncertainty

Table 1: Code Scaling, Applicability and Uncertainty Evaluation Methodology

5. Application Methodology for Santa Maria de Garoña

A combination of baseline and statistical calculations is performed to determine the Operating Limit Minimum Critical Power Ratio (OLMCPR). Only events that can affect the OLMCPR or the M CPR fuel limits are analyzed, being these pressurization and cold-water injection events.

Group	Ring #	Orifice type	Fuel type	Number	Average Peaking Factor
20	1	1	GE14	4	1.77
21	1	1	GE14	24	1.74
22	1	1	GE14	28	1.67
23	1	1	GE14	36	1.54
24	1	1 </td <td>GE14</td> <td>40</td> <td>1.43</td>	GE14	40	1.43
25	1	1	GE14	40	1.24
26	2	1	GE14	52	1.15
27	2	1	GE14	92	0.65
28	2	3 ⁽¹⁾	GE14	20	0.34
29	2	3 ⁽¹⁾	GE11	4	0.34
30	3	2 ⁽²⁾	GE11	60	0.23

(1)Intermediate Orifice (2)Peripheral Orifice

Table 2: Description of Channel Grouping Distribution

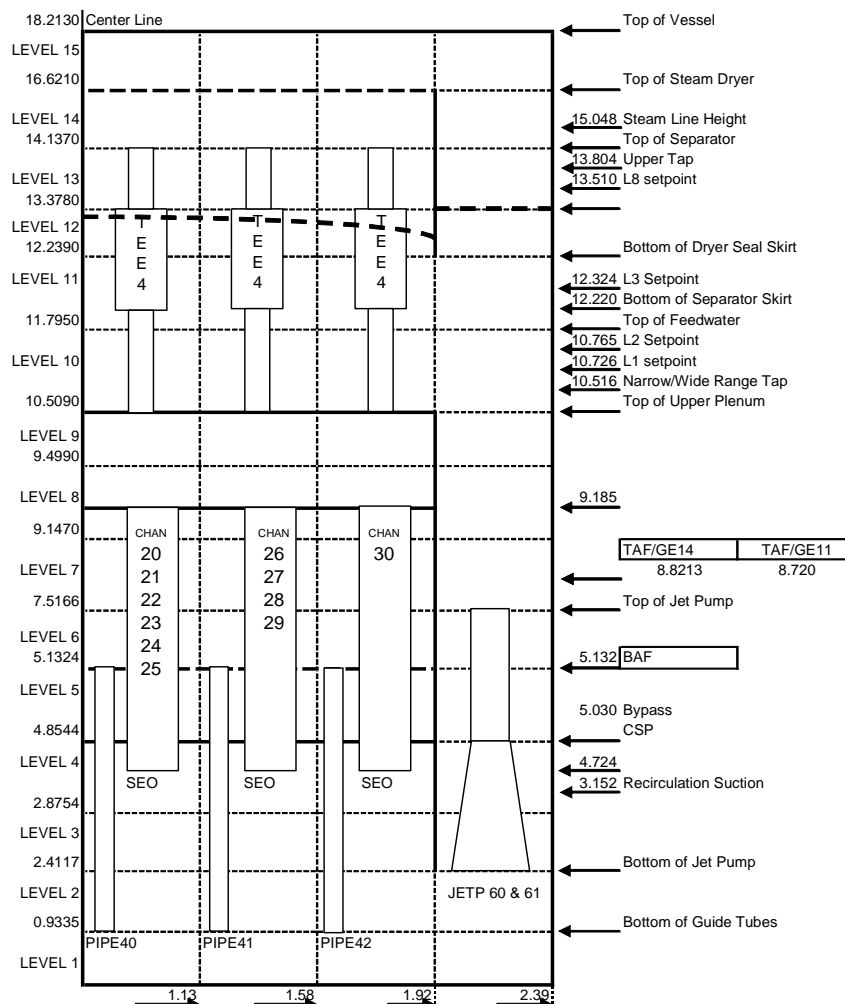


Figure 1. Nodalization Diagram of the Santa María de Garoña Vessel

5.1 TRACG Model and Base Cases

The vessel modeling is illustrated in Figure 1. The model has 15 axial level and 4 radial rings in order to perform a detailed 3 dimensional modeling of the thermal hydraulics. The model has rotational symmetrical geometry, because most of the events can be characterized in this simplified way. However for some analyses it could be convenient to model several azimuthal sectors.

The 400 bundles are treated individually from a neutronics point of view and are grouped in 11 separate groups to be modeled thermal-hydraulically. The maximum current number of groups in TRACG is 50, which for Santa María de Garoña is near the possibility of modeling individually all bundles in the core if quadrant symmetry is assumed. The plant is loaded with fresh and exposed GE14 10x10 fuel and contains exposed GE11 9x9 fuel in the periphery of the core.

5.2 Events Analyzed for the Licensing Process of TRACG AOO Methodology for Santa María de Garoña

After detailed evaluation of the Garoña Final Safety Analysis Report and the licensing documentation of the last cycle some specific events have been chosen for the analysis. The following events are analyzed with this model: Turbine trip without bypass (TTNBP), Generator load rejection without bypass (LRNBP), Feedwater controller failure (FWCF), Inadvertent High Pressure Coolant Injection Startup with turbine trip because of high water level (HPCIL8), Single recirculation pump fast flow runout (FFRO) and Main steam line isolation valve closure with the backup (flux) scram (MSIVF).

5.3 Statistical Analysis

To implement the TRACG Application, a TRACG statistical study will have to be performed for the type of AOO, for the class of BWR plant type, and for the fuel type, to determine the generic bias and uncertainty bases for each key output. It has been performed for the HPCIL8 and TTNBP pressurization events for the purpose of determining the transient CPR over initial CPR ($\Delta\text{CPR}/\text{ICPR}$) mean value and uncertainty. The HPCIL8 and TTNBP are phenomenological similar to FWCF and LRNBP, therefore the calculated generic adders will be also applicable to these events. Also the MSIVF event has been evaluated to obtain a pressure adder.

The statistical analysis is performed in two steps. First each high and medium ranked parameter from the phenomena identification and ranking process is evaluated at both the $+1\sigma$ and -1σ level (call this uncertainty screening). The second step is a random statistical evaluation. In this step each model parameter is varied randomly. After the first step, it is concluded that fewer than 10 parameters have a high influence on the $\Delta\text{CPR}/\text{ICPR}$ value. The influential parameters are the void coefficient, steam line pressure drop or steam separators pressure drop among others.

In the second step, the bias and uncertainty are obtained from the transient nominal case and a set of N random trials where each highly ranked parameter (between 20 and 30) is perturbed separately according with their own probability distribution. These biases and uncertainties will be the basis for the multipliers that will be applied in the following cycles to the $\Delta\text{CPR}/\text{ICPR}$ calculated for GE14 fuel or the maximum vessel pressure for the specific transients of every cycle.

The bias and uncertainty for the statistical analysis $\Delta\text{CPR}/\text{ICPR}$ are determined from the TTNBP and HPCIL8 events. These values are also applicable for the LRNBP and FWCF events. From the MSIVF statistical evaluation, a conservative adder has been obtained. The ASME code limit for vessel pressure is 1.1 times the vessel design pressure (8.62 MPa). The base pressurization calculation provides a maximum bottom vessel pressure far from the limit therefore it is concluded that a wide margin exists to the vessel pressure limit. Also, from HPCIL8 statistical evaluation, which is the limiting transient when L8 trip is assumed, the OLMCPR will be established using the new approach approved by the NRC. This approach is based on the combination of the $\Delta\text{CPR}/\text{ICPR}$ and its

uncertainty directly with the rest of uncertainties used in the standard methodology for the determination of the Safety Limit (SLMCPR). The improvements obtained for previous GENE analyses [6] and the one performed for Garoña NPP are given in table 3.

Method	M CPR Requirement	CPR Margin Recovered
One-Dimensional	1.48	-
TRACG	1.38	0.10
S^aM^a de Garoña		
One-Dimensional	1.50	-
TRACG	1.34	0.16

Table 3: TRACG OLMCPR Margin

6. Future Applications of TRACG for Sta. María de Garoña

For BWR2/6 plants, the TRACG code has been approved in the US for AOO transients and for the calculation of the CPR oscillation magnitude (DIVOM curve) for plants using the detect and suppress stability methodology [1], however, GE is currently working to license the TRACG LOCA methodology. Nuclenor is currently studying the possibility of using this new methodology for the licensing of the GE14 fuel loaded in the plant. Also the TRACG code will be used to determine the specific DIVOM curve for the next reload. This will allow the recovering of same margin in both aspects LOCA and Stability. Also, future plans include the determination of the stability protection Exclusion Region for operation at low power and flow. Further implementation could include RIA and ATWS scenarios. TRACG can be used to perform the simulation of operational transients to demonstrate actual margins or to obtain realistic calculated responses for parameters that are not monitored by the plant.

7. Conclusions

The introduction of the best-estimate methodology based on the TRACG code in the reload licensing analysis has represented a significant effort to all parts concerned.

The plant model has been generated according to the standard procedure, with modifications in some control systems to achieve a better simulation of the plant actual components. A null transient has been run showing adequate tuning of the steady state parameters. The bias and uncertainties of the Δ CPR/ICPR corresponding to the limiting transients considered have been determined for their later application in the reload licensing report. Also, comparisons with plant transients have been performed to check the reliability of TRACG. The model and results obtained thus far show the methodology represents a consistent, accurate and safe frame for the licensing analysis.

8. References

1. "General Electric Standard Application for Reactor Fuel", NEDO-24011-A-15, Revision 15 September 2005.
2. B. Boyack et. al., "Quantifying Reactor Safety Margins: Application of Code Scaling, Applicability, and Uncertainty Evaluation methodology to a Large-Break Loss-of-Coolant Accident", NUREG/CR-5249, December 1989.
3. U. S. Nuclear Regulatory Commission, Office of Nuclear Regulatory Research, Regulatory Guide 1.157, "Best-Estimate Calculation of Emergency Core Cooling System Performance", May 1989.
4. U. S. Nuclear Regulatory Commission, Office of Nuclear Regulatory Research, Regulatory Guide 1.203, "Transient and Accident Analysis Methods", December 2005.
5. U. S. Nuclear Regulatory Commission, "Standard Review Plan, Office of Nuclear Regulation", NUREG-800.
6. "Application of Advanced Thermal Hydraulic TRACG Model to Preserve Operating Margins in BWRs at Extended Power Uprate Conditions", Proceedings of ICAPP '06, Paper 6212, June 2006.

TANOXOS: AN ANALYTICAL IRRADIATION PROGRAM AIMING AT UNDERSTANDING THE BEHAVIOUR OF VARIOUS DOPED UO₂ FUELS.

L. CAILLOT¹, J. NOIROT¹, Y. PONTILLON¹, S. VALIN²

*1 Fuel Studies Department (DEC), CEA Cadarache
BP1, 13108 Saint Paul lez Durance, France*

2 DTN/SE2T, CEA Grenoble, 17 rue des Martyrs 38054 Grenoble Cedex 9, France

ABSTRACT

CEA has undertaken an irradiation and PIE program, aiming at getting better understanding of the in-pile behaviour of doped UO₂ fuels.

Different types of pre-selected doped UO₂ fuels were irradiated in the OSIRIS material testing reactor: chromia (2000 ppm) and chromia (2000 ppm) + silica (500 ppm) doped UO₂, with different oxidation state of chromium and different stoichiometry of UO₂. All these fuels have large grains (ranging from 60 to 80 μm). The program, including post-irradiation annealing tests at high burn-up, showed better gas retention values for Cr-doped fuels compared to standard UO₂. Large-grains and Cr or Cr₂O₃ precipitates play a favourable role on gas retention in the tested conditions. The addition of SiO₂ at grain boundaries gave also good results, but hyper-stoichiometric fuels not, probably because of higher diffusion coefficients.

1 Introduction

In parallel with the industrial development of chromia doped UO₂ in French PWRs in order to improve PCMI [1] and gas retention, CEA has undertaken a complementary experimental program, partly supported by EDF and AREVA NP, aiming at getting better understanding of the in-pile behaviour of doped UO₂ fuels.

This irradiation was performed on selected large-grain fuels doped with chromia and/or silica and submitted to different reducing or oxidising treatments after sintering. The selection was the result of the previous irradiation in SILOE reactor (TANOX), at lower burn-ups, in which different doped UO₂ were sorted as a function of their performance in terms of gas retention during annealing tests [2].

The TANOXOS analytical program consists in an accelerated experimental irradiation (high fission rates compared to LWRs) followed by PIE and annealing tests in hot cells facilities.

2 Characteristics of the doped UO₂ fuels

Five doped UO₂ fuels and a reference UO₂ (for comparison) were simultaneously irradiated. The main characteristics of these fuels are summarized in Table 1.

In all the doped UO₂ (TO1.3 to TO1.7), chromia at a concentration over its solubility limit in UO₂ was used to enhance the grain growth as a result of previous studies on the use of corundum-type oxide as additives. For these fabrications, the introduced quantity of chromia is 2000 ppm. Such a concentration permits to obtain a grain size higher than 60 μm and chromium oxide precipitates in intra and inter-granular positions, with the aim of increasing the length of diffusion path towards grain boundaries, and enhancing the gas bubble nucleation and pinning.

In TO1.5, 200 ppm of SiO₂ was introduced in order to obtain a glassy phase at grain boundaries.

After sintering the doped fuels (except TO1.6) were submitted to different types of annealing under oxidising or reducing atmospheres. The reducing atmosphere (TO1.3 to 1.5) aims at reducing the chromium oxide of the precipitates into metallic chromium, which is supposed to help controlling the oxygen potential in the fuel. Good results in terms of gas retention were obtained with this kind of fuel in the TANOX program [2].

The oxidizing treatment leads to UO_{2.02}, which gave unexpected good results in the TANOX irradiation. It is assumed that the structural defaults induced by the excess of oxygen enhance the nucleation and pinning of gas bubbles in intra-granular position.

The ^{235}U enrichment of UO_2 was 7% (mass) in order to get high fission rates.

Rod numb.	Fuel type	Grain size	Density	Sintering conditions	Post-sintering treatment (reducing or oxidizing annealing)
TO1-2	Standard UO_2	9 μm	10.46	4 h at 1700°C H_2 sec	/
TO1-3	UO_2 + 2000 ppm Cr_2O_3 (reduced)	80 μm	10.46	4 h at 1700°C H_2 + 1.7 % vol H_2O	10 h at 1400°C under dry H_2
TO1-4	UO_2 + 2000 ppm Cr_2O_3 (reduced)	80 μm	10.46	4 h at 1700°C H_2 + 1.7 % vol H_2O	4 h at 1400°C under dry H_2
TO1-5	UO_2 + 2000 ppm Cr_2O_3 (reduced) + 200 ppm SiO_2	75 μm	10.4	4 h at 1700°C H_2 + 1.7 % vol H_2O	4 h at 1400°C under dry H_2
TO1-6	UO_2 + 2000 ppm Cr_2O_3	61 μm	10.42	4 h at 1700°C H_2 + 1.7 % vol H_2O	/
TO1-7	$\text{UO}_{2.02}$ + 2000 ppm Cr_2O_3	61 μm	10.43	4 h at 1700°C H_2 + 1.7 % vol H_2O	5.5 h at 700°C under He + 100 vpm O_2 + 18 h at 700°C under He

Table 1: characteristics of the different fuels

3 Irradiation

The irradiation took place in the OSIRIS reactor (Saclay), in the specific device called TANOXOS designed to perform selection irradiation with an accelerated rate of burn-up increase. The design of this device aims at getting LWR representative irradiation temperatures in the samples in spite of high fissions rates, typically 3 to 6. 10^{13} fissions. $\text{s}^{-1}.\text{cm}^{-3}$ (factor 2 to 4 compared to standard LWR fission rates). The main point to achieve such specifications is to decrease the fuel rod and pellets diameters and to optimize heat transfers.

3.1 The fuel rods and the irradiation device

The diameter of the pellets is 4.9 mm, while their height is 5 mm. 20 pellets are placed in each fuel rod, clad with stainless steel, filled with helium and equipped with a W-Re thermocouple (the 10 upper pellets are annular with a 1.3 mm diameter central hole). The pellet-to-clad gap is reduced in order to improve thermal transfers. These fuel rods are placed in an over-cladding made of aluminium alloy (2nd wall), directly cooled by the OSIRIS reactor primary coolant. The six fuel rods are simultaneously irradiated, around a barrel allowing permutation or rotation of fuel rods in order to homogenise the burn-ups. The nuclear power is adjusted by moving the device in the flux gradient available at the periphery of the OSIRIS core.

3.2 Irradiation conditions and thermal analysis

The irradiation which lasted 3 years, was managed in order to get temperatures never higher than those encountered in nominal conditions of PWRs: <1100°C for solid pellets, and <900°C in hollow pellets instrumented with thermocouples. Such conditions are achieved by adjusting the position of the device, i.e. the power of all fuel rods, as a function of the temperature of the hottest one.

At the end of the irradiation, the fuel rodlets burn-ups ranged from 65 to 67 GWd.tM^{-1} , as given in Table 2. Nevertheless, it is important to note that in spite of the good homogeneity of the burn-ups, the fuel rods experienced very different power histories due to a two-step loading:

- fuels TO1.6 and TO1.7, loaded when other rods had reached 40 GWd.tM^{-1} , had a quite steady irradiation power history, with central temperatures of solid pellets between 750 and 950 °C up to 55 GWd.tM^{-1} ,

- fuels TO1.2 to TO1.5, first loaded, experienced high temperatures (central temperatures between 900 and 1050°C) up to 40 GWd.tM⁻¹ and very low temperatures (between 350 and 600°C) later, until the end of the irradiation.

These differences in power histories have to be carefully taken into account during further analyses.

The thermal behaviour of each fuel was analysed by comparing temperature measurements to calculations performed with the CEA fuel code METEOR. This analysis did not show any significant difference in thermal conductivity between the different types of fuel, except for UO_{2,02} of TO1.7 which exhibits a lower conductivity as previously observed in TANOX experiment [3].

4 Post-irradiations examinations

At the end of the irradiation, the fuel rodlets were transported and submitted to PIE and annealing tests in the LAMA (Grenoble) and LECA (Cadarache) hot laboratories.

Gas puncturing after irradiation gave low fission gas release values consistent with the rather low temperatures during irradiation in OSIRIS. No significant difference was detected between the fuels, as presented on Table 2. The beneficial effect of large grains is not exhibited because of the negligible diffusion of Xe at these temperatures

All fuels were characterized by optical microscopy, one by EPMA and one by SEM fractography. These PIE made possible direct comparisons between the different fuels.

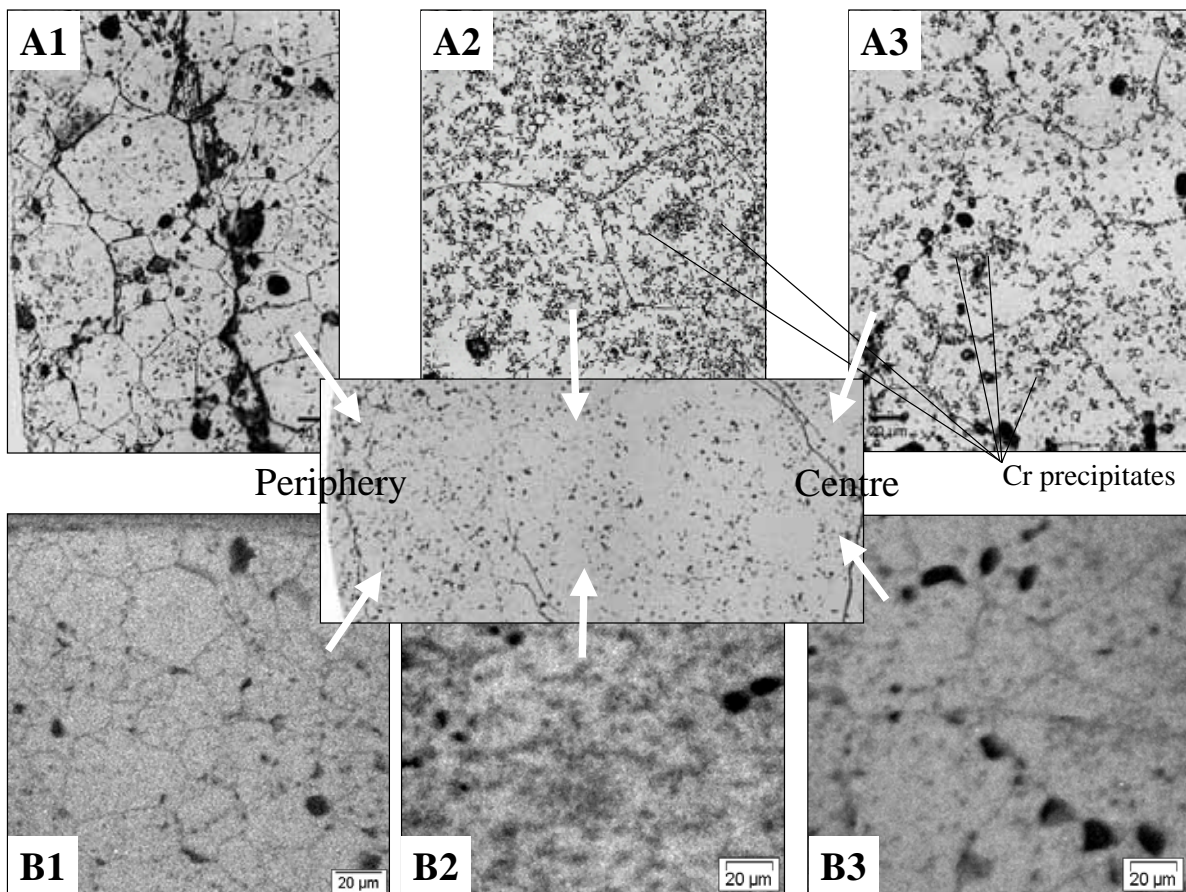


Figure 1: TO1.6 (UO₂ + 2000 ppm Cr₂O₃) – Optical microscopy after chemical etching (A) and Xe EPMA mappings (B) at different radial locations (1 = periphery, 2 = mid radius, 3 = centre)

The first noticeable point is the observation on ceramographies of the absence of rim structure at the extreme periphery, while a restructuring process (HBS type) appeared to be in progress in most of the other zones of the samples. At intermediate radii a great number of “planar defects” [4] is observed, while in the central area this restructuring is associated to massive intra-granular gas precipitation. The restructuring was confirmed by the SEM observation of a fractograph of the TO1.5 fuel.

These surprising observations which were made in doped fuels as well as in the reference UO₂ seem to be the consequence of the specific irradiation conditions in TANOXOS device compared to std LWR

fuels (higher fission densities, higher compressive stresses due to the double-clad, modified potential oxygen due to the stainless steel clad, ...) that probably played a role in the HBS.

Concerning the effect of additives, the observations tend to confirm the expected role of the Cr-based precipitates (whatever their chemical state: oxide or metallic) on the Xe bubble nucleation: high bubble concentrations seem to appear in Cr precipitates-rich areas, as shown on Figure 1. It is worth noting that only micron-size precipitates are observed by optical microscopy, but that nanometre-size ones are assumed to be present and to play a role in the Xe behaviour.

The presence of SiO₂ in TO1.5 fuel, assumed to be located at grain boundaries, appears to play a role onto fission gas behaviour: in intermediate areas a lot of small inter-granular bubbles are observed, while at the centre the grain boundaries seem to be gas-drained (absence of bubbles in their vicinity).

The last point is the absence of radial cracks in all pellet types, probably as a consequence of the high compression state of the material during the irradiation.

The TO1.6 (UO₂ + 2000 ppm Cr₂O₃) was analysed by EPMA. This examination confirmed that in many cases Xe bubbles are associated to Cr-based precipitates, and that Xe is less abundant near grain boundaries in doped fuels (seeing figure 1). Otherwise, metallic fission products precipitates are not associated with Cr-based ones.

5 Annealing tests and post-tests characterizations

PIE were followed by annealing tests and optical microscopy after tests. The fuels were submitted to different types of thermal history (from room temperature to 1300°C), some simulating LOCA conditions, others with the aim of determining the temperature threshold of fission gas release.

5.1 Equipment and experimental procedures

These tests were performed in the LAMA hot laboratory [5] with equipment similar to the MERARG one, now in Cadarache [6]: the sample (typically one pellet, with its clad) is heated in a high frequency furnace. The released fission gases are transported out of the hot cell by the sweeping gas (He) to be measured by gamma spectrometry. A treatment procedure gives the ⁸⁵Kr release kinetics. Two types of experimental sequences were used:

- All types of fuel were submitted to the first one (sequence A) consisting in a first temperature rise up to 1000°C (at 20°C.s⁻¹), a 10 second plateau, a cooling down to room temperature and a second rise up to 1200°C (at 20°C.s⁻¹), a 10 minute plateau, and finally a cooling down to room temperature.
- Only TO1.2 (reference) and TO1.6 were submitted to the second sequence (B) which consists in a series of rises up to increasing temperatures, from 400°C to 1000°C, separated by coolings down to room temperatures, and finally a rise up to a plateau of 3 hours at 1300°C.

5.2 Results

These tests gave good results in terms of gas retention for chromia doped UO₂, except for TO1.7 submitted to an oxidizing treatment after fabrication (UO_{2,02} + 2000 ppm Cr₂O₃) as summarized in Table 2.

For sequence A, it is worth noting that, for all fuels, the release occurred during the first rise up to 1000°C. This is consistent with previous experiments on UO₂ [5]: during short and rapid transients at low and intermediate temperatures (< 1200-1300°C), the main phenomenon is a release of the gas already located at grain boundaries. The better behaviour of Cr-doped fuels is thus attributed to the improved intra-granular retention of these fuels in base load conditions. TO1.3 submitted to a long reduction treatment (10 hours) after sintering gave very good results, confirming the conclusions of TANOX program [2]. Post-tests examinations by ceramography evidenced other slight evolutions: increase of the length of planar defects in intermediate areas, and decrease of the central porosity (the size of bubbles is stable while their number decreases). This last evolution tends to indicate that part of the release during annealing tests came from central areas, even if the release mechanism is not clearly understood.

Fuel rod number	Mean Burn-up (GWd.tM ⁻¹)	Fission gas release during OSIRIS irradiation (%)	Fission gas release during annealing test Sequence A (%)	Fission gas release during annealing test Sequence B	
				Up to 1000°C (%)	Total (%)
TO1-2	65	3,1	18.1	14.5	19.2
TO1-3	69	2,0	7.5		
TO1-4	65	2,0	13.5		
TO1-5	65	2,3	10.5		
TO1-6	65	3,0	10.9	11.9	13.0
TO1-7	67	Not measured	18.6		

Table 2: Mean burn-ups and fission gas release during the TANOXOS irradiation and following annealing tests

Sequence B showed release temperature thresholds very different for TO1.2 (~400°C) and TO1.6 (~800°C). Nevertheless this observation is not a consequence of the Cr-doping but of the irradiation conditions: the release of the available gas (at grain boundaries) occurs when the temperature at the end of irradiation is exceeded (seeing paragraph 3.2). The total release at the end of the last plateau of 3 hours at 1300°C is lower for TO1.6, as a consequence of the role of large grains and of Cr-based precipitates on the diffusion process.

6 Conclusions

The program confirmed the favourable role of large-grains and Cr or Cr₂O₃ precipitates on gas retention in the studied conditions (transients up to 1300°C) at high burn-ups (65 GWd.tM⁻¹).

The benefit of Cr-doped UO₂ during moderate temperature transients appears to be due to the combination of the grain size and the pinning of gas bubbles in intra-granular position, limiting diffusion process and thus the inter-granular inventory during the steady-state irradiation. The addition of SiO₂ at grain boundaries gave also good results, but not hyper-stoichiometric fuels, probably due to higher diffusion coefficients. In-pile temperature measurements showed the absence of significant effects of additives on the in-pile thermal conductivity.

Such an accelerated irradiation is interesting to compare different fuel materials, provided that all parameters are identical (not only burn-ups but also power histories). Qualification programs in PWR and BWR are under progress to assess the performance of Cr₂O₃-doped UO₂ fuel towards safety criteria at high burn up and the risk of PCI clad failure [7]

7 References

1. Delafoy, Ch. & al., Advanced UO₂ fuel with improved PCI resistance and fission gas retention capability, TOPFUEL 2003, Würzburg, March 16-19, 2003
2. Valin, S. & al., Synthesis of the results obtained on the advances UO₂ microstructures irradiated in the TANOX device, Proceedings of the IAEA TCM on Improved Fuel Pellet Materials and Designs, Brussel, October 20-24, 2003
3. Dehaut, Ph., & al., Irradiation of UO_{2+x} fuels in the TANOX device, IAEA TCM on advances in pellet technology for improved performance at high burn up, Tokyo, Oct 28-Nov 1, 1996
4. Lozano, N., Desgranges, L., Aymes, D., Niepce, JC., J. Nucl. Mater. 257 (1998) 78
5. Pontillon, Y. & al., Experimental and theoretical investigation of FGR from UO₂ up to 70 GWd/t under simulated LOCA conditions: The Gaspard program, Proceedings of the 2004 International meeting on LWR fuel performance, Orlando, September 19-22, 2004
6. Pontillon, Y., Fuel performance under different PWR conditions: an overview of the annealing test facilities at the CEA, Proceedings of the Water reactor fuel performance meeting, p 848-857, Kyoto, oct 2-6, 2005
7. Delafoy, Ch., Dewes P., AREVA new UO₂ fuel development and qualification for LWRs applications, TOPFUEL 2006, Salamanca, October 22-26, 2006

contributions was justified for moderately high rod average burnup, i. e., around 60 GWd/tU when the restructured region is narrow. It is no longer the case for recent data up to 100 GWd/tU [5] when the HBS can extend to mid-pellet radius. The model is plotted and compared to experimental data on Fig.1 for fuel rods irradiated 4 to 6 cycles in French PWRs. These data were obtained from SEM images analysis carried out by the CEA [6,7] with burnups derived from EPMA measurements.

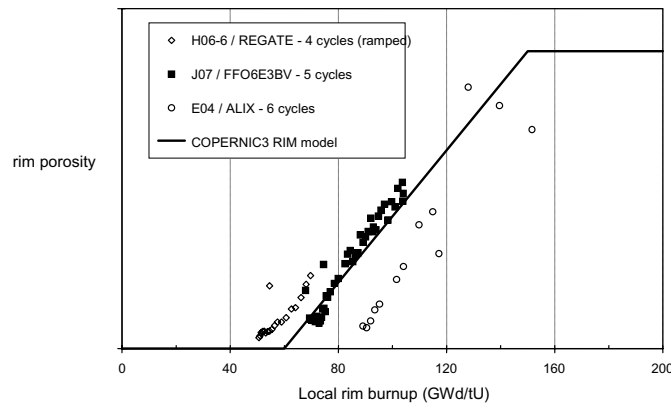


Fig. 1. Comparison of the COPERNIC3 rim porosity model and experimental data

In the model implementation, the burnup used to calculate the rim porosity is obtained by integrating the local power with respect to time only when the temperature is below a low temperature threshold. Otherwise this so-called “rim burnup” decreases exponentially with a relaxation time parameter, and then differs from the true local burnup. Indeed, the rim restructuring is prevented at higher temperature, and it naturally reproduces the fact that even at very high pellet burnup, the HBS is not formed in generally hot centre parts of the fuel. The model also contains a high limit value even if porosity greater than 20% has already been observed [8] (to compare with new rim porosity added to initial remaining porosity). This porosity threshold is necessary to obtain correct agreement with cladding diameter changes measured at high burnup. Moreover, the solid swelling model is reduced as soon as the rim porosity model is activated, still to avoid dimensional changes overestimations. It can also be justified because the fission gas products playing a major contribution (~ 70%) in the solid swelling before restructuring are then purged from the matrix and occupy the big rim pores. So an increase in volume due to rim pore formation is somewhat counterbalanced by solid swelling change, from which the simpler and satisfactory model consists in stopping this swelling. Eventually from a mechanical and macroscopic point of view, the rim phenomenon is hard to simulate because volume change conditions depart from the fundamental small strain hypothesis, combined with a huge radial strain gradient.

3. Fission gas release modelling

The new extended fission gas release (FGR) model in COPERNIC3 is based on the original model of Bernard [9], which is a classical two-step diffusion model (Booth model) following the 3-terms formalism of Turnbull for the diffusion coefficients, and which in addition to the steady-state thermal release, it also describes transient effects and athermal release. The thermal model takes into account grain boundary incubation and saturation and irradiation-induced resolution from the grain boundaries, which counteracts the diffusion flux and delays the onset of release. The transient model handles additional burst effects for relevant and rapid power changes. Future higher burnup and duty applications beyond about 65 GWd/tM were the focus of the model extension. The new model application range had to be extended to BWR power reactor conditions also.

Experimental feedback shows potential FGR enhancement with burnup, which starts at a burnup beyond about 60 GWd/tU for UO₂ low power fuel, above about 50 GWd/tU for UO₂ medium and high power fuel and exists throughout irradiation for very high power MOX fuel. New mechanisms were needed for the observed high burnup FGR enhancement.

There is clear experimental evidence for only small FGR from the high burnup rim structure to the rod free volumes [10]. The main contribution of the rim region to FGR enhancement is via pellet temperature increase, if any. The bulk of the gas produced in the pellet rim remains mainly in closed

spherical rim porosity. This is modelled in COPERNIC3 as a small athermal contribution to FGR. It amounts to about 1.0 – 1.5 % pellet release for a pellet burnup between 80 and 90 GWd/tU. The low release from the rim region implies that other mechanisms have to be found to explain high burnup effects.

An approach is chosen which is based on EPMA observations on pellet sections of irradiated fuel. In fuel rods with steady-state power there is a strong depletion of fission gases in the inner pellet regions at high burnup (beyond about 50 GWd/tM pellet average) despite low powers and temperatures for most of the irradiation time [2]. This is supported both by local FGR measurements in the fuel matrix (EPMA) and by the isotopic composition of the integral measured pellet release (there is much less plutonium here compared to the rim region; the xenon and krypton yields are consequently different). In ramped fuel rods with short hold times, EPMA radial profiles evidence an almost spontaneous decrease of the xenon concentration in the fuel matrix at burnups beyond about 30 GWd/tU and temperatures above about 1000 °C. The effect consistently shows distinct steps in EPMA profiles of such rods [2]. Both in steady-state and ramp conditions a coalescence process of submicroscopic bubbles is probably taking place and larger intragranular bubbles appear. The decreasing matrix concentration is thus explained by the capture of the migrating gas atoms by the intragranular bubbles. These observations led to the introduction of a xenon concentration limit in the fuel matrix which is dependent on local fuel burnup and temperature with a similar formulation to the Lassmann curve [11] but generalized to the whole pellet. Fig. 2 shows that such a saw tooth-like temperature-dependent shape of the matrix xenon concentration versus burnup is actually observed in plutonium-rich particles of MOX fuel [12] and that it is in reasonable agreement with the COPERNIC3 correlation.

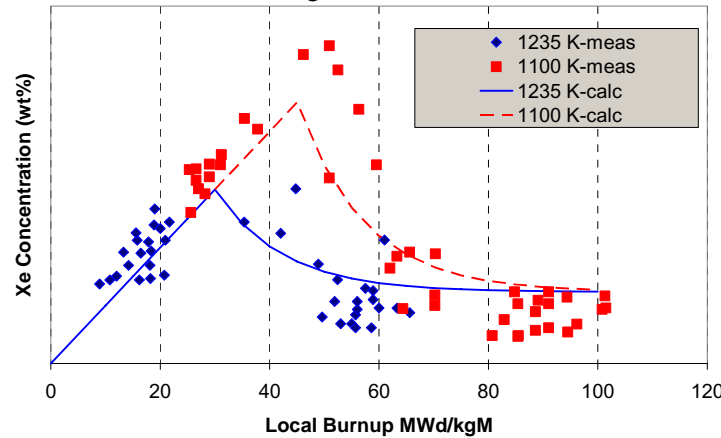


Fig. 2 Xenon concentration limit as measured on Pu particles in MOX fuel and calculated.

Just like the thermally released fission gas, the gas released from the fuel matrix, when the xenon concentration limit is reached and exceeded, is assumed to quickly reach grain boundary bubbles or big bubbles or pores inside grains (especially when the grains are big). How much of this gas is released to the void volume then depends on the degree of interlinkage of the bubbles and pores. The interlinkage process is modelled in a simple way as follows. If G_{BOOTH} is the gas thermally released as predicted without high burnup modelling, and G_{BUB} the gas produced in excess of the xenon concentration limit and assumed in big bubbles, the gas released from G_{BUB} is written:

$$G_{REL} = C_{BUB} \cdot G_{BUB} \text{ with } C_{BUB} = \min \left\{ \max \left[0, \frac{(G_{BOOTH} - G_-)}{(G_+ - G_-)} \right], 1 \right\}$$

G_+ and G_- are model parameters. The degree of interlinkage used in COPERNIC3 is determined from extensive PIE on irradiated fuel [13]. As at high burnup, interlinkage is normally well developed in the inner parts of the fuel pellet, much of this gas can leave the fuel and reach the rod free volumes and thus give a relevant contribution to the burnup enhancement of FGR.

As a demonstration of the effect of the xenon concentration limit, Fig. 3 shows the comparison of two measured and calculated EPMA profiles for the high burnup rod BK365 from the HBEP with annular pellet fuel, studied in the course of the IAEA CRP FUMEX-II exercise [14]. The results of EPMA on rod BK365 are very interesting. The central temperature of this rod is around 800°C for the last third of the irradiation. The central burnup near the central hole is about 70 GWd/tU. The central, sharp depression of the EPMA radial profile observed at this burnup (square points) is found to have the fuel

structure similar to the pellet rim structure with almost twice as large burnup of 140 GWd/tU. Thus, at the edge of the central hole at a burnup of only 70 GWd/tU, at which a rim structure is expected to just start developing, it seems that the fuel temperature of 800 °C had an enhancing effect on rim structure formation.

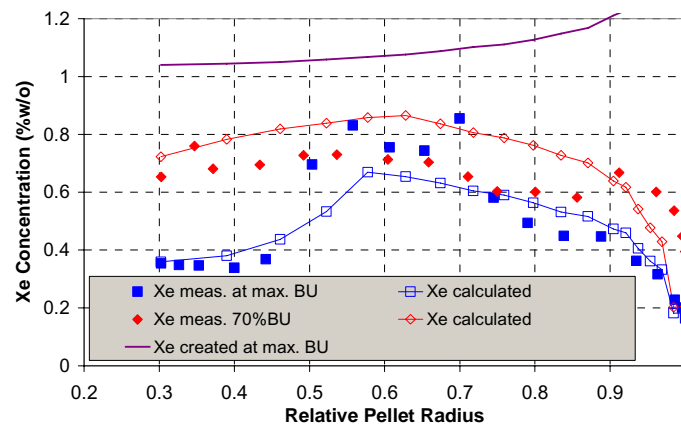


Fig. 3. Measured and Calculated EPMA Profiles on High BU Hollow Pellet Fuel

This enhancement is well described by the FGR model in COPERNIC3, where it is a consequence of the temperature and burnup dependent xenon concentration limit. The FGR enhancement corresponds to the development of the large intra-granular bubbles at high burnup, which have a strong similarity to the rim but start to form at a lower burnup threshold due to the higher temperature.

It has to be noted that the different model parameters used to define the xenon concentration limit and the interlinkage are fitted to predict final fission gas release measurements, which are the important quantities to predict. It implies that the xenon profile comparisons give an overall validation of the COPERNIC3 modelling ideas.

4. Pellet mechanical model

A mechanical model called MEFISTO has been implemented in COPERNIC3 and improved during the code development. The original model comes from the thermal-mechanical fuel rod code METEOR developed at CEA [15]. It consists in a classical finite element method to solve the mechanical problem, for which innovative algorithms have been added to combine a pellet cracking model, a plasticity model for cladding and a creep model for pellet and cladding.

The rod is considered axi-symmetric during the whole power history, with a mono-dimensional discretization in the radial direction of cylindrical coordinates. Stresses and strains are obtained as solutions of the equilibrium balance and compatibility relations with the proper boundary conditions. A generalized axial plane strain is assumed in the pellet shoulder whereas a generalized axial plane stress is chosen in the dish, which is more representative of this region and allows dish filling as it will be explained below. Perfect contact is assumed between pellet and cladding. Most of the important cladding models are described in [16] and we will concentrate in this paper on pellet mechanics.

As soon as the fuel viscoplasticity behaviour is introduced, it is necessary to take into account relaxation of tensile stresses by cracking in order to be more realistic. But we have to keep in mind that a 1D smeared crack model does not give much more realism. In particular no realistic cracking kinetics or cracking faces can be deduced from this model. Basically, it consists in rewriting the classical Hooke law by imposing a stress value in axial or tangential direction, representative of the cracked region. Compared to the original model, this imposed value is an input parameter and is taken by default to be opposite to the internal pressure. Then, the stress in this direction is not an unknown anymore, and as a consequence, elastic strains neither satisfy the compatibility relations. Finally, a new unknown appears with the crack strain to close the problem. This model is activated for a given element in one direction wherever the calculated stress in this direction exceeds the tensile fracture stress (typically 150 MPa for UO₂ but also defined as an input parameter). On the contrary, the crack closes when the calculated crack strain becomes negative supposing a given crack situation. The cracking strain can be considered representative of crack voids if the pellet remains roughly cylindrical after cracking, and then it contributes to the increase in the apparent pellet radius.

This last physical interpretation has been favourably used to introduce a dish filling model in MEFISTO. Roughly speaking, the dished ends can be considered as a large initial axial crack where mechanical conditions are close to plane axial stress conditions. It is exactly the kind of problem that the MEFISTO model is able to solve. When axial physical strains (thermal expansion, gaseous swelling, creep ...) fill the dish, the axial plane strain hypothesis is no longer physically justified. But in order to keep a consistent finite element formulation in dish and pellet shoulder regions, an additional strain balances the difference in such a way that plane strain remains mathematically valid. But in this case, the lower limit of this additional strain is no longer zero like in the classical crack model, but it corresponds to the opposite of the dish volume, that is to say the initial tank volume reserved for physical strains. Moreover, axial stress in the dish keeps a uniform value and then an axial plane stress is verified.

5. Conclusion

A representative sample of recent pellet models have been presented, especially those concerning high burnup behaviour. This period of the rod history is first of all characterized by a new rim structure which is carefully modelled from a macroscopic point of view. The FGR model presented here and developed in the COPERNIC3 code, will allow extending the validation range of the AREVA NP fuel rod design code to a very high burnup. The validation work will be continued and extended with other available experimental data, to strength the new models and concepts introduced in order to fit the needs of utilities. The FGR model initially based on well-validated models from present day AREVA NP codes, takes into account the formation of big bubbles at high burnup and, in addition, the resulting FGR, via the gas concentration limit model. The model satisfactorily matches the experimental profiles of xenon concentration from which it has been deduced, and the final FGR predictions at very high burnup are considerably improved. Finally, technical solutions have been described in order to introduce pellet cracking behaviour and dish filling phenomenon, necessary to precisely calculate void volumes especially at high burnup.

References

- [1] BERNARD L.C. & al. "The FRAMATOME COPERNIC fuel rod performance code, Recent high burnup and advanced cladding developments" International Topical Meeting in LWR fuel performance, Park City (2000)
- [2] SONTHEIMER F. & LANDSKRON H. "Puzzling features of EPMA radial fission gas release profiles: the key to realistic modeling of fission gas release up to ultra high burnup of 100 MWd/kg M with CARO-E", IAEA TCM on Nuclear Fuel Behaviour Modeling, Windermere (2000)
- [3] BILLAUX M.R. & al. " SIERRA: a fuel performance code to predict the mechanical behaviour of fuel rods up to high burnup" International topical meeting on LWR fuel performance, Portland (1997)
- [4] SONTHEIMER F. & al. "High burnup UO₂ fuel modelling with COPERNIC3" IAEA TM on Fuel Behaviour Modelling under Normal, Transient and Accident Conditions and High Burnups, Kendal (2005)
- [5] MANZEL R., WALKER C.T. , J. Nucl. Mat. 301 (2002) 170-182
- [6] BAGOT R. & al. , DEC/S3C/03-137, CEA Technical Note (2003)
- [7] PUJOL X. & al., DEC/SA3C/04-023, CEA Technical Note (2004)
- [8] SPINO J. & al. , J. Nucl. Mat. 354 (2006) 66-84
- [9] BERNARD L.C. & al. , J. Nucl. Mat. 302 (2002) 125-134
- [10] KINOSHITA M. & al. "High-Burnup Rim Project: (III) Properties of Rim-Structured Fuel" paper 1102, International Meeting on LWR Fuel Performance, Orlando, 2004.
- [11] LASSMANN & al. , J. Nucl. Mat. 226 (1995) 1-8
- [12] MERTENS L. & al., (BELGONUCLEAIRE) "HBS development in MOX fuel", International Workshop on the High Burn-up Structure in Nuclear Fuels, ITU Karlsruhe (2004)
- [13] SONTHEIMER F. & al. "Release of the volatile fission products Xe, Kr and Cs from PWR fuel under steady and transient conditions up to high burnup" IAEA TCM on Fuel Rod Internal Chemistry and Fission Product Behaviour, IAEA-TC 544 No. 9, Karlsruhe (1985)
- [14] SONTHEIMER F. "Participation in the IAEA Coordinated Research Project FUMEX-II: Final Report of FRAMATOME ANP" Work Report A1C-1317992-0 AREVA NP (2005)
- [15] GARCIA P. & al. , Nucl. Eng. & Design 216 (2002) 183-2001
- [16] GARNIER & al. "The COPERNIC mechanical model and its application to doped fuel" Int. seminar on pellet clad interaction in water reactor fuels, NEA, Aix-En-Provence (2004)

THE BENEFITS OF THE FUMEX-II PROJECT FOR EXTENDING THE VERIFICATION OF THE TRANSURANUS CODE

P. VAN UFFELEN, A. SCHUBERT, C. GYÖRI, J. VAN DE LAAR
*European Commission, Joint Research Centre, Institute for Transuranium Elements,
Postfach 2340, 76125 Karlsruhe, Germany*

D. ELENKOV
*Institute for Nuclear Research and Nuclear Energy,
72 Tzarigradsko Chaussee Blvd 1784, Sofia, Bulgaria*

ABSTRACT

We summarize the main results obtained by means of the TRANSURANUS code within the framework of the FUMEX-II round robin exercise. The agreement between calculated and measured fuel centre temperatures was very satisfactory for all but one case. The radial profiles of Nd, Xe and Cs could be well reproduced, apart from a normalisation issue in one case. The rod average burnup levels were under predicted by roughly 4% in 3 cases, requiring further clarification. The results of the analyses with the improved fission gas release model are satisfactory. Nevertheless, the present model cannot describe the release bursts observed during some rapid power variations.

In the last part of the paper we outline the future development work for oxide fuels, regarding mainly the high burnup structure as well as the simulation of LOCA events, and we suggest some topics for inclusion in a potential FUMEX-III project.

1. Introduction

FUMEX-II is the third round robin exercise organized by the IAEA for LWR fuel behaviour codes [1]. In collaboration with other TRANSURANUS users from Bulgaria Romania and Switzerland, ITU carried out the following calculations [2]: cases 1-4, case 7, cases 14-15, case 17 and all simplified (invented) cases. For the sake of conciseness, we limit ourselves in this report to the experimental (real) fuel rods. Two simulations were performed consistently for each case. The first corresponds to the standard code version with default models and input parameters as used before in FUMEX-II. The second represents the analysis with an improved code version as a result of FUMEX-II. This version includes grain boundary sweeping as an additional fission gas release mechanism when grain growth occurs. Additionally, the increased cracking observed in high burnup fuel during power ramps has been accounted for.

In general, one could conclude that the TRANSURANUS fuel performance code is mature and can deal with fuel behaviour up to high burnup; that no numerical problems arose in the simulations of the LWR fuel behaviour up to 100 MWd/kgHM; and that the inclusion of grain boundary sweeping and extended cracking significantly improved the predicted FGR results under high power conditions. In the next sections, we will discuss in more detail the various aspects of fuel behaviour that were addressed during the co-ordinated research project. In the last section, we delineate the perspectives of our model developments for oxide fuels and suggest items for a future FUMEX-III project.

2. Fuel temperatures

As illustrated in Figure 1, the agreement between calculated and measured fuel centre temperatures in ramp tests of re-fabricated fuel rods is very satisfactory for all re-irradiated cases, except for Case 14, where the temperature is under-predicted by 10%.

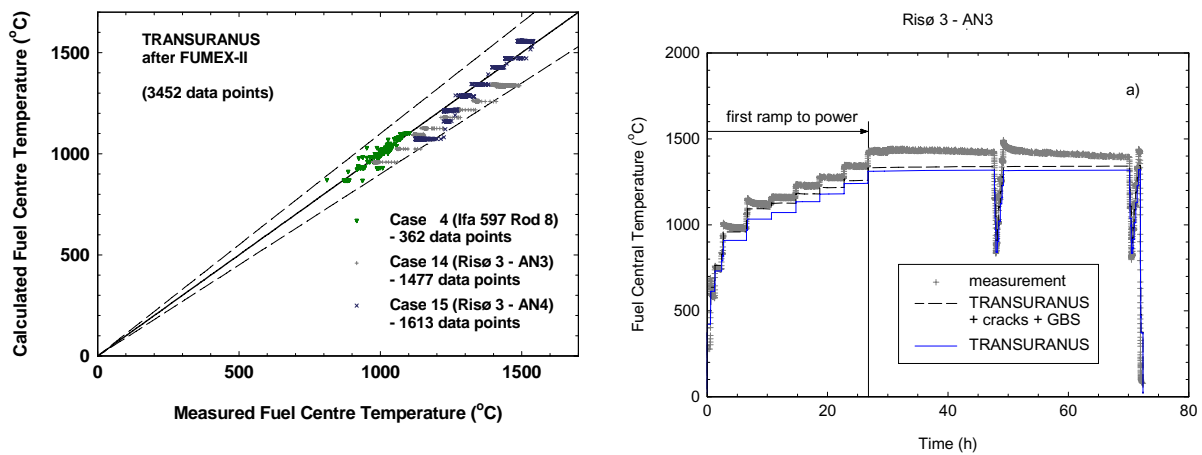


Figure 1: Comparison of central temperature predictions of the TRANSURANUS code with (left) all experimental results from FUMEX-II project, and (right) with the data of ramp test AN3 corresponding to Case 14 in FUMEX-II.

The predictions in FUMEX-II are therefore of the same precision as all previous predictions in the verification database of the TRANSURANUS code (Figure 2), which are based primarily on data from the IFPE database and from the OECD Halden Reactor Project. Nevertheless, the FUMEX-II calculations extend our verification database for UO_2 fuel both in number and in temperature range.

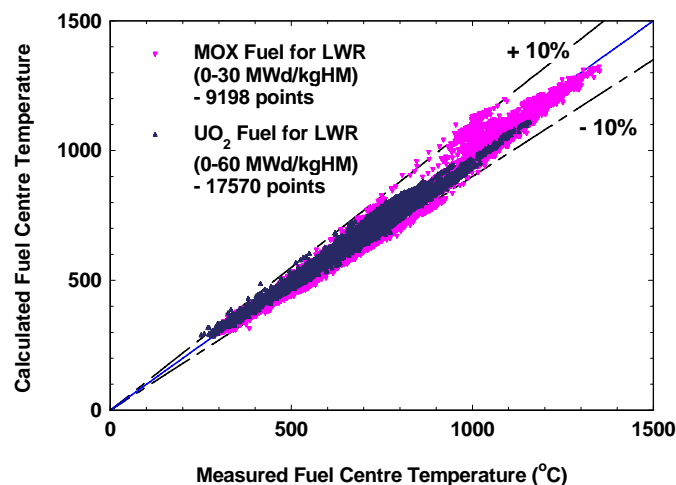


Figure 2: Comparison of central temperature predictions of the TRANSURANUS code with experimental results from the IFPE database and the OECD Halden Reactor project.

3. Cladding deformation

The comparison of predictions with measurements of cladding deformations receives generally less attention. Similarly, in FUMEX-II only two high-priority cases were chosen. For Case 3, Figure 3 shows the calculated elongation of the cladding during the irradiation of the re-fabricated rod. It is evident that the experimental data for the cladding deformation cannot be reproduced by the fuel performance code consistently throughout the irradiation. When shifting the experimental data of cladding elongation, either the prediction agrees with the initial phase or with the intermediate phase. When considering these parts of the irradiation separately, the TRANSURANUS code can satisfactorily model the relative evolution of the cladding elongation. However, the observed transition between the two considered phases (at a rod average burnup of approx. 59.4 MWd/kgHM) remains an open question. This could indicate shortcomings in the model (in particular in the models for creep

and axial friction) or an experimental offset. However, it is premature to draw definite conclusions from one single experiment without the completion of a sensitivity analysis.

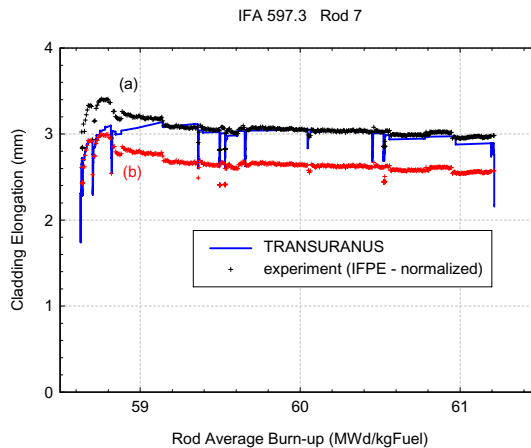


Figure 3: Comparison of measured and calculated cladding elongation as a function of rod average burnup in the re-irradiation of IFA-597.3, rod 7 (Case 3 of FUMEX-II). The measured results have been re-normalized to match the intermediate phase of the re-irradiation.

From the clad diameter changes reported in the REGATE case (Case 7 of FUMEX-II) we could conclude that the predictions are satisfactory both after base irradiation and after re-irradiation, apart from the oxide layer thickness calculations. Nevertheless, no firm conclusions can be drawn because of the incompleteness in the boundary conditions and experimental results provided in the IFPE database for this case, and mostly because of the limited number of experimental data analysed.

4. Fission gas release

Grain boundary sweeping, as an additional mechanism for fission gas release driven by UO_2 grain growth, has been recently incorporated in the TRANSURANUS code. The results of the analyses with the improved fission gas release model are satisfactory. For the re-fabricated fuel rods, the ratio of measured to computed fission gas release values remains below a factor of two, except in Case 7. Nonetheless, the simulation of fission gas release presently implemented in the TRANSURANUS code can not describe the release bursts observed during some rapid power variations. This contributes to the systematic (but acceptable) under-estimation of fission gas release during ramp tests. One should, however, underline the need to clarify the inconsistencies in some experimental data (e.g. discrepancies between on-line pressure measurements and post irradiation pressure measurements in Cases 1, 2, and 4).

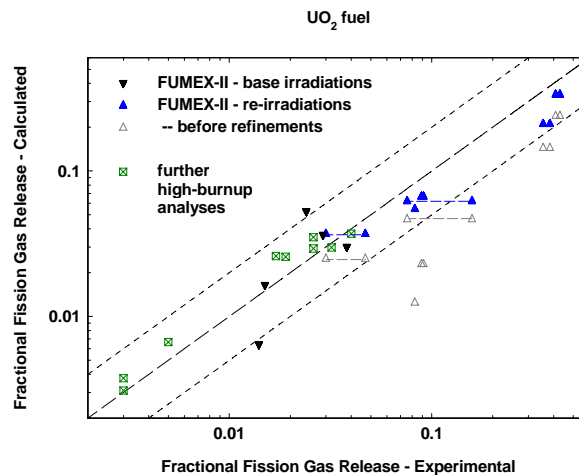


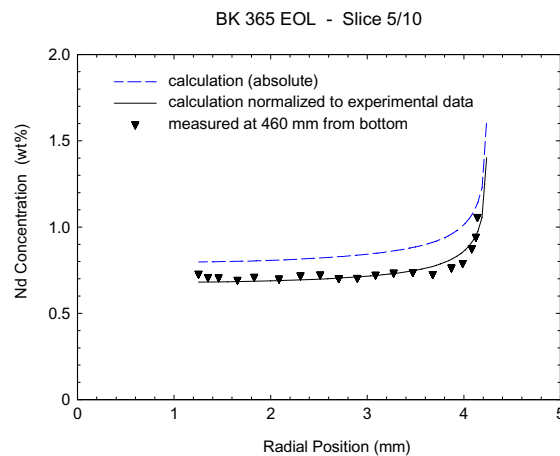
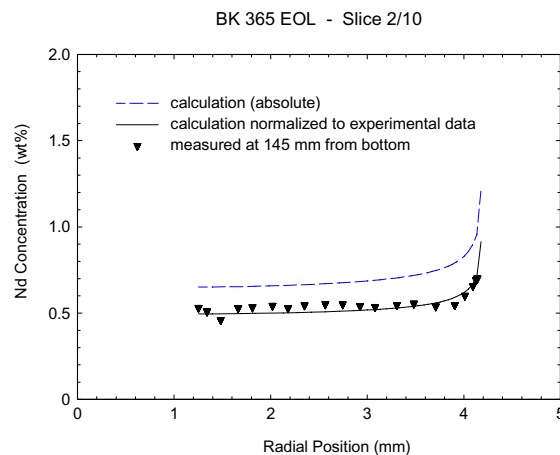
Figure 4: Fission gas release prediction by the TRANSURANUS code versus experimental data from the IFPE data base. The improvement resulting from the refinements of the fuel performance code stemming from the FUMEX-II CRP of the IAEA is also indicated.

For simulation of fission gas release at burnup values above 50 MWd/kgHM, the present version of the TRANSURANUS code contains a very simple model for release from the HBS. According to this model, the increase of the fission gas release at high burnup, as observed in commercial fuel rods, can be largely attributed to the release from the HBS. Recent experimental findings contradict this assumption. [3,4]. Before drawing consistent conclusions, however, the role of the HBS in the increase of the fission gas release should be further experimentally quantified.

5. Radial profiles of fission products

The TUBRNP module of the TRANSURANUS code has already been carefully verified against a large set of data [5]. In the present exercise, the radial profiles of Nd, Xe and Cs could be verified in the HBEP case 17 at three axial elevations (cf. Figure 5), as well as in the REGATE case (case 7). In case 17, the linear heat rate provided in the IFPE database had to be increased by 5% in order to obtain the burnup value of 66.75 MWd/kgHM mentioned in the IFPE database. This has contributed to the systematic overestimation of the radial profiles of Nd, Cs, Xe and Pu [2]. As the normalisation factor was the same for Nd, Cs and Xe, but different for each axial position, it is unclear whether the axial power distribution provided in the IFPE database was correct.

Apart from a normalisation issue noticed in the HBEP case, the radial profiles could be well reproduced. There is, however, room for improvement in the absolute radial profiles of Pu at burnup levels of the order of 100 MWd/kgHM, even though this has a negligible impact on the radial power density. Despite this, an improved set of effective one-group cross-sections is being developed.



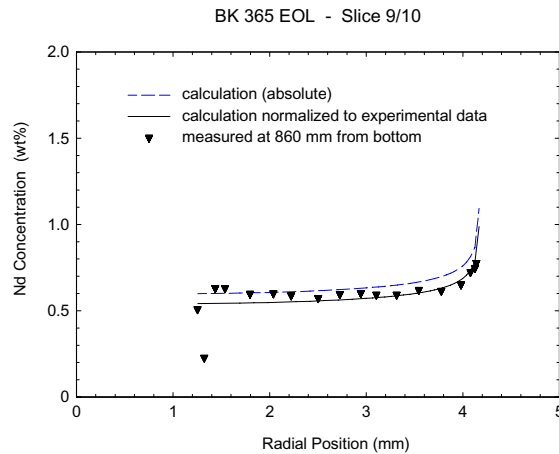


Figure 5: Radial distribution of Nd concentrations for Case 17 (HBEP, rod BK365) at three axial elevations, obtained by means of EPMA.

6. Perspectives

The computations have shown that the TRANSURANUS code can be regarded as a mature system for modelling integral fuel rod behaviour up to high burnup. No numerical problems or discontinuities were observed. Further efforts will nevertheless focus on the development of a more elaborate model for the HBS, in particular (1) the dependence of the formation of the HBS on the initial microstructure and (2) the capability of the HBS for retaining fission gas, as well as the completion of the sensitivity analysis to take into account some experimental uncertainties. Both are in progress. When the modifications necessary for the proper simulation of the LOCA cases are incorporated in the standard version of the TRANSURANUS code, the simulation of the LOCA case proposed in FUMEX-II CRP will be carried out as well.

In line with these perspectives, it seems appropriate to include in a potential FUMEX-III project a more extensive verification of the cladding deformation, the behaviour under accident conditions (e.g. LOCA) as well as an analysis of MOX fuel behaviour in a LWR.

Acknowledgements

The authors would like to express their gratitude to Drs. S. Boneva and M. Georgeva, and S. Asenov from INRNE in Bulgaria, Dr. A. Paraschiv from INR in Romania, and Dr. C. Hellwig as well as A. Nordström from PSI in Switzerland for their interesting discussions and many contributions in the preparation of the calculations.

References

- [1] "Fuel Modelling at extended burnup (Fumex-II)", to be published in 2006, IAEA TECDOC.
- [2] P. Van Uffelen, A. Schubert, Cs. Györi, J. van de Laar, "The high-priority cases of the FUMEX-II exercise simulated with the TRANSURANUS Code", 2005, ITU-report JRC-ITU-TN-2005/46.
- [3] M. Kinoshita, T. Sonoda, S. Kitajima, A. Sasahara, T. Kameyama, T. Matsumura, E. Kolstad, V.V. Rondinella, C. Ronchi, J.P. Hiernaut, T. Wiss, F. Kinnart, J. Ejton, D. Papaioannou, H. Matzke, "High-Burnup Rim Project: (III) Properties of Rim-Structured Fuel (Paper 1102)", International Meeting on LWR Fuel Performance, Orlando, Florida, 19-22 September 2004.
- [4] P. Van Uffelen, J. Jonnet, C. Ronchi, "Open Questions Related to the High Burnup Structure in Nuclear Fuels", Proc. of Workshop Materials Models and Simulations for Nuclear Fuels, No 18-19, Washington, DC, USA, 2004.
- [5] K. Lassmann, C.T. Walker, J. van de Laar, "Extension of the TRANSURANUS Burnup Model to Heavy Water Reactor Conditions", Journal of Nuclear Materials, Vol. 255, pp. 222-233, 1998.

RECENT MODELLING FEATURES IN THE COPERNIC3 AREVA NP FUEL ROD PERFORMANCE CODE

Ch. GARNIER, P. MAILHE

AREVA NP

10 rue Juliette Récamier, 69456 Lyon, France

F. SONTHEIMER, H. LANDSKRON, D. DEUBLE

AREVA NP GmbH

P.O. Box 3220, D-91050 Erlangen, Germany

V.I. ARIMESCU, M. BILLAUX

AREVA NP Inc.

Richland, WA, 99354, USA

ABSTRACT

COPERNIC3 is an advanced fuel rod performance code under development by AREVA NP. The main objectives of the code are to accurately predict fuel behaviour under steady-state, transient and storage conditions. The microstructure and the composition of nuclear fuel at high burnup are different from those of the as-fabricated fuel, in particular in the pellet rim region where restructuring occurs. It significantly affects fuel porosity and swelling, for which modelling changes are described. The migration of the fission gas atoms in the fuel matrix is also affected at high burnup. Modelling solutions for the high burnup FGR enhancement are presented in the paper. The mechanical modelling is detailed with emphasis on new pellet features including cracking, and dish filling evolutions. The models descriptions are illustrated by examples of code benchmarking for representative experimental and commercial cases. COPERNIC3 predictions compare very well with measurements for all cases presented, proving the accuracy of the code on a wide range of use and very different conditions.

1. Introduction

COPERNIC3 is an advanced fuel rod performance code in development by AREVA NP. Its starting point was the best of the models available in the AREVA NP codes COPERNIC2 [1], CARO-E [2], and SIERRA [3]. Close attention has been paid to the prediction of AREVA NP fuel behaviour at very high burnup [4]. An original HBS porosity model is presented, based on porosity measurements. The FGR model has been extended with new features to predict the enhancement of release observed at high burnup. As demonstrated by experimental data, this enhancement cannot be explained by a rim contribution. The additional release comes from the pellet centre. A gas concentration limit is introduced in the model. It is justified by the correct prediction of the enhancement and is supported by the xenon concentration radial profiles measured by EPMA. Finally, the pellet mechanical model is also discussed with emphasis on cracking and dish filling modelling.

2. Rim Porosity model

Fuel rim or High Burnup Structure (HBS) has been observed at the fuel pellet periphery when the local burnup exceeds roughly a value of 60 GWd/tU and the local temperature remains below 800 °C. The pore size in the rim region is more or less constant - about 1.1 to 1.5 µm – and the pore density decreases from the periphery going towards the pellet centre. A new model was introduced into COPERNIC3 to describe this fuel restructuring. The additional porosity generated in the rim region contributes to the local total porosity, by adding it with the as-fabricated porosity part remaining after densification. Then it is used to calculate density and all porosity-dependent parameters, especially the fuel thermal conductivity. In previous versions of COPERNIC, the contribution of the rim was only used for the pellet thermal conductivity and athermal fission gas release models. Neglecting these

contributions was justified for moderately high rod average burnup, i. e., around 60 GWd/tU when the restructured region is narrow. It is no longer the case for recent data up to 100 GWd/tU [5] when the HBS can extend to mid-pellet radius. The model is plotted and compared to experimental data on Fig.1 for fuel rods irradiated 4 to 6 cycles in French PWRs. These data were obtained from SEM images analysis carried out by the CEA [6,7] with burnups derived from EPMA measurements.

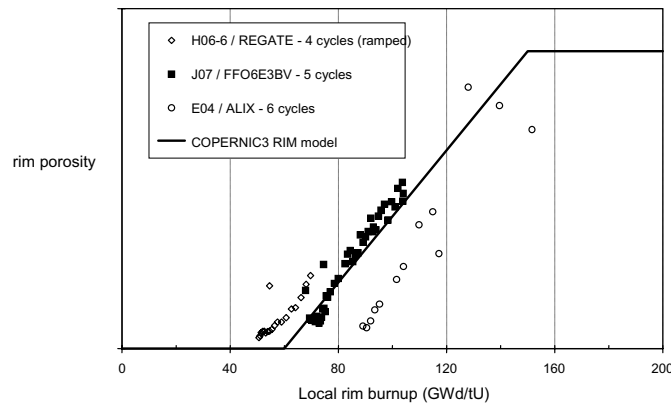


Fig. 1. Comparison of the COPERNIC3 rim porosity model and experimental data

In the model implementation, the burnup used to calculate the rim porosity is obtained by integrating the local power with respect to time only when the temperature is below a low temperature threshold. Otherwise this so-called “rim burnup” decreases exponentially with a relaxation time parameter, and then differs from the true local burnup. Indeed, the rim restructuring is prevented at higher temperature, and it naturally reproduces the fact that even at very high pellet burnup, the HBS is not formed in generally hot centre parts of the fuel. The model also contains a high limit value even if porosity greater than 20% has already been observed [8] (to compare with new rim porosity added to initial remaining porosity). This porosity threshold is necessary to obtain correct agreement with cladding diameter changes measured at high burnup. Moreover, the solid swelling model is reduced as soon as the rim porosity model is activated, still to avoid dimensional changes overestimations. It can also be justified because the fission gas products playing a major contribution (~ 70%) in the solid swelling before restructuring are then purged from the matrix and occupy the big rim pores. So an increase in volume due to rim pore formation is somewhat counterbalanced by solid swelling change, from which the simpler and satisfactory model consists in stopping this swelling. Eventually from a mechanical and macroscopic point of view, the rim phenomenon is hard to simulate because volume change conditions depart from the fundamental small strain hypothesis, combined with a huge radial strain gradient.

3. Fission gas release modelling

The new extended fission gas release (FGR) model in COPERNIC3 is based on the original model of Bernard [9], which is a classical two-step diffusion model (Booth model) following the 3-terms formalism of Turnbull for the diffusion coefficients, and which in addition to the steady-state thermal release, it also describes transient effects and athermal release. The thermal model takes into account grain boundary incubation and saturation and irradiation-induced resolution from the grain boundaries, which counteracts the diffusion flux and delays the onset of release. The transient model handles additional burst effects for relevant and rapid power changes. Future higher burnup and duty applications beyond about 65 GWd/tM were the focus of the model extension. The new model application range had to be extended to BWR power reactor conditions also.

Experimental feedback shows potential FGR enhancement with burnup, which starts at a burnup beyond about 60 GWd/tU for UO₂ low power fuel, above about 50 GWd/tU for UO₂ medium and high power fuel and exists throughout irradiation for very high power MOX fuel. New mechanisms were needed for the observed high burnup FGR enhancement.

There is clear experimental evidence for only small FGR from the high burnup rim structure to the rod free volumes [10]. The main contribution of the rim region to FGR enhancement is via pellet temperature increase, if any. The bulk of the gas produced in the pellet rim remains mainly in closed

spherical rim porosity. This is modelled in COPERNIC3 as a small athermal contribution to FGR. It amounts to about 1.0 – 1.5 % pellet release for a pellet burnup between 80 and 90 GWd/tU. The low release from the rim region implies that other mechanisms have to be found to explain high burnup effects.

An approach is chosen which is based on EPMA observations on pellet sections of irradiated fuel. In fuel rods with steady-state power there is a strong depletion of fission gases in the inner pellet regions at high burnup (beyond about 50 GWd/tM pellet average) despite low powers and temperatures for most of the irradiation time [2]. This is supported both by local FGR measurements in the fuel matrix (EPMA) and by the isotopic composition of the integral measured pellet release (there is much less plutonium here compared to the rim region; the xenon and krypton yields are consequently different). In ramped fuel rods with short hold times, EPMA radial profiles evidence an almost spontaneous decrease of the xenon concentration in the fuel matrix at burnups beyond about 30 GWd/tU and temperatures above about 1000 °C. The effect consistently shows distinct steps in EPMA profiles of such rods [2]. Both in steady-state and ramp conditions a coalescence process of submicroscopic bubbles is probably taking place and larger intragranular bubbles appear. The decreasing matrix concentration is thus explained by the capture of the migrating gas atoms by the intragranular bubbles. These observations led to the introduction of a xenon concentration limit in the fuel matrix which is dependent on local fuel burnup and temperature with a similar formulation to the Lassmann curve [11] but generalized to the whole pellet. Fig. 2 shows that such a saw tooth-like temperature-dependent shape of the matrix xenon concentration versus burnup is actually observed in plutonium-rich particles of MOX fuel [12] and that it is in reasonable agreement with the COPERNIC3 correlation.

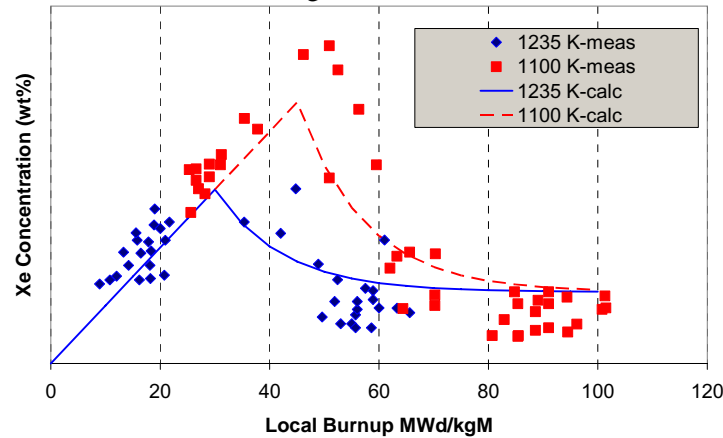


Fig. 2 Xenon concentration limit as measured on Pu particles in MOX fuel and calculated.

Just like the thermally released fission gas, the gas released from the fuel matrix, when the xenon concentration limit is reached and exceeded, is assumed to quickly reach grain boundary bubbles or big bubbles or pores inside grains (especially when the grains are big). How much of this gas is released to the void volume then depends on the degree of interlinkage of the bubbles and pores. The interlinkage process is modelled in a simple way as follows. If G_{BOOTH} is the gas thermally released as predicted without high burnup modelling, and G_{BUB} the gas produced in excess of the xenon concentration limit and assumed in big bubbles, the gas released from G_{BUB} is written:

$$G_{REL} = C_{BUB} \cdot G_{BUB} \text{ with } C_{BUB} = \min \left\{ \max \left[0, \frac{(G_{BOOTH} - G_-)}{(G_+ - G_-)} \right], 1 \right\}$$

G_+ and G_- are model parameters. The degree of interlinkage used in COPERNIC3 is determined from extensive PIE on irradiated fuel [13]. As at high burnup, interlinkage is normally well developed in the inner parts of the fuel pellet, much of this gas can leave the fuel and reach the rod free volumes and thus give a relevant contribution to the burnup enhancement of FGR.

As a demonstration of the effect of the xenon concentration limit, Fig. 3 shows the comparison of two measured and calculated EPMA profiles for the high burnup rod BK365 from the HBEP with annular pellet fuel, studied in the course of the IAEA CRP FUMEX-II exercise [14]. The results of EPMA on rod BK365 are very interesting. The central temperature of this rod is around 800°C for the last third of the irradiation. The central burnup near the central hole is about 70 GWd/tU. The central, sharp depression of the EPMA radial profile observed at this burnup (square points) is found to have the fuel

structure similar to the pellet rim structure with almost twice as large burnup of 140 GWd/tU. Thus, at the edge of the central hole at a burnup of only 70 GWd/tU, at which a rim structure is expected to just start developing, it seems that the fuel temperature of 800 °C had an enhancing effect on rim structure formation.

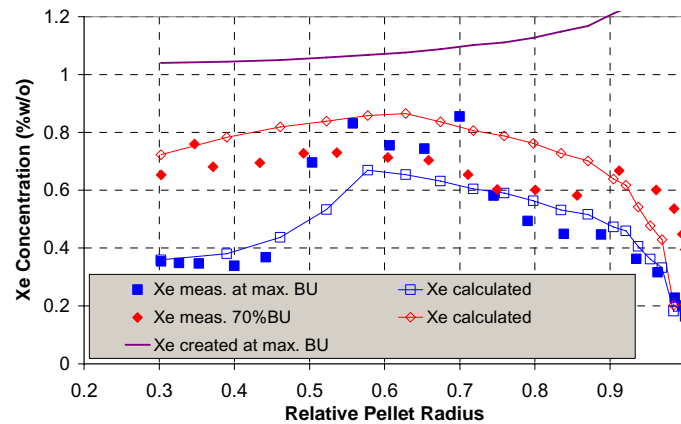


Fig. 3. Measured and Calculated EPMA Profiles on High BU Hollow Pellet Fuel

This enhancement is well described by the FGR model in COPERNIC3, where it is a consequence of the temperature and burnup dependent xenon concentration limit. The FGR enhancement corresponds to the development of the large intra-granular bubbles at high burnup, which have a strong similarity to the rim but start to form at a lower burnup threshold due to the higher temperature.

It has to be noted that the different model parameters used to define the xenon concentration limit and the interlinkage are fitted to predict final fission gas release measurements, which are the important quantities to predict. It implies that the xenon profile comparisons give an overall validation of the COPERNIC3 modelling ideas.

4. Pellet mechanical model

A mechanical model called MEFISTO has been implemented in COPERNIC3 and improved during the code development. The original model comes from the thermal-mechanical fuel rod code METEOR developed at CEA [15]. It consists in a classical finite element method to solve the mechanical problem, for which innovative algorithms have been added to combine a pellet cracking model, a plasticity model for cladding and a creep model for pellet and cladding.

The rod is considered axi-symmetric during the whole power history, with a mono-dimensional discretization in the radial direction of cylindrical coordinates. Stresses and strains are obtained as solutions of the equilibrium balance and compatibility relations with the proper boundary conditions. A generalized axial plane strain is assumed in the pellet shoulder whereas a generalized axial plane stress is chosen in the dish, which is more representative of this region and allows dish filling as it will be explained below. Perfect contact is assumed between pellet and cladding. Most of the important cladding models are described in [16] and we will concentrate in this paper on pellet mechanics.

As soon as the fuel viscoplasticity behaviour is introduced, it is necessary to take into account relaxation of tensile stresses by cracking in order to be more realistic. But we have to keep in mind that a 1D smeared crack model does not give much more realism. In particular no realistic cracking kinetics or cracking faces can be deduced from this model. Basically, it consists in rewriting the classical Hooke law by imposing a stress value in axial or tangential direction, representative of the cracked region. Compared to the original model, this imposed value is an input parameter and is taken by default to be opposite to the internal pressure. Then, the stress in this direction is not an unknown anymore, and as a consequence, elastic strains neither satisfy the compatibility relations. Finally, a new unknown appears with the crack strain to close the problem. This model is activated for a given element in one direction wherever the calculated stress in this direction exceeds the tensile fracture stress (typically 150 MPa for UO₂ but also defined as an input parameter). On the contrary, the crack closes when the calculated crack strain becomes negative supposing a given crack situation. The cracking strain can be considered representative of crack voids if the pellet remains roughly cylindrical after cracking, and then it contributes to the increase in the apparent pellet radius.

This last physical interpretation has been favourably used to introduce a dish filling model in MEFISTO. Roughly speaking, the dished ends can be considered as a large initial axial crack where mechanical conditions are close to plane axial stress conditions. It is exactly the kind of problem that the MEFISTO model is able to solve. When axial physical strains (thermal expansion, gaseous swelling, creep ...) fill the dish, the axial plane strain hypothesis is no longer physically justified. But in order to keep a consistent finite element formulation in dish and pellet shoulder regions, an additional strain balances the difference in such a way that plane strain remains mathematically valid. But in this case, the lower limit of this additional strain is no longer zero like in the classical crack model, but it corresponds to the opposite of the dish volume, that is to say the initial tank volume reserved for physical strains. Moreover, axial stress in the dish keeps a uniform value and then an axial plane stress is verified.

5. Conclusion

A representative sample of recent pellet models have been presented, especially those concerning high burnup behaviour. This period of the rod history is first of all characterized by a new rim structure which is carefully modelled from a macroscopic point of view. The FGR model presented here and developed in the COPERNIC3 code, will allow extending the validation range of the AREVA NP fuel rod design code to a very high burnup. The validation work will be continued and extended with other available experimental data, to strength the new models and concepts introduced in order to fit the needs of utilities. The FGR model initially based on well-validated models from present day AREVA NP codes, takes into account the formation of big bubbles at high burnup and, in addition, the resulting FGR, via the gas concentration limit model. The model satisfactorily matches the experimental profiles of xenon concentration from which it has been deduced, and the final FGR predictions at very high burnup are considerably improved. Finally, technical solutions have been described in order to introduce pellet cracking behaviour and dish filling phenomenon, necessary to precisely calculate void volumes especially at high burnup.

References

- [1] BERNARD L.C. & al. "The FRAMATOME COPERNIC fuel rod performance code, Recent high burnup and advanced cladding developments" International Topical Meeting in LWR fuel performance, Park City (2000)
- [2] SONTHEIMER F. & LANDSKRON H. "Puzzling features of EPMA radial fission gas release profiles: the key to realistic modeling of fission gas release up to ultra high burnup of 100 MWd/kg M with CARO-E", IAEA TCM on Nuclear Fuel Behaviour Modeling, Windermere (2000)
- [3] BILLAUX M.R. & al. " SIERRA: a fuel performance code to predict the mechanical behaviour of fuel rods up to high burnup" International topical meeting on LWR fuel performance, Portland (1997)
- [4] SONTHEIMER F. & al. "High burnup UO₂ fuel modelling with COPERNIC3" IAEA TM on Fuel Behaviour Modelling under Normal, Transient and Accident Conditions and High Burnups, Kendal (2005)
- [5] MANZEL R., WALKER C.T. , J. Nucl. Mat. 301 (2002) 170-182
- [6] BAGOT R. & al. , DEC/S3C/03-137, CEA Technical Note (2003)
- [7] PUJOL X. & al., DEC/SA3C/04-023, CEA Technical Note (2004)
- [8] SPINO J. & al. , J. Nucl. Mat. 354 (2006) 66-84
- [9] BERNARD L.C. & al. , J. Nucl. Mat. 302 (2002) 125-134
- [10] KINOSHITA M. & al. "High-Burnup Rim Project: (III) Properties of Rim-Structured Fuel" paper 1102, International Meeting on LWR Fuel Performance, Orlando, 2004.
- [11] LASSMANN & al. , J. Nucl. Mat. 226 (1995) 1-8
- [12] MERTENS L. & al., (BELGONUCLEAIRE) "HBS development in MOX fuel", International Workshop on the High Burn-up Structure in Nuclear Fuels, ITU Karlsruhe (2004)
- [13] SONTHEIMER F. & al. "Release of the volatile fission products Xe, Kr and Cs from PWR fuel under steady and transient conditions up to high burnup" IAEA TCM on Fuel Rod Internal Chemistry and Fission Product Behaviour, IAEA-TC 544 No. 9, Karlsruhe (1985)
- [14] SONTHEIMER F. "Participation in the IAEA Coordinated Research Project FUMEX-II: Final Report of FRAMATOME ANP" Work Report A1C-1317992-0 AREVA NP (2005)
- [15] GARCIA P. & al. , Nucl. Eng. & Design 216 (2002) 183-2001
- [16] GARNIER & al. "The COPERNIC mechanical model and its application to doped fuel" Int. seminar on pellet clad interaction in water reactor fuels, NEA, Aix-En-Provence (2004)

UTILIZATION OF SIMTAB METHODOLOGY IN TRANSLATING THE KINETICS PARAMETERS FROM SIMULATE-3 TO RELAP5/PARCS FOR REA 3D-DYNAMIC ANALYSIS IN TRILLO NPP

R. MIRÓ, T. BARRACHINA, F. MAGGINI, O. ROSELLÓ, G. VERDÚ

*Departamento de Ingeniería Química y Nuclear. Universidad Politécnica de Valencia.
Cami de Vera, s/n. 46022, Valencia. Spain.*

A. GÓMEZ, A. ORTEGO

IBERINCO. Avenida de Burgos, Madrid. Spain.

J. C. MARTÍNEZ-MURILLO

CNAT, Av. Manoteras, Madrid. Spain.

ABSTRACT

The Reactor Ejection Accident (REA) belongs to the Reactor Initiated Accidents (RIA) category of accidents and it is part of the licensing basis accident analyses required for pressure water reactors (PWR). The REA at hot zero power (HZP) is characterized by a single rod ejection from a core position with a very low power level. The evolution consists basically of a continuous reactivity insertion. The main feature limiting the consequences of the accident in a PWR is the Doppler Effect. To check the performance of the coupled code RELAP5/PARCS2.5 and RELAP5/VALKIN a REA in Trillo NPP is simulated. These analyses will allow knowing more accurately the PWR real plant phenomenology in the RIA most limiting conditions.

The present work consists of developing an in-house methodology, called SIMTAB, to characterize, in a simplified way, the reactor core of LWR Nuclear Power Plants. Specifically, a cross-sections and kinetic parameters set are obtained as a function of the prompt and control variables. So that, the core can be modeled using a limited number of neutronic regions, in such a way that the reactor kinetic behavior is properly characterized. This simplification of the reactor core permits, from an operative point of view, the use of few cross sections data sets in coupled 3D neutronic-thermohydraulic codes.

1. Introduction

Nuclear industry and licensing authorities need to be able to rely on the good performance of methods and computer programs used in safety analysis calculations. This is best achieved through validation and benchmarking.

With the implementation of advanced fuel management, margins to safety and licensing limits are frequently reduced. This leads to general development of advanced methods that reduce the level of conservatism by implementing kinetics methods that capture spatial effects occurring during reactor transients more accurately. The performance of physical models and numerical methods needs to be established over a realistic range of applications.

The progress in analytical methods has evolved the classical thermohydraulic codes such as RETRAN, TRAC and RELAP towards modern codes with full capability of performing 3D kinetics analyses in a dynamic way, for simulating the behaviour of specific cores in a realistic manner and so to predict the localized power excursions as occurs in the RIA. These codes must be feed with the Kinetics information of physics codes like CASMO4-SIMULATE3 [1], [2]. SIMTAB methodology [3] provides an easy tool for properly extracting and formatting the X-sections and neutronic kinetic parameters from SIMULATE to the coupled neutronic-thermohydraulic codes, making feasible reactivity-based studies in BWR and PWR cores. SIMTAB allows to accurately transfer the initial kinetic status of the core from the physics code to the thermohydraulic code and provides the adequate kinetics response during the full transient.

The Reactor Ejection Accident (REA) belongs to the Reactor Initiated Accidents (RIA) category of accidents, and it is part of the licensing basis accident analyses required for pressure water reactors (PWR). The REA consist of a rod ejection due to the failure of its drive mechanism. The evolution is driven by a continuous reactivity insertion. The main factor limiting the consequences of the accident is the Doppler Effect.

In this paper it has been analyzed the behavior of a Trillo NPP core configuration in a REA (Rod Ejection Accident) with hot zero power (HZP) conditions at the beginning of cycle (BOC) and at the end of cycle (EOC), using the coupled neutronic-thermohydraulic codes RELAP5/PARCS2.5 [4] and RELAP5/VALKIN [5], [6]. The steady-state results have been compared with the physics code CASMO4-SIMULATE3, which provides the cross-sections sets and other neutronic parameters for the full transient by using the SIMTAB Methodology.

2. Parameterization of the cross sections

The cross-sections generation has been calculated by means of the simultaneous variation of various thermohydraulic parameters in SIMULATE3 following the methodology developed in PSU [7].

Fig. 1 shows the origin of the value of the cross sections obtained for averaged values of the local variables (exposure, control rod insertion (yes or not), historic, boron concentration, moderator temperature and fuel temperature) and around of this value it has been generated variations of the cross-sections by means of the perturbation of the moderator temperature and fuel temperature. This terms are named "Cross Term Cross-Sections" and they have a 2D dependence that can be generalized to a 4D dependence when also includes the perturbation of boron concentration and control rod insertion.

The nuclear parameters code generator has been called SIMTAB. This code uses the function AUDIT of SIMULATE3 to obtain the cross-sections.

Fig. 1 shows the process of generating the cross-sections set used by this computer code. The unique input deck needed by this program is the file DECISIO that contains the exposure criterion that the user imposes in function of exposure differences to distinguish two fuel elements segments. Another data that the user has to introduce is the number of axial neutronic regions that consider different and the variation range of fuel temperature and moderator density in which the obtained tables are valid.

The output files are *nemtab* and *nemtabr* which contain the cross-sections for rodded and unrodded conditions respectively, as function of the moderator density and fuel temperature.

The methodology runs in UNIX (64 or 32 bits), LINUX and PC platforms. The calculation to obtain 4500 compositions takes approximately seven minutes of real time in a LINUX platform (64 bits) against a time of 30 minutes that takes in a PC platform. In both platforms the Intel© Fortran 90 compiler has been used.

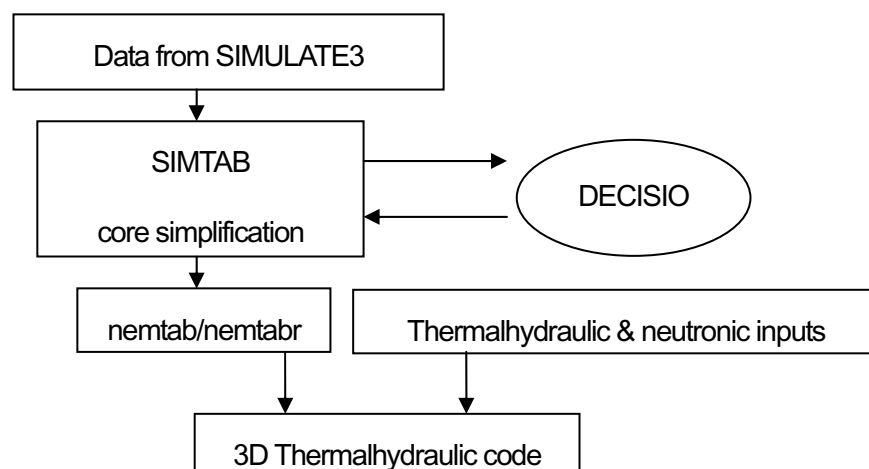


Fig 1: SIMTAB Methodology.

3. Description of the Model

The model used for simulating this transient is formed by a very detailed 3D core with boundary conditions.

The reactor core studied is composed of 177 fuel elements, being the number of fuel rods per fuel element equal to 236 with 20 guide tubes. The neutronic nodal discretization consists of 177 x 32 active nodes, considering 20 different fuel elements with 611 neutronic compositions. The cross-sections tables are generated with the SIMTAB methodology from CASMO4-SIMULATE3 code. A sensitivity analysis, using more compositions and comparing the results with CASMO4-SIMULATE3 code, demonstrates that the considered number of neutronic compositions is adequate.

The coupled codes RELAP5/PARCS2.5 and RELAP5/VALKIN are neutronic-thermalhydraulic codes to simulate 3D-geometry complex neutronic phenomena and thermalhydraulic events in multiple 1D-geometries channels. The reactor core has been modeled with 10 thermalhydraulic channels connected with branches (BRANCH) and the by-pass has been modeled as an independent channel (see Fig. 2). A time dependent volume (TMDPVOL) and a time dependent junction (TMDPJUN) simulate the boundary conditions at the entrance and exit of the reactor core as is shown in Fig. 4. Each thermalhydraulic channel representing the core is connected to a heat structure.



Fig 2. Thermalhydraulic channels.

The inlet mass flow through the core is 15605.7 kg/s and it is distributed uniformly among the channels.

The neutronic model uses two prompt neutron groups and six delayed neutron groups, while the boundary condition for the neutron diffusion equation is zero-flux at the outer reflector surface.

Radially, the core is divided in 23 cm x 23 cm cells, each corresponding to one fuel assembly, plus a radial reflector. There are 177 fuel assemblies and 64 reflector assemblies. Axially, the core is divided into 34 layers (32 fuel layers plus top and bottom reflector) with 10.625 cm height each one, with a total active core height of 340 cm.

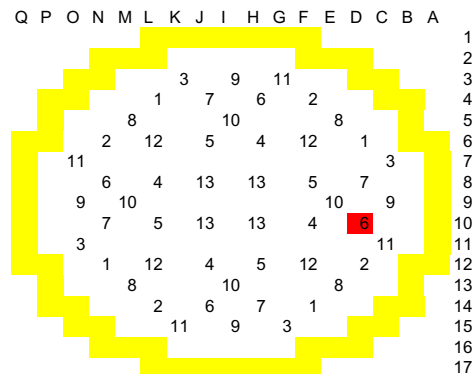


Fig 3. Control rod banks.

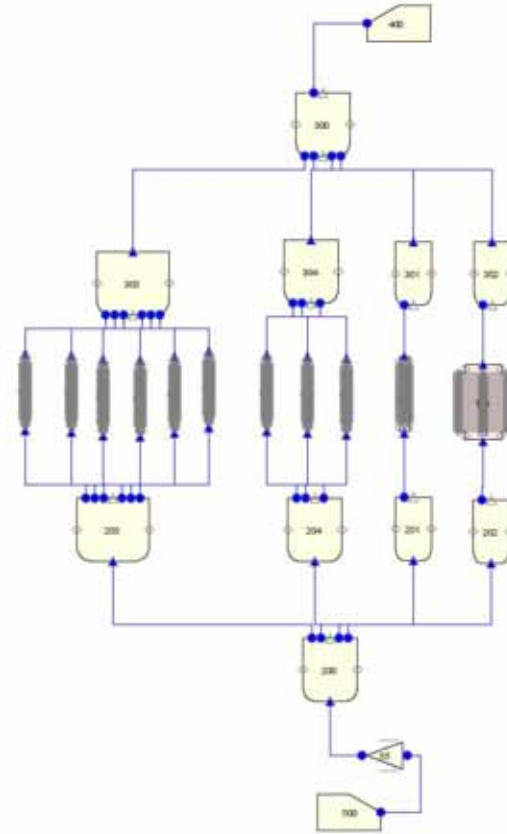


Fig 4. RELAP5 model.

A previous analysis determined that the control rod with the maximum worth belongs to the bank number 6 and it is located at position D-10 (see Fig. 2 and Fig. 3). The thermalhydraulic channels surrounding the ejected control rod have been modeled as independent channels, while the others have been grouped in a unique channel, because the phenomena of this kind of transients in HZP conditions are localized around the ejected control rod.

Control rods are grouped in 13 banks: initially banks 1, 5 and 6 are totally inserted and the other ones are out of the core. Fig. 3 shows the control rod banks and the ejected rod D-10 is highlighted in red.

The initial steady state is a HZP where the moderator density is 734 kg/cm^3 and the fuel temperature is 569.55 K .

The transient is started by the ejection of the rod D-10 which is completely extracted in 0.1 s . The values of control rod worth and β_{eff} for BOC and EOC are presented in Tab. 1.

Case	β_{eff}	Control rod worth (pcm)	Control rod worth (\$)
BOC	0.000605	408	6.74
EOC	0.000527	408.8	7.75

Tab 1: Values of β_{eff} and control rod worth.

4. Numerical results

4.1 Steady state results

Initial steady state has been simulated with the RELAP5/PARCS and RELAP5/VALKIN coupled codes. The Tab. 2 shows the obtained results of the k_{eff} and the Fig.5 shows the axial power profile for the different simulations.

Case	k_{eff} SIMULATE3	k_{eff} RELAP5-PARCS	desviation (pcm)	k_{eff} RELAP5-VALKIN	desviation (pcm)
BOC	0.982855	0.983032	17.7	0.983029	17.4
EOC	0.982733	0.983570	83.7	0.983180	44.7

Tab 2: Values of k_{eff} .

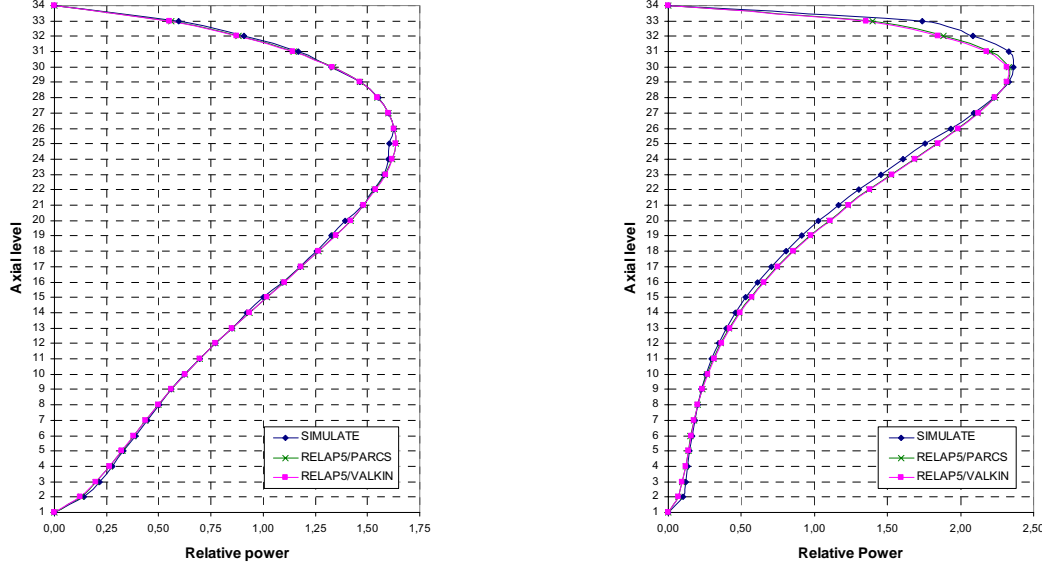


Fig 5. Axial power profiles at BOC and EOC.

4.2 Transient results

In both cases, BOC and EOC, zero-power state was considered as initial state and the control rod group 6 completely inserted, then the control rod D-10 is ejected. The evolution consists of a continuous reactivity insertion. The transient is terminated by the Doppler Effect caused by the increased fuel temperature, but this occurs before it reaches the limit that can be dangerous for the nuclear power plant safety, as it was expected.

Fig. 6 shows the power evolution during the transient in both analyzed situations BOC and EOC.

Both neutronic modules, PARCS and VALKIN give practically the same transient results. The Fig. 6 to 9 correspond to PARCS calculations.

The Doppler temperature calculated by PARCS and VALKIN codes is found from the fuel temperature at the fuel rod center T_{fc} and the fuel rod surface T_{fs} via the relation:

$$T_f = (1 - \alpha) \cdot T_{fc} + \alpha \cdot T_{fs}, \quad (1)$$

where α is taken equal to 0.7.

5. Results and Discussions

Figs. 6 to 9 show the transient evolution of the six parameters selected for the analyses: power, Doppler temperature, average coolant outlet temperature, enthalpy rise, fuel centerline temperature and reactivities. It can be seen, that in the EOC scenario a first power peak occurs, followed by a relatively slow power increase, until it reaches a plateau value around 160 times the initial power. In this case the averaged Doppler temperature plateau is 600.56 K. In EOC the power increase is very fast; this fact is coherent with the central rod worth and the β -effective values. Otherwise, in the BOC scenario the power increases slowly reaching a plateau level around 320 times the initial power, higher than the EOC case; in this scenario the Doppler temperature is around 634.07 K, higher than the EOC case. In both cases, the Doppler feedback is the mechanism which drives the evolution of the parameters. In general, for this real best estimate case, in HZP conditions and for the two scenarios BOC and EOC, the maximum power reached is very lower than the scram trip level. In the same way, the maximum Doppler temperatures are lower than the specifications limit. For Trillo NPP, these analyses show that this event is irrelevant concerning the nuclear safety.

Furthermore, comparing the figures we can see that in the BOC case, the feedback moderator reactivity effect is neglectable in comparison with the Doppler reactivity, otherwise in the EOC case, both feedback reactivities play the same role during the transient.

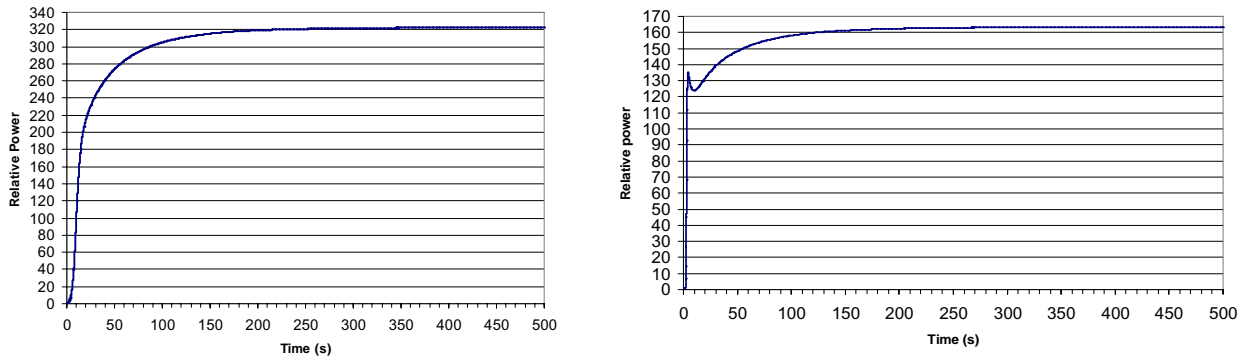


Fig 6. Power evolution during the transient at BOC and EOC.

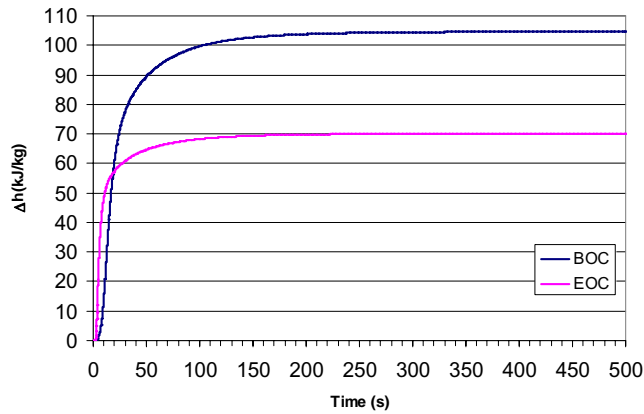


Fig 7. Enthalpy rise.

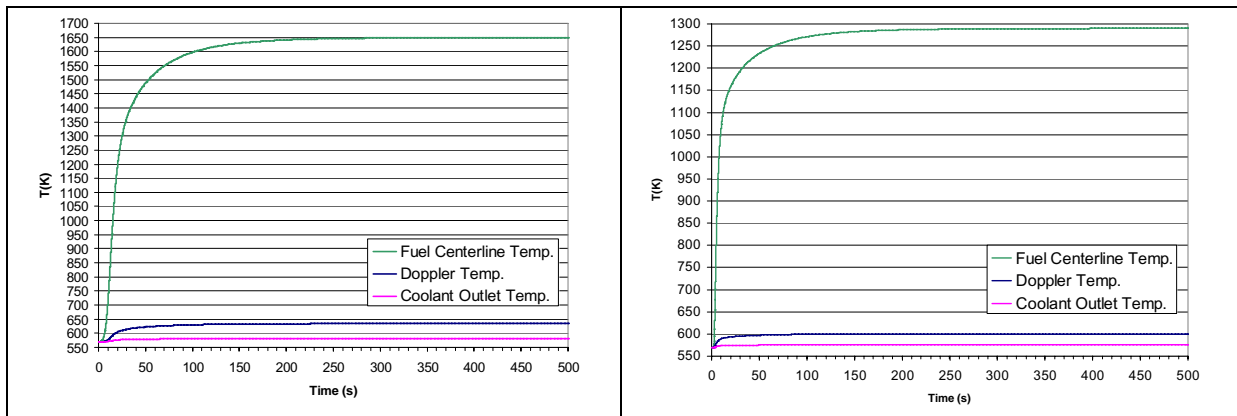


Fig 8. Temperatures at BOC and EOC.

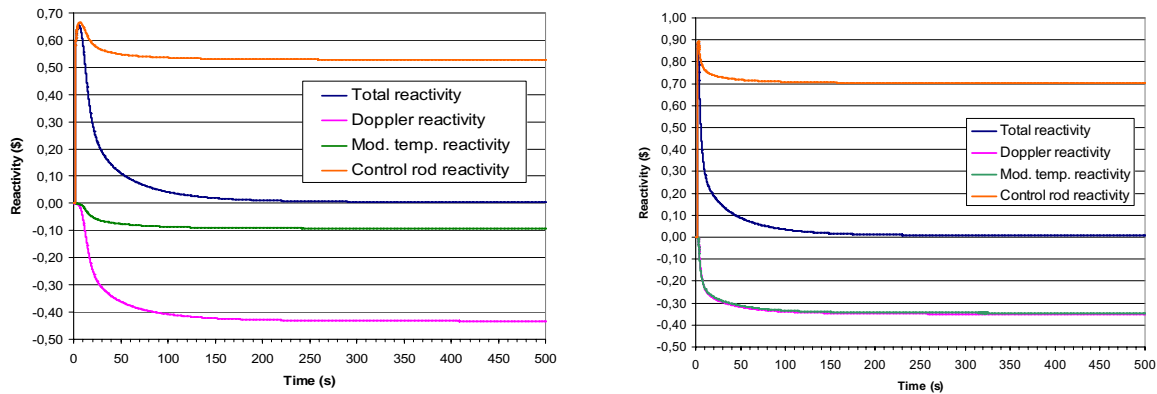


Fig 9. Reactivity at BOC and EOC.

6. Conclusions

The methodology SIMTAB characterizes, in a simplified way, the reactor core of LWR NPP. Cross-sections are obtained as a function of the control rod and thermalhydraulic variables (fuel temperature and moderator density) for a specific point of operation (History and Exposure).

With the SIMTAB methodology the reactor core can be modelled using few neutronic regions, in such a way that the nuclear kinetic behaviour is adequately characterized. This simplification permits the use of few cross-sections data set in coupled 3D neutronic-thermalhydraulic codes, saving memory and CPU times in simulation of real transients in LWR NPP.

These analyses of Trillo NPP allow knowing more accurately the PWR real plant phenomenology in the RIA most limiting conditions, in this way the conclusions are realistic. They also serve as a start point for subsequent studies of the effect of high burnup in the RIA consequences.

References

- 1) D. Knott, B. H. Forssén, M. Edenius, "CASMO-4. A fuel assembly burn-up program", Studsvik/SOA-95/2 (1995).
- 2) J. T. Cronin, K. S. Smith, D. M. Ver Planck, "SIMULATE-3. Advanced three-dimensional two-group reactor analysis code", Studsvik/SOA-95/18 (1995).
- 3) O. Roselló, "Desarrollo de una metodología de generación de secciones eficaces para la simplificación del núcleo de reactores de agua ligera y aplicación en códigos acoplados neutrónicos termohidráulicos". PhD Thesis. (2004).
- 4) T. Downar, D. Lee, Y. Xu, T. Kozlowski, J. Staundenmier, "PARCSV2.6 US NRC Core Neutronics Simulator" (2004).
- 5) D. Ginestar, G. Verdú, V. Vidal, R. Bru, J. Marín, J. L. Muñoz-Cobo, "High Order Backward Discretization of the Neutron Diffusion Equation", Ann. Nucl. Energy, 25,1-3,47, (1998).
- 6) R. Miró, D. Ginestar, G. Verdú, D. Hennig, "A Nodal Modal Method for the Neutron Diffusion Equation. Application to BWR Instabilities Analysis ", Ann. Nucl. Energy, 29, 1171, (2002).
- 7) J. Watson, K. Ivanov, "Improved Cross-Section Modeling Methodology for Coupled Three-Dimensional Transient Calculations", Ann. of Nucl. Energy, 29, 937-966, (2002).

CYRANO3: the industrial PLEIADES fuel performance code for EDF PWR studies

P. THEVENIN, R. MASSON, D. BARON

EDF-R&D, MMC/T25

Site des Renardières, 77818 Moret-sur-Loing – France

Phone : +33 4 42 25 49 76, E-Mail : philippe-florent.thevenin@edf.fr

B. PETITPREZ

EDF-SEPTEN, Nuclear Engineering Division

69628 Villeurbanne – France

D. PLANCO

CEA Cadarache – DEN/DEC/SESC/LSC

Bât 151, 13108 Saint Paul-Lez-Durance – France

ABSTRACT

In order to survey the supplier's fuel rod design studies, to establish the operation technical specifications, to build safety studies for new fuel management and to define the fuel initial conditions of accidental situations, EDF needs a reliable code to simulate the PWR thermo-mechanical fuel behaviour. The industrial reference code CYRANO3 has been developed to fulfil these objectives. CYRANO3 is basically composed of fuel physical models established on separate parameter measurements (e.g. thermal diffusivity, annealing, sintering, gaseous diffusion...) performed on both fresh and irradiated fuel pellets and of cladding mechanical models identified by mechanical tests on as-fabricated and irradiated cladding tubes out and under irradiation for different fast neutrons flux levels, strain/stress loadings and temperature ranges.

1. Introduction

CYRANO3 is the actual “home made” computer code used by EDF [1] to perform all the design calculations and therefore provides the safety reports for core reloading or new core management justifications for EDF fuel suppliers (AREVA and EFG) commercial rods. It simulates the behaviour of UO_2 , UO_2+Gd fuel, and more recently UO_2 with various additives. For MOX fuel, heterogeneity of the material is accounted for. Within the PWR safety studies framework, the verification of the fuel safety criteria, the integrity of the fuel rod (first safety barrier) has to be guaranteed in any class I and II operating conditions, and then challenge the industrial licensing requirements [2,3].

CYRANO3 is a second-generation code written by the EDF R&D department during the nineties. It has taken benefit of the experience acquired in the past by the nuclear fuel designers, is adapted to follow closely the evolution of the computers capabilities and brings a high conviviality for the user and for the developer as well. The architecture is modular. All modules can be disconnected for eventual bug research. CYRANO3 is totally dedicated for computing fuel rod thermal-mechanical behaviour with a dynamic memory management, and all results are stored in standard a binary file usable then independently by any post-processor's applications via a request procedure.

Computing systems are still evolving more and more quickly, offering faster computing time and new capabilities. The “object” architecture concept is a new challenge able to favour sharing of specialist components, solving algorithms or pre and post processors, or to favour codes coupling as well. CYRANO3 is already engaged in this process.

2. General code presentation

Taking benefit of the skill accumulated from the sixties to the eighties on fuel rod computer codes, CYRANO3 has been designed with respect to Quality Insurance exigency. The first line was written in

1990 and first release for fuel industrial design calculations was only achieved in 2000 after a long qualification period. However, it has been used for several years as a “laboratory” to develop new models. It has been built around a standard thermo-mechanical kernel.

As it is designed for parametric studies allowing computing a quarter or a eighth of the core, computing time is a major challenge. This high constraint must be kept in mind. Therefore the choice of the algorithms and of the models results from a compromise between the accuracy of the modelling and the computing time. Obviously this balance is evolving in permanence with computers capabilities.

CYRANO3 is basically composed of fuel physical models established on separate parameter measurements (e.g. thermal diffusivity, annealing, sintering, gaseous diffusion...) performed on both fresh and irradiated fuel pellets, and of cladding mechanical models identified by mechanical tests on as-fabricated and irradiated cladding tubes, out and under irradiation for different fast neutrons flux levels, strain/stress loadings and temperature ranges. Most of models used for the materials and gases behaviour are non-linear. This is a major concern regarding equation's convergence.

The initial time steps subdivision is define “a priori” relatively to the given local power histories. However internal flags during calculation processing are able to detect a too large variation of the sensitive parameters. In order to avoid convergence troubles the time step is automatically subdivided to insure the best convergence. More over, alternative convergence methods can, in extreme cases, supply the standard Newton robust method.

Inputs offer three level of access depending upon the quality of the user:

- level 1 : fuel rod designer, provided with a qualified configuration and fixed options. The user provides calculations with material, dimensions and power history data. He can choose the axial and radial mesh
- level 2 - research engineer in charge of developing models or new options. It allows an access to model variants, fitting parameters, optimisation options and so on
- Level 3 - code management: access to deep options of the algorithms

Moreover, CYRANO3 is integrating new capabilities to be used in the future to simulate the post-irradiation fuel rod behaviour, from unloading to storage period. This code has also been used inside an exhaustive analysis framework on the reactor primary coolant activities carried out by EDF for the last four years. Thermal-mechanical fuel rod calculations have been taking into account in the improvement of fuel failure assessment based on radiochemical parameters provided by the EDF MERLIN code [4]. For an exhaustive analysis, the radio-nuclides balance can be provided by the EDF STRAPONTIN code through a coupling with CYRANO3

3. Models overview

3.1 Thermal-Mechanical Kernel

The actual thermal-mechanical kernel is based on a 1D finite element simulation, solving the thermal and mechanical radial equilibrium at different axial positions (axial slices), at mid-pellet and at pellet-pellet interfaces. A static mechanical algorithm is associated with stationary and transient thermal algorithms to simulate both irradiation period (class I) and transient power events (II). Axial interactions between fuel stack and cladding (available with sliding friction) are taken into account through contact conditions.

The fuel and cladding properties are recalculated at each time step, for each Gauss point accounting for local temperature, burn-up and porosity. Time stepping is a priori deduced from power history and characteristic time of the overall fuel phenomena and refined in case of need during calculation. Commercial and segmented rods irradiated in experimental reactors can be both simulated. For fuel rod re-fabrication a restart procedure, combined with an axial slice refining allow to proper simulate ramp tests on rod segments. Internal pressure can be imposed as well as cladding surface temperature.

Moreover, especially for code development management, the code architecture allows to process any software configuration from a full fuel description to a more or less reduced configuration (tube mechanical testing for example) .

3.2 Physical models

The fundamental fuel physical models are implemented in the CYRANO3 code using empirical and analytical formula to simulate the numerous physical, chemical, metallurgical and core physics phenomena induced by irradiation in the fuel rod .

In most cases, CYRANO3 offers various modelling level for the user. Beyond the first access level (dedicated to industrial licensing configuration), many options are proposed to fit or optimise modelling. Beside industrial reference formula, alternative models can be used and sometimes a more mechanistic formula offers to the research engineer a numerical way to test new hypothesis, to develop and validate the main models.

All these models are established on separate parameter measurements (e.g. thermal diffusivity, annealing, sintering, gaseous diffusion...) performed on both fresh and irradiated fuel pellets as explained in the associated industrial paper [3].

In the last years, the fuel performance code has integrated many improvements:

- to fulfil high burn-up requirements (porosity and fission gaz added component due to RIM effect, solid and gaseous swelling, extended thermal conductivity decay, higher cladding corrosion thickness, increased irradiation induced creep, ...)
- to dissociate physical properties on UO₂ fuel with Cr additive
- to make progress in MOX modelling, accounting for heterogeneous effects.

For MOX fuels modelling, a homogenisation approach was employed to derive overall mixed-oxide (MOX) fuel constitutive laws (thermal conductivity as well as fission gas release). These improved laws will allow simulating MOX fuel rods behaviour for increased values of burn-up fuel. MOX Fuel consists in two or three main phases having different Plutonium contents: (Pu,U)O₂ cluster with 20 to 30 % plutonium, UO₂ cluster with less than 1 % plutonium and the matrix containing 4 to 8 % plutonium. Consequently the local fission densities are different from phase to phase. To correctly predict the macroscopic behaviour of all MOX fuel types, it is then necessary to model properly each phase and their exchanges. The concept of heterogeneity of materials is usually related to the microstructure and the presence of various phases.

From the thermal properties point of view, average conductivity is related to the individual conductivity of each phase. Defining their combination, the equivalent conductivity of an elementary representative volume can be evaluated. The methods employed to pass from the microscopic scale to macroscopic scale are homogenisation techniques. We have then improved this way the fuel centreline temperature prediction.

From the point of view of the physical-chemical properties, and more precisely in term of fission gas release, the concept of heterogeneity is especially related to the difference in the effective local Xenon concentration, the local diffusion coefficient, the porosity and the local fission density in each phase. CYRANO3 is using the J.A.Turnbull three terms diffusion coefficient [5][6]. For better prediction, implantation from phase to phase must be taken into account. The size of the phases is then determinant. Bubble nucleation and HBS transformation are also evaluated independently in each phase. The PuO₂ clusters located in the cold zones of the MOX fuel, because of the high local fission density, achieve indeed the High Burn-up Structure (HBS) faster than the other phases.

3.3 Mechanical models

3.3.1 Mechanical behaviour models

Initially focused on cladding behaviour, the thermal-mechanical kernel proposes two complementary numerical schemes to simulate the constitutive mechanical behaviour of cladding and fuel pellet on Gauss point.

The first one is dedicated to process standard creep laws (cladding) using strain hardening assumption in an implicit scheme; cladding irradiation and thermal creep laws are combined with a stress criteria to overlay all power history. Starting from recent theoretical and experimental works [7], the fuel constitutive law have been adapted to fit the cladding constitutive behaviour's integration framework: the non linear problem to solve is reduced to a single non linear scalar equation. This reduction allows to model the main features of the fuel constitutive law (low and high stress thermal steady creep regimes, known irradiation effects), computing times remaining realistic.

The second one integrates more sophisticated behaviour models as the phenomenological Lemaître model, taking into account material anisotropy and internal state scalar variables (as equivalent plasticity strain or irradiation influence). Such a constitutive law supplies more accurate stress-strain response under typical hardening-relaxation PCMI loading. Moreover, a unified anisotropic damaged viscoplastic model has been developed (as a "laboratory" constitutive law) to give a better description of material state under overall mechanical and thermal fuel loadings. [8] This model is able to simulate mono-axial and non-proportional tensile tests, creep and relaxation loadings in typical fuel temperature range. The irradiation effects are integrated by means of an internal state scalar variable representing neutron damage. This variable simulates a larger strain hardening and smaller static recovery.

3.3.2 Specific 1D modelling in PCMI studies

Thermal stresses associated with the fragile tensile behaviour of fuel lead to pellet's fragmentation during the first power rise. Corresponding radial cracks decrease the tensile stresses distribution throughout the pellet and enhances pellet diametric strains. The fuel elastic law have to be modified to represent these two-dimensional effects in a mono-dimensional finite-element code [9]. This constitutive law is associated to specific relocation and opening-closing models [10].

In order to give a more accurate PCMI simulation, the radial resolution is also enhanced by adequate simulations of the most important phenomena in the axial and hoop directions: pellet hour glassing effect (calculation of the conditions at mid-pellet and pellet-pellet interfaces), pellet dish filling mechanisms, stress concentration on the cladding location facing the fuel pellet cracks (at pellet-pellet interfaces) [9].

4. Extended operating tools

As mentioned above, CYRANO3 is designed for PCMI studies, computing a eighth of the core, with the simulation of parametric power transient events. A dedicated pre/post-processor tool (C3IPG) has been developed managing a large number of CYRANO3 calculation batches. Future work to be done will lead to extend such a massive computing, connecting irradiation and post-irradiation period in a same parametric process.

In parallel, we are also investigating sensitive analysis and structural reliability methods. CYRANO3 is now coupled with PROBANTM software for reliability analysis. As a result, for safety and design criteria, failure probability, importance factors and design point could be evaluated thanks to the limit-state function based on failure criterion

5. PLEIADES: the new environment of CYRANO3

Computing systems are still evolving more and more quickly, offering faster computing time and new capabilities. The "object" architecture concept is a new challenge able to favour sharing of specialist components, solving algorithms or pre and post processors, or to favour codes coupling as well. In this new framework concept, the code FORTRAN modules are embedded in components with standard interfaces written in more adapted language (C++, Python for example). The code static chaining (main program) of the subroutines is then replaced by a dynamic chaining of the professional components, written in the same evolved language [11].

In the fuel simulation field, EDF and CEA decided early 2002 to join and engage the development of such a platform named PLEIADES, aiming to provide applications dedicated for any reactor fuel concept (LWR, RNR, generation IV, MTR's applications) [12]. Within this project, the fuel performance code CYRANO3 becomes the LWR 1,5D industrial application. Aiming this target, the

code has been deeply restructured. The modules containing the specialists modeling, the material properties or the solvers have been embedded, driving all data transfers in the interface fields (suppression of FORTRAN COMMONs). The interfaces and the dynamic calculation chaining are written in C++ language.

Always performed assuming a mono-dimensional representation of the whole rod cut by slices for good balance between modeling accuracy and processing time cost, CYRANO3 can now easily share most of the advanced physical models aggregated in the PWR CEA application ALCYONE [13].

As the ALCYONE application also gives the possibility to perform one and three-dimensional multi-scale studies, using a common database of physical models and material laws, this new environment represents an extensive sophisticated way to develop 1D industrial scheme from unified 3D simulation.

3D simulations are devoted to comprehensive works such as parametric studies of fuel thermal primary creep on the PCMI interactions during a power ramp. These simulations are also used to calibrate 1D models (modification of the 1D constitutive law to take into account radial and axial cracks or micro-cracks, for instance).

References

- [1] N.Cayet, D.Baron, S.Béguin, "CYRANO3, EDF's Fuel Rod Behaviour code: Presentation and Overview of its qualification on HRP and various other Experiments", Enlarged Halden Reactor Project Meeting, Lillehammer, Norway, March 16-20 1998
- [2] B.Petitprez, B.Delhaye, S.Béguin "No clad lift-off" criterion and associated methodology developed by EDF and FRAMATOME-ANP on the basis of IFA-610 experiments", Enlarged Halden Programme Group Meeting, Lillehammer 2005
- [3] B. Therache, P. Thevenin, "EDF experience feedback and Research & Development contributions to the update of the fuel performance code CYRANO3 to challenge the high burnup licensing requirements", Topfuel meeting, Salamanque (October 2006)
- [4] A. Tigras and al. "Improvement of Fuel Failure Assessment based on Radiochemical parameters (MERLIN code) taking into account the Thermal-Mechanical fuel rod calculations (CYRANO3 code)", Chemistry Meeting ,Korea 2006
- [5] J.A.Turnbull et al, "The Diffusion Coefficients of Gaseous and Volatile Species during Irradiation of Uranium Dioxide", JNM107 (1982), pp168
- [6] J.A.Turnbull et al, "The Diffusion Coefficients for Fission Gas Atoms in Uranium Dioxide", IAEA TCM on Water Reactor Fuel Element Computer Modelling in Steady State, Transient and Accident Conditions, Preston UK 1988, IAEA-TC-959/3.5, pp174
- [7] Y. Monerie, J. M. Gatt "Overall viscoplastic behaviour of non irradiated porous nuclear ceramics", Mechanics of materials, 38 (7), 608-619, 2006.
- [8] F. Richard, P. Delobelle, S. Leclercq, P. Bouffieux, G. Rousselier "Modeling of the cold work stress relieved Zy-4 cladding tubes mechanical behavior under PWR operating conditions", Smirt 17, Prague 2003
- [9] V. Guicheret-Retel, F. Trivaudey, M. L. Boubakar, R. Masson, Ph. Thevenin "Modelling 3-D mechanical phenomena in a 1-D industrial finite-element code; results and perspectives" Pellet-clad Interaction in Water Reactors Fuels seminar, Aix en Provence, 453-464, 2004.
- [10] C.Callu, D.Baron, J-M.Ruck, "EDF Fragment Relocation Model based on the Displacement of Rigid Bodies", International Conference on CANDU fuels, Toronto, Ontario, Canada, Sept 21-25, 1997
- [11] D. Palermo, C. Grondein "Méthodologie de migration : codes Fortran en composants C++", Yantra-Technologies (ISBN 2-9527-3440-2)
- [12] D. Plancq and al. "PLEIADES : A unified environment for multi-dimensional fuel performance modelling" Proceeding of the 2004 International Meeting on LWR Fuel Performance, Orlando, Florida, paper 1060 (September 2004)
- [13] G. Touvenin and al. "ALCYONE : the PLEIADES fuel performance code dedicated to multidimensional PWR studies", Topfuel meeting, Salamanque (October 2006)

Analytical and experimental studies of fretting-corrosion and vibrations of fuel assemblies of a VVER-1000 water cooled and water moderated power reactor

**Dr. Yu.N.Drozdov¹, Dr. Al.A.Tutnov², Dr. A.A.Tutnov³, Dr.E.E.Alexeyev⁴,
V.V.Makarov⁵, A.V.Afanasyev⁶.**

¹ IMASH Machine Study Institute named after A.A.Blagonravov
of the Russian Academy of Sciences, Moscow,
drozdov@imash.ac.ru;

^{2,3,4} Kurchatov Institute Russian Research Centre, Moscow, Russia
tutnov-rncki@rambler.ru

^{5,6} Experimental and Design Organization “Gidropress”, Podolsk, Russia
makarov@grpress.podolsk.ru)

ABSTRACT

The report covers the methods and results of the latest analytical and experimental studies of fretting corrosion and natural vibrations of a VVER-1000 reactor fuel assemblies (FA). The process of fretting-corrosion was investigated using a multi-specimen facility that simulated fragments of fuel rod-to-spacer grid and lower support grid mating units. A computational model was developed for vibrations in the mechanical system of a fuel rod fragment and a spacer grid fragment. A calculational and experimental modal analysis of a FA was performed. Natural frequencies, modes and decrements of FA vibrations were determined and a satisfactory coincidence of analytical and experimental results was obtained. The assessment of fretting-corrosion process dynamics was made and its dependences on operational factors were obtained.

Key words: fretting wear, VVER-1000, fuel rod, oxide film, vibration, coolant, natural frequency.

Introduction

Under the conditions of vibration corrosion-resistant part made of structural alloys can be subjected to significant damage in the contact area. This kind of damage is generally called fretting-wear or fretting-corrosion.

Fretting was first detected in nuclear engineering in the spacer grids of PRTR reactor fuel rods (USA) [1].

Vibrations arise in nuclear reactors due to coolant flow turbulence and pressure pulses. Typical fuel rod vibration frequencies are within the interval of 80 – 150 Hz [2].

The problem of fuel assembly (FA) service life limitation due to fretting that came into view at the end of the 60-ies in the past century had been successfully solved by the beginning of the 80-ies based on the engineering solutions. However, thirty years had passed and the nuclear engineers find the study of fretting of practical interest. This interest stems from the issue of fuel assembly service life extension and reliability enhancement, the way it used to be thirty years ago [3,4].

The damage due to fretting wear [5] depends on the structural and operational parameters.

Consequently, the methods of fuel assembly, fuel rod and spacer grid behaviour modeling shall be oriented at the calculation of these parameters.

2. Experimental study of FA and fuel rod vibration characteristics

The study of vibration characteristics of a full-scale FA mock-up was performed in the air at 20 °C with load applied with impact hammer and electrodynamic shaker. The study was carried out at a testing rig designed for FA vertical fastening as a two-support beam, loading it with alternating force applied to one of the spacer grids and measuring the driving force and FA vibrational accelerations.

Prior to the tests the FA mock-up was installed into support thimble and loaded with axial compression force. The design of the FA top and bottom fastening units is standard, the value of the longitudinal springing corresponds to FA springing at reactor operational temperature. The vibrational load was applied to fuel rods, spacer grids and FA supports, the FA vibrational resonance was measured with piezoelectric accelerometers and a 16-channel analyzer and was processed with Pulse LabShop software.

The tests resulted in determination of frequencies, modes and decrements of natural vibrations of FA proper, as well as those of fuel rods within the spacer grid spans. Two main groups of vibrations of FA proper were determined, namely bending and torsional vibrations. The frequency of the first mode of bending vibrations is equal to 5 Hz and the frequency of the first mode of torsional vibrations is equal to 7,5 – 8 Hz.

Apart from the harmonics typical of FA vibrating as a single whole, harmonics with frequencies typical of the monitored span as well as adjacent spans can be observed in the fuel rod vibration spectra. The frequency of fuel rod vibrations in the spacer grid span is first of all defined by the span length and also by the fuel rod linear mass in the span as well as the spacer grid stiffness to angular turn. Fuel rod natural frequencies are within the range of 2-3 kHz in the lower 100 mm long span, from 83 69 138 Hz in the 340 mm long spans and from 280 to 380 Hz in the 260-mm span with a lower linear mass. In order to study the spacer grid location effect on the fuel rod natural frequencies in detail, a study of model vibration was performed, the model comprising a fuel rod taken out of a FA and spacer grid fragments. The tests modeled three cases of spacer grid locations: a FA with 15, 13 and 12 spacer grids. Two kinds of fuel rod positioning in the spacer grid, tight fitting-in and loose fitting-in with a gap were applied.

The results of the studies of a single rod mock-up vibration show that if the length and linear mass of the span and the type of spacer grid cell fitting-in coincide, the natural frequencies of a single fuel rod are close to those of a standard fuel assembly. In case there is a gap in the fuel rod-to-spacer grid cell mating unit, the natural frequencies of the fuel rod go down by 9% on the average. At an impact excitation of any fuel rod span

the vibrations of the span attenuate as the distance from the excited span increases. The vibrations of the span can only be seen in the amplitude-frequency spectra of adjacent span vibrations and they are not found in distant spans.

3. Calculational analysis of FA and fuel rod vibrational characteristics

When the natural frequencies of the fuel rod fragments were being calculated with FEM [6], two cases of mathematical model were considered that account for the fuel column structure: a monolithic fuel column and a fuel column that only resists to contraction. In the latter case the fuel column does not resist to tension: axial gaps generate. The former is a stiffer one and produces higher values of the fuel rod fragment natural frequencies as compared to the actual fuel rod fragment and the latter results in smaller values. Besides, neither the possible pellet-to-pellet gaps nor the pellet-to-cladding gaps in actual fuel rods have been considered.

The calculation results of the natural frequencies of the specified fuel rod fragments and experimental data defined for the fuel rod fragments in the air are provided in Table 1 below. The smaller value of the resonance frequency in Column 3 corresponds to fuel rod Type II, the larger one corresponds to Type I.

Table 1.

Experiment	Natural frequencies defined in the experiment	Calculational values of natural frequencies
Tests of 9 fuel rod fragment simulators at OKB Gidropress testing bench in 2002	72 Hz	68 – 88 Hz
Experimental studies of natural frequencies of a single fuel rod model at OKB Gidropress in 2005 for a 15 spacer grid TVS-2 fuel assembly: All spans 255 mm long	140 - 260 Hz	202 – 259 Hz
12- spacer grid TVS-2 fuel assembly: SG1-to-SG2, SG2-to-SG3 spans 255 mm long	140 - 260 Hz	202 – 259 Hz
SG4-to-SG5 spans 255 mm long	48 - 66 Hz and 140 - 260 Hz	202 – 259 Hz
SG7-to-SG8 spans 510 mm long	48 - 66 Hz	50 – 64 Hz
SG10-to-SG11 spans 255 mm long	140 - 260 Hz	202 – 259 Hz
TVS-2M: Spans 340 mm long	90 до 150 Hz	113 – 146 Hz

The values of natural frequencies defined in the experiment basically agree well with the provided calculational assessments which supports the correctness of the mathematical model of the fuel rod fragment vibrations. For the case of TVS-2 with 12 spacer grids for SG4-SG5, the detected low frequencies of 48-66 Hz correspond to the frequencies of fuel rod fragment vibrations in adjacent 510-mm spans.

The highest values of natural frequencies in fuel rod fragments correspond to the mathematical model that considers a fuel column as if it were monolithic, not a stack made up of pellets. It simplifies the finite-element model and the respective calculations are conservative at fretting-wear assesement.

4. Experimental study of fretting wear in the fuel rod-to-spacer grid cell unit

At the first stage the experimental studies were being carried out in still water at 20 °C with two-and three-span specimens that contained fuel rod cladding with pellet simulators, lower support grid simulator and two or three spacer grid simulators. All in all, 18 specimens of two structural designs and vaiuos combinations

of 100, 255 and 340 mm long spans were tested. The angle of specimen axes varied from 0 to 45 or 90 degrees against the direction of vibration, i.e. specimen longitudinal and transversal vibration was excited. Fig.1 provides the model and the specimens on the outside. The model is a plate with organic glass cover, suspended vertically from the springs above the shaker. Fuel rod specimens were fastened on the plate. Submerged accelerometers were attached to the fuel rod specimens. The plate was covered with the cover, filled up with water and was attached to the shaker. The tests comprised 8 stages 50-55 hours long, the amplitude and frequency of vibrations being maintained the same within each stage. As every stage was completed, the transversal backlash was measured in the fuel rod-to-spacer grid mating unit which could indirectly indicate the beginning of the wear process. If no new indications of backlash were found, the amplitude or vibration frequency was increased twice at the next stage. The vibration test parameters of the stages varied within the following ranges: the frequency of sine-shaped vibrations within 16,5-99 Hz, the amplitude of vibration accelerations within 1-25 m/s^2 , test duration was about 50 hours.

Following stages 6-8, when transverse backlash appeared in the fuel rod-to-spacer grid unit and traces of vibrational wear were detected in the fuel rod-to-spacer grid cell bulge contact area, roughness measurement of claddings and measurement of the cell inscribed diameters in specimens with the largest backlash. Based on the results of the measurements curves of cladding wear depth versus the vibrational acceleration amplitude were plotted as well as the curves of increment of the cell inscribed diameter versus the number of vibrational loading cycles (Fig.2). Fig.2 shows that cladding wear starts at spacer grid cells and the fuel rod vibration amplitudes for a 100-mm span within the ranges from 14-17 to 22-25 m/s^2 , for the 340 mm span – from 37 to 57 m/c^2 . The maximum depth of fuel rod cladding wear was about 30 μm .

The inscribed diameter of the spacer grid cells increased by 0,1 mm on the average. The maximum diameter increment occurred at stages 5 and 6 at amplitudes of about 16 m/s^2 , and later on irrespective of vibration amplitude increase, the rate of increment decreased 15 times.

Experiments similar to the above ones were carried out at operating temperatures, pressure, chemical composition of coolant at a special testing rig within 750 hours [5]. Fuel rod mock-ups with different gaps and fitting-in tightness in the cladding-to-spacer grid cell contact area were tested. The amplitude of vibrational acceleration for different mock-ups varies within the range of 5-30 m/s^2 . The total number of mock-ups tested was 18. Only one mock-up ended up with a 300- μm deep cladding wear. The mock-up was tested at amplitude of vibrational acceleration of about 30 m/s^2 and vibration frequency 32 Hz. The original diametral gap in the cladding-to-spacer grid cell contact area was 0,1 μm . The other specimens showed no cladding wear that would exceed the unevenness of the surface roughness.

5. Development of empirical model of fuel rod cladding-to-spacer grid fretting wear in the contact area.

An empirical model of fuel rod cladding-to-spacer grid fretting wear in the contact area was developed based on the experimental data investigation. For the case of wear due to fuel rod transverse vibrations the experimental data confirm the susceptibility to fretting wear of those fuel rod-to-spacer grid mating units where the tight fitting-in has loosened with gap generation. It confirms that even at minimum contact pressures fretting wear is considerably less than in the presence of a gap between the colliding parts. In this respect the model that describes the wear of the cladding and the bulging requires equations that describe the change of the contact forces in the presence of initial tight fitting-in as well as the kinetic equations of tight fitting-in loosening and diametral gap formation. If a fuel rod is installed with the initial tight fitting-in $\Delta < 0$ into a spacer grid cell, then for elastic-plastic material behaviour the contact force on the cladding P_k in the area of each bulge b can be described in the expression:

$$P_k = 0 \text{ at } \Delta \geq 0, P_k = -P_R \left(1 - \exp\left(-\frac{c|\Delta|}{2}\right)\right), \text{ where:} \quad (1)$$

$$c = \frac{\chi}{P_R} \quad \text{at } P_R > 0. \quad (2)$$

χ - stiffness of spacer grid cell bulges, defined in a calculation and depending on material properties and spacer grid cell geometry.

P_R – an absolute value of the limiting possible contact force acting by the bulge on the cladding under the conditions of the developed plastic deformation of the bulge.

The actual elastic tight fitting-in that remains after fuel rod installation into the spacer grid cell with account for the plastic deformations received by the bulge, will be represented as follows:

$$\Delta_e = -2 \frac{P_R}{\chi} \left(1 - \exp\left(-\frac{\chi|\Delta|}{2P_R}\right)\right) \text{ at } \Delta < 0 \quad (3)$$

In case $\Delta \geq 0, \Delta_e = 0$.

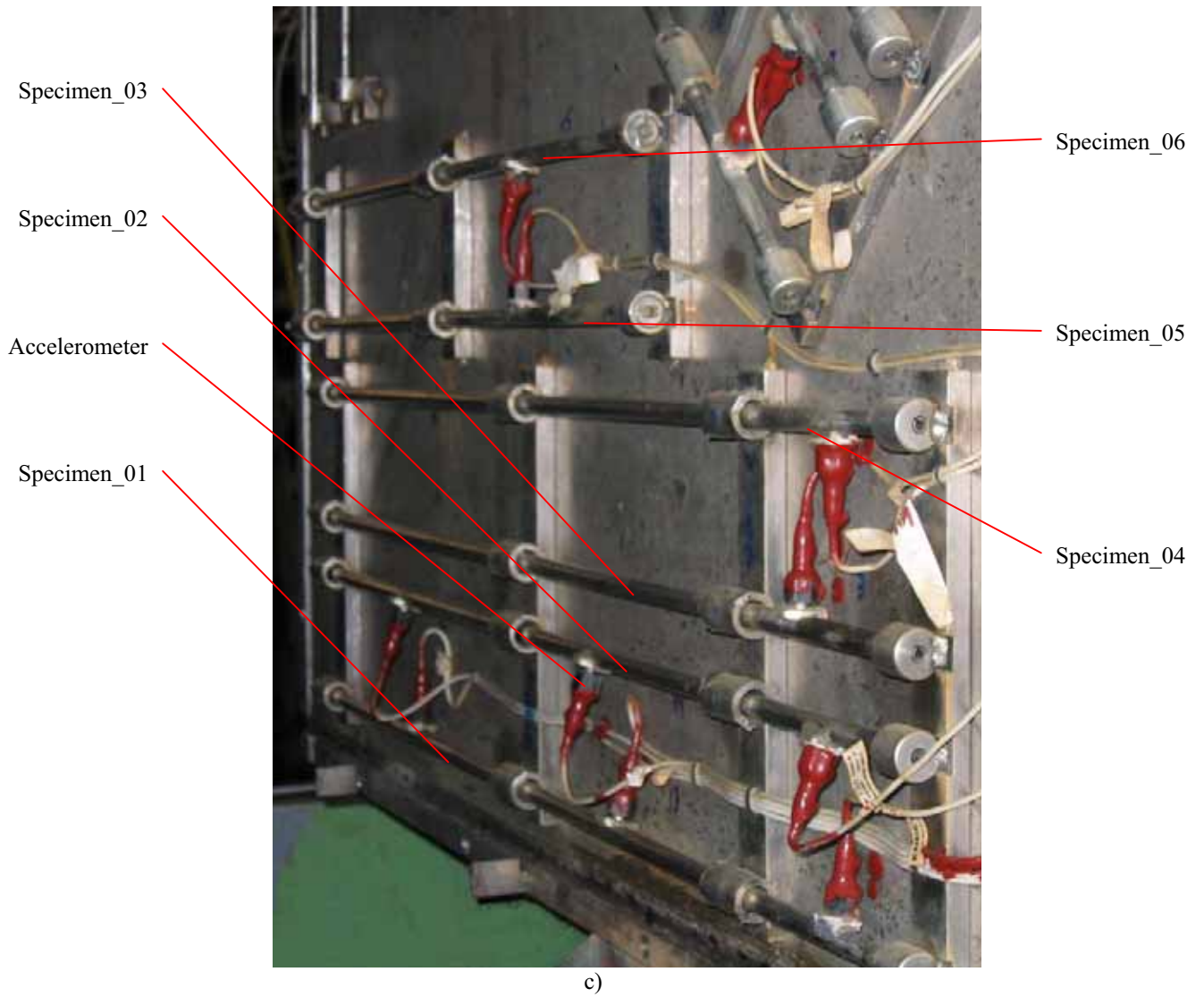
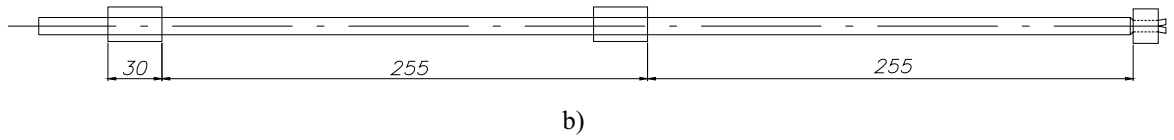
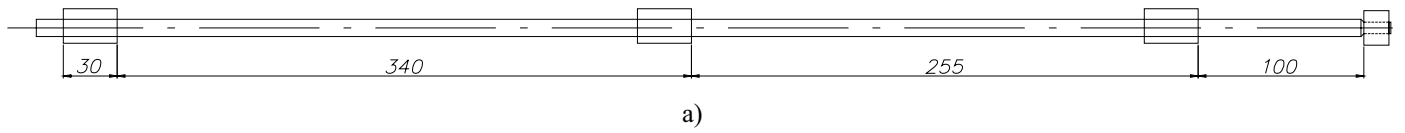
In the course of operation the fitting-in tightness will decrease due to stress relaxation in the bulge. Besides, there will be an increase in the inscribed circumference diameter of the spacer grid cell due to cyclic load caused by fuel rod vibration. The change of tight fitting-in (gap) in time can be defined by an equation:

$$\Delta_t = \Delta_e + \int_0^T d\Delta_{v_n}, \quad (4)$$

$$d\Delta_{v_n} = d\Delta_v + d\Delta_n + d\Delta_D, \text{ где:}$$

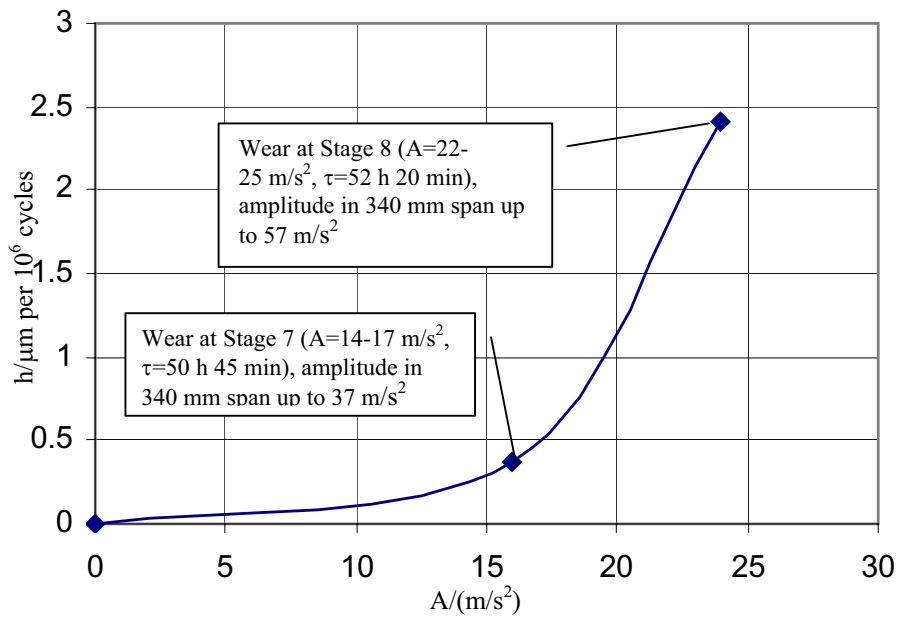
Δ_t - current fitting-in tightness (gap);

$\frac{d\Delta_v}{dt}$ - rate of change of fitting-in tightness due to stress relaxation in the bulge;

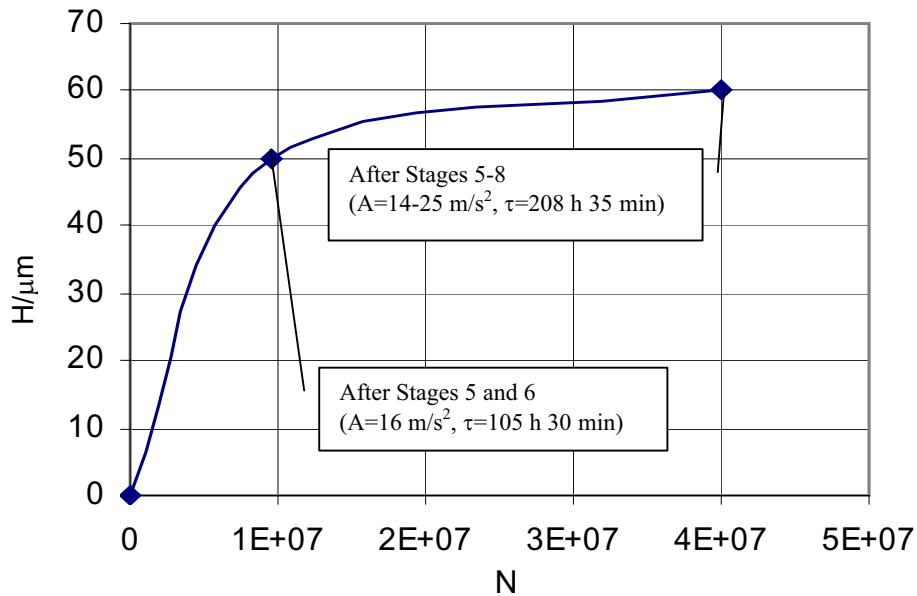


a) Type I
 b) Type II
 c) specimens installed in the model

Figure 1 – Model for fretting-wear testing



a)



b)

a) correlation of cladding wear depth versus vibrational acceleration amplitude

b) correlation of bulge wear depth versus the number of cycles

Figure 2 – Bulge and cladding wear depth assessments

$\frac{d\Delta_n}{d\tau}$ - rate of tight fitting-in (gap) variation due to an increase in the spacer grid cell inscribed circumference diameter resulting from cyclic load caused by fuel rod vibration.

$d\Delta_D$ - tight fitting-in (gap) variation due to a change in cladding diameter caused pressure differential under the conditions of thermal and irradiation creep.

The variation of $d\Delta_D$ in the course of operation is defined in a calculation with computer codes that model the fuel rod thermal and irradiation mechanics.

To calculate the tight fitting-in (gap) variation due to a change in vibration-induced cell diameter increase we assume the correlation:

$$d\Delta_n = kdN = kvd\tau$$

where: N – the number of cycles of contact force variation;

k - factor of vibration-induced diameter increase rate that depends on the contact force amplitude (as the first approximation this correlation will be considered linear).

ν - frequency of contact force variation, i.e. the frequency of fuel rod vibration in the grid-to-grid span.

The contact force in the support is proportional to fuel rod bowing in the middle of the span between the supports and is inversely proportional to the span length to power 3. In its turn, at harmonic vibrations the bowing amplitude in the middle of the span between the supports is linearly connected with acceleration amplitude in the point with the same coordinate by coefficient $\frac{1}{(2\pi\nu)^2}$.

Consequently, the expression for $d\Delta_n$ can be defined in the form

$$d\Delta_n = \frac{\bar{k} \cdot a}{\nu^2} d\tau \quad (5)$$

where: a - acceleration amplitude in the middle of the span;

ν - fuel rod vibration frequency;

\bar{k} - experimentally defined coefficient.

It is worth mentioning that in the course of the experiments in 2005 during the initial six stages of loading with acceleration amplitude increased at each one, there were no traces of fretting-wear in the claddings and bulges exceeding the surface roughness. However, a gap generated within this period of time. Since the tests were performed at 20 °C, the thermal creep at the temperature can be neglected and there was no irradiation, the component $d\Delta_V$ in equation (4), that characterises the decrease in fitting-in tightness due to stress relaxation is close to zero. Similarly, component $d\Delta_D$ connected with the change of the fuel rod outside diameter is neglectingly small. Consequently, once we know the value of the gap generated within 6 stages of the tests, we can choose coefficient \bar{k} , that characterises the rate of cell diameter vibration-induced increase.

If we apply in expression (5) acceleration in m/s^2 and frequency in Hz, coefficient \bar{k} will be equal to $5.2 \cdot 10^{-5}$. At this, the value of cell diameter increase will be in mm.

This value of coefficient \bar{k} refereers to spacer grid cells with a short bulge. To get the values of \bar{k} for the spacer grid cells of other designs similar experimental studies shall be performed.

The value of fitting-in tightness variation due to stress relaxation in the spacer grid cell is assessed by three-dimensional modeling of fuel rod and spacer grid cell deformation with the finite element method.

Now we pass to deducing the dependence for cladding wear rate under the conditions of fuel rod transverse vibrations. The model will be based on Preson hypothesis [7] that wear in an assigned point is proportional to the work of friction forces on the element surface that contains the point [1]. Then the rate of cladding wear depth variation will be defined the following way:

$$\frac{dh}{dN} = \frac{dh}{\nu \cdot d\tau} = \bar{\zeta} \cdot f_{mp} \cdot \frac{R_k}{S^1} \cdot U \quad (6)$$

where: h – wear depth;

f_{tp} – friction coefficient;

R_k – contact force acting along the normal on the cladding on the part of the bulge;

U – tangential motion of cladding with respect to the bulge;

ζ – coefficient that characterises wear rate;

N – number of loading cycles;

ν_v - frequency of fuel rod vibration-induced oscillations in the spacer grid-to-spacer grid span;

S^1 – bulge-to-cladding contact area.

Friction coefficient, according to the classical theory, does not depend on the size of the plateau the contact force is applied to. However, in case the contact area is small, this rule is violated. Strictly speaking, sliding friction transforms into friction of ploughing as the contact pressure increases. At this, the friction coefficient can increase several times. The correlation of the value of friction coefficient versus contact pressure can be described in terms of expression:

$$f_{tp} = f_{tpo} \left(1 + \bar{A} P_k^n\right) \quad (7)$$

where: f_{tpo} - sliding friction coefficient for zirconium against zirconium friction pair.

For zirconium components covered with oxide film the sliding friction coefficient depends on the friction path and can increase several times in the course of film wear out;

P_k –contact pressure;

A, n – coefficients, defined experimentally with special hardware.

$$P_k = \frac{R_k}{S} = \frac{R_k}{l_p g} \quad (8)$$

where: S – bulge-to-cladding contact area;

l_p – bulge length;

g – contact area width.

The value of g increases as the cladding wear depth increases. The correlation of g versus wear depth can be concluded from geometry analysis. Having assumed that in case of no wear the contact area width is close to zero, and the bulge geometry is plotted as a parabola:

$$y = A * x^2, \quad (9)$$

following simple transformations the following expression for contact area width can be obtained.

$$g = 2 \sqrt{\left(R - 10^{-3} h(1 + \mu)\right) - \frac{1}{2A} + \sqrt{\left(R - 10^{-3} h(1 + \mu) + 1\right)^2 + \frac{(2R + 10^{-3} h \cdot (1 + \mu))}{A}}} \quad (10)$$

where: h – cladding wear depth;

μ – bulge wear rate-to-cladding wear rate ratio.

Since usually the bulge width and cladding outside diameter are given in the drawing in mm, the wear depth wear depth is measured in microns, 10^{-3} factor precedes h in formula (10).

Coefficient $\bar{\zeta}$ is assumed to depend on parameter ω , that characterises the level of accumulated cyclic damage. Parameter ω is an integral taken around the accumulated number of loading cycles-to-damaging number of cycles ratio. It will indirectly account for fatigue damage accumulation in the cladding material and the effect of accumulated damage on the material wear resistance.

The damaging number of cycles N_p can be linked with the amplitude of stress variation $\Delta\sigma$ with a

Waller function:
$$\Delta\sigma = \frac{C}{(N_p)^p} + \sigma_{-1},$$

where: σ_{-1} - endurance strength;

C, p – experimentally defined coefficients.

Here we should refrain from the temptation to define coefficients σ_{-1} , C, p on the basis of a direct transformation of fatigue curve as the structural parameter of capacity to be damaged ω , that controls the decrease in the rate of wear resistance, will not necessarily coincide with the parameter that controls the damage process at cyclic loading. In this respect value σ_{-1} shall be considered as the threshold of material sensitivity to wear based on the level of stresses available in the surface layer, not as the endurance strength. Stress amplitude is proportional to the amplitude of contact pressure variation $K\Delta\sigma = D \cdot R_k$. With account for the above, we obtain:

$$\bar{\zeta} = \zeta_1 * \left(\frac{N}{N_p} \right)^m = \zeta * (v * \tau)^m * \left(\frac{DR_k}{S} - \sigma_{-1} \right)^{\frac{m}{p}} \quad (11)$$

where: N- number of contact force variation cycles;

v - fuel rod vibration frequency in a single grid-to-grid span;

τ - time;

S – bulge-to-cladding contact area ($S = g(h) \cdot l_p$);

D, B, m – experimentally defined coefficients.

Let us consider the relation of contact force R_k and the motion at cladding sliding transverse to the bulge symmetry axis with fuel rod transverse vibration parameters. Let the vertical plane the fuel rod vibrates in, makes angle α with bulge symmetry angle (Figure 3).

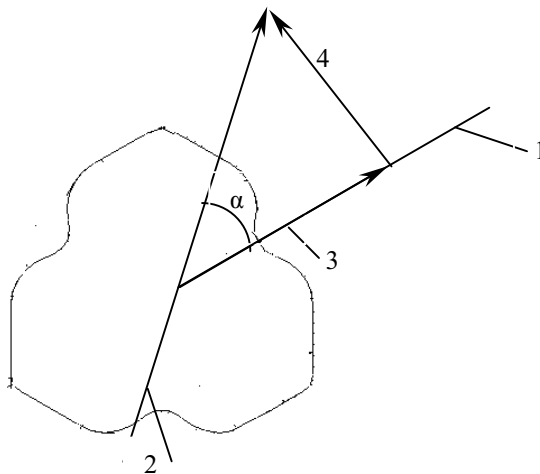


Figure 3. Fuel rod vibration diagram.

1 – bulge symmetry axis; 2 – direction of fuel rod vibration, 3- v_r , 4- v_θ - radial and azimuthal fuel rod vibration amplitudes.

The amplitude of motion in the spacer grid cell can be presented as the motion amplitude of the middle of a double grid-to-grid span of a fuel rod. Having denoted the amplitude by v , we resolve it into components along and transverse to the symmetry axis of the bulge, v_r and v_θ . At this:

$$v_r = v * |\cos \alpha|, \quad v_\theta = v * |\sin \alpha| \quad (12)$$

Since in experimental studies of fuel rod vibrations, as a rule, acceleration amplitude is recorded in the middle of the spans, we shall define motions v_r , v_θ with it considering the harmonic nature of a particular vibration mode.

$$v_r = \frac{a_D}{(2\pi v_D)^2} |\cos \alpha|, \quad v_\theta = \frac{a_D}{(2\pi v_D)^2} |\sin \alpha| \quad (13)$$

where: a_D - amplitude of vibrational accelerations in the middle of a double span for the mode of vibration at frequency v_D , corresponding to span $2L$;

L – distance between the middle planes of spacer grids.

The fuel rod motion in a spacer grid cell is limited by the value of diametral gap. So the amount of fuel rod slip in the cell transverse to the bulge symmetry axis in equation (6) will be equal to the smaller value out of the two ones: diametral gap and motion range transverse to the bulge symmetry axis.

$$U = \min \left\{ \frac{2a_D \Delta}{(2\pi v_D)^2} |\sin \alpha| \right\} \quad (14)$$

It is worth mentioning, that having assumed the hypothesis on the harmonic nature of vibrations, acceleration in the middle of the double span can be written in terms of acceleration of the middle of a single span:

$$a_D = \sqrt{2}a \quad (15)$$

where:

a - acceleration in the middle of a single span with vibration mode typical of double span.

If along with transverse vibrations axial vibrations are observed in a fuel assembly, function U shall be replaced by expression:

$$U_{zz} = \sqrt{U^2 + U_z^2}$$

$$\text{where: } U_z = \frac{a_z}{(2\pi v_z)^2} - U_{z_{\text{perm}}};$$

a_z, v_z - acceleration and frequency of fuel rod longitudinal vibrations, $U_{z_{\text{perm}}}$ - axial motion of grid in the area of a particular fuel rod installation due to the action of friction forces in all cells.

The value of $U_{z_{\text{perm}}}$ is calculated at modeling fuel assembly longitudinal vibrations considering the possibility of fuel rod slip in the spacer grid cells.

At fuel rod vibrations depending on the correlation of diametral gap and fuel rod vibration amplitude in the spacer grid cell the cladding will collide with one or several bulges. At this, the contact force acting on the cladding on the part of the bulge, will be proportional to fuel rod bowing in the middle of a single span v_r and reversely proportional to span length to power 3:

$$R_K = B_1 \frac{v_r}{L^3} \quad (16)$$

or, considering the harmonic nature of vibrations:

$$R_K = B_1 \frac{a_v |\cos \alpha|}{(2\pi v_v)^2 L^3} \quad (17)$$

where: a_v - acceleration in the middle of a fuel rod single span for the mode of single span vibration at frequency v_v .

The rate depends on the azimuth of direction fuel rod vibrates in, which changes every time it has collided with a bulge. With $\Phi(\alpha)$ to denote the probability density of vibration vector (angle α), the expression for the averaged wear rate considering the random nature of vibration direction distribution will be as follows:

$$\frac{dh}{d\tau} = L^3 l_p g(h(\tau) v_v^2) * \int_0^\pi \Phi(\alpha) \left(\int_0^\tau v_v \left(B \frac{a_v |\cos \alpha|}{v_v^2 L^3 l_p g(h(\tau))} - \sigma_{-1} \right)^{\frac{1}{p}} dt \right)^m \left(1 + A \left(\frac{a_v |\cos \alpha|}{v_v^2 L^3 l_p g(h(\tau))} \right)^n \right) * |\cos \alpha| * \min \left\{ \frac{\Delta}{\sqrt{2\pi^2 v_D^2}} |\sin \alpha| \right\} d\alpha \quad (18)$$

The random nature of hydrodynamic excitation loads at longitudinal-transverse coolant flow, fuel rod collisions at different angles with respect to the bulge symmetry axis and resulting continuous changes of the direction of fuel rod jumps bring about the uniform distribution of angles that define the direction of fuel rod vibration.

$$\Phi(\alpha) = \frac{1}{\pi}$$

When creating the fretting-wear model, the appearance of hard oxide film on the cladding surface within the first few hours of fuel rod operation in a VVER-type reactor or within the first few hours of testing in an autoclave at a temperature above 300 °C shall be taken into consideration.

The film is about 5 μm thick. In the course of fuel rod operation, cladding oxidation results in surface film thickness growth. Consequently, two competing processes take place simultaneously: oxide film thickness growth due to oxidation and its reduction caused by fretting wear in the places of its contact with the spacer grid. The differential equation for the kinetics of oxide film thickness in the contact area is written as follows:

$$\partial \delta / \partial \tau = F1(T, \delta) - F2 \text{ on initial condition of } \delta(\tau=0) = 5 \mu\text{m},$$

where δ is the oxide film thickness, τ is the time, $F1(T, \delta)$ is the rate of oxide film growth thickness, depending on the temperature and the thickness of film proper, $F2$ is the rate of oxide film wear out. Function $F1$ for zirconium alloys is known to look as follows:

$$F1 = A \exp(-B/T) / 2\delta,$$

where A, B - constants, T - temperature.

So far, it is not clear whether the film further generated is as hard as the one initially generated. In this respect we conservatively assume that the thickness of initially generated hard film does not grow.

With account for the presence of hard oxide film with thickness h_0 , correlation (18) can be rewritten as follows:

$$h = \frac{\zeta_1}{L^3 l_p} * \int_0^\tau \left(\frac{a_v}{g(h(\tau)) v_v^2} \int_0^\pi \int_0^\tau v_v \left(B \frac{a_v |\cos \alpha|}{v_v^2 L^3} - \sigma_{-1} \right)^{\frac{1}{p}} dt \right)^{m_1} \left(1 + A_1 \left(\frac{a_v |\cos \alpha|}{v_v^2 L^3 l_p g(h)} \right)^{n_1} \right) |\cos \alpha| \cdot \min \left\{ \frac{\Delta}{\sqrt{2\pi^2 v_D^2}} |\sin \alpha| \right\} d\alpha d\tau$$

at $h < h_0$ or $\tau \leq \tau_0$,

where: h_0 - hard oxide film thickness,

τ_0 - time when the wear depth is equal to R_0 .

(19)

$$h = h_0 + \frac{\zeta_2}{L^3 l_p} * \int_0^\tau \left(\frac{a_v}{g(h(\tau)) v_v^2} \int_0^\pi \left(\int_0^\tau v_v \left(B \frac{a_v |\cos \alpha|}{v_v^2 L^3} - \sigma_{-1} \right)^{\frac{1}{p}} dt \right)^{m_2} \left(1 + A_2 \left(\frac{a_v |\cos \alpha|}{v_v^2 L^3 l_p g(h)} \right)^{n_2} \right) |\cos \alpha| \cdot \min \left\{ \frac{a_D |\sin \alpha|}{\sqrt{2} \pi^2 v_D^2} \right\} d\alpha \right) d\tau$$

at $h > h_0$ or $\tau > \tau_0$.

It is worth mentioning that since the trigonometric functions are taken in formulae (19) in absolute value, the integral over angle α from 0 to π can be taken within the range from 0 to $\frac{\pi}{4}$ with its subsequent multiplication by 2.

14 experimentally determined constants: $m_1, m_2, \zeta_1, \zeta_2, A_1, A_2, n_1, n_2, B_1, B_2, P_1, P_2, (\sigma_{-1})_1, (\sigma_{-1})_2$ are present in provided correlations for wear depth. Evidently, the results of not less than twelve experiments on cladding wear depth definition shall be available to define them. Unfortunately, the available database on both operational and testing bench results for cladding wear, in most cases provides indirect and insufficiently precise data on wear depth. Three experiments can only be pointed out with wear depth estimated using section metallographic study. In particular, in the course of two experiments performed in OKB "Gidropress" testing bench referred to in the beginning of the article, having tested the specimens for about 50 hours at loading stage 7 and for the same time at loading stage 8 at 20 °C and at different levels of acceleration amplitude and vibration frequencies, the wear depth was determined equal to 10 and 30 μm , respectively. Besides, in experiments at temperature close to operating, the fuel rod cladding wear depth of 300 μm for 750 hours of testing was recorded in one specimen. In all the other cases we deal with either mentioning of wear without indicating its depth, or with wear signs within surface roughness, or no wear at all.

Under the circumstances, the search of the 14 unknown coefficients in equations (26) and (27) can only be realized by linear programming method with determination of the minimum of Φ function below:

$$\Phi = \sum_{i=1}^N f_i(h_i, \bar{h}_i),$$

where: h_i, \bar{h}_i - rated and experimentally determined wear depth

$$f_i(h_i, \bar{h}_i) = (h_i - \bar{h}_i)^2$$

for experiments in which the wear depth was determined for the metallographic sections.

For the experiments in which the wear depth was not determined by metallographic method, function $f(h, \bar{h}_i)$ will be written as follows:

$$f_i(h_i, \bar{h}_i) = \begin{cases} 0 & \text{at } \bar{h}_{i1} \leq h_i \leq \bar{h}_{i2} \\ (h_i - \bar{h}_{i1})^2 & \text{at } h_i < \bar{h}_{i1} \\ (h_i - \bar{h}_{i2})^2 & \text{at } h_i > \bar{h}_{i2} \end{cases}$$

$\overline{h_{i1}}$ and $\overline{h_{i2}}$ are the limits of possible wear depth set up by an expert on the basis of the data available in the test reporting documents that specify oral explanations of the specialists engaged in performing the experiments.

In case the reporting documents indicate no wear, $\overline{h_{i1}}$ is assumed to be equal to zero, and $\overline{h_{i2}}$ to be equal to the maximum height of the rough surface dents.

Despite a sufficiently high effectiveness of the above approach to a search of the unknown coefficients in the cladding wear equations, the available experimental database is not enough to create a complete mathematical model with fourteen coefficients that characterise the material resistance to wear. Along with the three experiments mentioned above, only two more experiments contain totally new information on lack of traces of cladding wear after tests in hot and cold states. We can conservatively assume for one experiment in the series with maximum loading level and no traces of wear the wear depth equal to the height of rough surface texture. The other experiments either to a certain extent repeat the information obtained in the above five experiments or do not provide reliable data on the cladding wear depth.

In this respect the number of unknown coefficients needs to be decreased by reducing the effects accounted for in the created model. Thus, having assumed coefficients A_1 and A_2 equal to zero, we will not consider the dependence of friction coefficient on the contact force, i.e. the effect of run-in setting in the cladding-to-bulge contact area. At this, there will automatically be no need in defining coefficients n_1 and n_2 , since the multiplier they are incorporated in will be multiplied by zero. Let us also assume that in the transverse section the bulge is sufficiently obtuse and in the process of bulge and cladding wear the contact spot width does not change ($g(h) = \text{const}$).

Besides, let us conservatively assume the threshold of material sensitivity to wear by the level of stresses σ_{-1} equal to zero.

It will result in only six unknown coefficients in the model, and formulae (19) and (27) take the form:

$$h = \frac{\zeta_1}{L^3 l_p} \left(\int_0^\tau \frac{a_v(\tau)}{g(h(\tau))v_v^2(\tau)} \int_0^\pi \left[\int_0^\tau v_v \left(\frac{a_v(t) |\cos \alpha|}{v_v^2(t) L^3} \right)^{\frac{1}{P_1}} dt \right]^{m_1} |\cos \alpha| \cdot \min \left\{ \frac{a_D \cdot |\sin \alpha|}{\sqrt{2\pi^2 v_D^2}} \right\} d\alpha \right) \cdot d\tau \quad (20)$$

$$h = h_0 + \frac{\zeta_2}{L^3 l_p} \left(\int_0^\tau \frac{a_v(\tau)}{g(h(\tau))v_v^2(\tau)} \int_0^\pi \left[\int_0^\tau v_v \left(\frac{a_v(t) |\cos \alpha|}{v_v^2(t) L^3} \right)^{\frac{1}{P_2}} dt \right]^{m_2} |\cos \alpha| \cdot \min \left\{ \frac{a_D \cdot |\sin \alpha|}{\sqrt{2\pi^2 v_D^2}} \right\} d\alpha \right) \cdot d\tau$$

at $h > h_0$ or $\tau > \tau_0$

The porcessing of experimental database with linear porgramming method provided the following values of coefficients in formulae (20)

$$\zeta_1 = 3,673225 \cdot 10^{26}; \quad \zeta_2 = 2,5289025 \cdot 10^{10}; \quad S1=3,0874; S2=0,9119; m_1 = 0,4; m_2 = 0,4.$$

The calculational assesements with the obtained formulas show that under the conditions of fuel rod operation as a part of fuel assemblies in VVER-1000 reactor cores at typical values of vibrational accelerations $1,5 \text{ m/s}^2$ and fuel rod vibration frequency 74 Hz for 1500 days, in case of 0,1 mm initial tight fitting-in of the fuel rod-to-spacer grid mating unit, the cladding wear depth is $10^{-5} \mu\text{m}$. In case the initial tight fitting-in is 0,01 mm under the same loading parameters, the wear depth is $0,2 \mu\text{m}$.

REFERENCES.

1. Уотерхауз Р. Б. Фреттинг-коррозия. Ленинград, Машиностроение, 1976.
2. Paidossis M. P., A Review Of Flow-induced Vibrations In Reactor Components, Nuclear Engineering And Design, 1983, v.74, N1
3. Ю.Н. Дроздов, Ю.Г. Драгунов, В.В. Макаров. Экспериментальные исследования фреттинг-коррозии твэлов в дистанционирующих решетках тепловыделяющих сборок водоводяных энергетических реакторов. Доклад на конференции по безопасности ВВЭР, ОКБ «Гидропресс», г. Подольск, 2004г.
4. С. А. Brown, F. T. Adams and G. C. Cooke, K. Koebke and J. Stabel,
5. FUEL ROD VIBRATION AND FRETTING IMPACT ON RELIABILITY, Proceedings of the 2004 International Meeting on LWR Fuel Performance, Orlando, Florida, September 19-22, 2004, Paper 1059.
6. Ko P.L., Wear Of Zirconium Alloys Due To Fretting And Periodic Imacting, Wear, 1979, V. 55, h. 369-384.
7. Зенкевич О. Метод конечных элементов в технике. – М.: Мир, 1974. – 341 стр.
8. Цеснек Л.С. Механика и микрофизика истирания поверхностей. Москва, Машиностроение, 1979г. 264 стр.

EFFECT OF MECHANICAL PROPERTIES OF SPACER GRID SPRINGS ON THE FRETTING WEAR OF A NUCLEAR FUEL ROD

Y.-H. LEE, H.-K. KIM

*Korea Atomic Energy Research Institute
150 Dukjin-dong, Yuseong-gu, Daejeon, 305-353 -KOREA*

ABSTRACT

Fretting wear tests of nuclear fuel rods have been performed by using a spacer grid spring with a concave shape. The main focus of this study is to quantitatively evaluate the wear behaviour of a fuel rod with a variation of the spring stiffness. In order to change the spring stiffness, spring specimens were heat-treated for 2 hours in a vacuum condition below the recrystallization temperature of Zirconium alloy and then cooled with three kinds of cooling rates (i.e. a furnace cooling, an air cooling and a water quenching). The results showed that the wear volume of each exponentially condition increased with increasing slip amplitude in both test environments. However, the wear volume did not have a linear relationship with the stiffness. It seems that the wear behavior of the nuclear fuel rods was considerably affected by the debris behavior rather than the different stiffness of each spring condition. Based on the present results, the details of a spring stiffness effect are discussed.

1. Introduction

Up to now, many fuel vendors and utilities have investigated the development of high performance fuels with an improved economy and reliability under severe operating conditions such as a high burn-up, plant power uprates, long-term operating cycles, etc. In order to increase a fuel performance in these operating conditions, the development of new materials, improvement of the water chemistry, design improvement for strengthened grid structures, etc. should be preceded to overcome the major degradation mechanisms such as curd/corrosion, grid-fretting, pellet-cladding interaction (PCI), debris-induced failure, manufacturing errors, etc. Among those degradation mechanisms, however, a grid-fretting is one of the complex and hardly accessible phenomenon in PWR fuel failures.

For example, it is difficult to simulate actual fretting conditions in operating plants though fretting wear experiments have been performed without considering an effect of a neutron irradiation. This is because the contact conditions between the fuel rod and grid spring/dimple are time-dependently changed with a neutron irradiation and thermal aging during an operating temperature. In other words, sliding wear is expected to be dominant at the initial stage of an operating period because a nuclear fuel rod is supported with a positive spring force by an elastic deformation of a grid spring/dimple in the regular positions of a fuel assembly. However, the degradation of grid materials due to a neutron irradiation and thermal aging could result in a gradual decrease of the spring force and finally a gap between the contact surfaces will appear. At this time, the wear mode could be changed from a sliding to an impact/sliding mode. Furthermore, the contact force could also be considerably decreased due to excess wear damage during a sliding mode, which accelerates the transition of a wear mode [1].

There are various methods to improve the wear resistance of a nuclear fuel such as a material development for wear resistance claddings, an anti-vibration structure in the fuel assembly, a variation of the contact condition for the spacer grid, etc. However, a relatively easy method is to change the grid spring shape when considering the economy and the development period. The previous experiments in this laboratory [2,3] have demonstrated the effects of a spring shape on the wear-resistance of a nuclear fuel rod. However, it has not been sufficiently investigated to see whether a variation of the spring stiffness (defined as a ratio of force to displacement) for the same spring shape affects the wear behavior

of a nuclear fuel rod. In this study, fretting wear tests have been carried out by using a specific spring shape with different spring stiffness in room temperature air and water. The objectives are to examine the wear behavior with a variation of the spring stiffness which was obtained by a heat-treatment below the recrystallization temperature of Zirconium alloy and to evaluate the optimized stiffness of a tested spring for its wear-resistance.

Chemical compositions [wt%]						
Nb	Sn	Fe	Cr	T.E.	O	Zr
1.0	1.0	0.11	-	-	-	Bal.
Mechanical properties						
Yield stress [MPa]		Tensile strength [MPa]		Elongation [%]		
565		807		17		

Tab 1: Chemical composition and mechanical properties of the tested Zr alloy.

2. Experimental procedure

Fuel rod specimens were prepared with a commercial Zirconium alloy (9.5 mm in outer diameter and 0.6 mm in wall thickness). A concave shape of the grid springs (thickness of 0.46 mm) was also fabricated with the same alloy. The chemical composition and mechanical properties are summarized in Table 1. The schematic views of a rod, spring specimen and contact condition are illustrated in Fig. 1. The fuel rod specimen attached to the sliding axis oscillates with a peak-to-valley amplitude of 50, 80 and 100 μm at a frequency of 30 Hz. Normal loads were 10 N and the tests were carried out for up to 10^5 cycles in room temperature air and water. Each test at the same test condition was performed two or three times and the average values of the wear results were used for a comparison of the wear behaviours. Fig. 2 shows the schematic view of the wear tester used in this study. Details of the wear tester can be found in a previous paper [2]. In order to change the spring stiffness, the spring specimens were heat-treated for 2 hours in a vacuum condition below the recrystallization temperature (470 $^{\circ}\text{C}$) of Zirconium alloy and then cooled with three kinds of cooling rates (i.e. a furnace cooling, an air cooling and a water quenching; abbreviated as FC, AC and WQ, respectively). Before and after the wear tests, both the rod and spring specimens were acoustically cleaned in acetone for 10 minutes and dried in air. After finishing the worn surface examination by using an optical microscope (OM), the profile of the worn surface on the tested rod specimen was measured by using a surface profilometer, thus a wear volume and a maximum wear depth could be obtained by integrating and analyzing the measured profiles, respectively.

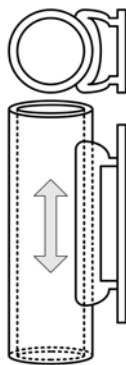


Fig 1. Specimens and contact condition.

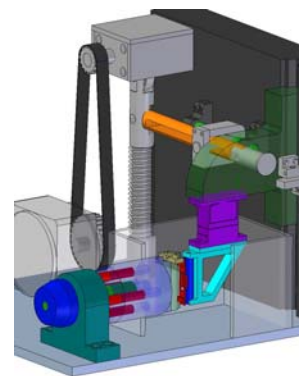


Fig 2. Schematic views of the fretting wear tester.

3. Results and discussion

Fig. 3 shows the variation of the spring stiffness with increasing cooling rate after a heat-treatment. It is apparent that the spring stiffness gradually increased with increasing cooling rates. The maximum stiffness value appeared in the WQ condition and the spring stiffness increased by about 18% when

compared with the as-received (AR) condition. Therefore, it is possible to change the spring stiffness by using a heat-treatment without any significant change of the spring characteristics.

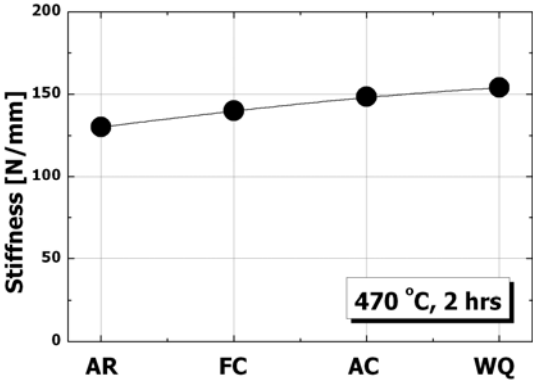


Fig 3. The variation of the spring stiffness with increasing cooling rate.

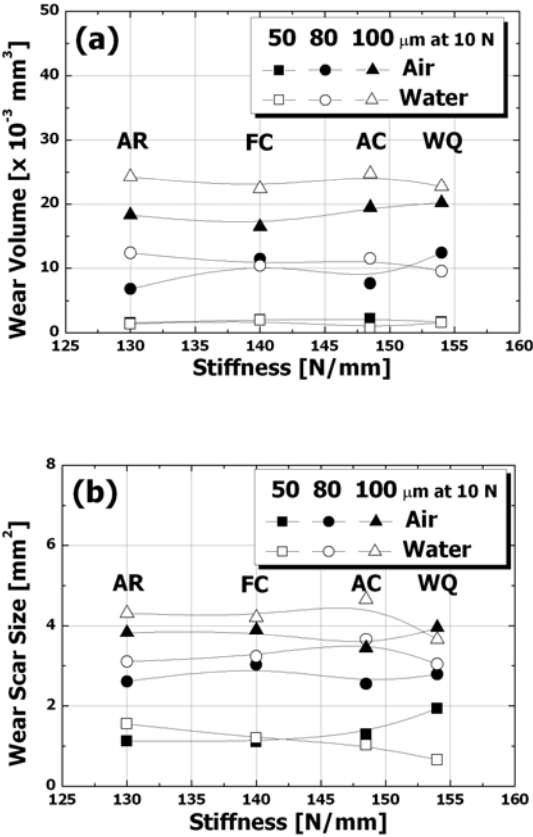


Fig 4. The variation of the wear volume and wear scar size with increasing spring stiffness for both the air and water conditions.

Fig. 4(a) shows the variation of the wear volume with increasing spring stiffness for both the air and water conditions. Contrary to our expectations, the variation of the spring stiffness did not have a significant effect on the wear volume while it is clearly shown that the wear volume rapidly increased with increasing slip amplitude. It seems that a governing factor for determining a wear behavior is the debris behaviour between the contact surfaces rather than the spring stiffness itself. Generally, a generated wear debris could be adhered to or rapidly detached from a worn surface, which depends on the environments. In the air condition, an accumulated wear particle layer shows beneficial effects due to the formation of a load-bearing layer. But the wear debris is rapidly removed from the contact surfaces

in concurrence with its generation in the water condition. As shown in Fig. 4(a), however, the effect of the test environment (i.e. wear volume difference between air and water condition) is gradually reduced with increasing spring stiffness especially at a slip amplitude of 100 μm . This result indicates that the generation of the wear particle, the formation of a wear particle layer and its removal behavior could be affected by the contacting spring stiffness.

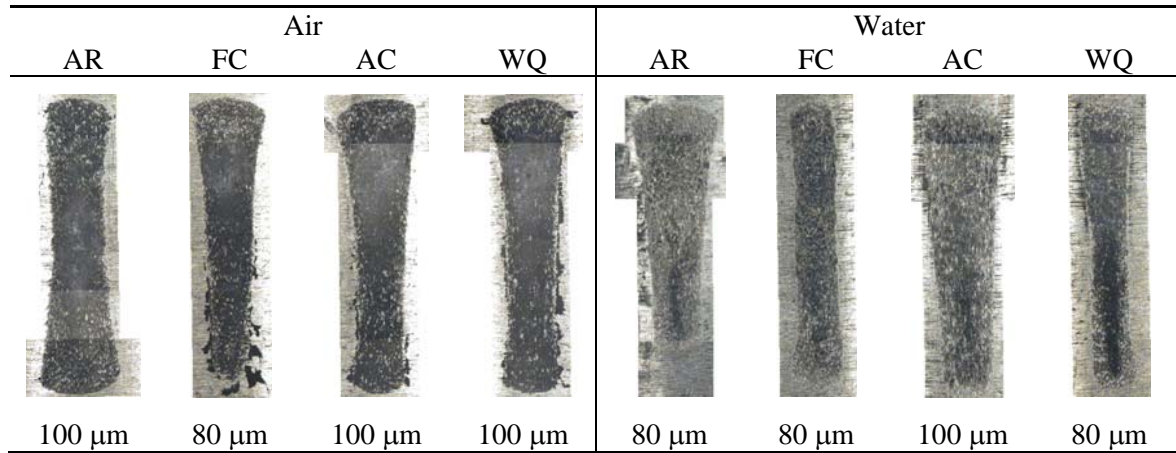


Fig 5. The OM result of worn surface observation.

When considering the contact behavior by an elastically deformable spring, it is expected that the contacting spring could be deformed in the slip direction (i.e. tangential direction). If a shear stiffness is linearly proportional to a (normal) stiffness, the amount of deformation during a sliding and a displacement of the deformed spring under the same applied normal load (10 N) would decrease with increasing spring stiffness. So, it is expected that the contact area (i.e. the wear scar size) after the wear tests could be varied with the spring stiffness even though the variation of the contact length is almost negligible due to the tested spring shape. The result indicates that the wear scar size at the WQ condition was increased and decreased in the air and water conditions as shown in Fig. 4(b), respectively. This means that with increasing spring stiffness, a third-body abrasion due to the generated wear debris in the air condition was dominant between the contact surfaces while it is expected that the wear debris in the water condition was generated and then removed after it had undergone a severe deformation in a subsurface of the fuel rod. In order to confirm the debris behaviour, the worn surfaces were observed by using an OM after the wear tests and their typical results are shown in Fig. 5. It is apparent that the generated wear debris was always adhered to the worn surface in the air condition while the amount of the removed debris was increased with increasing spring stiffness in the water condition. Therefore, the spring stiffness has a significant effect on an expansion of a wear scar, which determines the wear volume.

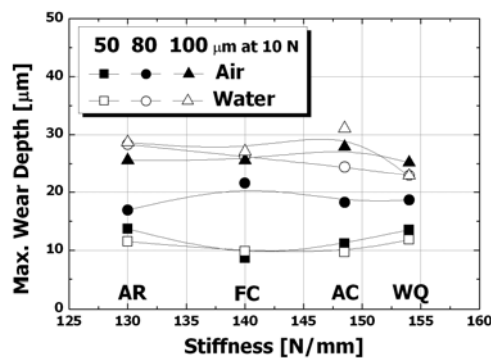


Fig 6. The variation of the maximum wear depth with increasing spring stiffness.

In the nuclear power plants, however, the reliability of the nuclear fuel rod is evaluated and estimated by the extent of a thickness decrease. This means that a spring condition which has a lower maximum wear

depth could be expressed as an optimized spring stiffness for considering a wear-resistance regardless of the larger wear volume and wear scar size. Fig. 6 shows the variation of the maximum wear depth with increasing spring stiffness. With similar results for the wear volume and the wear scar size, the WQ condition shows a smaller maximum wear depth in the water condition when compared with the other conditions. When considering the actual environment in operating plants, the WQ condition of the concave shape spring used in this study shows a relatively small wear volume, wear scar size and a maximum wear depth up to 10^5 cycles.

4. Summary

The following observations can be drawn from the results of the present study:

- (1) By using a heat-treatment under a recrystallization temperature, it is possible to change the spring stiffness without any significant change of the spring characteristics.
- (2) The variation of the spring stiffness did not have a significant effect on the wear volume. However, it is expected that the generation of a wear particle, the formation of a wear particle layer and its removal behavior could be affected by the contacting spring stiffness.
- (3) The water quenching (WQ) condition of the concave shape spring used in this study showed a relatively small wear volume, wear scar size and maximum wear depth up to 10^5 cycles.

Acknowledgement

This study has been carried out under the Nuclear R&D Program by Ministry of Science and Technology in Korea.

References

- [1] Y.-H. Lee, H.-K. Kim, Comparison of a supporting ability of spacer grid springs under fretting wear condition in room temperature air, Proceedings of KNS Autumn meetings (2005).
- [2] Y.-H. Lee, H.-K. Kim, Evaluation of spring shape effect on the nuclear fuel fretting using worn area, Proceedings of KSTLE Autumn meetings (2003) 313-323.
- [3] H.-K. Kim, Y.-H. Lee, Influence of contact shape and supporting condition on tube fretting wear, Wear 255 (2003) 1183-1197.

EXPERIENCE ON FUEL INSPECTION SYSTEM:

JOSÉ ROMÁN FERNÁNDEZ MÍGUEZ, TECNATOM, S.A.

Nuclear Fuel Unit

Tecnatom, S.A.

Avda. Montes de Oca, 1, 28709 San Sebastián de los Reyes, Madrid – Spain

JUAN JOSÉ SERNA GALÁN

Fuel Performance and Procurement

ENUSA Industrias Avanzadas, S.A.

C/ Santiago Rusiñol, 12, 28040, Madrid-Spain

ABSTRACT

In order to respond to the needs of on-site performance information, the industry is developing state-of-the-art equipments from both the technical and commercial points of view. In Spain, TECNATOM and ENUSA have developed a set of equipments.

These equipments have capabilities for dimensional characterization of the fuel rod (rod length, profilometry) and fuel assembly (assembly length, envelope and grid width) and rod corrosion measurement. Dimensional measurements are based on automated visual techniques or LVDT and corrosion on eddy current technique. In the case of single rod it has been developed the capacity of determining the cladding cross section loss and crack characterization.

The experience acquired in commercial use of the inspection systems, have made possible to demonstrate the capacity of the equipment for the performance of quality inspections on different types of irradiated fuel and different nuclear plants.

Along the paper these equipments for fuel on-site inspection, their characteristics and main features are described.

1. Introduction

As a result, on the one hand, of current fuel operating conditions, which are increasingly demanding, and, on the other hand, of the advances incorporated to the fuel design and even changes in the operating conditions themselves, different programs are being carried out in order to survey and enlarge the knowledge of the performance of the fuel through inspections carried out at the plant.

Facing these needs, the industry is developing new equipments aimed at improving competitiveness, from both the technical and commercial points of view. In Spain, TECNATOM and ENUSA have developed a set of equipments to satisfy this demand.

An important part of this characterisation is made using non destructive examination methods, NDE, on-site after or even during the refuelling outages. The characteristics to be measured in this circumstances use to be the following: general condition of the assembly and its main parts, dimensional variations, oxide layer thickness and fuel rod tightness.

Tecnatom and ENUSA have developed a set of equipments to be used in spent pools in order to characterize fuel assemblies: SICOM, SICOM-COR, SICOM-DIM and SICOM-ROD. Along the paper these equipments for fuel on-site inspection, their characteristics and main features are described.

2. SICOM

The initial system called SICOM was created in 1995. SICOM has both capabilities, fuel assembly and fuel rod dimensional characterization and fuel rod cladding corrosion measurement. An interesting feature

of SICOM is that works independently of the manipulator crane because it is designed to safely hold the fuel assembly, make it turn so each face can be inspected, and provide precise axial movement of the inspection modules.

The system is made up of an inspection module and the data acquisition, processing and storage equipment. The inspection module, located on the mechanical equipment, includes a radiation-resistant television camera and four spotlights. The acquisition system consists of a personal computer including a digitizer card and software for image processing and for automatic calculation of the corresponding measurements by means of artificial vision algorithms.

Figure 1 is a general representation of the SICOM equipment. The main parts of the equipment are described in the following paragraphs.

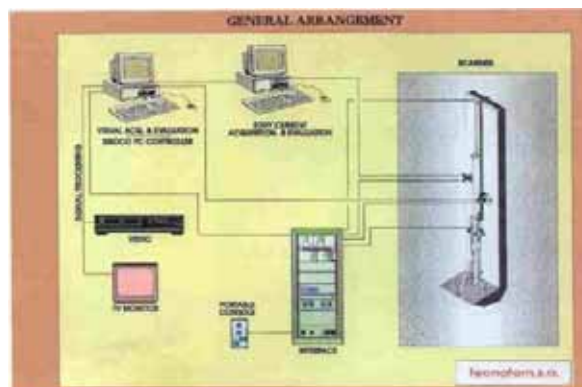


Figure 1: Representation of SICOM equipment.

Since this equipment must be installed in spent fuel pools of different plants, it is possible to adapt the equipment to fit in the different existing configuration of each plant.

The mechanical equipment is designed and manufactured taking into account the high levels of radiation to which it will be exposed and the fact that it will operate under water. The main sub-assemblies of the mechanical equipment are as follows:

- Upper anti-seismic assembly: This assembly, from which hangs the rest of the mechanical equipment, is anchored outside the pool and allows the overall assembly to be levelled. It is designed such that the SICOM is capable of withstanding an earthquake, even though a fuel assembly is being inspected at the time.
- Mast: The mast hangs from the upper support and rests on the floor of the pool. The inspection modules are displaced along its faces via linear guides and rack and pinions.
- Mast support: This part provides the base for support of the equipment on the floor of the pool.
- Fuel assembly support: This part supports and rotates the fuel assemblies in order for each face to be lined up with the inspection modules.
- Clamp: The clamp prevents the fuel assembly from falling, ensuring the security of the assembly during the inspection. The clamp has no contact with the fuel assembly.
- Displaceable modules: The function is to transport the eddy current modules, remote cameras, lights, etc. to any position along the length of the fuel assembly faces.

The controller of the equipment allows the operation of all the assemblies of the mechanical equipment providing also accurate information of the position of the inspection module and of the fuel assembly during its rotation.

A summary of the main characteristics SICOM measures using automatic visual techniques is presented below:

- a) Distance between top and bottom nozzles measured in the centre of each face.
- b) Length of peripheral rods.
- c) The rod-to-nozzle gap of peripheral rods on top and bottom nozzle.
- d) The gap between rods in the centre of each span.
- e) Assembly distortion, i.e. bow tilt and twist.
- f) Height of the top nozzle springs.
- g) Grids width.

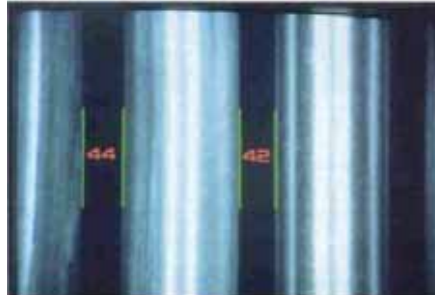


Figure 2. Gap between rods.

As already mentioned, these measurements are obtained directly with the digital image processing system. Figure 2 is an example of the system while gathering rod-to-rod gaps.

Measurement of the oxide layer on the peripheral fuel rods is accomplished using eddy current techniques based on measuring the separation between the sensor and the cladding material, since the oxide layer is not conductive.

The corrosion inspection module includes the sensor (coil) which moves in constant contact with the fuel rod, and a television camera for observation of sensor coupling. In order to ensure accurate alignment of the probe tip to the circular surface of the rod, the system counts with three degrees of freedom.



Figure 3. General overview of SICOM.

3. SICOM-COR

SICOM-COR equipment is developed to measure the corrosion thickness layer in peripheral rods. This development is a response to satisfy the utility generic needs such as reduced equipment size, short inspection time, adaptable to different fuel designs, etc. Its main characteristics are:

- Portable. Installation over the spent fuel rack.
- Fast assembling (only 15 minutes)

- The crane supports the fuel assembly during the inspection.

Based on the “precursor” equipment, SICOM-COR uses essentially the same corrosion inspection module than SICOM. This new tool has been developed since April 2000 and it was first used in a commercial NPP in February 2001.

One interesting feature of this equipment is that the calibration module is composed by three calibration rods allowing a faster inspection of cladding of different materials in the same fuel assembly. The inspection of a full length rod depends on the speed of the vertical movement of the handling crane, though typically takes about 10 minutes.



Figure 4: General view of SICOM-COR portable equipment

4. SICOM-DIM

SICOM-DIM is another equipment developed under the same requirements as SICOM-COR, reduced equipment size, short inspection time, adaptable to different fuel designs, etc. The performance of this equipment started the year 2000.

This equipment is dedicated to carry out dimensional measurements on PWR fuel assemblies such as:

- Length of fuel assembly (using two alternative methods: visual and LVDT)
- Fuel assembly bowing at each grid elevation
- Fuel assembly torsion at each grid and upper nozzle
- Inclination of the upper nozzle
- Grid width

SICOM-DIM uses twelve LVDT sensors (three on each face), placed on a support plate. This plate can be displaced along the fuel assembly taking measurements at the required elevation of each nozzle or grid. In this equipment, as in SICOM-COR, the crane supports the fuel assembly during the inspection.

A complete dimensional examination takes about 20 minutes for each fuel assembly.



Figure 5: General view of SICOM-DIM and fuel assembly.

5. SICOM-ROD

SICOM-ROD is devoted to the inspection of individual rods. It has the capability to measure the oxide layer thickness and the outer diameter profile on single fuel rods (PWR and BWR). Also, it can perform eddy current inspection using bobbin and RPC coils for cladding cross section loss and crack characterization.

SICOM-ROD has two different parts; the upper part is composed by:

- Pancake coil for measurement of the thickness of the oxide layer. With probe holder.
- Bobbin coil for the integrity inspection of the fuel rod.
- Two LVDT sensors for profilometry measurement of the fuel rod.
- Axial encoder for acquisition of axial elevation coordinates.
- Centring device.

The lower part is composed by:

- RPC for eddy current inspection. It can detect wear.
- Motor with circumferential encoder. For the RPC examination.
- Pressurized connecting box.

This equipment requires a motorized pole in order to provide the axial movement to the single fuel rod. Finally, it is noted that the first inspection campaign took place in a BWR power plant in May, 2006.

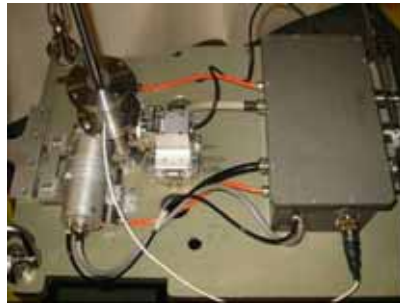


Figure 6: SICOM-ROD equipment.

8. Experience

The operation experience is wide including a variety of fuel assembly types, from different vendors, and different nuclear plants. It shows the adaptability and flexibility of the SICOM systems.

This experience is summarized in the following table:

Dimensional fuel assembly	> 180
Fuel rod corrosion	> 2000
Sites	7
Fuel type	PWR: 17x17 (12" & 14"), 16x16 BWR: GE14

7. Conclusions

The qualification and validation test performed, along with the experience acquired in commercial use of the inspection systems, have made possible to demonstrate the capacity of the equipment for the performance of quality inspections on different types of irradiated fuel and different power plants.

COMPARISON OF THE CODE PREDICTIONS WITH PIE DATA FOR WWER-1000 FUEL RODS, AND COMPARATIVE CALCULATIONS OF WWER AND PWR TYPE FUEL RODS

G. PASSAGE, S. STEFANOVA,

(Institute for Nuclear Research and Nuclear Energy – BAS, Bulgaria)

A.S. SCHEGLOV, V.N. PROSELKOV

(Russian Research Center "Kurchatov Institute", Russian Federation)

ABSTRACT

Operational and PIE data for the Zaporozhye NPP, FA-E0325, WWER-1000 fuel rods irradiated up to ≈ 49 MWd/kgU burnup from the OECD NEA IFPE database are used to perform comparative calculations for 55 fuel rods among three fuel performance codes: PINw99, TRANSURANUS (V1M1J03) and TOPRA-2. The PIE data enable the comparison for fission gas release and gas pressure, cladding elongation, cladding diameter creepdown and gap closure. All calculated results are presented and compared with the available PIE data. It can be concluded that the codes PINw99, TRANSURANUS and TOPRA-2 are capable of adequate predicting the thermophysical and the mechanical performance of the WWER-1000 fuel rods. Comparative thermomechanical calculations of WWER and alternative PWR type fuel rod operational behaviour are presented applying the PINw99 and TRANSURANUS codes. Two fuel rods with diverse design features, a WWER-1000 type (older design) fuel rod and a PWR (VVANTAGE6) type fuel rod, are compared applying the power history and the cooling conditions of the WWER fuel rod.

1. Introduction

Operational and PIE data for the Zaporozhye NPP, FA-E0325, WWER-1000 fuel rods provided in the OECD NEA IFPE Database [1, 2] were used to perform comparative calculations among three fuel performance codes, PINw99 [3], TRANSURANUS (V1M1J03) [4, 5] and TOPRA-2 [6]. The fuel assembly had been irradiated up to ≈ 49 MWd/kgU burnup. The PIE data enable the comparison of experimental measurement with code-calculated values for FGR, internal gas pressure and free volume, cladding elongation, cladding diameter creepdown and pellet-cladding gap size.

The code PINw99, developed and validated primarily for WWER fuel, and TRANSURANUS (V1M1V03), used across Europe for LWR fuel and since 1996 also applied for WWER fuel, have been applied to compare the fuel rod performance of two types fuel rods with diverse design features: a WWER-1000 type (older design) fuel rod and the PWR / VVANTAGE6 type fuel rod [7–9].

2. Calculation to PIE data comparison for assembly E0325, WWER-1000, fuel rods

The power history of the 312 fuel rods consists of 403 time points along 10 axial zones. For the calculations 55 fuel rods have been selected, for which PIE results are available. The data contain the relevant fuel rod design and geometry parameter values with the maximum and minimum possible deviations and the input values have been corrected according to the statistical data of the WWER-1000 fuel rods [10]. The following initial parameters have been chosen: fuel stack length 3.55 m; fuel mass 1465 g; cladding outer/inner diameters 9.13 mm/7.755 mm; fuel pellet outer/inner diameter 7.55 mm/2.3 mm; 4.4% uniform enrichment; 10.585 g/cm^3 initial density; 6 micron grain size; 0.8% volume in-reactor densification; initial filling gas (helium) pressure 2.0 MPa and fuel rod upper plenum volume 11.4 cm^3 .

The calculation results vs. available PIE data are presented (a) for a single fuel rod No.148, the one with the highest measured burnup, as a function of time, and (b) for all measured rods, as a function of burnup. Figures 1–4 show the results for rod No.148 dependent on time: average and maximum LHR (Fig. 1); fuel central temperature (Fig. 2); inner gas pressure (Fig. 3) and rod elongation (Fig. 4). In

Figures 3–4 the measured values are also given. Figures 5–8 present the comparison of the calculated and measured (for normal conditions) results as a function the calculated burnup: FGR from fuel (Fig. 5); inner gas pressure (Fig. 6); cladding elongation (Fig. 7) and cladding diametral displacement (Fig. 8). More details and comparison results are presented in [11].

Fission gas released from fuel. The relative low values of the measured FGR ($< 0.7\%$) for most of the assembly E0325 fuel rods can be explained by the moderate to low levels of LHR, especially at the end of reactor operation. The FGR calculated by PINw99 and TOPRA-2 overpredict the measured values. The values predicted by TRANSURANUS are in good compliance with the measured ones up to burnups of ≈ 52 MWd/kgU and lower at higher burnup. A specific feature of the PIN code series, including PINw99, is the BOL $\sim 0.5\%$ FGR, which reflects an older conservative concept.

Inner gas pressure. The results obtained by the TRANSURANUS and TOPRA-2 codes are close to the measured ones, but slightly underpredicting. The calculated by PINw99 pressure is higher than the measured values. The differences may be explained by the measurement uncertainties, uncertainties in initial void volume, and the possible deviation of initial fill gas pressure from the nominal 2 MPa.

Cladding elongation. The TRANSURANUS and TOPRA-2 calculated results can be considered as being in good compliance with the measured ones. Most of the calculated by TRANSURANUS results have a trend to increase with burnup increase. The TOPRA-2 results are in better agreement and have a different trend of decreasing with burnup after the onset of a hard contact. This is a consequence of the applied "axial force" model, which implies prevailing cladding shortening, due to its diameter decrease after PCMI. The calculated by PINw99 elongation values are lower than the measured ones, which can be explained by the lack of accounting for the appearing at PCMI axial force.

Cladding diameter change. Accounting for the measurement uncertainty, the comparison of this parameter may be observed as a rather qualitative one. The PINw99 and TRANSURANUS results give a smaller diametrical change and the TOPRA-2 calculated results give a more reasonable compliance with the measurement. As a whole, the measured and the calculated values are in good agreement.

It can be concluded from this comparison, that the codes PINw99, TRANSURANUS and TOPRA-2, are capable of adequate predicting the thermophysical and the mechanical performance of the WWER-1000 fuel rods at normal operation conditions. The PINw99 code predicts conservative BOL FGR values and conservative gas pressure at higher burnups, thus the models must be improved [12]. Refinements are indicated for the TRANSURANUS code, which are subject of the ongoing research projects and further improvements [13]. A detailed comparison of measured and calculated fuel rod geometry allowed for an empirical adjustment of the creep model leading to improved results [14]. More experimental data are however required to come to better quantitative conclusions.

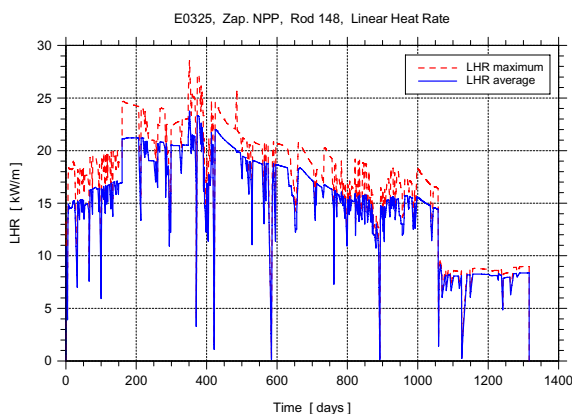


Fig. 1. Rod No.148 average and max. LHR.

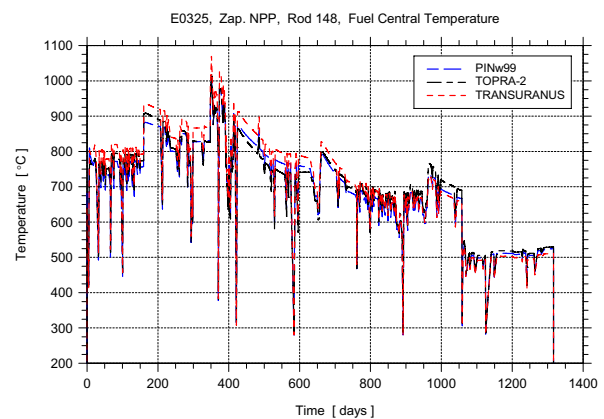


Fig. 2. Rod No.148 central fuel temperature.

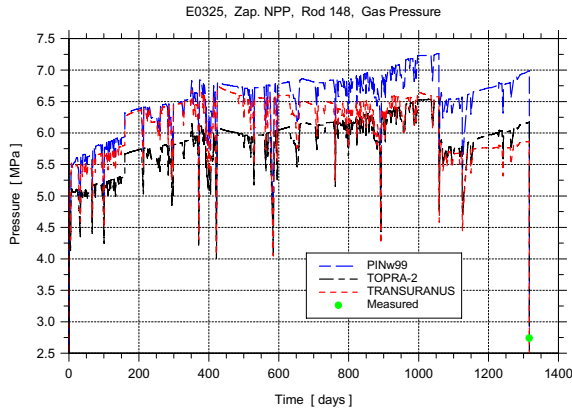


Fig. 3. Rod No.148 inner gas pressure.

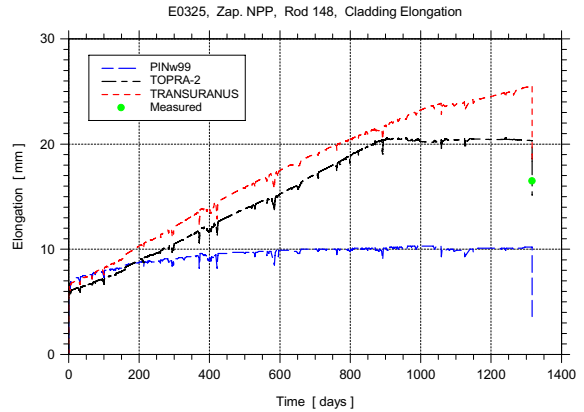


Fig. 4. Rod No.148 cladding elongation.

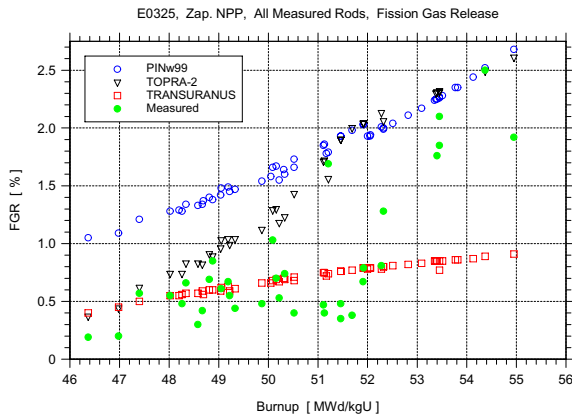


Fig. 5. Calculated/measured FGR, all rods.

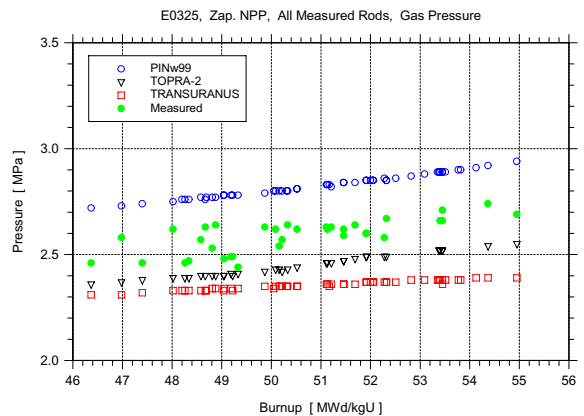


Fig. 6. Calculated/measured gas pressure, all rods.

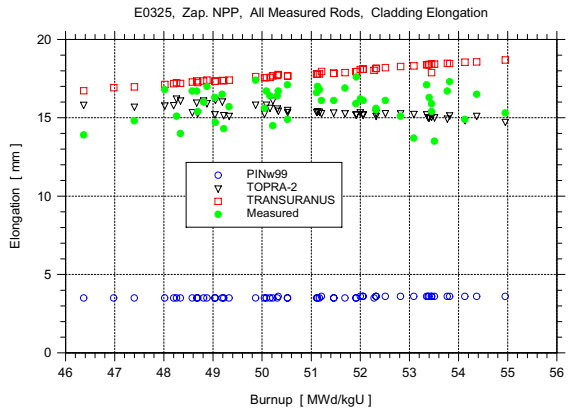


Fig. 7. Calculated/measured rod elongation, all rods.

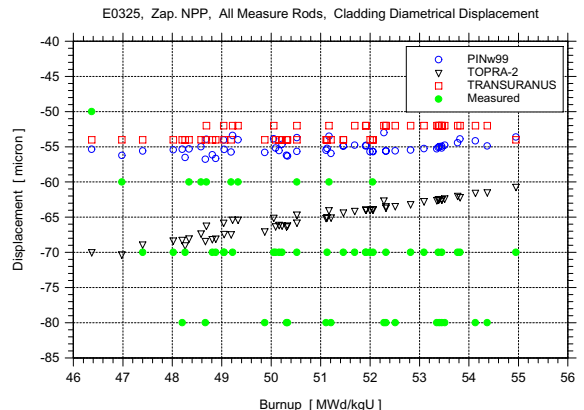


Fig. 8. Calculated/measured clad diameter change, all rods.

3. Comparative calculations of WWER-1000 and PWR type fuel rods

The comparative thermomechanical calculations and analyses of WWER and alternative PWR type fuel rod operational behaviour are performed by the codes PINw99 and TRANSURANUS (V1M1V03). Fuel rods with two design features have been considered: a WWER-1000 type (older design) fuel rod described in the previous chapter above and a PWR / VVANTAGE6 type fuel rod [7–9]. For both rods the LHR history of rod 148 has been applied. The PWR power history was adjusted by time step multiplication with an approximate PWR to WWER fuel mass ratio factor of ~ 1.2, in order to compare the calculated values at equal / comparable burnups. The main initial geometrical and technological parameters of the fuel rods are summarised in the Table below:

Table. WWER-1000 (older design) and PWR (VVANTAGE6) type fuel rod input parameters

Parameter	WWER-1000	VVANTAGE6
Fuel pellet inner diameter, mm	2.3	–
Fuel pellet outer diameter, mm	7.550	7.840
Cladding inner diameter, mm	7.750	8.000
Cladding outer diameter, mm	9.130	9.14
Initial fuel density, % TD	96.5	95.0
Volumetric densification, %	0.8%	1.0%
Initial filling gas pressure, MPa	2.0	2.0
Plenum volume, cm ³	11.4	8.9
Fuel grain size, micron	6.	10.
Fuel uniform enrichment, %	4.4	4.4
Cladding alloy	N1 (Zr1%Nb)	Zircaloy-4
Coolant pressure, MPa	15.7	15.7

The calculated results are presented in Figures 9–14 for the 5th (of 10) axial slice, where the LHR is the highest during the prevailing part of the power history.

Figures 9 and 10 present the FGR predicted by the codes. The PWR rod BOL values are higher due to the higher central fuel temperatures, coming from the lack of pellet central hole (by ~ 150°C (PINw99) and by ~ 130°C (TRANSURANUS)). Figures 11 and 12 show the calculated inner gas pressure. At BOL the WWER rod gas pressure is higher, due to the larger amount of gas with high temperature in the central hole. At EOL, the difference in the decreased gas free volumes becomes governing, due to the faster closure of the PWR rod pellet-cladding gap inclusive, thus the PWR rod value is higher by ~ 1.6 MPa (PINw99) and by ~ 0.8 MPa (TRANSURANUS) at final cold state. Figures 13 and 14 present the fuel outer and the cladding inner radii, revealing the different burnup of closure, ~ 42–45 MWd/kgU for the WWER fuel rod and ~ 25–30 MWd/kgU for the PWR rod. For both rods, the gap closure burnup is in good compliance with the known published data. It can be also seen from Figures 13 and 14, that after the cladding-to-fuel contact onset, the calculated fuel and cladding radii remain almost unchanged, which corresponds to the soft contact onset, when the fuel radius due to swelling is compensated by the backward relocation of the fuel fragments under the pressure of the collapsing due to creepdown cladding. Fig. 13 reveals also a specific feature of the PINw99 code cladding-to-fuel contact model, assuming that the gap remains always slightly “open” and never decreases below 10.8 micron diametrically, as a result of the input cladding and fuel roughness.

It can be preliminarily concluded from the presented results, that the differences in the WWER-1000 and the PWR fuel rod steady-state performance at equal irradiation conditions depend on the initial geometrical parameters (e.g. the PWR rod larger linear fuel mass, absence of central hole in fuel, thinner cladding, smaller gas plenum volume), on the diverse performance of the Zr1%Nb and Zry-4 cladding alloys and on the initial fuel density and in-reactor densification.

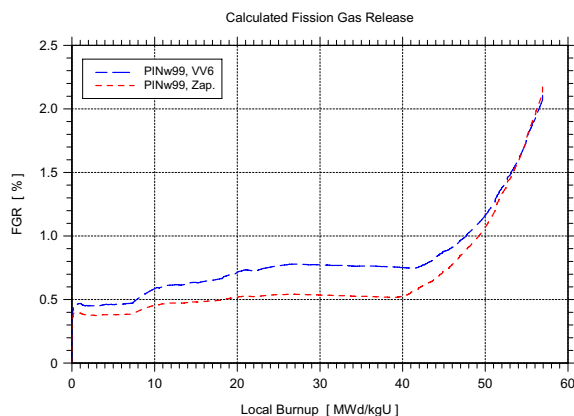


Fig. 9. FGR calculated by PINw99.

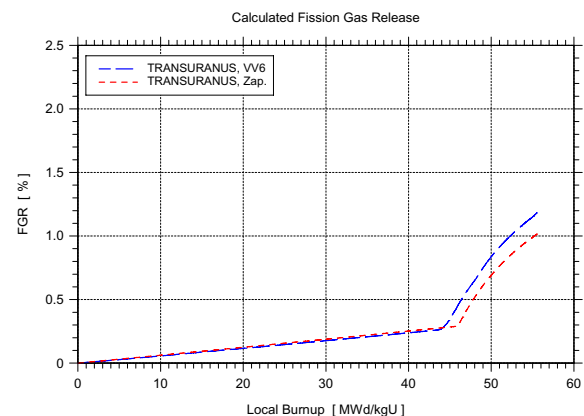


Fig. 10. FGR calculated by TRANSURANUS.

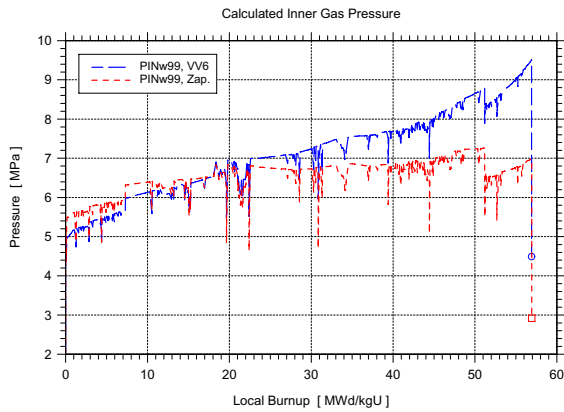


Fig. 11. Inner gas pressure, PINw99.

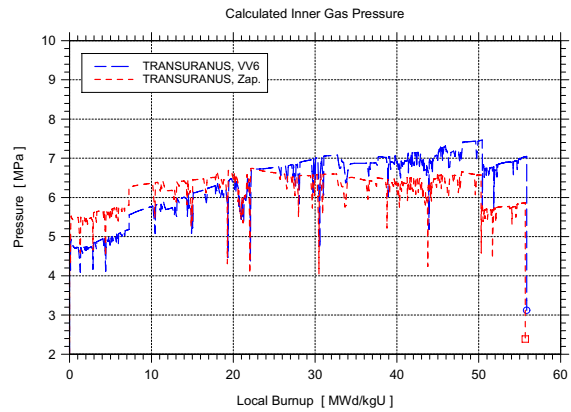


Fig. 12. Inner gas pressure, TRANSURANUS.

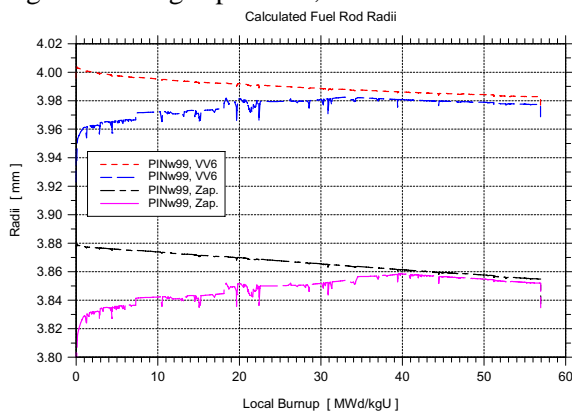


Fig. 13. Fuel rod radii, PINw99.

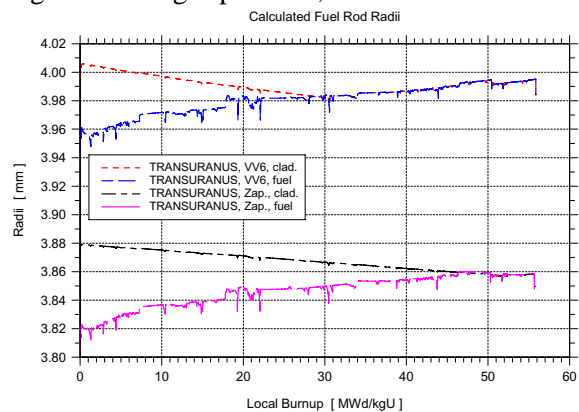


Fig. 14. Fuel rod radii, TRANSURANUS.

4. References

- [1] Chantoin P., Turnbull J., The compilation of a public domain database on nuclear fuel performance for the purpose of code development and validation. Proc. of the International Topical Meeting on LWR Fuel Performance, March 2-6, 1997, Portland, Oregon, pp. 515–522.
- [2] Database for FA E0325 irradiated at the first Unit of Zaporozhskaya (Zaporozhye) NPP, WWER-1000, 1988-1994. Prepared by D.V. Elenkov (2002) and J. A. Turnbull and G. Khvostov (2004).
- [3] P. Strijov, M. Valach, UJV Draft-T,M, NRI Rez plc, August 1999.
- [4] K. Lassmann, Journal of Nuclear Materials, 188 (1992).
- [5] Lassmann K., Elenkov D., Gyori C., Cvan M., European Atomic Energy Community – INRNE Study Contract No. 16588-2000-08-F1ED KAR BG, 2001.
- [6] Scheglov A., Proselkov V., Proceedings of the Fourth International Conference “WWER Fuel Performance, Modelling and Experimental Support”, October 2001, Albena, Bulgaria. pp. 220–228.
- [7] Fuel Review 2003: VVER Fuel Design, Nuclear Engineering International, September 2003.
- [8] V. Mecir, Z. Durdak, D. Ernst, P. Dvorak, Proceedings of ENS/ANS TopFuel 2003, Germany.
- [9] D. Ernst, R. Ernst, V. Mecir, J. Neubauer, R. Svoboda, Proceedings of 2004 International Meeting on LWR Fuel Performance, 2004, USA.
- [10] Scheglov A., Proselkov V., Yenin A., Atomic Energy, 1991. vol. 71. iss. 6, pp. 503–506.
- [11] G. Passage, S. Stefanova, A.S. Scheglov, V.N. Proselkov, Proceedings of the 6th International Conference on WWER Fuel Performance, Modelling and Experimental Support, Albena, 19–23 September 2005.
- [12] G. Passage, I. Mandev, S. Stefanova et al., Presentations in the IAEA CRP FUMEX-II Meetings in Halden, Norway, 7–10 September 2004 and in Vienna, Austria, 5–9 December 2005.
- [13] A. Schubert, P. Van Uffelen, J. van de Laar, Presentation in the IAEA CRP FUMEX-II Meeting in Halden, Norway, 7–10 September 2004.
- [14] P. Van Uffelen, C. Bruynooghe, Cs. Györi, J. Jonnet, A. Schubert, J. van de Laar, Proceedings of the 6th International Conference on WWER Fuel Performance, Modelling and Experimental Support, Albena, 19–23 September 2005.

ENSURING FUEL ECONOMY AND SAFE BWR CONTROL ROD MOVEMENTS THROUGH BWR FUEL CHANNEL MEASUREMENTS

Andreas Fristedt-Åblad, Jan Möller, Per Collin
Westinghouse Electric Sweden AB

Introduction

Proofing the fuel channels geometry is necessary for running the fuel. If fuel does not fulfill the requirements of straightness, there is a risk of jamming the control rods when running them during normal operation. The deviation in fuel channel dimension also influences the water flow and thus affects the fuel economy and cooling of the core.

The Westinghouse Fuel Channel Dimensional Surveillance Equipment (FDS) used for BWR channel measurements; rely on modern ultrasonic technology to assure an accurate result of the bow, twist, bulge and length of a BWR fuel channel.

The first channel measurement system from Westinghouse was developed 25 years ago and has been modified numeral times to its current standard. Mayor benefits with the FDS are that it does not use any moving parts, which increases the reliability and accuracy of measurements and that it rapidly measures all types of fuel channels.

FDS today

The latest channel measurement system from Westinghouse has a LabVIEW program working interactively with the ultrasonic instrument, which gives several benefits to the operator of the channel measurement system and the power plant owner.

It is neither the hardware nor the software alone that makes this equipment unique, but the entirety of the hardware and software combined into a unique process for measuring BWR fuel channels.

Equipment – hardware and software

The hardware consists of a fixture with transducers, standard and cabinet; the cabinet withholding multiplexers, an ultrasonic instrument, a laptop or an industrial computer and a printer.

The fixture is manufactured with stainless steel and is placed along the side of the spent fuel pool. The fixture withholds all transducers and has two locking arms for fixing the fuel assembly during measurements (see figure 1a). Transducers are positioned at different levels in a specific pattern to make measurements on different types of fuel channels possible.

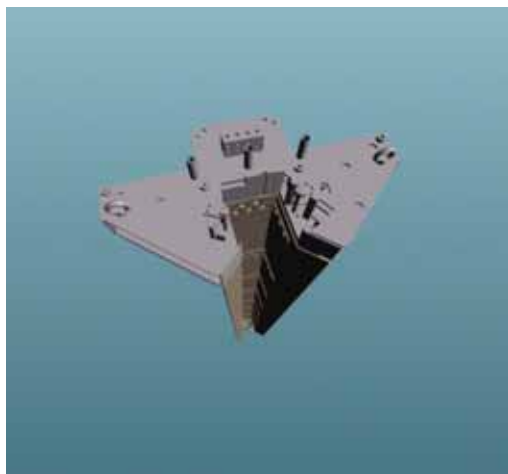


Figure 1a: Computer animation of measuring fixture.

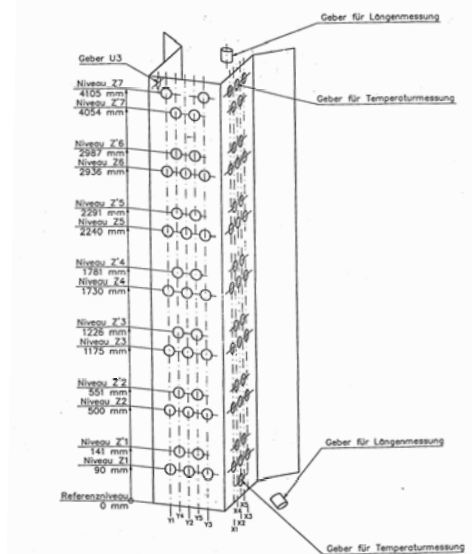


Figure 1b: Transducer outline.

The equipment is connected as described in figure 2. The transducers placed in the fixture are connected to the multiplexer modules positioned in the multiplexers. The two multiplexers are connected to the ultrasonic instrument, which on its part corresponds through an RS 32 connection with the computer and the LabVIEW program. The LabVIEW program is controlled and monitored by the operator and a printout version of the results is feasible.

System lay-out and functions

The system is calibrated with a standard before each measurement session. The system is also continuously calibrated for variance in temperature during the calibration and measurement sessions.

The fuel channel measurement fixture holds 57-73 transducers depending on original version and different upgrades made in various plants. Today's Westinghouse standard is 72 or 73 transducers placed according to figure 1b (72 transducer version).

Two transducers continuously monitor the temperature, this is necessary in order to adjust for variance in temperature. The water temperature along the fuel channel behaves almost linearly. Therefore only two temperature transducers are required, one at the top and one at the bottom of the fixture. Two transducers, one placed at the top of the fixture and one placed at 45° angle at the bottom of the fixture make it possible to measure length on all types of fuel channels. The top transducer used for length measurements is mounted on the locking arm and determines the total growth of the upper part of the fuel channel. In addition, for channel types not fixed to the bottom nozzle, the lower 45° angle transducer detects the fuel channel's lower end growth (figure 3). 28 linear focusing transducers placed towards the edges are used to measure channel types with reinforced edges and channel types with water cross. 40 point focusing transducers enables fuel channel bulge measurements. The two offset placed transducers in each level are necessary for measuring SVEA-channels with a water cross and fuel channels with reinforced edges with a bulge greater than 6 mm (levels Z'(z) according to figure 1b).

The ultrasonic device sends a signal through the multiplexer, which directs the signal to the correct transducer. The signal bounces towards the surface of the fuel channel and back through the multiplexers to the ultrasonic device where the signal is received, transformed and sent to the laptop computer for transformation and display. The LabVIEW program monitors and controls the level of the outgoing signal from the ultrasonic device in order to correct for variance in material echo.

Directed by the computer, the multiplexers allow each transducer 10 measurements during 1 second then they switch to the next transducer. The sequence, in which the

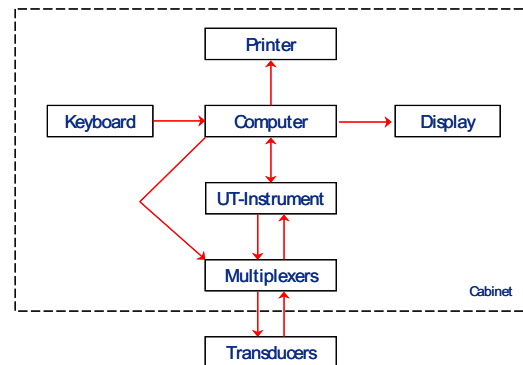


Figure 2: Equipment lay-out.

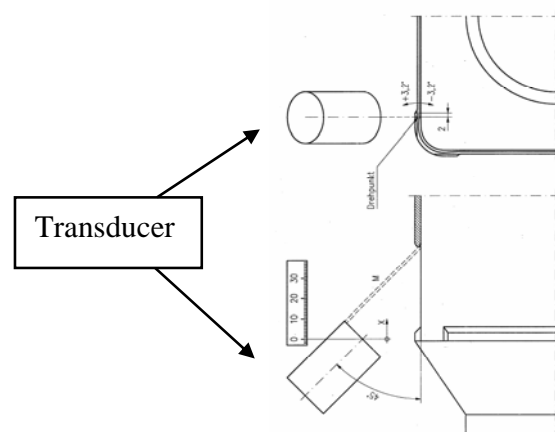


Figure 3: Length measurement at bottom nozzle. The transducer is seen from two perspectives.

multiplexers switch from one transducer to another, is predetermined in the LabVIEW program. If a transducer in level 2-6 breaks down, the measuring sequence is automatically altered by the LabVIEW program and the broken transducer is omitted. Data from earlier measurements can be loaded on to the computer and automatically be compared with new measurements, which give analysts a powerful tool in following the fuel channel evolution concerning the bow, bulge, twist and length.

Measuring procedure

The standard is placed in the fixture and locked down with the locking arms, thereafter the system is calibrated and the standard is removed. The first fuel assembly is positioned in the fixture and locked down. The LabVIEW program is run in approximately 1 minute and the results of the bow, bulge, twist and length are graphically and numerically displayed on the screen. The fuel assembly is exchanged once the data has been gathered.

Measurement accuracy

Different tests are made during SAT (Site Acceptance Test) to ensure the system's preciseness. The system can be adapted to measure bows up to approximately 30 mm.

The accuracy of the system is ± 0.2 mm for bow, ± 0.2 mm for bulge, ± 0.2 mm for twist and ± 0.5 mm for length measurements.

Summary

Due to irradiation, the length and shape of fuel channels in BWR: s varies. In order to confirm economical and safe operation of the plant it is necessary to verify the geometry of the fuel assemblies. The new Westinghouse Fuel Channel Dimensional Surveillance Equipment (FDS) uses a newly developed LabVIEW program to measure and calculate the fuel channels' bow, bulge, twist and length. The new LabVIEW program is, through its modularity, easy to service and offers the result both numerically and graphically.

Due to the variance of the fuel channels' material properties, the return signal from the transducers differs. The LabVIEW program enables the computer to correspond with the ultrasonic technique (UT) instrument and senses the return signal. It thereafter adjusts the out-put level from the UT-instrument in order to compensate for variation in return signal.

The equipment's measuring fixture uses no moving parts, hence increasing the system's accuracy and durability. The accuracy is ± 0.2 mm for bow, ± 0.2 mm for bulge, ± 0.2 mm for twist and ± 0.5 mm for length measurements and the equipment can be adapted to measure bows up to 30 mm. One fuel assembly takes 1 minute to measure and the equipment is able to handle all types of fuel channels.

FDS systems delivered and upgraded by Westinghouse

Customer	Plant	Delivery	Upgraded
Sweden:			
Swedish State Power Board	Ringhals 1	1981	
Forsmarks kraftgrupp AB	Forsmark 1,2	1982	1998
Oskarshamns Kraftgrupp	Oskarshamn 1,2	1982	1999
Sydskraft AB	Barsebäck 1,2	1984	
Finland:			
Tellisuuden Voima OY	Olkiluoto 1,2	1982	1990, 2003
Germany:			
Rheinisch Westfälisches Elektrizitätswerke AG	Gundremmingen B,C	1983	1993, 2006
Hamburgische Elektrizitäts- tätswerke AG	Brunsbüttel/Krümmel	1986	1997
Switzerland:			
Gesellschaft Kernkraftwerk Leibstadt	Leibstadt	1987	1994, 2006
USA:			
Energy Northwest	Columbia, CGS	1986	

Contact information

Westinghouse Electric Sweden AB, Finnslätten
721 63 Västerås
Sweden

Commercial: Andreas Fristedt-Åblad
 andreas.fristedt-ablad@se.westinghouse.com
 Tel. +46-21-34 74 89

Technical: Jan Möller
 jan.moller@se.westinghouse.com
 Tel. +46-21-34 79 85

RESULTS OF POST-IRRADIATION EXAMINATIONS (PIE) OF E110 CLADDINGS AND ALLOY UPGRADING FOR VVER

V.V. NOVIKOV, V.A. MARKELOV, V.N. SHISHOV,
A.V. TSELISHCHEV, A.A. BALASHOV

FSUE A.A. Bochvar VNIINM, 123060, Moscow, P.O. Box 369 - Russia

ABSTRACT

In the existent VVER-1000 reactors fuel assemblies operate in four year cycles to reach the average fuel burnup of the order of 55 MW·d/kg U. Under those conditions fuel rods demonstrate high serviceability with E110 alloy claddings showing adequately resistances to corrosion and shape changes. On account of bringing the sponge zirconium production to the commercial level and its using for the E110 alloy fabrication it has been shown that the resistance of fuel claddings to irradiation induced growth is enhanced and their behaviour is improved during high temperature oxidation in LOCA.

Key words: E110, fuel cladding, burnup, PIE, corrosion resistance, resistance to shape changes, electrolytic and sponge zirconium, high temperature oxidation, oxide, irradiation induced growth.

1. Introduction

For more than 40 years in the water cooled reactors of Russia E110 (Zr-1%Nb) alloy has been used the base of which is formed by an electrolytic powder blended with zirconium iodide [1, 2]. To-day, in the VVER-1000 reactors that are the main type of reactors evolving in Russia E110 alloy clad fuel rods operate in a four year cycle to reach the fuel assembly burnup to 55 MW·d/kg U and demonstrate the adequately high performance in terms of corrosion and shape change resistances [3-5].

Currently in Russia under way is the programme aimed at optimizing the production of zirconium sponge and its application as the base of E110 alloy for fuel claddings and other items of fuel assemblies. The change of the metallurgical base of E110 alloy has brought forth the challenge of studying the characteristics of fuel claddings fabricated from this alloy; some results of the studies are dealt with in this communication.

2. Results of PIE of Fuels Clad in E110 alloy

2.1 Corrosion and hydrogen uptake

In terms of corrosion resistance under the VVER conditions E110 alloy reveals high properties with no acceleration of corrosion up to the burnup of ~ 65 MW·d/kg U [3, 4]. An oxide coat at the outer surface of a cladding along a fuel rod height is comparatively uniform throughout its thickness, dense and well bonded to the metal. After four cycles of operation in VVER-1000 the thickness of an oxide coat on claddings does not exceed 10 µm (figure 1a). The hydrogen content of the E110 alloy cladding is not more than 120 ppm at the burnups reached in VVER-1000 (figure1b) [4].

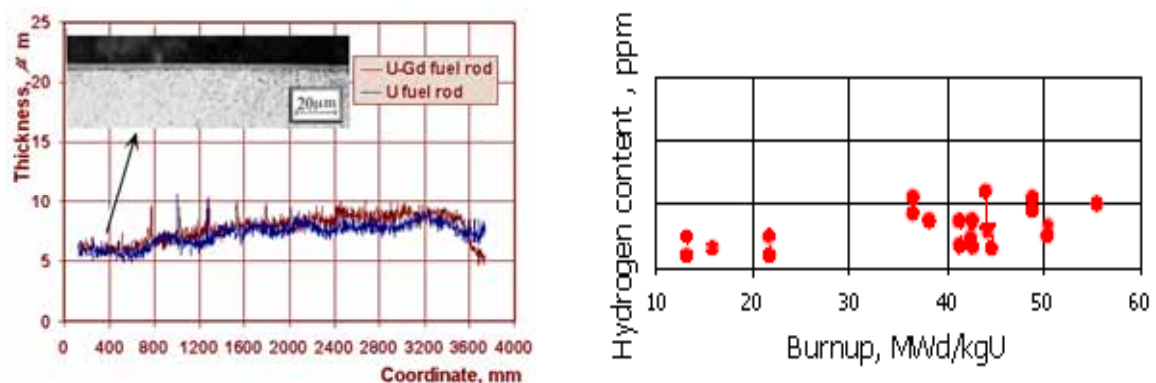


Fig 1. Size distribution of oxide coat thickness along E110 alloy cladding height at burnup of 55.6 MW·d/kg U (data of [3]) (a) and burnup dependence of hydrogen content of E110 alloy claddings (data of [4]) (b)

2.2 Dimensional changes

As a result of creep due to a difference in pressures of a coolant and gases within a fuel rod the diameter of a cladding decreases in an essentially linear mode as the burnup extends to 55 MW·d/kg U (figure 2a). At the same time the length of a fuel cladding increases also in an essentially linear mode (figure 2b) [5].

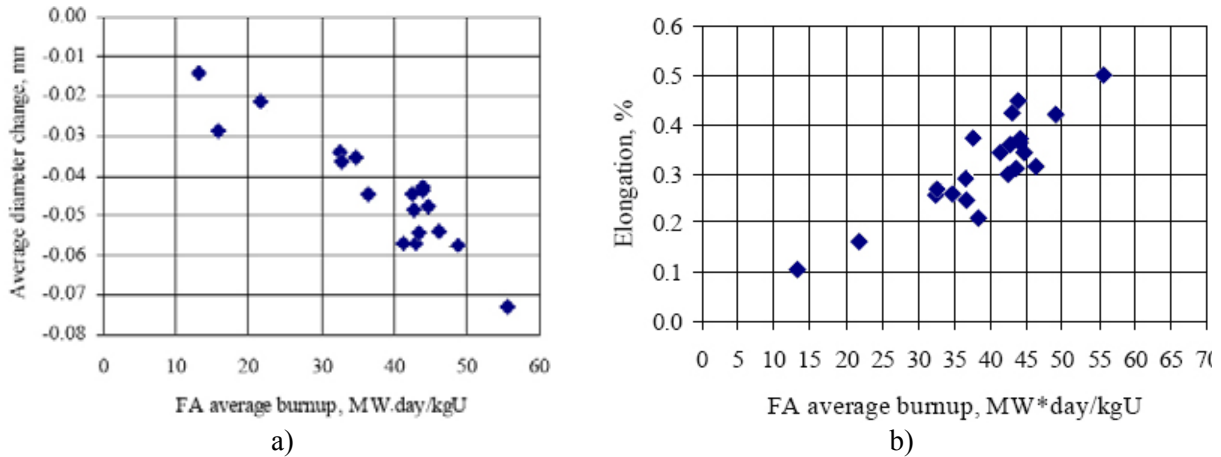


Fig 2. Variations in diameter (a) and elongation (b) of fuel rod clad in E110 alloy vs fuel assembly averaged burn up (data of [5])

Since the cladding diameter decreases while the fuel pellet diameter increases due to swelling the gap between them is being reduced with a burnup by the law close to the linear one (figure 3a) up to the cladding-pellet contact at the burnup of ~ 48 MW·d/kg U (figure 3b) [5]. Nonetheless, this behaviour of fuel and cladding does not restrict the further operability of fuels to higher burnups.

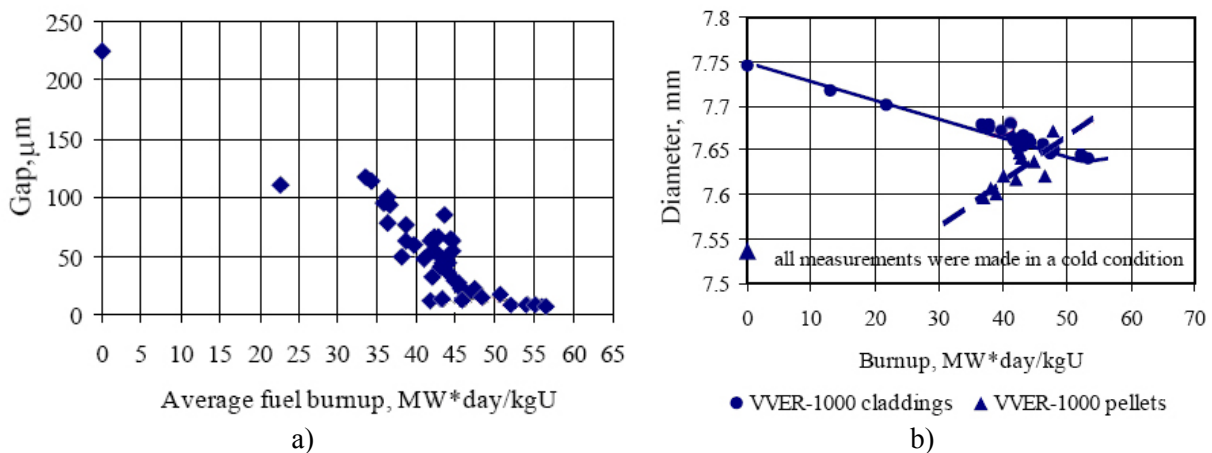


Fig 3. Burnup dependence of fuel-cladding gap size (a) and diameter (inner) of cladding and pellet (b) (data of [5])

3. Results of Investigating Claddings from E110 Alloy on Zirconium Sponge Base

The application of zirconium sponge as the E110 alloy base called for implementing studies into the main characteristics of fuel claddings produced thereof in comparison to claddings from the standard E110 alloy based on electrolytic zirconium. The acquired results revealed that tubes produced from those alloys had no substantial differences in their structures, short-term tensile properties, in resistance to autoclave corrosion and thermal creep.

At the same time interesting data on zirconium sponge E110 alloy were acquired from studies into its high temperature oxidation and irradiation induced growth.

3.1 Resistance to high temperature oxidation

According to the data of [6, 7] the process of a high temperature oxidation of claddings from electrolytic base zirconium alloy E110 might proceed at an unstable rate attended with the formation

of porous crumbling out oxide coats (figure 4a) which in this instance gives rise to a cladding ductility reduction.

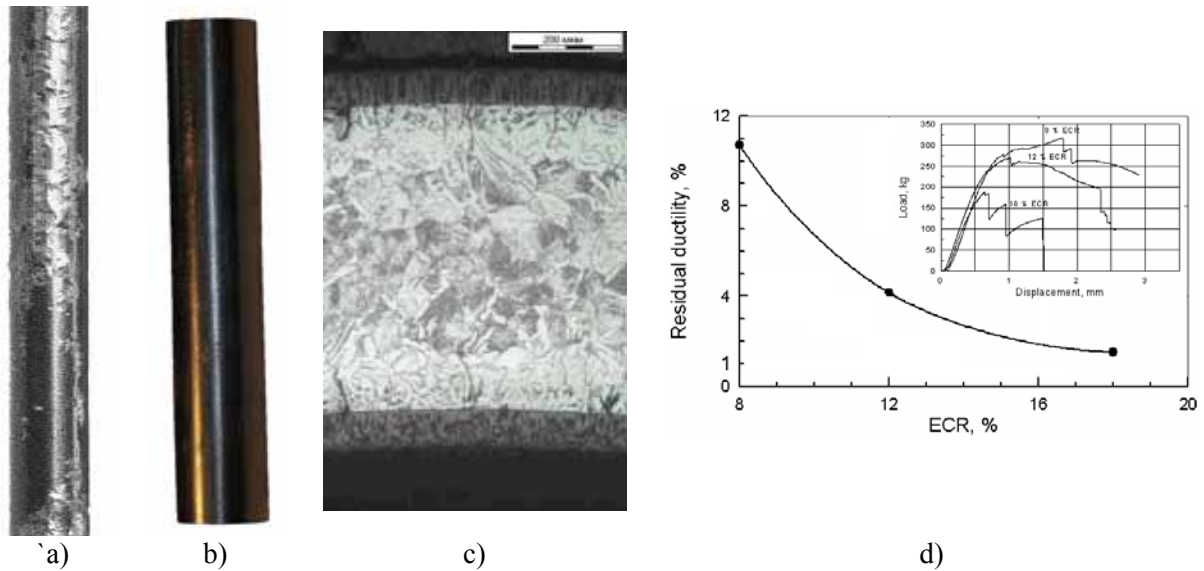


Fig 4. Appearance of cladding tube from E110 alloy on electrolytic zirconium base (a) and on zirconium sponge base (b) after oxidation in steam at 1100°C to ECR = 9.8 % and ECR = 18% respectively. Structure in transverse section (c) of tested cladding from sponge base E110 alloy. Residual ductility of claddings from sponge base 110 alloy vs ECR (d) (according to data [7,8]).

In a similar alloy on a zirconium sponge base as oxidized at 1100°C the surface of a cladding is covered with a dense lustrous black coherent oxide coat up to ECR=18% (figure 4 b, c); the material having the residual ductility above 1% (figure 4d) [8].

Different corrosion behaviour of claddings fabricated from E110 alloy on electrolytic and zirconium sponge bases was revealed at temperatures of 1000-1100°C. After oxidation at 1200°C room temperature tests for compression revealed that brittleness is inherent in Zr-1%Nb alloys independent of electrolytic or sponge zirconium base which is also true for other zirconium sponge base alloys [7, 9].

The investigations carried out in this work have demonstrated that after testing in steam at 1100°C to 10% ECR the surface of electrolytic zirconium E110 alloy cladding might be coated with a non-uniform oxide: in some areas it is black and dense, in others it is white and crumbles out. A black dense oxide forms at the surface of a cladding fabricated from zirconium sponge E110 alloy.

Investigations carried out with a scanning electron microscope («Hitachi S-800») at the accelerating voltage of 20 kV have revealed that in an oxide coat on a sample of electrolytic E110 alloy that is detached from the base metal the following is observable: a high disorientation of grain packets and cracks available on grain joints (figure 5a). A high temperature oxide available on sponge base E110 alloy features a uniform highly oriented columnar structure throughout the thickness of an oxide coat densely adherent to the base metal (figure 5b).

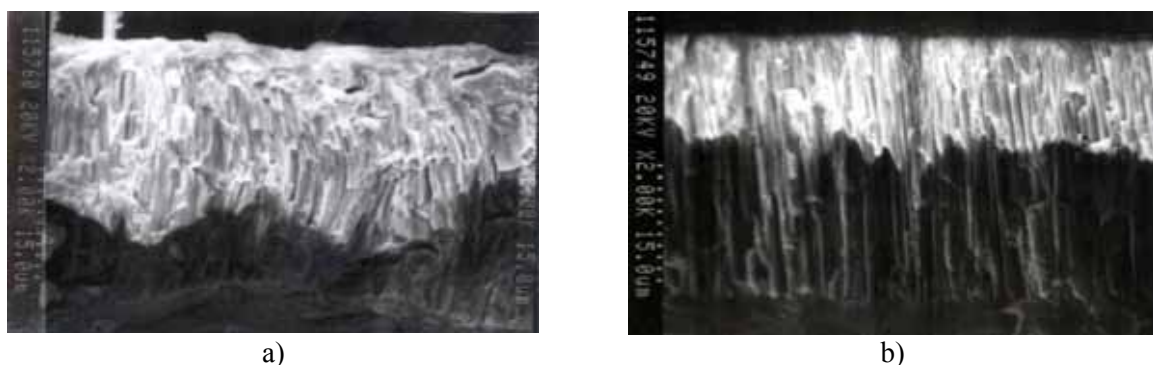


Fig 5. Microstructure of transverse fracture in oxide coat at surfaces of cladding tube samples from E110 alloy on electrolytic (a) and sponge (b) bases after oxidation in steam at 1100°C to ECR = 10 %.

Differences in the structures of oxide coats as revealed at a microlevel with a scanning electron microscope are confirmed at a statistically higher level by the data of an x-ray diffraction analysis of oxide textures (figure 6).

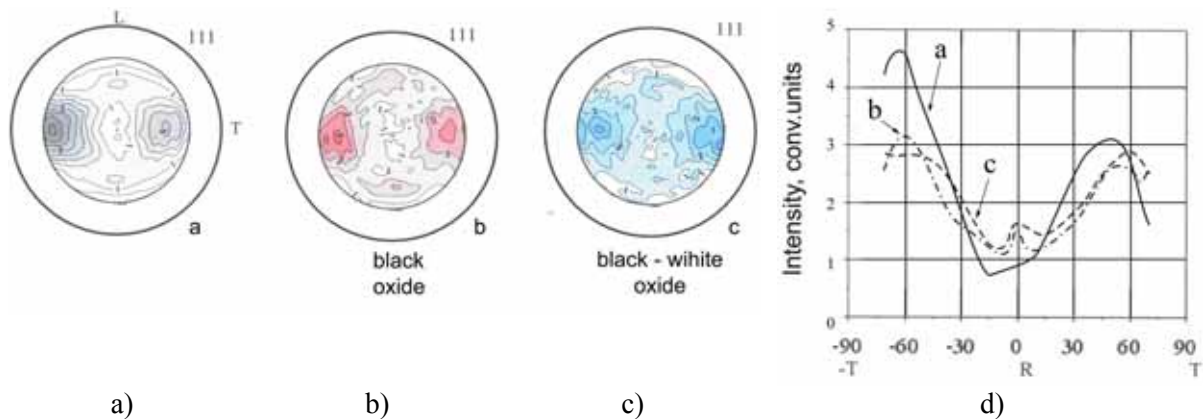


Fig 6. Texture of oxides on cladding tubes from E 110 alloy based on sponge (a) and electrolytic (b,c) zirconium, DPF {111}. Distribution of normals {111} in R-T section (d)

According to the data of figure 6 texture $\{001\}\langle 110\rangle$ forms in oxide coats. The perfection of texture component $\{001\}\langle 110\rangle$, i.e., the sharpness of its texture maxima was assessed via measuring the semi-width of texture maxima at a half of their height as well as from the ratio of pole densities in the maximum and minimum of the DPF section.

It is evident from the presented data that the sharpest and most perfect one is the texture of an oxide that formed on a tube sample from E110 alloy on a sponge base. The texture of an oxide on a tube sample from standard E110 alloy (electrolytic base) is dissipated even in a black dense oxide; the dissipation increasing with passing to white oxide areas.

The specific process of standard E110 alloy oxidation in comparison with sponge base alloy at 1000 and 1100°C and the identical behaviour at 1200°C allowed an assumption that the cause of the observed difference lies in various temperatures of the polymorphic transformation in the oxide coats of both the materials.

However, the investigations did not confirm the assumption of different temperatures of the polymorphic transformations of the matrix and the oxide of E110 alloy on sponge and electrolytic bases. The results of the differential thermal analysis have shown that these temperatures of the transformation onset in both the alloys are equal and make up 825°C for $((\alpha + \beta)_{Zr} \rightarrow \beta_{Zr})$ matrix and 1185-1190°C for $(\alpha \rightarrow \beta)$ oxide.

The difference in the high temperature oxidation behaviour of E110 alloys having different zirconium bases is likely to be explained by the impurity composition of the material.

3.2 Irradiation induced growth

The studies into the irradiation induced growth of samples of fuel claddings produced by the same deformation - thermal outline using E110 alloys having sponge and electrolytic zirconium bases were implemented in BOR-60. The measurements of the axial strain revealed differences between those materials in their resistance to irradiation growth (figure 7). Zirconium sponge E110 alloy claddings show a lower irradiation growth strain at the incubation period stage and a less intensive growth acceleration after a breakthrough.

This mode of zirconium sponge E110 alloy behaviour suggests that aside from the higher resistance to high temperature oxidation fuel claddings produced from this alloy shall also have a higher resistance to shape changes during reactor operation in comparison to the ones from the standard E110 alloy on electrolytic zirconium base.

Currently zirconium sponge alloy E110 was used to fabricate representative batches of fuels and fuel assemblies comprising them were loaded into VVER-1000 and RBMK-1000 reactors.

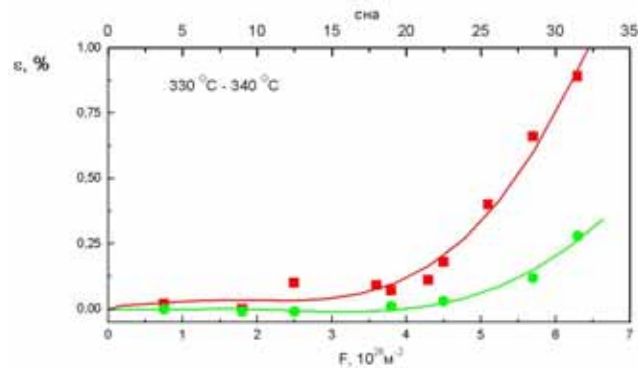


Fig 7. Fluence dependence of irradiation growth strain of cladding tubes from E110 alloy on electrolytic (■) and sponge (●) zirconium bases (BOR-60 irradiation)

4. Conclusions

The results of PIE of fuels clad in electrolytic zirconium alloy E110 evidence the high resistance of their claddings to oxidation and hydriding upon corrosion and their adequate resistance to shape changes which provides for the safe operation of fuels in the VVER-1000 fuel cycles.

The E110 alloy perfection through the application of zirconium sponge as its base provides the fuel claddings with the characteristics identical to those of electrolytic zirconium alloy claddings as well as improves their resistances to high temperature oxidation and irradiation effected growth.

Acknowledgments

The authors would like to thank V.M.Troyanov, Yu.V.Pimenov and A.B.Dolgov of the JSC TVEL for the fruitful discussions.

References

1. P.V. Shebaldov, M.M. Peregud, A.V. Nikulina at el. "E110 Alloy Cladding Tube Properties and Their Interrelation with Alloy Structure-Phase Condition and Impurity Content" 12 International Symposium of Zr in the Nuclear Industry.–1996.–ASTM STP–1354.–P.545–559.
2. A.S. Zaimovsky, A.V. Nikulina, N.G. Reshetnikov. "Zirconium in nuclear power engineering". 2nd ed., Energoizdat, Moscow, 1994.
3. A.V. Smirnov at el. "Results of post-irradiation examination of WWER-1000 uranium fuel rods and uranium-gadolinium fuel rods to validate 4 and 5-Year fuel cycles". The 5th International Conference «WWER Fuel Performance, Modelling and Experimental Support», Albena, Bulgaria, September 29 - October 3, 2003, Paper 4.1.A.
4. A.V. Smirnov at el. "Results of post-irradiation examination of WWER-1000 uranium fuel rods and uranium-gadolinium fuel rods to validate 4 and 5-Year fuel cycles". 6TH International Conference "WWER Fuel Performance, Modelling and Experimental Support, Albena, Bulgaria, 19 September – 23 September 2005, Paper 3A.3.
5. V.P. Smirnov at el. "VVER FUEL: RESULTS OF POST IRRADIATION EXAMINATION", Proc. 2005 Water Reactor Fuel Performance Conference, Kyoto, Japan, 2005, pp. 217-226
6. L. Egorova at el. "LOCA behavior of E110 alloy", Nuclear Safety Research Conference, Washington, USA, 2003.
7. L.Yegorova, K.Liotov, V.Smirnov, "Major findings of E110 studies under LOCA conditions", SEGFSM Topical Meeting on LOCA issues, ANL, USA, 2004.
8. P.V. Fedotov, O.A. Nechaeva, V.V. Novikov, at el. "Studies of WWER fuel rods behavior under LOCA condition. Current status.", Ad-hoc LOCA meeting, Paris, 27 – 28 June 2006.
9. M.C. Billone at el. "Post-quench ductility of Zircaloy, E110, ZIRLO and M5", SEGFSM Topical Meeting on LOCA issues, ANL, USA, 2004.

DETERMINISTIC BWR CORE DESIGN

R. HÖGLUND

*VTT Technical Research Centre of Finland
P.O.Box 1000, FI-02044 VTT, Finland*

M. SOLALA

*Teollisuuden Voima Oy
FI-27160 OLKILUOTO, Finland*

ABSTRACT

Deterministic core design means that it should be possible to find a useful new loading pattern for a reactor directly as an “initial guess” with a minimum of computational effort. In short, the iterative optimisation of the core is replaced by an optimisation of the rules upon which the core design is based. Such rules, utilized in computer codes developed at VTT and based upon ICFM work on TVO’s boiling water reactors in Olkiluoto, are described in this study.

1. Introduction

Nuclear reactor core design has always involved analysing many different alternatives in a process largely based upon trial-and-error. In recent years, the need for manual work has decreased, as optimisation programs that in many situations are capable of delivering useful solutions have become available. Such a program does not, however, start from scratch – it needs more or less detailed instructions about the desired structure of the core. If the instructions are too detailed and too unrealistic, then sometimes no satisfactory solution at all will be possible. If they on the other hand are “suitable”, a good solution can be achieved very fast, or even immediately. This is what is here called deterministic core design, where optimisation of the core is in a way replaced by optimisation of the rules upon which the core design is based. Fast results are very valuable when many different fuel bundle designs or different strategies for the use of these fuels in the reactor are to be compared, especially if long-term use of the fuels is analysed by simulating many consecutive cycles of operation.

2. Deterministic design rules

The deterministic core design rules are to some extent quite general, but some details are inevitably reactor and fuel dependent. The current study is made for the Olkiluoto boiling water reactors using certain kinds of fuels, but similar results could be obtained for other reactors and fuels, although various adjustments would be necessary. The configuration of fuel bundles in the core is determined by three simultaneously utilised, overlapping systems of core maps:

- 1 A ranking number map, where the position of a certain fuel bundle depends on its reactivity (multiplication factor) – a suitable map is picked from a set covering different degrees of in-out or out-in loadings, where for instance the size of the fresh fuel batch is important for the choice.
- 2 A fuel bundle generation map, where the contents of a certain control cell (2x2 bundle “supercell”), i.e. the numbers of fresh, once-burnt, and older bundles in the cell, will depend on its location in the core.
- 3 A map defining different regions in the core within which balancing of the supercells is performed in order to make them more equal on an average, together with a map defining different regions in the core within which low reactivity at a certain axial level or for the

bundle as a whole is supposed to be desirable in order to obtain better thermal and shutdown margins.

It was found that this system in several cases can produce core designs that as such already satisfy the requirements and in many other cases are quite close to acceptable solutions although some further adjustments are necessary, made either manually or with the aid of an optimisation program.

2.1 Core position ranking

A map that gives a ranking number for every fuel bundle position in the core can be taken as the basis of the core design. The fuel bundles are then placed according to these numbers so that the lower the ranking number of a position, the lower should the multiplication factor be of the bundle placed there.

All core maps here are shown in half core form, as a 180-degree rotational symmetry has been assumed in the calculations made in this study for the 500-bundle Olkiluoto-1 and -2 reactors.

In order to reduce radial leakage of neutrons and achieve better fuel economy, low-reactivity fuel should be placed in a peripheral region where the ranking number increases going inwards. In the central region, on the other hand, the number increases going outwards, to avoid too bad power peaking in the middle. Where the border between the areas of out-in and in-out loadings is to be drawn depends on the reactor, the loading strategy, and especially the number of fresh and once-burnt bundles and how they are placed. The 60/40-% division of Fig 1 is rather suitable; sometimes 70/30 or 50/50 can work better. For reasons related to thermal or shutdown margins it is often necessary to give certain smaller regions a ranking number that differs from the one shown in the general map (in practice a lower number).

		1	2	3	4	5	6	7	8	9	10	11	12	13
1		3	2	1										
2		10	9	8	6									
3		18	17	15	13	11	7	4						
4		54	55	21	19	18	14	10	5					
5		48	49	51	52	55	19	16	12	6				
6		43	44	46	47	50	53	20	17	12	5			
7		38	39	40	42	46	48	52	20	16	10	4		
8		34	35	36	38	41	45	48	53	19	14	7		
9		30	31	33	35	37	41	46	50	55	18	11		
10		27	28	29	32	35	38	42	47	52	19	13	6	
11		25	26	27	29	33	36	40	46	51	21	15	8	1
12		23	24	26	28	31	35	39	44	49	55	17	9	2
13		22	23	25	27	30	34	38	43	48	54	18	10	3
14		22	23	25	27	30	34	38	43	48	54	18	10	3
15		23	24	26	28	31	35	39	44	49	55	17	9	2
16		25	26	27	29	33	36	40	46	51	21	15	8	1
17		27	28	29	32	35	38	42	47	52	19	13	6	
18		30	31	33	35	37	41	46	50	55	18	11		
19		34	35	36	38	41	45	48	53	19	14	7		
20		38	39	40	42	46	48	52	20	16	10	4		
21		43	44	46	47	50	53	20	17	12	5			
22		48	49	51	52	55	19	16	12	6				
23		54	55	21	19	18	14	10	5					
24		18	17	15	13	11	7	4						
25		10	9	8	6									
26		3	2	1										

Fig 1. Core position ranking map: 60 % out-in, 40 % in-out loading.

2.2 Definition of supercell categories

When burnable absorbers are used, however, a choice of position cannot be based solely on the fuel's multiplication factor, as this can be rather low for a fresh bundle compared to a once-burnt one. This problem can be solved by the use of another core map which defines the distribution of bundle generations, i.e. whether an individual position is to be used for fresh, once-burnt, or older fuel. The ranking numbers are then only used to determine the order of the bundles within each one of the different bundle categories (generations). Even this method is not always successful, though, when once-burnt bundles are considered. If they still contain enough burnable absorber, the multiplication factor of a less-burnt bundle can be lower at the beginning of a new cycle of operation than the corresponding value of a bundle with higher burnup, which is in reality less valuable.

In such cases, it may become necessary to define allowable burnup intervals for certain positions or core regions in addition to the ranking and fuel generation maps. A need for defining burnup intervals can also arise, if a maximum burnup limit exists. In order to avoid exceeding the limit, the bundles with the highest burnups must then sometimes be placed in the most peripheral locations, even if their reactivity for some reason should be higher than values of some other bundles.

It is convenient to systematize the choice of positions for bundles of different generations by dividing the core in 2x2-bundle supercells (equal to the control cells, i.e. the four positions surrounding a control rod) and group these together for geometrical reasons, i.e. how they are situated in the core in relation to the centre and the periphery. In Fig 2 there are 21 such groups, denoted A - U, each containing 4 or 8 supercells (if the whole core is considered), except for the single supercell in the centre. The coloured (shaded) cells are those chosen for control rods to be used during the cycle, either as ordinary reactivity-control rods (darker) or shallow power-shaping rods (lighter).

	1	2	3	4	5	6	7	8	9	10	11	12	13
1	T	U											
2													
3	N	P	Q	S									
4													
5	J	K	M	O	R								
6													
7	G	H	I	L	O	S							
8													
9	D	E	F	I	M	Q							
10													
11	B	C	E	H	K	P	U						
12													
13	A	B	D	G	J	N	T						
14													
15	B	C	E	H	K	P	U						
16													
17	D	E	F	I	M	Q							
18													
19	G	H	I	L	O	S							
20													
21	J	K	M	O	R								
22													
23	N	P	Q	S									
24													
25	T	U											
26													

Fig 2. Supercell categories.

It is decided in advance what mix of fresh, once-burnt, and older fuel should be used in a supercell belonging to a certain group. This mix is not necessarily always identical for all supercells in the same group, if the total numbers of fresh, once-burnt, and older bundles make such equal shares impossible.

2.3 Taking advantage of radial levelling and axial distributions

Even though bundle generation and ranking number maps usually produce rather similar supercells if they belong to the same group, it is useful to have some means for radial levelling over selected core regions. Eight such regions are defined in Fig 3. In order to avoid unnecessary power peaks accompanied by problems with thermal or shutdown margins, a computer code makes some shuffling of the bundles in the region. Regardless of the original ranking map, the shuffling ensures that the average multiplication factors of all supercells within the same region will be as equal as possible, provided they contain the same mix of fresh, once-burnt, and older fuel bundles. How individual bundles or supercells are selected for different regions mainly depends on how they are situated in relation to the core's periphery, centre, and the control rods that are in use.

		1	2	3	4	5	6	7	8	9	10	11	12	13
1		1	1	1										
2		1	1	1	1									
3		7	7	7	1	1	1	1						
4		7	7	7	8	1	1	1	1					
5		2	5	5	3	3	7	7	1	1				
6		2	5	5	3	3	7	7	8	1	1			
7		4	6	6	5	5	6	6	7	7	1	1		
8		4	6	6	5	5	6	6	7	7	1	1		
9		2	4	4	2	2	5	5	3	3	1	1		
10		2	4	4	2	2	5	5	3	3	8	1	1	
11		4	6	6	4	4	6	6	5	5	7	7	1	1
12		4	6	6	4	4	6	6	5	5	7	7	1	1
13		2	4	4	2	2	4	4	2	2	7	7	1	1
14		2	4	4	2	2	4	4	2	2	7	7	1	1
15		4	6	6	4	4	6	6	5	5	7	7	1	1
16		4	6	6	4	4	6	6	5	5	7	7	1	1
17		2	4	4	2	2	5	5	3	3	8	1	1	
18		2	4	4	2	2	5	5	3	3	1	1		
19		4	6	6	5	5	6	6	7	7	1	1		
20		4	6	6	5	5	6	6	7	7	1	1		
21		2	5	5	3	3	7	7	8	1	1			
22		2	5	5	3	3	7	7	1	1				
23		7	7	7	8	1	1	1	1					
24		7	7	7	1	1	1	1						
25		1	1	1	1									
26		1	1	1										

Fig 3. Regions for smoothening of reactivity distribution.

So far, in the considerations above, fuel bundles have been treated as "single numbers" describing ranking order and generation. However, in a successful deterministic core design the differences in axial distributions of burnup and multiplication factor between the different bundles has to be taken into account from the very beginning. Experience will show that certain areas in the core are susceptible to problems with thermal or shutdown margins. Moreover, such problems are often linked to high reactivity at certain axial levels. Choosing fuel bundles with as low multiplication factor as possible at the level in question will often reduce the troubles considerably.

In the example illustrated by Fig 4, the total number of axial nodes in the core is 25. In the region where node 4 is pointed out, high linear heat generation rates are expected near the beginning of the cycle, whereas node 19 indicates such problems in some control cells near the end of the cycle. In the node 16 area again, low shutdown margins are suspected. The number -1 near the periphery and in most control cells (where control rods are to be inserted for a large part of the cycle) stands for regions with no special requirements concerning axial distributions, only low reactivity for the bundle as a whole, and 0 for bundles without any specific rules in this respect.

	1	2	3	4	5	6	7	8	9	10	11	12	13
1	-1	-1	-1										
2	-1	-1	-1	-1									
3	16	16	16	-1	-1	-1	-1						
4	16	16	16	-1	-1	-1	-1	-1					
5	-1	0	0	16	16	-1	-1	-1	-1				
6	-1	0	0	16	16	4	4	-1	-1	-1			
7	0	0	0	0	0	4	4	4	-1	-1	-1		
8	0	0	0	0	0	4	4	4	-1	-1	-1		
9	-1	0	0	19	19	0	0	16	16	-1	-1		
10	-1	0	0	19	19	0	0	16	16	-1	-1	-1	
11	0	0	0	0	0	0	0	0	16	16	-1	-1	
12	0	0	0	0	0	0	0	0	16	16	-1	-1	
13	-1	0	0	-1	-1	0	0	-1	-1	16	16	-1	-1
14	-1	0	0	-1	-1	0	0	-1	-1	16	16	-1	-1
15	0	0	0	0	0	0	0	0	0	16	16	-1	-1
16	0	0	0	0	0	0	0	0	0	16	16	-1	-1
17	-1	0	0	19	19	0	0	16	16	-1	-1	-1	
18	-1	0	0	19	19	0	0	16	16	-1	-1		
19	0	0	0	0	0	4	4	4	-1	-1	-1		
20	0	0	0	0	0	4	4	4	-1	-1	-1		
21	-1	0	0	16	16	4	4	-1	-1	-1			
22	-1	0	0	16	16	-1	-1	-1	-1				
23	16	16	16	-1	-1	-1	-1	-1					
24	16	16	16	-1	-1	-1	-1						
25	-1	-1	-1	-1									
26	-1	-1	-1										

Fig 4. Definition of the axial nodal level most important for the thermal/shutdown margin optimisation. -1 refers to bundle average only, 0 stands for “no special requirements”.

The implementation of these two last maps in the process can sometimes be somewhat counterproductive, if making the supercells more even leads to an axially more unfavourable burnup distribution or vice versa, if optimisation of axial distributions causes larger variations between the supercells. In such cases, a compromise has to be found between these two objectives.

3 Conclusion

Deterministic core design stands for creation of loading patterns using "intelligent rules". In this way, much, albeit usually not all, of the iterative fuel bundle shuffling, which traditionally is the main part of the BWR core design work, can be avoided. The aforementioned procedure for deterministic core design is carried out by the code combination CORFU (COre ReFUelling) + SMART (Smoothen Modules, Axial Reactivity Treatment), developed at VTT based upon experience from ICFM work on TVO's boiling water reactors in Olkiluoto.

LONG TIME STORAGE OF FAILED FUEL RODS

Andreas Fristedt-Åblad, Jan Möller, Per Collin
Westinghouse Electric Sweden AB

Introduction

The Westinghouse LFR QUIVER-container is designed for long time dry storage of leaking fuel rods, fuel rod remnants and fuel rod fragments. It can be stored after vacuum drying and permanently sealing. The design also allows transportation of the quiver and it is fully compatible with a regular fuel assembly. The PWR LFR QUIVER is designed to be compatible with regular 16x16 and 15x15 PWR assemblies and the type B BWR LFR QUIVER^{1,2} is being designed for compatibility with regular 10x10 BWR assemblies. All handling in the spent fuel pool, during transportation, storage or reprocessing is also identical to regular fuel assembly handling. After being properly sealed, the quiver will be tight for more than 40 years.

Design and design requirements

The quiver is designed, manufactured and qualified according to KTA (3602, 3902, 3903 and 3905), European Standards, ANS/ASW 57.1 and NRC 10CFR 50 Appendix B standards.

The quiver is made of stainless steel and the quiver handling tools are made of stainless steel and aluminum. Seals are made of non-organic material and are guaranteed to last a minimum of 40 years in dry storage.

The quiver is leak proof from an absolute pressure of 5 mbar to an absolute pressure of 4 bar. The quiver's tightness is tested by pressurizing the quiver with helium from an absolute pressure of 0.5 mbar to an absolute pressure of 4 bar and generating vacuum on the outside of the sealings.

The quiver can reach a maximum of 60°C (140°F) in the spent fuel pool where it is surrounded by de-ionized and borated water. When contained in the Castor-container, the centre of the quiver can reach temperatures of approximately 360°C (680°F). However, since the seals are placed in the quiver's dry storage lid at the top of the quiver and not at the quiver's centre, the quiver seals will never be exposed to temperatures higher than 220°C (428°F) in the Castor-container. These temperatures can be reduced by placing the quiver in the outer region of the quiver. The quiver itself can resist a fire test with a 60°C (140°F) increase in temperature.

¹ LFR QUIVER-Container will in this compact be referred to as quiver. PWR or PWR-quiver and BWR or BWR-quiver will be used where the difference must be pointed out.

² Type A BWR-quivers are compatible with regular 8x8 fuel assemblies

The quiver is also dimensioned to withstand greater accelerations than required. It can be dropped onto a concrete floor from heights greater than 30 cm without leaking and it can survive a greater than 9 m fall, contained in a Castor-container, onto a concrete floor without rupturing. Computer simulations of 110 G, corresponding to these demands, show small plasticization zones in the edges of the quiver lid.

General description of the system

The system consists of two head lids and one quiver housing. One of the head lids is used for long time dry storage and the other one for handling in the spent fuel pool (see figure A for a principle sketch).

Manual handling tools are needed for handling the quiver in the spent fuel pool and for the evacuation and vacuum drying procedures.

Head lid for dry storage

The head lid has two connection valves. One of the connection valves is a compressed air inlet and the other one is a water and air outlet. They are used for draining and drying the quiver.

Head lid for fuel pool handling

The head lid for fuel pool handling has pressure-discharging holes provided with a filter mesh.

Quiver housing

The tubes for inserting the damaged fuel rods have different dimensions for fitting variously damaged fuel rods.

The PWR housing has one evacuation tube $\phi 20/18$, 4 tubes $\phi 20/18$ for severely damaged fuel rods and 80 tubes $\phi 16/14$ for slightly damaged fuel rods.

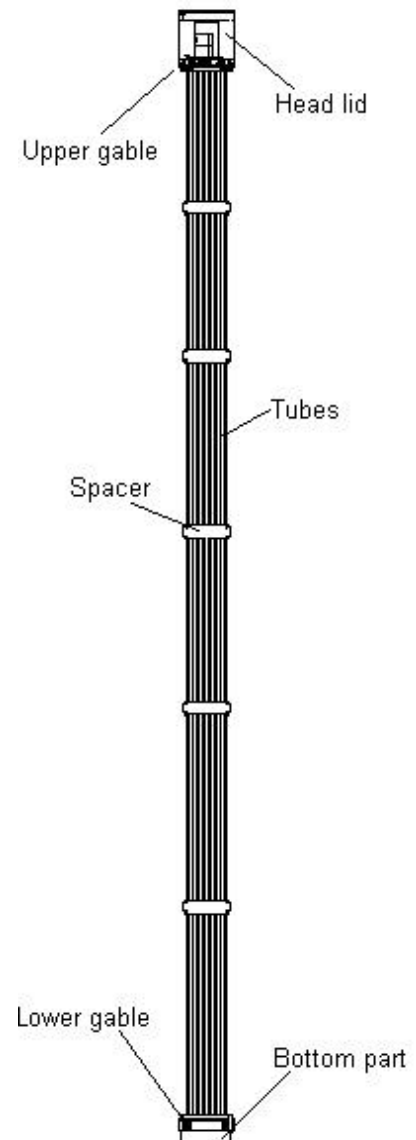


Figure A: A principle sketch of a quiver for damaged fuel rods

The BWR housing has one evacuation tube $\phi 16/14$, 12 tubes $\phi 18/16$ for severely damaged fuel rods and tie fuel rods or spacer capture rods and 27 tubes $\phi 16/14$ for slightly damaged fuel rods.

The quiver housing also consists of two gables, which are welded to the tube ends and a number of spacers welded to the tubes.

The bottom support is welded to the lower gable and has a funnel-shaped accommodation and a base frame. Inside the bottom support, is a funnel-shaped strainer screen with a filter mesh to prevent fissile material and fragments from reaching the evacuation system.

Tools for handling the quiver

All handling tools are designed for handling the quiver when it is positioned in the turnover basket in the upper working position (PWR), or in the so called “Brennelementhandhabungseinrichtung” (BEH), in the upper position (BWR).

Handling

During filling, the PWR-quiver is positioned in its side position in the lower working position. For the permanent sealing, draining and drying procedures, the quiver is positioned in the turnover basket in the upper working position.

For BWR filling, the Quiver is placed in the BEH, together with the fuel assembly and other equipment necessary for fuel rod handling. For the permanent sealing, draining and drying procedures, the BEH with the quiver is placed in the upper position.

Evacuation and drying

The evacuation of water and the vacuum drying procedures must be performed in direct succession.

The evacuation system has to be equipped with a water separator and a filter and it connects to the plants standard vacuum system. Two different principles can be used to drain the water. Either by using compressed air from an air supply (approx. 2-3 bar) or by using a vacuum pump.

After the water is removed, a vacuum pump is used to remove all air inside the quiver and, as absolute pressure drops towards 20 mbar, have all remaining moisture evaporate. Depending on the type of equipment used, this procedure takes between 30 minutes and a week.

Quiver deliveries and licenses

Quivers have been delivered to sites world wide since 1979. Open quivers have been delivered to Ringhals 1, Oskarshamn 1 and 2, Barsebäck 1 and 2 (1979); Forsmark 3, Oskarshamn 3, TVO 1 and 2 (1984); Forsmark 1 and 2, TVO 1 and 2, Ringhals 1 (1987); Barsebäck 1 (1989); Leibstadt (1992); Oskarshamn 2 (1994); Oskarshamn 1 and 3, Forsmark 3 (2000); Hope Creek (2002).

Quivers for dry transport to reprocessing plant have been delivered to Grohnde (1998); Gösgen (1999); Krümmel (2004).

Leibstadt has received quivers for long time dry storage in Switzerland (2001) and there are quivers in order going to Brokdorf, Unterweser, Grohnde and Krümmel for long time dry storage in Germany.

Cogema has approved the quiver design regarding quiver material, handling and dry fragmentation at the Hague; TÜV Nord regarding quiver material and handling at a German nuclear power plant (NPP); NTL Regarding quiver integrity during transportation from an NPP to a reprocessing plant or storage facility; Transnucleaire regarding criticality safety during handling at the NPP, transportation and handling at the reprocessing plant. GNS are in the process of approving the quiver design regarding quiver transportation and long time dry storage. BNFL has almost completed an approval of the quiver design regarding transportation.

Summary

The Westinghouse LFR QUIVER-Containers are designed according to current standards for long time storage. The quivers have the same outside measurements as regular fuel assemblies and can therefore be handled likewise. PWR-quivers are compatible with regular PWR fuel assemblies and BWR-quivers are compatible with regular BWR fuel assemblies. When sealed correctly, the LFR QUIVER-Containers will be tight for more than 40 years.

Contact information

Westinghouse Electric Sweden AB, Finnslätten
721 63 Västerås
Sweden

Commercial: Andreas Fristedt-Åblad
 andreas.fristedt-ablad@se.westinghouse.com
 Tel. +46-21-34 74 89

Technical: Jan-Olov Nygren
 jan-olov.nygren@se.westinghouse.com
 Tel. +46-21-34 72 73

EXPERIMENTAL DATABASE OF E110 CLADDING OXIDISED IN HYDROGEN RICH STEAM

E. PEREZ-FERÓ, P. WINDBERG, Z. HÓZER, M. HORVÁTH, I. NAGY,
A. PINTÉR-CSORDÁS, E. SZABÓ, K. KULACSY
*Hungarian Academy of Sciences KFKI Atomic Energy Research Institute
H-1525 Budapest P.O.B. 49, Hungary*

CS. GYŐRI
*European Commission, Joint Research Centre, Institute for Transuranium Elements
P.O.B. 2340, D-76125 Karlsruhe, Germany*

ABSTRACT

The oxidation and the H-uptake play crucial role in the embrittlement of the zirconium cladding. In 2004 a new experimental programme (COHYRA) started at the AEKI in order to map the combined effects of steam and H-contents on the mechanical properties of VVER fuel cladding. The experimental data have been compiled in an electronic database for E110 (Zr1%Nb) alloy. The contents of the database along with the conditions, the results and some conclusions of the involved oxidation, hydriding and mechanical tests are summarised in the paper.

1. Introduction

Due to the Zr-steam reaction, hydrogen-rich steam atmosphere may evolve in accident conditions. An increased hydrogen absorption of Zr-based claddings in this atmosphere may cause significant embrittlement of the material and failure of the fuel rod under thermal and/or mechanical loads. Several series of separate effect tests have been performed at the AEKI to study the high temperature oxidation and the mechanical properties of these alloys [1]. In the recent COHYRA (Cladding Oxidation in HYdrogen Rich steam Atmosphere) project experimental data on hydrogen uptake of E110 type cladding are evaluated in order to map the combined effects of steam and H-contents on the mechanical properties. It is intended to account for the hydrogen uptake by the Zr cladding material under accident conditions.

The performed experiments covered

- oxidation phenomena in hydrogen rich steam atmosphere,
- mechanical investigation of oxidized and hydrided samples in ring compression, tensile and burst tests and
- determination of hydrogen content in the samples.

The experimental data, the results of post-test investigations, figures, information concerning the test conditions and the corresponding English-language publications have been compiled in an electronic database. The new tests involved in the database were grouped as follows:

Oxidation tests complemented by determination of hydrogen content

- Double-side oxidation of Zr1%Nb rings with 8 mm length in hydrogen-steam mixture at 900 - 1100 °C (pre-oxidation for ring compression tests)
- Double-side oxidation of Zr1%Nb rings with 2 mm length in hydrogen-steam mixture at 900 - 1100 °C (pre-oxidation for ring tensile tests)
- One-side oxidation of Zr1%Nb tubes with 100 mm length in hydrogen-steam mixture at 900 - 1100 °C (pre-oxidation for ballooning tests)

Ring compression tests

- Tests with pre-oxidized Zr1%Nb rings specimens (length: 8 mm) to study ductile-brittle transition

Ring tensile tests

- Tests with pre-oxidized Zr1%Nb rings specimens (length: 2 mm)

Ballooning experiments

- Isothermal burst tests with as-received and pre-oxidized Zr1%Nb tube specimens (length: 100 mm)

Post-test investigations

- Visual observations
- Metallographic analysis
- SEM analysis

The compiled experimental data facilitate the development of new models for the simulation of E110 cladding performance under accident conditions paying special attention to the role of hydrogen uptake. This paper gives an overview of the experiments involved in the database, the test facilities and conditions. It presents the most important results and consequences.

2. Oxidation experiments

The experiments were performed in order to provide pre-oxidized samples for mechanical tests and to study the effect of the presence of hydrogen in steam atmosphere on the oxidation kinetics. Un-irradiated, original VVER cladding specimens (outer diameter: 9,14 mm) were oxidized in a controlled, mixed steam-hydrogen atmosphere under isothermal conditions between 900 and 1100 °C. The hydrogen content in the steam was fixed between 0 and 36 vol.%. After steam exposure for different time periods the samples were characterized by their oxygen content measured through the weight gain of the specimens. Prior to testing, the specimens were degreased in acetone.

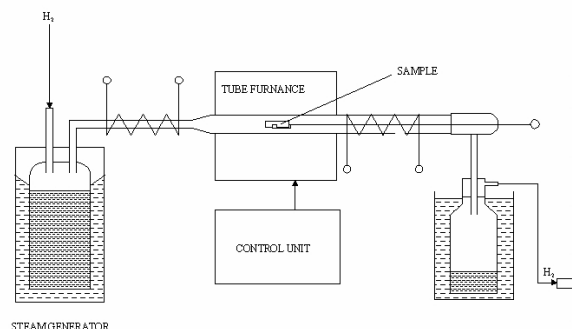


Fig 1. Scheme of the experimental set-up for oxidation tests

A high temperature tube furnace was used for the oxidation of the samples (Figure 1.). The experimental set-up consisted of a steam generator, a three-zone furnace and a condensing system. The outlet hydrogen flow rate was measured by calibrated Soap Bubble Gas Flow Meter, the steam flow was evaluated through the measured weight of the condensed water. When the temperature of the furnace and the steam + hydrogen flow became stabilized, the sample in a quartz boat was pushed to the centre of the furnace. At the end of oxidation the sample was withdrawn to the cold part of the quartz tube.

After a high temperature desorption (hot extraction) the amount of absorbed hydrogen was determined by gas chromatographic method using CHROMPACK MODEL 438A Gas Chromatograph with thermal conductivity detector (TCD). The experiments confirmed that the mass gain due to the hydrogen-rich steam oxidation is linearly proportional to the square root of the exposure time. The oxidation rates constants measured in pure steam and in different steam-H₂ mixture are represented in Figure 2.

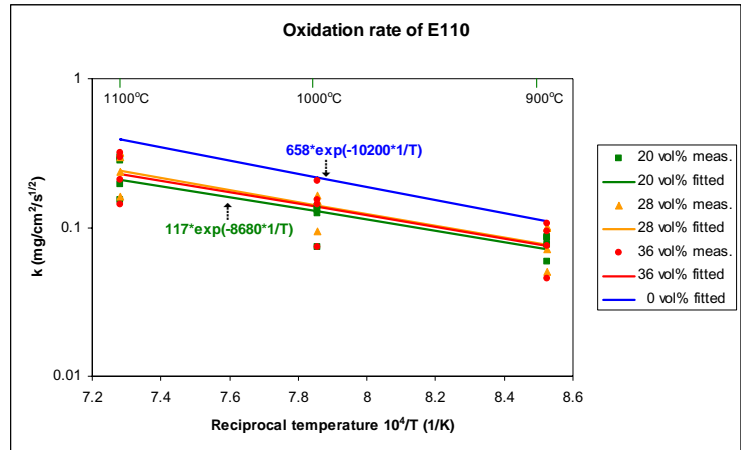


Fig 2. Oxidation rate constants for E110 as a function of reciprocal temperature in steam-hydrogen mixture

The oxidation mass gain rates measured in 20, 28 and 36 vol. % H₂-steam mixture have no significant difference. However, comparing the oxidation rate constants measured in pure steam and in hydrogen-rich steam atmosphere, it can be concluded that the hydrogen content in the steam decelerates the cladding oxidation [2]. Comparing the hydrogen contents of the cladding specimens oxidized to similar extents in pure steam and in steam-hydrogen mixture, increased hydrogen absorption was also observed in hydrogen rich steam atmosphere.

3. Ring compression tests

Investigation of the ductile-brittle transition of the cladding was the primary objective of the ring compression tests. The oxidized ring samples with 8 mm length were examined in radial compression tests at room temperature using INSTRON 1195 universal testing machine. The velocity of the crosshead moving was 0,5 mm/min. The rings were loaded until the total plastic deformation or at least until the first indication of cracking. The load-displacement curves were recorded and the crushing force and deformation were determined. The cladding ductility was characterized with the specific energy at failure (i.e. the integral of the load-displacement curve for the unit length of the ring specimen). Representing the specific energy as a function of the hydrogen content of the specimens (Figure 3) it becomes obvious that the hydrogen uptake strongly reduced the ductility of the cladding.

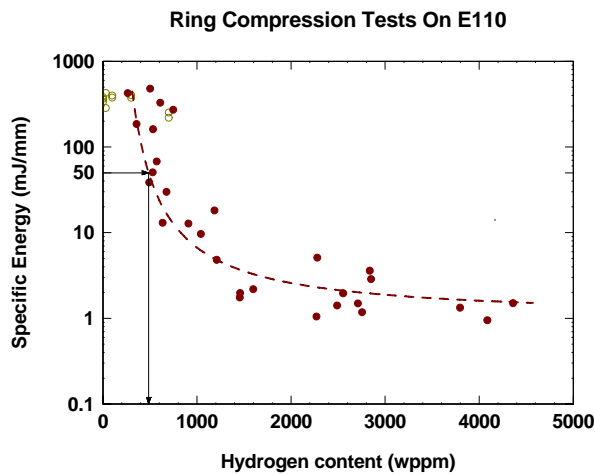


Fig 3. Specific energy at failure as a function of hydrogen content of the samples

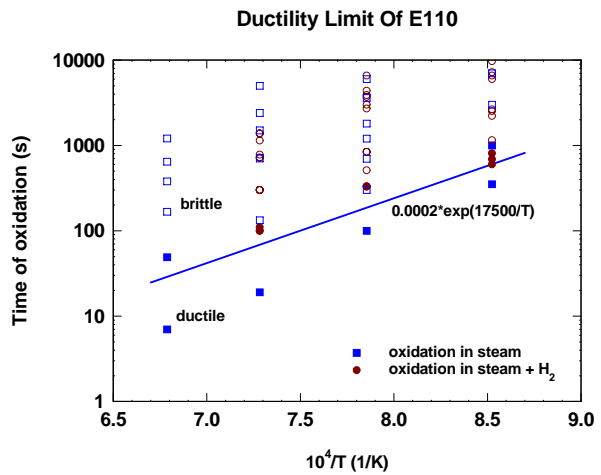


Fig 4. Time of oxidation versus the reciprocal of the oxidation temperature

According to our earlier studies with E110 rings oxidized in pure steam [3, 4], 50 mJ/mm specific energy was found as the lower bound of ductility (i.e. specific energy below 50 mJ/mm indicates brittle cladding). In view of this limit, the VVER cladding above ~500 ppm hydrogen content becomes

brittle (Figure 3.). Representing the time of oxidation as a function of the temperature and distinguishing brittle and ductile specimens on the basis of the specific energy of ring compression, a ductility limit (τ - oxidation time till cladding embrittlement) could be defined (Figure 4):

$$\tau_{E110} = 2 \cdot 10^{-4} \exp(17500/T) \quad (1)$$

According to the results of the ring compression tests, the above correlation for the ductility limit of E110 is valid in steam as well as in H₂-steam mixture. It means that the cladding embrittlement does not occur earlier in hydrogen-rich atmosphere than in pure steam, since the slow down of the oxidation compensates the mechanical deterioration of the cladding due to more intense hydrogen uptake.

4. Ring tensile tests

The main objective of the tensile tests was to investigate the effect of hydrogen rich steam oxidation and the effect of the hydrogen content on the strength of the E110 alloy. The tensile tests of cladding rings with 2 mm length were carried out at room temperature using INSTRON 1195 universal testing machine. The extent of the equivalent oxidation (ECR) was lower than 6 % in the performed experiments. Figures 5 and 6 illustrate the load-displacement curve of ductile and brittle samples and the tensile strength as a function of the oxidation rate and the hydrogen content, respectively. The effect of oxidation is consistent with the results of earlier tensile and burst tests, i.e. at low oxygen concentration (ECR \approx 2 %) the cladding strength increases, but considerably decreases with further oxidation. On the other hand, the mechanical deterioration due to the hydrogen uptake of the cladding has been observed only above 600 ppm hydrogen content.

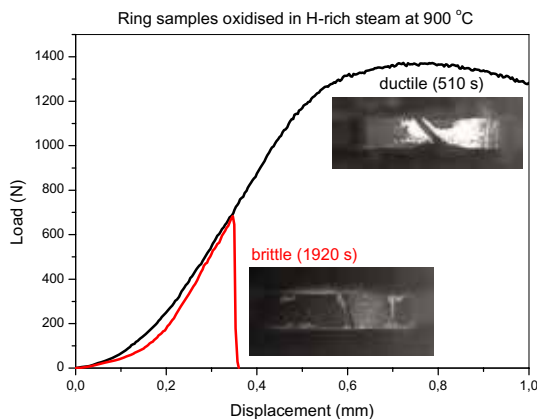


Fig 5. Load-displacement curves for ductile and brittle samples

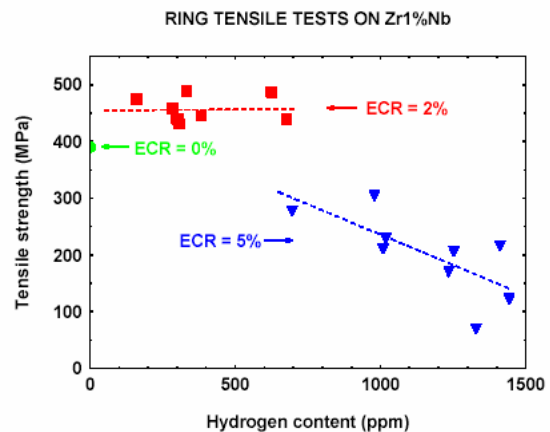


Fig 6. Tensile strength of E110 as a function of relative oxidation and hydrogen content

5. Ballooning tests

The ballooning experiments aimed to provide information about the effect of hydrogen rich steam oxidation and the effect of the hydrogen content on the cladding strength and deformation under simulated LOCA conditions. The specimens were 100 mm long pieces of the original VVER claddings. The samples were closed with end-plugs. The pressurization was performed through a pipe attached to one end of the specimen. The tests with oxidized and as-received specimens were carried out under isothermal conditions in argon atmosphere. The inner pressure of the test tube was increased linearly until the burst of the sample. The pressure history was monitored on-line.

On the basis of the measured data the conclusions are the followings:

- The burst pressure of the pre-oxidized samples was higher than that of the as-received specimen.
- At low oxidation ratio (ECR=0.5-1.5%) the strength of the cladding increased and the cladding deformation decreased.

- The effect of hydrogen uptake is not obvious. The measurements of the hydrogen contents of the specimens carried out after the burst tests have indicated that most of the hydrogen absorbed in the pre-oxidised specimens was released during the high temperature burst tests. To correct this problem a set of burst test were performed in hydrogen atmosphere, as well. These latter experiments clearly indicate the decrease of the circumferential deformation due to hydrogen absorption but the spread of the measured burst pressures does not allow to draw further conclusions concerning the strength of the hydrided cladding.

6. Summary

New experimental programme (COHYRA) has been carried out to investigate the effect of hydrogen rich steam oxidation and hydrogen uptake on the mechanical behaviour of the Zr1%Nb cladding.

The experimental programme covers oxidation tests, ring compression tests, tensile tests and ballooning experiments. These tests were complemented by post-test investigations like visual observations, metallographic analysis, SEM analysis and hot extraction of hydrogen.

More than 60 oxidation tests were performed to provide pre-oxidized samples for mechanical tests. The results of the oxidation tests demonstrate that the cladding oxidation decelerates in hydrogen-rich steam atmosphere. On the basis of the mass gain data measured in steam-H₂ mixture with 20 vol. % hydrogen a new correlation was derived for the oxidation rate constants versus temperature.

The ductile-brittle transition of E110 was expressed as a function of temperature and time considering the results of ring compression tests with pre-oxidised specimens. The experimental data demonstrate that the hydrogen content of the steam atmosphere does not influence the ductility limit of the E110 cladding.

The ballooning experiments can give new information on the ballooning behaviour and burst type failure of pre-oxidised and hydrided Zr1%Nb cladding.

Several photographs, cross sections and secondary electron images were made and collected.

These new set of experimental data on Zr1%Nb cladding have been compiled in commented ascii files in order to extend the electronic database of the former EXTRA project [5] for model development and code validation.

7. References

- [1] Z. Hózer, L. Matus, M. Horváth, L. Vasáros, Á. Griger, L. Maróti: Ring Compression Tests with Oxidised and Hydrided Zr1%Nb and Zircaloy-4 Claddings. KFKI-2002-01/G Report.
- [2] Cs. Gyóri, Z. Hózer, E. Perez-Feró, Paul Van Uffelen, Arndt Schubert and Jacques van de Laar: Applying the TRANSURANUS Code to VVER Fuel Under Accident Conditions. SMiRT 18, Beijing, China, August 7-12, 2005.
- [3] Z. Hózer, Cs. Gyóri: Derivation of LOCA Ductility Limit from AEKI Ring Compression Tests, SEGFSM Topical Meeting on LOCA Issues, ANL, May 2004.
- [4] Cs. Gyóri, P. Van Uffelen, A. Schubert and J. van de Laar, Z. Hózer: Implementing Experimental Data on the Accidental Behaviour of the WWER Cladding Obtained at the AEKI in the TRANSURANUS Fuel Performance Code, 6th Int. Conf. on WWER Fuel Performance, Modelling and Experimental Support, Albena, September 2005.
- [5] Cs. Gyóri, Z. Hózer, K. Lassmann, A. Schubert, J. van de Laar, M. Cvan, B. Hatala: Extension of the TRANSURANUS Code Applicability with Niobium Containing Cladding Models (EXTRA); FISA 2003: Symposium on EU Research in Reactor Safety, Luxembourg, 10-13 November 2003. Proceedings p. 589-594.

FAILURE BEHAVIOR OF ZIRCONIUM CLADDING AFTER THE LOSS OF THE COOLANT ACCIDENT (LOCA)

J. H. KIM, M. H. LEE, B. K. CHOI, Y. H. JEONG

*Advanced Core Materials Laboratory, Korea Atomic Energy Research Institute,
P.O.Box 105, Yuseong, Daejeon, 305-600 - Republic of Korea*

ABSTRACT

The objectives in this study are to analyze the failure behavior of the fuel cladding quantitatively and to construct a failure map of the fuel cladding under a LOCA situation. Zircaloy-4 claddings were oxidized in a steam environment from 900 to 1250°C followed by an injection of cool water. Mechanical tests were carried out to determine the failure behavior of the oxidized cladding. The results showed that the minimum ECR (Equivalent Cladding Reacted) above which cladding fails during thermal shock was 20% regardless of test temperature. However, the threshold ECR to withstand a ductile bending decreased as the test temperature increased. Microstructural analysis revealed that boundary of ductile failure fitted well when the absorbed oxygen content inside the prior-beta layer was below 0.5wt%.

1. Introduction

Loss of coolant accident (abbreviated as LOCA) is treated as one of the most important design-basis accidents at the fuel systems in light water reactor (LWR). When a LOCA occurs, the temperature of the fuel system rises so that the cladding undergoes an oxidation caused by the reaction of the mixture of water and steam. After a certain time interval, the emergency core cooling system activates, and water is injected to cool down the hot core, which is inevitably accompanied by a thermal shrinkage of the cladding. When the embrittled cladding cannot stand the stress involved, the cladding fragments, which results in a release of the radioactive fission product. To maintain the fuel integrity under postulated LOCA conditions, the Nuclear Regulatory Commission (NRC) established the fuel safety criteria related to a LOCA, where the peak fuel temperature and the total oxidation cannot exceed 1204°C and a 17% level respectively [1]. However, such criteria have been founded by applying a safety margin based on the Hobson's ring compression test [2], and it is reported that there exist differences between the existing safety criteria and the behavior of a actual cladding [3, 4].

The objectives in this study are to quantitatively analyze the failure behavior of the fuel cladding and to construct a failure map of the fuel cladding under a simulated LOCA situation. First, cladding was oxidized at various temperatures and times followed by an injection of cool water. Second, mechanical tests, such as the ring compression test and the 3-point bend test were carried out at the oxidized cladding to analyze the failure behavior. Finally, mechanical test result after LOCA test was incorporated into the conventional failure map and the revised failure diagram of the fuel cladding was evaluated to quantitatively determine the failure behavior of the oxidized cladding.

2. Experimental

2.1 Simulated LOCA test

Fig. 1(a) shows an illustration of a facility used for simulated LOCA test. A 200mm-long Zircaloy-4 cladding tube, which respectively has 9.5mm outer diameter and 0.57mm of thickness, was used in this study. Detailed description on the facility and test procedure are shown elsewhere [5].

2.2 Mechanical tests

After the thermal shock test, ring compression test and 3-point bend test were performed to evaluate the oxidized cladding ductility. Fig. 2 shows a schematic illustration of the mechanical tests. In the ring compression test, the oxidized cladding was cut into 15 mm length, and compressed by an Instron-type test machine at the rate of 1mm per minute until a fracture. In the case of the 3-point bend test, the oxidized cladding with a length of 180mm was put into the bending jig then it was bent at the

rate of 1mm per minute until a fracture. Span (distance between the loading jigs) length of the test was 70mm. All the tests were performed at room temperature.

2.3 Microstructural analysis

When cladding is exposed to a high temperature steam environment, a diffusion of the oxygen results in the development of three distinct layers across the Zircaloy-4 cladding, namely zirconium oxide, a stabilized alpha phase, and a prior-beta phase. To determine the oxidation rate more quantitatively, the term ECR (Equivalent Cladding Reacted) was introduced to be defined as the ratio of the converted metal thickness to the initial cladding thickness [1]. Using a dimensional conversion, the ECR value of zirconium can be derived according to the relationship;

$$ECR(\%) = 2.693 \times 10^{-3} \cdot (3.36 \times 10^{11} \times \exp(-22,900/T) \times t)^{0.5} \quad (1)$$

T and t respectively denote oxidation temperature in K and oxidation time in second. The Baker-Just equation [6] was adopted as the weight gain formula in this study. Hydrogen and oxygen pickup occur at the cladding surface as the oxidation proceeds, and they diffuse and penetrate into the cladding to play an important role in the mechanical properties. Absorbed hydrogen content in the oxidized cladding was measured by a gas analysis. Three or four specimens were sampled in the middle part of the cladding then they were analyzed and averaged. To measure the absorbed oxygen content inside prior-beta layer, sample was collected from the oxidized cladding. It was ground on both sides to leave a thickness as 50µm to remove the surface oxide, and an attempt to measure the oxygen content inside the prior-beta layer was initiated. Similar to the hydrogen analysis, several oxygen contents from the single specimen were analyzed and averaged.

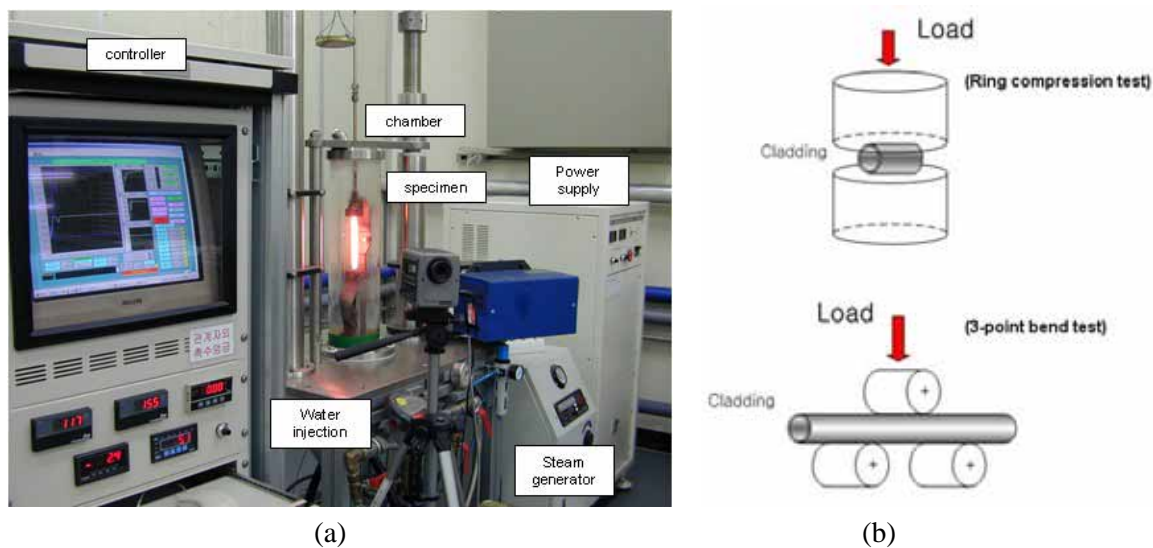


Fig. 1 (a) Simulated LOCA facility (b) Mechanical tests

3. Results and Discussion

3.1 Thermal shock test

Fig. 2 shows the failure behavior of Zircaloy-4 cladding after the thermal shock test with various oxidation temperatures and ECR. Open and closed symbols respectively denote the specimens which survived and failed after a cold water injection followed by a high temperature oxidation. When the heated cladding was quenched by the cold water, the cladding undergoes thermal shrinkage so that the length of the cladding abruptly reduced. Slightly oxidized cladding which has either low temperature or short oxidation time can accommodate such shrinkage to maintain its integrity during the quench. However, heavily oxidized cladding like either high temperature or long oxidation time cannot maintain the shrinkage then it fails during the water quench. Oxidized cladding during quenching

usually fails by cutting in halves across the cladding diameter. In the case of heavily oxidized claddings, they are shattered in pieces immediately after cold water injection. The minimum ECR which is defined as the minimum point where a cladding fails, lies between 20 and 30%, indicates that the conventional 17% ECR criteria for a cladding failure is somewhat conservative.

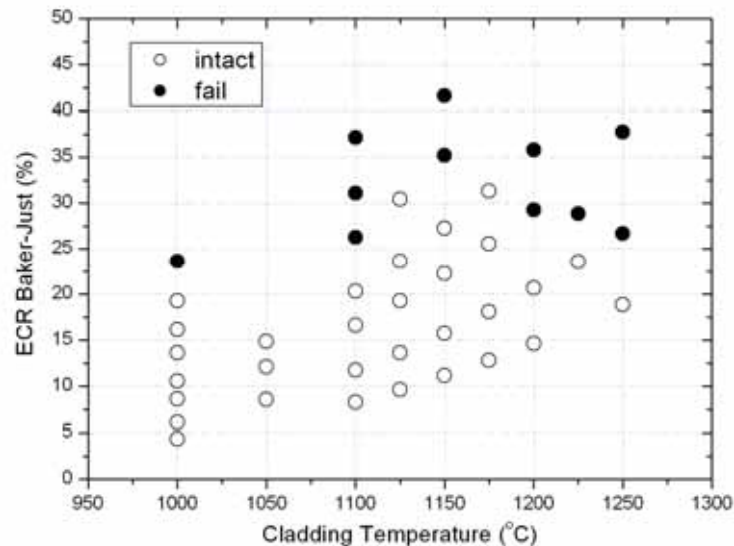


Fig. 2 Failure map of Zircaloy-4 cladding under simulated LOCA condition

3.2 Mechanical tests

Fig. 3 shows the behavior of the absorbed energy during the mechanical test with the oxidation temperature, where oxidation time was set constant for 300sec. The absorbed energy can be defined as the area under the load-displacement curve which has a dimension of the energy. Both energies obtained by the ring compression and 3-point bend tests decreased with the oxidation temperature, and they showed an abrupt decrease between 1100°C and 1150°C. Energy of the 3-point bend specimen was larger than that of the ring compression because the specimen size of the bend test is larger than that of the compression test. From this result, one can conclude that the 3-point bend test is more sensitive for evaluating the failure criterion in that the changes of the absorbed energy measured by 3-point bend test is more distinct than that by the ring compression test. Fig. 3 also shows the changes of the absorbed contents of the Zircaloy-4 cladding with the oxidation temperature. Both the absorbed hydrogen content and the oxygen content inside the prior-beta layer increased with the oxidation temperature. Absorbed hydrogen content gradually increased in all the temperature regions. Hydrogen content shows 270ppm, when the Zircaloy-4 cladding oxidized at the 1150°C above which it exhibited a brittle fracture. In this figure, the Zircaloy-4 cladding shows a brittle failure when the oxygen content of the prior-beta phase was above 0.5wt%.

3.3 Development of revised failure diagram

Fig. 4 is the failure diagram of the Zircaloy-4 cladding according to the Arrhenius form when collated with the calculated 3-point bend energy based on the previous section. Same in the Fig. 2, closed symbol represents the failed cladding during the water quench. The ductile bending can be easily distinguished from the brittle fracture in that absorbed energy in the ductile bending lies in the value over 1200kgf-mm, whereas brittle failure lies below 100kgf-mm value. When separating each region based on the fracture energy, one can obtain the empirical failure behavior of the Zircaloy-4 cladding under the LOCA condition. 'Ductile bending' (blue region) means that the cladding can assure its mechanical ductility after a thermal shock, not to mention a survival during a water quenching. 'Brittle fracture at the mechanical test' (green region) means that although the cladding at first survived the water quenching, it has already lost its mechanical ductility so that it could be failed during a handling, such as refueling or transporting the fuel bundles to the spent fuel storage [7]. 'Brittle failure at a thermal shock' (red region) indicates that the cladding is too brittle to withstand even a thermal stress

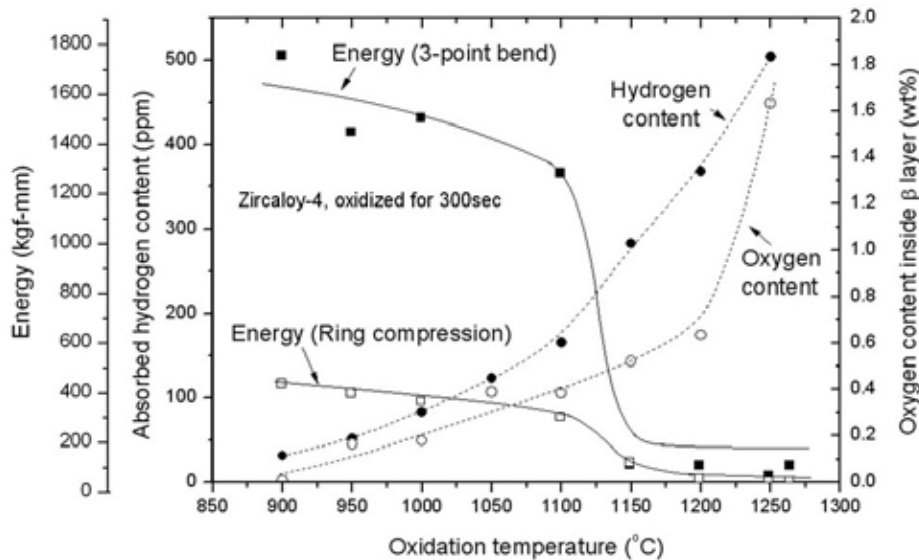


Fig. 3 Changes of the absorbed energy and the absorbed contents of the fuel cladding with the oxidation temperature

during a water quenching. From the diagram, ‘Ductile bending’ region decreases with the oxidation temperature. For instance, a ductile bending occurs irrespective of the oxidation time when oxidized below 950°C. Oxidized cladding at 1000°C starts to lose its mechanical ductility above 5000sec. Finally, oxidized cladding at 1150°C shows its mechanical ductility only at 300sec. The threshold ECR to withstand a ductile bending is around 15% when oxidized at 1000°C. It gradually decreases to have the ductility below 10% when oxidized above 1100°C. The changes of the absorbed oxygen contents inside the prior-beta with oxidation temperature and time were also overlaid in Fig. 4. It was shown that cladding whose oxygen contents in the prior-beta layer are less than 0.5wt% showed a ductile failure, which exactly corresponds to the result of the 3-point bend test as mentioned in Fig. 3.

So far, the approach on the construction of the revised failure diagram, where the thermal shock test was combined with the mechanical test after thermal shock, can be extended to the another study. That is, revised failure diagram as proposed in this study can be extended to the cladding ballooned prior to high temperature oxidation, axially constrained condition, high-burnup conditions such as pre-hydrided cladding, and Nb-contained advanced cladding. Quantitative evaluation how each region (Ductile bending, Brittle fracture at the mechanical test, and Brittle fracture at thermal shock) will be changed with the change of condition (ballooning, axial stress, pre-hydride, and Nb content, and so on) will be of importance. For example [8], the existence of hydride inside zirconium matrix generated during normal operation would induce small decrease in minimum ECR above which cladding will fail during thermal shock (red region would remain same compared to the as received condition.), whereas large decrease in threshold ECR above which cladding will behave brittle failure at mechanical test after thermal shock test (blue region would shrink rapidly compared to the as received condition.) because pre-hydride increases oxygen content inside prior-beta layer to decrease mechanical ductility of oxidized cladding.

4. Conclusion

To analyze the failure behavior of fuel cladding under a LOCA condition, a simulated LOCA test and subsequent mechanical tests on the Zircaloy-4 were conducted. After conducting the thermal shock test at the temperature ranges from 900°C to 1250°C with various times followed by mechanical tests and their associated microstructure analysis, the followings were obtained.

- 1) 3-point bend test is more sensitive than the ring compression test in determining the failure behavior of an oxidized cladding.
- 2) The minimum ECR on the Zircaloy-4 cladding to cause a brittle fracture during thermal shock is around 20%, regardless of oxidation temperature. On the other hand, threshold ECR value,

below which mechanical ductility of the cladding can be assured, decreased as the oxidation temperature increased.

- 3) The absorbed oxygen contents in the prior-beta layer had an influence on the mechanical energy of the cladding after LOCA event. When the absorbed oxygen content was less than 0.5wt%, the cladding maintained its mechanical ductility after the LOCA test.

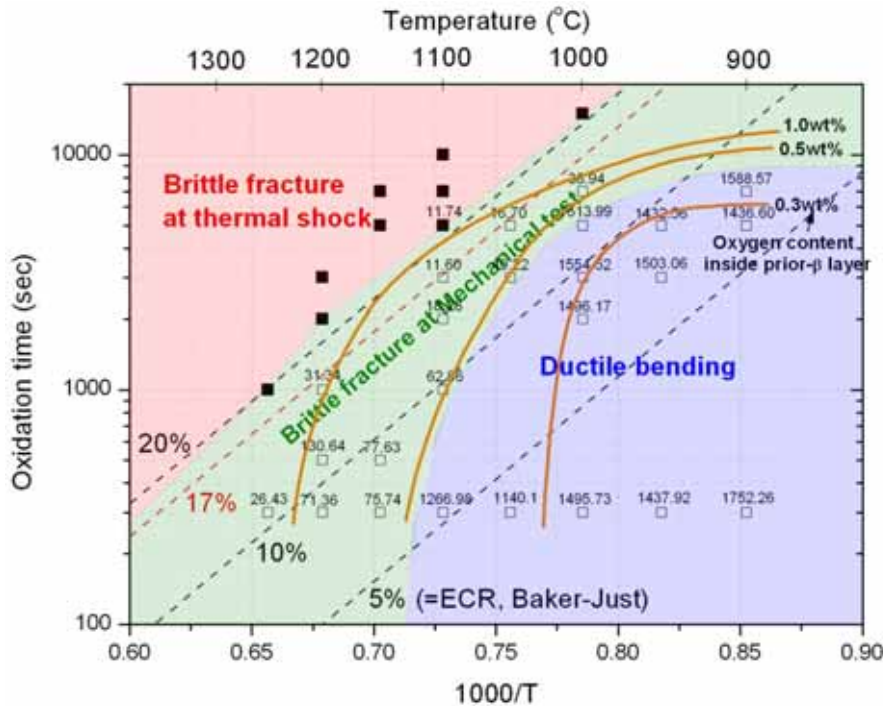


Fig. 8 Changes of the 3-point bend fracture energy and oxygen content inside prior-beta phase of the Zircaloy-4 cladding with the oxidation temperature and time

Acknowledgement

This study was supported by Korea Institute of Science and Technology Evaluation and Planning (KISTEP) and Ministry of Science and Technology (MOST), Korean Government, through its national nuclear technology program

References

- [1] Nuclear Regulatory Commission, 10 CFR 50.46, (1973).
- [2] D. O. Hobson and P. L. Rittenhouse, ORNL-4758 (1972).
- [3] H. M. Chung and T. F. Kassner, NUREG/CR-0344 (1980).
- [4] F. Nagase and T. Fuketa, NUREG/CP-0185 (2003).
- [5] J. H. Kim, M. H. Lee, B. K. Choi and Y. H. Jeong, Nucl. Eng. and Des., 235, 67 (2005).
- [6] L. Baker and L. C. Just, ANL-6548 (1962).
- [7] A. Machiels, Nuclear Safety Research Conference 2004, (2004).
- [8] J. H. Kim, B. K. Choi, J. H. Baek and Y. H. Jeong, Nucl. Eng. and Des., in press (2006).

HIGH POWER AND HIGH SPEED RAMPS IN THE OSIRIS REACTOR

F. CHAMIOT-BISSON, G. THELLIER & S. LOUBIERE

*Service for Reactor Irradiations and Nuclear Studies
Bât 527*

S. MARTIN & P. DURANDE AYME

*Service for Osiris Operation
Bât 633*

*Nuclear Energy Division
Commissariat à l'Energie Atomique
91191 GIF SUR YVETTE Cedex
France*

ABSTRACT

The requirements set by the operators of the French nuclear program, EDF, AREVA and the safety authority, for the determination of the technological limit of pressurized water reactor fuels in transient conditions in the frame of the French nuclear program, led the CEA to extend the capacities its power ramp test facility ISABELLE 1 in the OSIRIS reactor. In the 90's this loop has been equipped with sophisticated instrumentation for power determination by heat balance. A full qualification program helped to qualify these thermal measurements. Since two year a full revision of the safety analysis in addition to facility upgrades allow to perform high power and high speed ramp test in the ISABELLE 1 loop.

1. ISABELLE 1 description

1.1 General Design

The ISABELLE facility (Fig. 1), installed in the OSIRIS 70 MW pool type reactor, is a loop system designed for experimental irradiations of nuclear fuels for pressurized water reactors. It is used to perform tests in thermal-hydraulic and chemical operating conditions which are representative of those in industrial power and prototype reactors.

It is divided into three main parts:

- **The in pile part:** a pressure tube/sample holder assembly containing one experimental fuel rod is placed on a mobile support, at the periphery of the OSIRIS core. Manual and automatic operations help to adjust the linear power of the test fuel, and to make power steps at variable speeds. The fuel rod is cooled by significantly boosting the coolant flow rate using a jet/nozzle at the top of the test channel and heat exchangers;
- **The out of pile part:** on one side the pressurization of the circuit and feed water supply to the in-pile part from a thermal pressurizer and a circulating pump are sheltered in a ventilated bunker, on the other side electrical racks, surmounted by a mimic panel, are used to control and monitor the experiment, and a computer makes the data storage and real-time calculations necessary to run the test. Other electrical racks ensure the safety of the installation. This part includes also delayed neutron detectors and γ detectors dedicated to the monitoring of the cooling water activity. It has been enriched by an on line γ spectrometry;
- **The connection between those two parts:** for both electric (power, monitor, control, measurement) and water supply.

The experimental load consists in one fuel rod with or without instrumentation, fresh or irradiated of about 50cm length.

1.2 Instrumentation

Two sample holders are available. Each has 18 thermocouples for temperature measurements, eight of which are placed at the inlet and six at the outlet of the test channel. Each sample holder is equipped with elongation sensor to measure the changes in length of the rod and to detect clad failures.

In addition, an external probe holder located outside the pressure tube, integrated with the displacement device, and placed at the level of the maximum flux from the reactor, has four silver SPND and four cobalt SPND. This instrumentation was also developed for improvement of control and reproducibility of ramp sequences [1] [2].

This instrumentation is completed by a neutronography and a γ spectrometry that are performed before and after each power ramp to verify the status of the fuel pin and to confirm the value of the power shape.

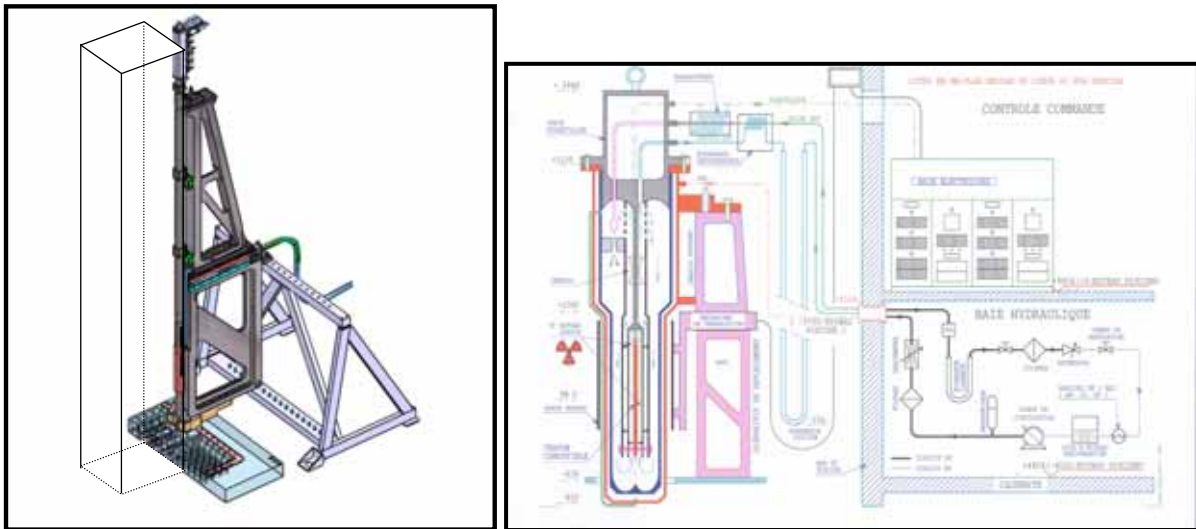


Figure 1 – Isabelle fuel irradiation loop

1.3 Loop environment

In the pool near the core the irradiation conditions are the following:

- Thermal flux at cladding from 10^{12} to $8 \cdot 10^{13}$ n.cm⁻².s⁻¹;
- Fast flux (E> 1 MeV) from $2 \cdot 10^{11}$ to $2.7 \cdot 10^{13}$ n.cm⁻².s⁻¹;
- γ heating from 0.2 to 1.4 W.g⁻¹ (in the graphite)

2. Device improvements

The main evolution is the conception of a new movable module that has been designed to resist to reference earthquake and to be conform to new mechanical norms.

Regarding safety analysis, accidental thermal hydraulic transient calculations, radio protection studies, mechanical calculations have been updated. They have induced some changes in the ISABELLE 1 device (for instance extra biological protection has been implemented around the bunker in case of transfer of the fission products in this location due to clad failure).

New command control programs have been implemented to permit to reach high speed and keep it as constant as possible without any deterioration of the “landing precision” we have for the targeted power.

3. High power ramps

All those improvements allowed us to increase the maximum linear power reached by the fuel pin at the end of the transient over 600 W.cm⁻¹.

A first high power ramp has been performed in March. The ISABELLE 1 behaviour has been very satisfactory. The targeted power has been reached with a precision of 2%.

4. High speed ramps

The second parameter improved on the ISABELLE loop is the speed of the power rise during the transient. The velocity of the power increase is a parameter that can be scanned during the irradiation programs. Up to last year the device was limited to slopes of 100 W.cm⁻¹.mn⁻¹. A big test program has

been performed in 2005 and 2006 to qualify the command control and instrumentation adaptation needed to increase this speed up to $700 \text{ W.cm}^{-1}.\text{mn}^{-1}$.

During the first campaign we used a UO_2 fuel pin enriched at 3.25% with Zy4 clad provided by EDF and AREVA. The aim of those ramps was to validate the new command control devices and programs. The monitoring was performed by neutronic power follow up through cobalt SPND. The stop criteria used were successively thermal power (for speed of $100 \text{ W.cm}^{-1}.\text{mn}^{-1}$) and neutronic power (for others).

Twelve power ramps have been performed the here-under table gives the results obtained regarding the precision of the power reached for each of them.

#	Targeted Power W.cm^{-1}	P neutronic W.cm^{-1}	P thermal W.cm^{-1}	Targeted Slope $\text{W.cm}^{-1}.\text{mn}^{-1}$	Reached slope $\text{W.cm}^{-1}.\text{mn}^{-1}$
1	500	502	496	100	99
2	500	493	497	100	100
3	420	440	437	300	298
4	420	426	420	300	286
5	420	433	434	300	306
6	420	429	432	500	506
7	420	436	436	500	497
8	420	437	437	500	503
9	420	436	430	500	491
10	480	490	496	500	492
11	500	504	502	100	100
12	420	422	432	700	705

Table 1 – Results of the first high speed test campaign.

The figure 2 and 3 give (in green) the shape of the linear heat rate calculated with the thermo hydraulics measurements and parameters (flow rate, C_p , Δt) during the transient. The distance from the core appears in red. In the process, the input temperature of the cooling water is fixed by a PID regulator driving a heating device located at the entrance of the sample holder.

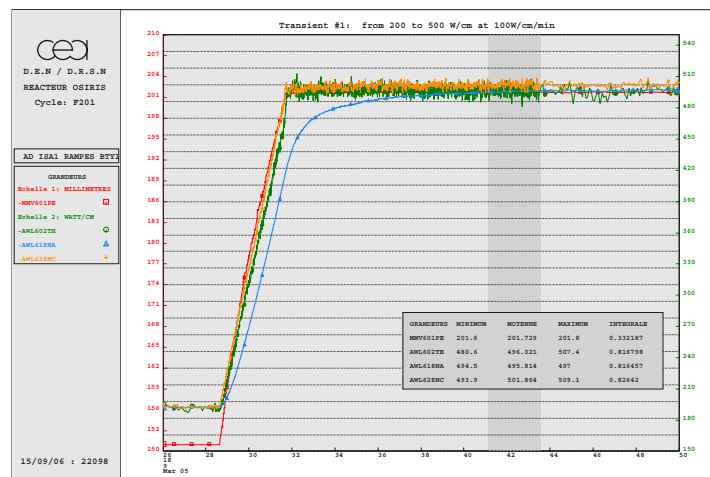


Figure 2 – Low speed power ramp tests at $100 \text{ W.cm}^{-1}.\text{mn}^{-1}$

If this design gives very good results for $100 \text{ W.cm}^{-1}.\text{mn}^{-1}$ power ramps [figure 2], unfortunately it introduces a delay which makes the value of the thermal power irrelevant during height speed power transient [figure3] and therefore, it is impossible to drive the device with this parameter.

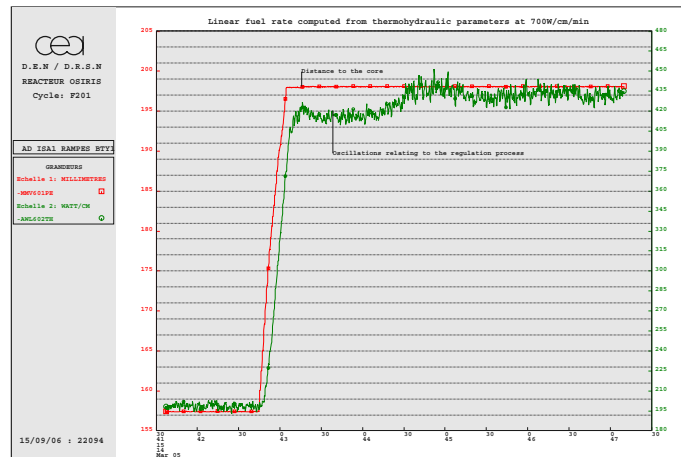


Figure 3 – High speed power ramp tests at $700 \text{ W.cm}^{-1}.\text{mn}^{-1}$

A second test campaign allowed us to perfect the “landing process” anticipating to the power evolution and minimizing the power discrepancy. Four new power ramps have been processed. To solve this problem, the shape of the transient is driven by the linear fission heat rate given by the cobalt SPNDs while the moment to stop is determined by the value given by silver SPNDs coupled to a mathematical anticipation treatment developed in our laboratory. In fact, the linear heat rate calculated with the thermo hydraulics measurements and parameters is used to give a reference in permanent state just before the transient, and after a calibration procedure, the transient is driven by the information given by SPNDs. This ensures a good respect of the target value.

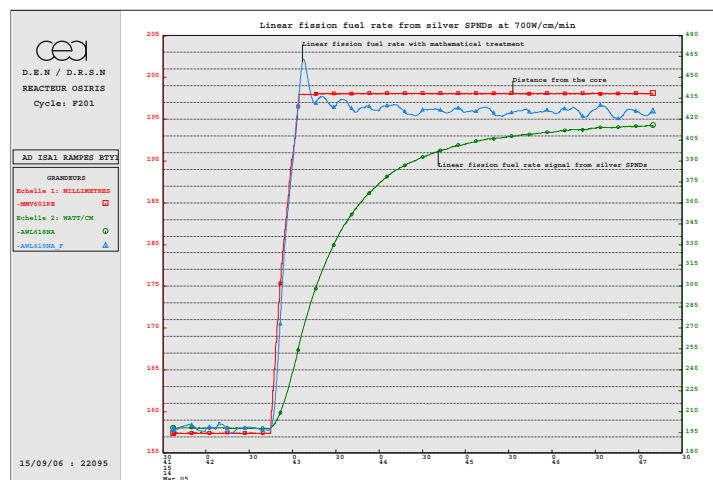


Figure 4 – silver SPND signal for a $700 \text{ W.cm}^{-1}.\text{mn}^{-1}$ transient

The figure 4 shows the shape of the linear fission heat given by silver SPNDs during the transient without (green) and with (blue) mathematical treatment. The overshoot that we can see at the end of the transient is due to the algorithm. It is of no importance as the signal is disturbed once the device is stopped.

More over from the treatment point of view, the device is driven with a PLC conversing with two real-time specialized computers. The PLC computes the distance from the core to respect the transient shape with the linear heat rate given by the real-times computers. The values are transmitted on a fieldbus with a time resolution of 0.1 sec. At the end of the campaign all the measurements and calculated values are stored in a SBGD with the same resolution and are available for post treatment.

After those tests we can ensure our clients a precision of $\pm 20 \text{ W.cm}^{-1}$ for the final power. The first commercial high speed power ramp has been performed in July the intended speed was of $600 \text{ W.cm}^{-1}.\text{mn}^{-1}$. The speed reached was of $609 \text{ W.cm}^{-1}.\text{mn}^{-1}$. and the final power was reached with a precision of less than 2%.

5. Future improvements

ISABELLE 1 has a twin sister device in the OSIRIS reactor called ISABELLE 4. It is right now dedicated to fuel burn up accumulation and slow transient. As for ISABELLE 1 during last two years, its safety analysis renewal is under process. At the end of these studies the OSIRIS power ramp irradiation capacity will be twice the one we have today.

During this time we will have extended ISABELLE 1 new capacities to MOX fuel in 2008, and make the studies and changes needed to be able to receive BWR fuel rods by 2009 in the ISABELLE 4 device.

6. Conclusions

The ISABELLE 1 loop is now qualified to perform high power and high speed power ramp transient. It will be joined in the near future by the ISABELLE 4 device to answer to the need for such irradiation programs from the French companies such as EDF and AREVA but also from other utilities or vendors abroad since we are open to work for international partners on PWR programs and hopefully in some time on BWR irradiation programs.

7. References

[1] Alberman A., Roche M., Couffin P., Bendotti S., Moulin D.J., Boufroy J.L., **“Technique for power ramp tests in the ISABELLE 1 loop of the OSIRIS reactor”** *Nuclear Engineering and Design* 168 (1997) 293-303, Elsevier Science B.V. 1997

[2] Alberman A., Morin C., Marchand L., and Marcault A., **“Comprehensive Nuclear Fuel Dosimetry Program in OSIRIS Reactor”** *Reactor Dosimetry, ASTM STP 1398*, J. G. Williams, D. W. Vehar, F. H. Ruddy, and D. M. Gilliam, Eds., American Society for Testing and Materials, West Conshohocken, PA, 2001

[3] Loubière S., Durande-Ayme P. **“OSIRIS Réacteur d’irradiation pour matériaux et combustible”** *Revue Générale Nucléaire* n°2, mars-avril 2006 Eds. SFEN 670 rue Blomet 75015 Paris France.

WATERCARE™ PROGRAM OVERVIEW

C. ENNEKING, J. SCHARDT

GE Energy, Nuclear

3901 Castle Hayne Road, Wilmington, NC 28402 – USA

ABSTRACT

WaterCare™ is a comprehensive program for nuclear power plants that integrates GE Energy's Nuclear and Water and Process Technology businesses into one holistic program to improve plant water quality and material condition, lower overall operating costs, and improve overall fuel reliability.

Most of today's operating nuclear plants were designed and built using 1960's and 1970's technology, the standard power plant technology at the time. Today, the nuclear plant operator finds the assumptions and bases that were part of the original design to have room for refinement based on leading edge technology and proven operating experience. Issues such as significantly high radwaste handling and burial costs, 700 day operating cycles, 15 day refueling outages, power uprates, cost reduction pressures driven by the deregulated market, asset management, license renewal, and dealing with obsolescent equipment and processes are all elements that plague today's nuclear plant operator.

WaterCare™ is focused on the following key areas:

1. Improving overall water quality
2. Reducing plant operating costs
3. Improving overall plant safety, while maintaining regulatory acceptance
4. Integrating GE's water and nuclear chemistry business into one GE for the customer
5. Improving chemistry monitoring and diagnostics

GE has integrated the core competencies of our nuclear business and our water business to focus on implementing "Next Level Performance" solutions for our customers. Integrating material condition assessments with state of the art monitoring and diagnostic technology yields cost effective actions that our customers can implement today and improve their overall competitive situation.

1. Introduction

The *WaterCare™* program is one of GE Nuclear's initiatives for innovation in the water-chemistry area. Innovation can come to life through new products, new processes, and also new approaches. This program was born after listening and watching nuclear customers in their daily tasks of water sampling, monitoring and balancing pure water with treatment chemicals to meet operational goals and component lifetime expectations.

The objective of this paper is three-fold.

- (1) Provide information on origins of the program,
- (2) Illustrate the current vision of the *WaterCare™* program, and
- (3) Explain the key roll-out phases of the program.

2. Origins of WaterCare™

The origins of the WaterCare™ program started with observation of customers, both at Boiling Water Reactors (BWRs) and Pressurized Water Reactors (PWRs) in the United States. By observing the patterns and behaviors of people, repetitive actions can be seen, process improvements can be developed and areas for technology to complement streamlined processes can be designed.

The evolution of the WaterCare™ can best be summarized by answering three key questions:

- (1) What is the nature of the problem?
- (2) What data tells you so?
- (3) What is the impact?

The nuclear industry faces the challenge to eliminate fuel failures. Known causes of fuel failures include foreign material (debris) fretting, manufacturing defects, duty or environmental conditions (fuel rod cladding waterside corrosion-related). Two US plants recently experienced a number of fuel rod cladding waterside corrosion-related fuel failures, where the plant operators followed all recommended water-chemistry guidelines, were within all tolerances of identified critical chemistry parameters, and yet still experienced an unidentified water chemistry event or condition that resulted in fuel failures. Thousands of person-hours of operator and fuel supplier root cause analysis were expended, including expensive hot-cell examinations, and still the precise initiating condition remained unidentified. This is obviously an undesirable situation, and represents the primary issue for WaterCare™ focus and resolution.

The other fuel failure category addressed by WaterCare™ is debris fretting. More than eighty percent of fuel failures today occur from debris getting to the fuel and causing fretting damage and failure. A multitude of mitigating actions are available or being developed by the plant operators and the fuel suppliers for addressing debris issues. WaterCare™ will complement these activities through the provision of a system response in the form of system debris strainers. However, the issue that is most complex and represents the primary WaterCare™ focus is that of defining and maintaining the appropriate water chemistry balance for maximum operational performance and fuel reliability.

The impact, as one US utility Vice-President recently stated, is extremely high. The utility impact from a single fuel rod failure can be on the order of \$500-\$700 thousand dollars, as a starting point, and “it grows from there.”

3. The Foundation of WaterCare™ - Customer Observations

We worked with one nuclear customer who is a top-quartile performer in plant operations and continues to set industry expectations for water-chemistry best practices. We co-developed a pilot program to perform water system walk-downs as well as observe daily chemistry practices at both a BWR and PWR. We brought in teams of system engineers, water system experts, quality program resources and a PWR consultant. We spent over three weeks at these sites and delivered over sixty-five observations and recommendations. For both sites, we delivered recommendations where process improvements could be implemented or areas where technology could provide human performance improvements. We had our teams shadow the utility chemistry personnel in their daily tasks including the water-chemistry grab sample process, data tracking and trending, and overall analysis tasks. We reviewed current monitoring and diagnostic tools & capabilities. These actions were performed to truly feel “a Day in the Life” of our customer ... and it became the foundation for the WaterCare™ program.

4. WaterCare™ Vision and Phases

The program is in its infancy, but we are excited about the direction of the program and expected customer and industry benefit. There are three key phases to the program, which simply stated, are:

- Phase I: provide a simple and unified portfolio of products & services for nuclear primary & balance of plant solutions for near term outstanding water-chemistry characterization and treatment.
- Phase II: provide a robust, less resource intensive, solution for monitoring and diagnostics. Our aim is to invoke “smart” diagnostics by utilizing predictive models to analyze environment conditions that could result in adverse fuel performance effects and provide alerts and recommended corrective actions before the issues occur.
- Phase III: offer interactive water-chemistry monitoring by a team of experts trained in the ability to identify, treat, and mitigate potential adverse water chemistry conditions during sustained plant operations and times of potentially most adverse conditions such as plant startup and shutdown. This service would be in conjunction with reliability-centered performance contracts.

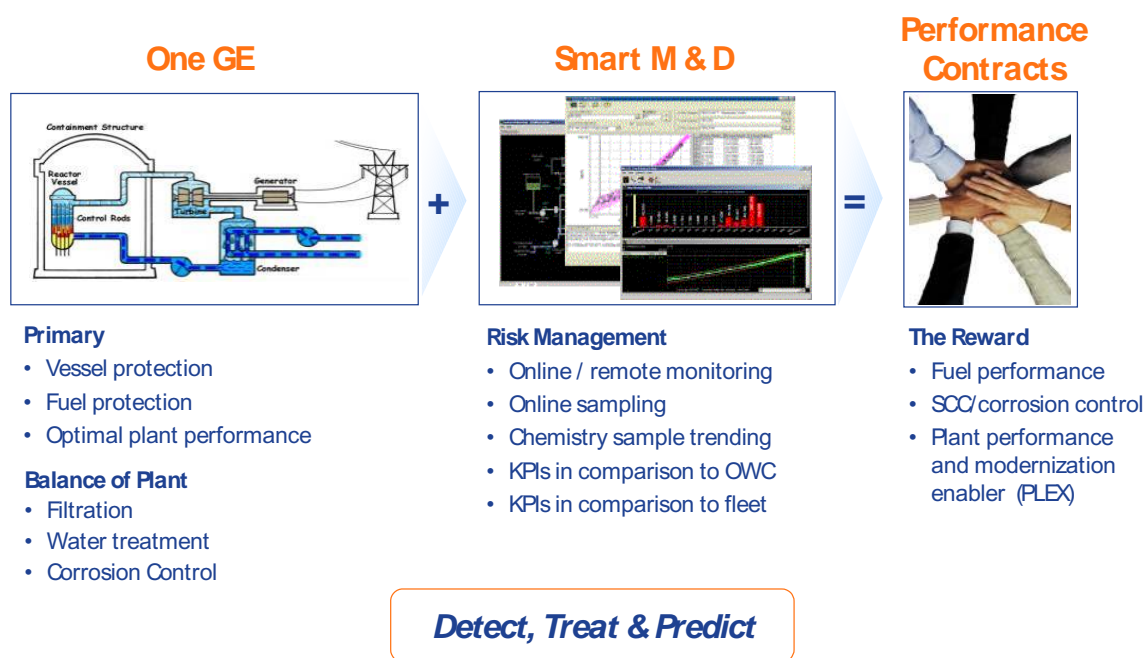


Fig 1. Vision of WaterCare™ Program

5. Customer Challenges

We collected numerous examples of issues that our customers face. For example:

- Nuclear plant operators are pushing plants harder with longer fuel cycles, shorter outages, extreme price competition and expectations for capacity factors at or near one-hundred percent.
- Regulatory trends are to increase sample frequency and decrease personnel dose requirements. At some plants, these two directives are difficult to achieve based on the locations of sample sinks and current grab sample processes.
- Skilled chemistry personnel are difficult to find, as chemistry staffs are looking to hire and train early-career individuals.

- Current sampling processes and equipment are labor-intensive, not human-factored and ridden with maintenance and calibration issues.

6. Pilot Findings

Various chemistry sampling frequencies exist at a typical plant. For example, EPRI requires sixty-three samples be taken at a BWR. Thirty percent of these samples are taken daily and seventy percent are weekly or monthly. This means two things. One, much time is spent on the sampling process as seen by the lion-share of activity for a fifteen-person, three-shift staff. Second, most samples are not real-time. In short, visibility of critical chemistry parameters is less than optimal in most of today's power plants. Furthermore, evidence shows that half of transient events happen during startup or shutdown, but the ability to collect, analyze data, and mitigate any potential adverse condition is not routinely performed by the industry.

In addition, more than fifteen analytes of interest require a special technology called ion chromatography (IC) to properly analyze the samples. Today, very few plants own this technology, and those that do experience instrumentation and calibration issues.

Looking at processes, over seventy-five percent of sampling and analytical methods are manual and require skilled staffs to perform the measurements and enter data into multiple systems for review. As we talked with many of our customers, many of these processes are less than adequate. Customers would like to see processes more human-factored to help the newer members of the staff execute tasks error-free.

All in all, the goal for the *WaterCare*TM program is to Predict, Detect, and Treat the issues that could cause an interruption of reliable plant operation. This goal can be accomplished by improving the visibility of plant water-chemistry and mitigate conditions before they contribute to adverse fuel performance effects and possibly fuel failure. It is also important to find ways that technology can be used as an enabler for process and productivity improvements, but also ensure any technology improvements are grounded in clear, error-free, robust processes.

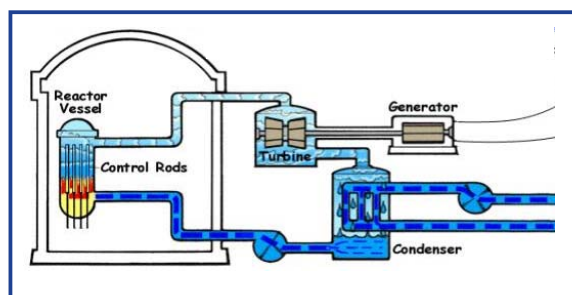
7. *WaterCare*TM Value Chain

When the *WaterCare*TM program was initially scoped, we looked at the key elements of water use at the plant. We evaluated (a) water treatment from the source, (b) water utilization in the plant and (c) waste processing. The scope of *WaterCare*TM is predominantly in the middle area, Water Utilization. The concentration is on filtration, treatment and advanced monitoring of plant water-chemistry. In addition, we do include any solutions that will provide opportunities for waste reduction.

The *WaterCare*TM portfolio currently includes the primary & balance of plant systems and processes for vessel & fuel protection, optimal plant performance, dose & corrosion resistance & critical water treatment.

8. *WaterCare*TM Holistic Solution

In reviewing the portfolio of services that are currently available, both on primary and secondary systems, GE has extensive experience in providing solutions for IGSCC resistance, corrosion control, and dose reduction and filtration & treatment options. One advantage of GE's Nuclear & Water businesses working as one unit is the development of a holistic plant solution spanning across all of plant operations.



Primary Solutions:

- NobleChem™
- HWC
- DZO/DZA with GEZIP
- MMS monitoring
- Fuel sampling/analysis
- Online NobleChem™
- Fuel debris mitigation
- Tritium remediation facilities
- Outage chemistry monitoring
- Chemistry & fuel monitoring

Balance of Plant Solutions:

- Makeup demin system
- Biofouling control
- Corrosion control
- Radwaste membranes
- Cooling water treatment
- Closed loop cooling water treatment
- Mobile water services
- Once through cooling treatment
- PAA
- Steam Gen blowdown/EDI
- On Point/Lab on a disk

Integrated Monitoring & Diagnostics:

- ECP monitoring
- Durability monitoring
- Ion detection
- Process area/RAD monitoring
- Off-gas monitoring
- Steam quality monitoring
- Heat exchanger performance monitoring
- TOC detection
- Fouling monitoring
- Residual monitoring
- Steam pipe corrosion monitoring
- Closed loop corrosion monitoring

Fig 2. WaterCare™ Holistic Portfolio

9. WaterCare™ Summary

The primary intent of the WaterCare™ program is to find the balance that will efficiently manage fuel performance risk to eliminate water chemistry-related fuel failures and thereby enable stable and reliable plant operations. A key to success in this area is in improving the monitoring and diagnostic capabilities with prognostic models and more real-time, continuous data.

The highly manual and/or inefficient processes of today can be simplified, human factored, and technology can be introduced as an enabler to automate the collection of necessary analyte sampling & analysis.

The loss of skilled resources is a critical issue and we are evaluating the ability to set-up a remote monitoring center for reviewing water chemistry parameters at various plants. We are also in discussions with industry leaders to partner and improve current technology and predictive models, as well as provide consulting expertise on the right “balance” of chemistry parameters in any given plant.

Finally, the WaterCare™ component that will be rolled out first, is the combination portfolio of primary & secondary water filtration, treatment & corrosion control products for optimal performance.

This program is continuing with innovation through observing, piloting, and ultimately creating solutions for and in concert with our customers.

Proposal for a Fuel Integrity Evaluation System under a BWR Post-BT Condition

Hiroshi Ono, Akira Mototani

*Toshiba Corporation, Power System Company, Isogo Nuclear Engineering Center
8, Shinsugita-Cho, Isogo-Ku, Yokohama-Kanagawa pref.*

Nobuaki Abe, Yutaka Takeuchi

*Toshiba Corporation, Power System Company, Power and Industrial System R&D Center
8, Shinsugita-Cho, Isogo-Ku, Yokohama-Kanagawa pref.*

ABSTRACT

Since a rise of fuel cladding temperature under the temporary boiling transition (BT) condition in Boiling Water Reactor (BWR) does not affect fuel integrity, the Nuclear Safety Commission of Japan approved the fuel integrity criteria under BT condition (Post-BT) on June 2006. In light of these new criteria, we are developing a fuel integrity evaluation system which consists of a computer network and a detailed thermal-hydraulic code with three-dimensional kinetics. The TRACG02modT code is a newly developed thermal-hydraulic code which includes three-dimensional kinetics and which can model all fuel channels individually in a BWR core. This allows prediction of the location of each BT fuel bundle, the BT duration, and fuel temperature rise after BT during any type of transient phenomena experienced by a nuclear plant. Furthermore, we developed a technique for quickly restoring the core conditions of a BWR plant. Through this improvement, we can reproduce the operating plant core condition in the TRACG02modT code by using an intermediate file created by the core management system.

1. Introduction

In order to secure fuel integrity, Boiling Water Reactor (BWR) cores are designed to avoid the onset of boiling transition (BT) inside the fuel assembly. BT leads to a temporary rise in fuel cladding temperatures due to deteriorated heat transfer, even if they are regarded as “Anticipated Operational Occurrences (AOOs)”. However, temporary BT in BWR fuel under an AOO condition would not cause fuel failure regardless of the resulting rise of fuel cladding temperature.

The Atomic Energy Society of Japan (AESJ) instituted a standard for Post-BT criteria applicable to BWR core and safety design, which was conditionally endorsed by the Nuclear Safety Commission of Japan in June 2006. Licensing of the latest Advanced BWR (ABWR) may be performed according to these criteria in Japan. The Post-BT standard enhances plant efficiency by instituting rational plant system and core design. If an AOO occurs that might cause BT in fuel bundles, it is essential to confirm the integrity of the fuel rods by simulation analysis after the event.

Based on the above, Toshiba has developed a system for evaluating fuel integrity, named TRACG02modT.

2. Post-BT criteria

Deteriorated heat transfer due to BT would pose a threat to fuel integrity. Therefore, current licensing criteria in Japan does not permit the inclusion of BT as an AOO either in regard to the fuel design or during plant operation. The nuclear safety committee in Japan recently approved Post-BT criteria which allow the occurrence of BT under the condition to limit Peak Clad

Temperature (PCT) to under 650 °C and dry-out duration time within 10 seconds as shown in Figure 1. This criterion includes the fuel cladding integrity, which poses no threat to fuel integrity and does not allow the affected fuel to be reused.

When an AOO occurs that presents the possibility of BT occurrence, it is necessary to confirm whether the criteria for restarting the plant’s operation are satisfied. For that purpose, the location of BT bundles must be determined, cladding temperature estimated, and dry-out duration time in the AOO estimated as quickly as possible in order to restart the plant.

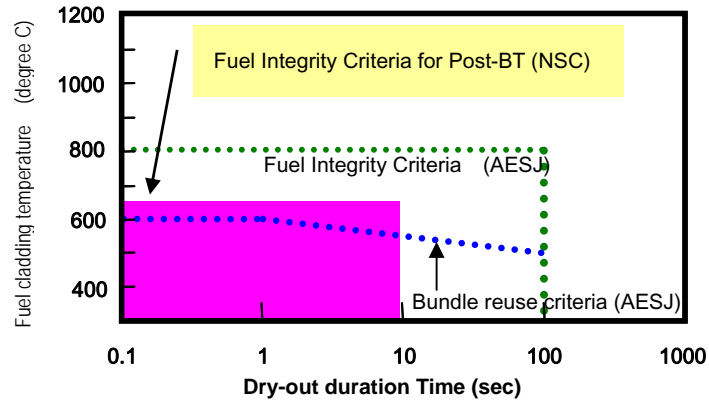


Fig 1. Post-BT criteria

3. Reliability evaluation of Analysis for BT

In order to analyze fuel integrity following a BT event, Toshiba has developed an analytical assistant system based on the transient 3D best estimate code TRACG02modT which can treat all individual bundles within an entire core (1)(2).

Classification	Parameter	BT bundle number	
		Min.	Max.
Base Case		76	
Core	Void coefficient	68	80
	Doppler coefficient	76	76
	Scram reactivity	76	76
Model	Interfacial shear	72	76
	Subcooled void	76	76
	Temperature difference between rods	68	80
	Minimum stable film boiling temperature	76	76
	Film boiling heat transfer coefficient	76	76
Plant	Orifice coefficient	76	76
	LTP pressure drop	76	76
	Spacer pressure drop	68	92
	UTP pressure drop	76	76
	Down comer void rate	76	76
	RIP inertia	68	108
	Separator carry under	76	76
	Separator L/A	76	76
	Separator pressure drop	72	80
Process Computer data	Reactor power	68	96
	Pressure	72	76
	Scram speed	76	76
	Power distribution	61	93

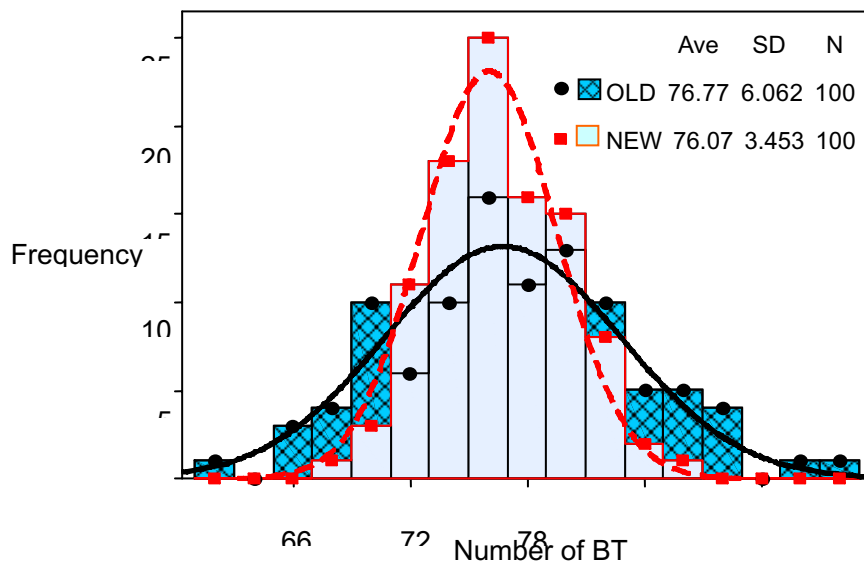
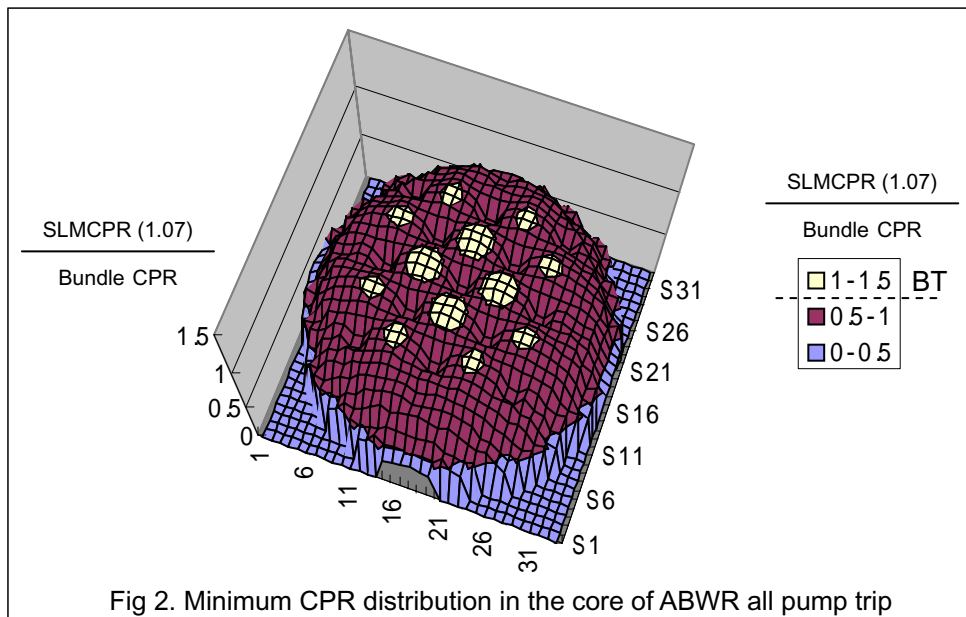
Table 1. Maximum and minimum BT bundle numbers within uncertainty band of each parameter

This code furnishes rewet correlation equations as well as heat transfer correlation, modified Dougall-Rohsenow (D-R) as stipulated by the AESJ standard. In order to confirm the prediction accuracy of TRACG, sensitivity analyses were performed regarding 21 major parameters which would have significant impact on fuel behavior. All pump trip events of an ABWR were selected as typical occurrences which could potentially lead to a BT incident.

Table 1 shows the evaluation results regarding a range of BT bundle numbers within the uncertainty band for each parameter. Initial power distribution, initial reactor power, and the inertia of the recirculation pump indicate significant effects on the number of BT bundles.

4. Proposal of fuel integrity evaluation system for BWR AOO

The results of the reliability analysis indicate a need to focus on improving the prediction accuracy of the initial power distribution. From the perspective of the practical application of the off-line 3D transient code, it is essential that a system be devised in which data concerning



transient plant behavior can be rapidly transferred to TRACG analysis inputs.

First, we developed a 3D neutron kinetic model equivalent to the latest core management system. Using this new mode, we calculated all ABWR pump trip events, as shown in Figure 2. In this case, input data regarding the recirculation pump inertia constant is smaller than that of its nominal value, a condition necessary for the occurrence of BT.

The results shows that 80 bundles (white in Fig. 2) reached the Safety Limit Minimum Critical Power Ratio (MCPR) (1.07), which were conservatively adopted as a BT criteria. Some rods in these bundles reached the film boiling point, and the fuel cladding temperature was increased beyond the normal nucleate boiling condition. The prediction results obtained using the improved model for power distribution were more than twice as accurate as the previous estimate. Figure 3 shows that the standard deviation of the BT estimation error was improved by about 40%. Because the TRACG code cannot use the results of the on-line data for calculating core performance used in the core monitoring system, a function that reproduces the plant's core conditions in the TRACG model was developed. This function has been realized using an intermediate file that consists of the core parameters based only on the operation conditions which are determined by the calculation of core performance. This function allows the TRACG code to quickly reproduce the core conditions of the actual operating plant.

Secondly, a study was performed regarding a method for incorporating plant behavior data into the TRACG code through a computer network. The data include plant parameter such as core flow and core pressure etc., but not core detailed conditions. Figure 4 shows the data flow of the fuel integrity evaluation of BWR AOOs.

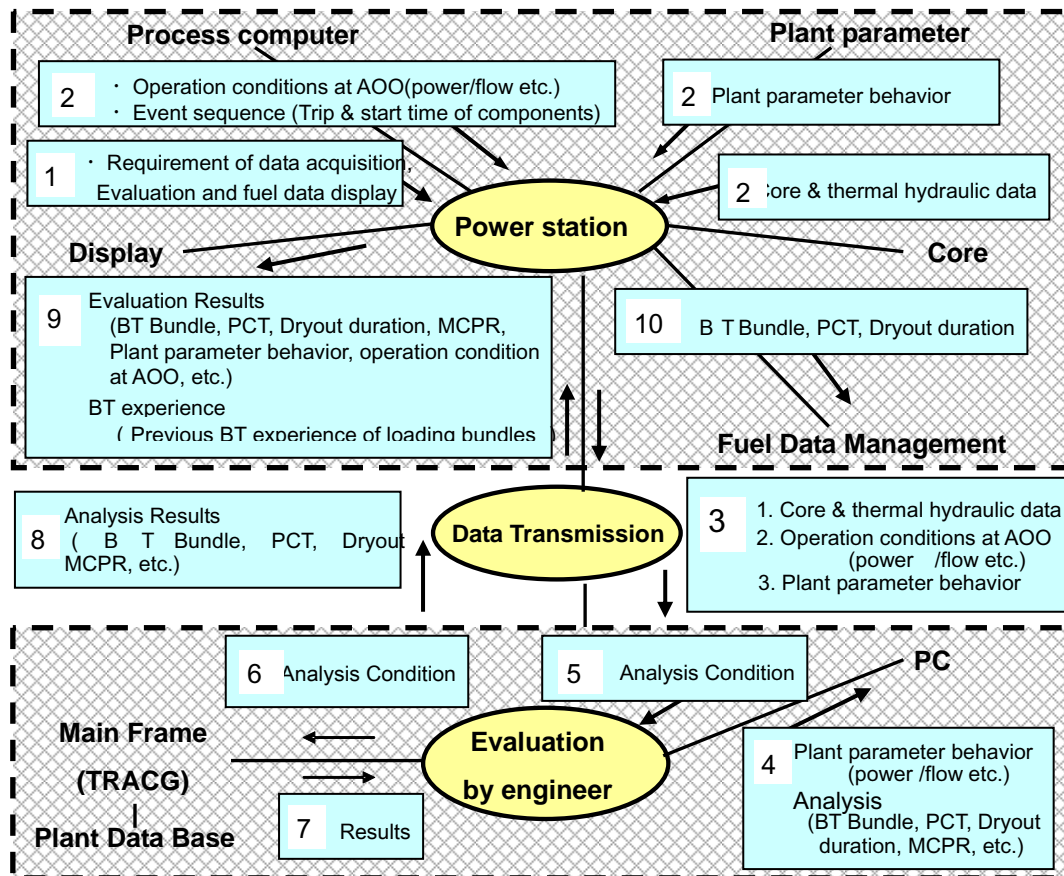


Fig.4 Data flow of fuel integrity evaluation for BWR AOO

In case of a BT occurrence, data collected in the power station, including operation condition, core data and plant parameters, are transmitted to an evaluation engineer who performs BT bundle analysis using the TRACG code, and returns estimated results as soon as possible. The functions and conditions evaluated in the above study were a) automatic data collection and transmission, b) security and compression of data, c) delivery of analysis result, d) the state of the database of analysis input data for each plant, e) the dynamic data link among applications, and f) visualization of the result. It might be impossible to design functions such as data transmission, security, and data linking unless the intended network is identified.

However, the layered approach of linking as shown in Figure 5 is considered useful for system design. Concretely speaking, we allow each local node's local agent the function of mail transmission. The local agents perform the linking between the plant database and the TRACG code, while their mail functions link the local nodes. This system needs no extraordinary infrastructure except e-mail and makes it possible to design a system according to the specific security policy of an electric power company's pre-existing email system.

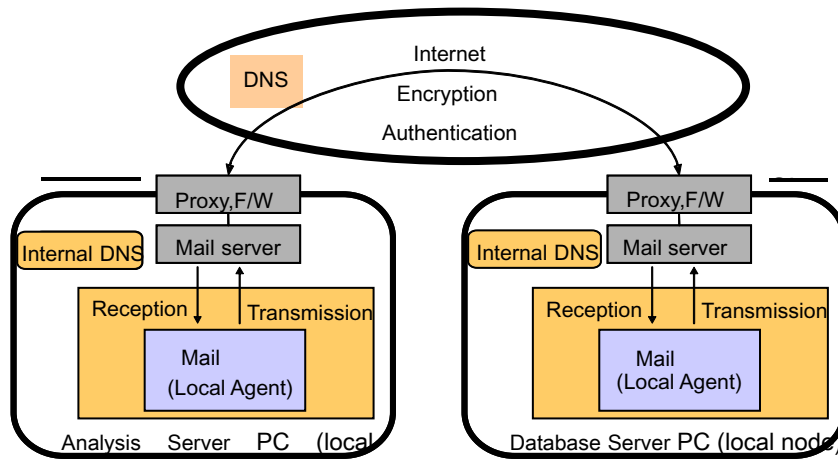


Fig 5 Hierarchized network by agent and node

5. Summary

Post-BT criteria make an important contribution to a plant's economic efficiency. Therefore, as a support system, a 3D analysis system, which evaluates fuel integrity accurately and promptly after an incident has occurred, was developed. Pilot evaluation demonstrated the system's effectiveness.

6. References

1. H.Ono and N.Abe et al., "Development of a Detailed BWR Core Thermal-Hydraulic Analysis Method Based on The Japanese Post-BT Standard Using a Best-Estimate Code", The 6th International Conference on Nuclear Thermal Hydraulics, Operations and Safety (NUTHOS-6) Nara, Japan, October 4-8, 2004.
2. H.Ono and Y. Takeuchi et al., "Development of TRACG02MODT1 for Whole Bundle Simulation", International Meeting on Updates in Best Estimate Methods in Nuclear Installation Safety Analysis (BE2004, ANS), Washington, D.C. November 14-18, 2004.

OUT-OF-PILE TESTS UNDER LOCA CONDITIONS FOR J-Alloy™, HIGH CORROSION-RESISTANT ALLOY FOR PWR FUEL CLADDING TUBE

S.WATANABE

Nuclear Fuel & Back-End Systems Designing Department, Mitsubishi Heavy Industries, Ltd.

1-1, Wadasaki-cho 1-Chome, Hyogo-ku, KOBE 652-8585 JAPAN

T.KIDO

Nuclear Development Corporation

622-12, Funai-shikawa, Tokai-mura, Naka-gun, IBARAKI 319-1111 JAPAN

Y.TSUCHIUCHI

Nuclear Fuel Industries, Ltd.

1-950 Asashiro-nishi, Kumatori-cho, Sennan-gun, Osaka 590-0481 JAPAN

H.TAKABATAKE

The Kansai Electric Power Co., INC.

8, Yokota, 13, Goichi, Mihama-cho, Mikata-gun, FUKUI 919-1141 JAPAN

In order to confirm the applicability of J-Alloy™ to the irradiation test in a Spanish commercial reactor, the material properties and the characteristics under LOCA conditions were investigated. One of the significant difference between J-Alloy and conventional Zr-Sn alloys was observed in phase transformation temperature. And this difference caused slight and tolerable difference in high temperature creep and burst properties. Another difference was related to the post quench ductility, that is, the residual ductility of J-Alloy was lower than Zircaloy-4 in ring compression test. However, integral thermal shock test indicated that the fracture limit of J-Alloy could meet the LOCA criterion of 17% ECR. Therefore, it was convinced that J-Alloy was applicable to the irradiation test in a Spanish commercial reactor from the viewpoint of the performance under LOCA conditions.

1. Introduction

New Zr-base alloys for future PWR fuel cladding named "J-Alloy™" have been developed by the J-Alloy project in collaboration between Japanese utilities-vendor-intellecets joint committee and Spanish vendors and utilities^{[1][2]}. The aim of J-Alloy development is improvement of corrosion resistance, especially under demanding environments supposing future high burnup and high LHR. Taking account of in-pile performance and manufacturability, the project has finally picked out three alloys as shown in **Tab.1**, among several kinds of alloys, as candidates for J-Alloy subjected to the irradiation test in a Spanish commercial reactor. Since J-Alloy would have essentially different metallurgical states from the conventional Zr-Sn alloys due to zero percent of tin and high niobium

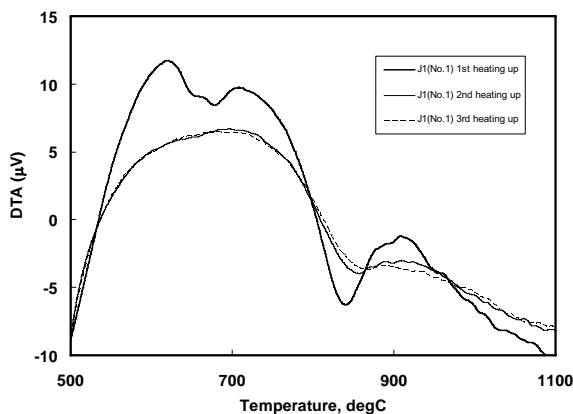
content, the thermo-mechanical properties of J-Alloy have been investigated in terms of the out-of-pile tests under LOCA conditions.

Name	Compositions [wt%]			
	Nb	Cr	O	Zr
J1	1.8	-	0.1	balance
J2	1.6	0.1	0.1	balance
J3	2.5	-	0.1	balance

2. Experimental results

Phase transformation temperature

In order to determine phase transformation temperature ($T_{\alpha \rightarrow \alpha+\beta}$, $T_{\alpha+\beta \rightarrow \beta}$), three-time-repetitive Differential Thermal Analysis (DTA) was performed between room temperature through 1100°C (heat up and cool down) with heating/cooling rate of 20°C/min. **Fig.1** shows DTA curves of J1 as-fabricated specimens during 1st, 2nd, and 3rd heating-up. The DTA curves during 1st heating-up have three inflection points (around 630, 670, and 730°C) near $T_{\alpha \rightarrow \alpha+\beta}$ range, while DTA curves during 2nd and 3rd heating-up have one rough inflection point so that it is difficult to specify $T_{\alpha \rightarrow \alpha+\beta}$. On the other hand, according to the XRD analyses upon specimens quenched from several annealing temperatures, it was found that β phase existed at 650°C. Therefore, it is supposed that as-fabricated J-Alloy has three stages of $\alpha \rightarrow \alpha+\beta$ transformation at different temperatures at around 630, 670, and 730°C, but those at around 630 and 670°C disappear after 1st heating up to 1100°C. Hypothetically, such three different $T_{\alpha \rightarrow \alpha+\beta}$ would indicate the existence of locally different metallurgical regions which could be detected by DTA, though further analysis is necessary to clarify this issue. **Tab.2** summarizes $T_{\alpha \rightarrow \alpha+\beta}$ and $T_{\alpha+\beta \rightarrow \beta}$ of three candidates of J-Alloy compared with those of Zircaloy-4. Both $T_{\alpha \rightarrow \alpha+\beta}$ and $T_{\alpha+\beta \rightarrow \beta}$ of J-Alloy are generally lower than Zircaloy-4, because J-Alloy consists of zero percent tin (α stabilizing element) and high content of niobium (β stabilizing element).



Alloy	$T_{\alpha \rightarrow \alpha+\beta}$ [°C]			$T_{\alpha+\beta \rightarrow \beta}$ [°C]
	J1	630	670	720
J2	630	670	730	920
J3	630	670	740	920
Zircaloy-4	810			990

Fig.1 : DTA curve of as-received J1 specimen Tab.2 : Transformation temperature in 1st heating up

High temperature creep

Sealed tube specimen was held at high temperature and high pressure for several seconds and then depressurized to atmospheric pressure. After that the circumferential strain was measured. **Fig.2** shows

circumferential strain vs holding time at 700°C, 27MPa and 950°C, 2MPa respectively. At 700 °C, in which J-Alloy would have transformed into $\alpha+\beta$ phase while Zircaloy-4 would still stay α phase, (1) circumferential strain of J-Alloy is significantly higher than that of Zircaloy-4. On the other hand, at 950°C where both J-Alloy and Zircaloy-4 would have transformed into β phase, circumferential strain of J-Alloy is comparable to Zircaloy-4.

High temperature burst

Tube specimen was pressurized firstly, then heated up at several °C/sec until the specimen burst. **Fig.3** shows burst temperature vs burst pressure of J-Alloy compared to the conventional Zr-Sn base alloys. Burst temperature of J-Alloy seems generally lower than those of the conventional Zr-Sn base alloys. This could be because $\alpha \rightarrow \alpha+\beta$ transformation of J-Alloy begins at lower temperature than the conventional Zr-Sn base alloys so that creep deformation of J-Alloy would be accelerated at lower temperature than Zircaloy-4. However, it should be noticed that the difference in burst temperature between J-Alloy and the conventional Zr-Sn base alloys is relatively small while the difference in $T_{\alpha \rightarrow \alpha+\beta}$ is quite large. One possible reason of this small difference in burst temperature could be rise of $T_{\alpha \rightarrow \alpha+\beta}$ due to relatively low diffusivity of niobium in J-Alloy when heating rate is greater during like LOCA condition than DTA condition.

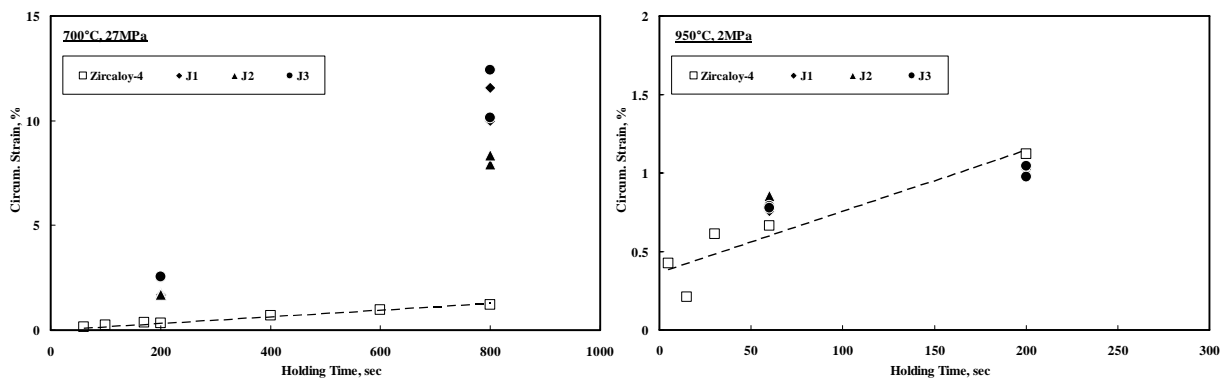


Fig.2 : Result of creep test at 700°C, 27MPa and 950°C, 2MPa.

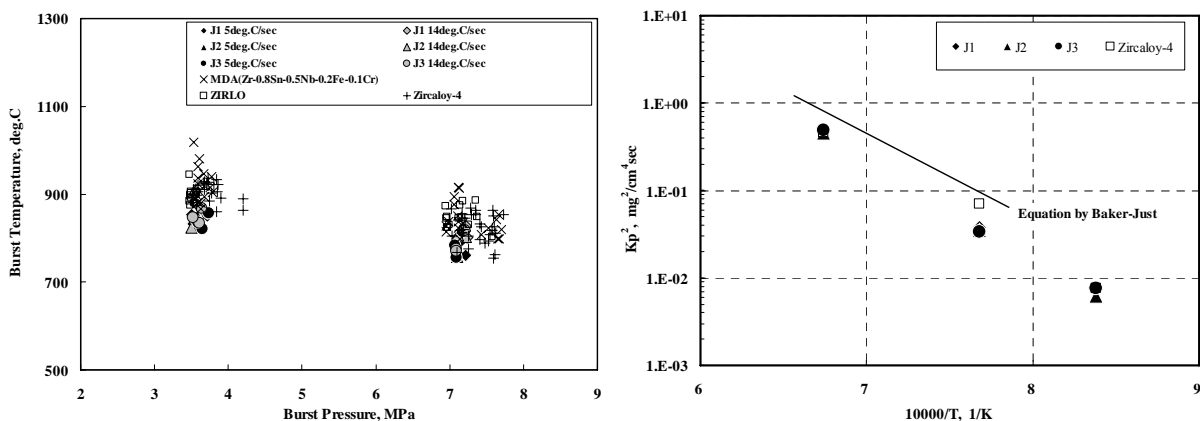


Fig.3 : Result of LOCA burst test^[3]

Fig.4 : Result of H.T. oxidation test^[4]

High temperature oxidation

High temperature oxidation test in the atmospheric pressure steam was performed. In **Fig.4**, oxidation rate of J-Alloy is compared to those of the conventional Zr-Sn alloys and to the Baker-Just equation in terms of the Arrhenius plot. It is confirmed that oxidation rate of J-Alloy is comparable to the conventional Zr-Sn base alloys at high temperature, and the Baker-Just equation is conservatively applicable for safety evaluation.

Post-quench ductility

Some of the specimens subjected to the high temperature oxidation tests were supplied to the ring compression tests in order to evaluate residual ductility after oxidation. **Fig.5** shows residual ductility vs actual Equivalent Corrosion Ratio (ECR) of J-Alloy and Zircaloy-4 oxidized at 1029°C. It is clear that residual ductility of J-Alloy is lower than that of Zircaloy-4. On the other hand, in order to confirm the compliance of J-Alloy with the LOCA criterion ($17\% \leq \text{ECR}$, PCT (Peak Cladding Temperature) $\leq 1204^\circ\text{C}$) in 10 CFR 50.46(b), integral thermal shock tests were performed. Firstly the tube specimens which contained 0~800ppm hydrogen were heated up until burst, then they were subjected to the oxidation in steam at 1200°C. After oxidized at around 17% ECR or more, the specimens were quenched without axial constraint simulating re-filling of water introduced by ECCS. **Fig.6** shows the result of the test, where the ECR is calculated by the Baker-Just equation. All the specimen oxidized below 26% (fully higher than 17%) survived after quench even in case of high hydrogen content. Therefore, it is confirmed that the LOCA criterion in 10 CFR 50.46(b) is applicable to J-Alloy.

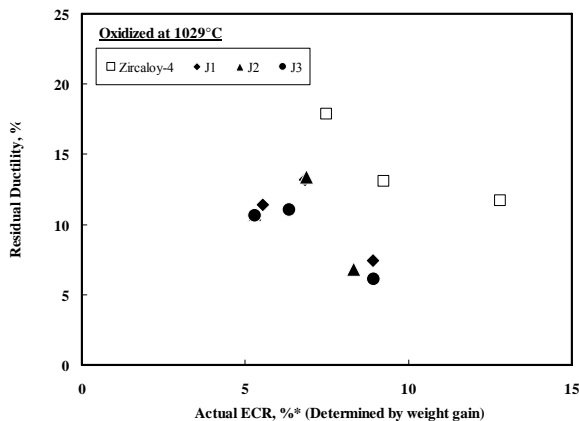


Fig.5 : Result of ring compression test

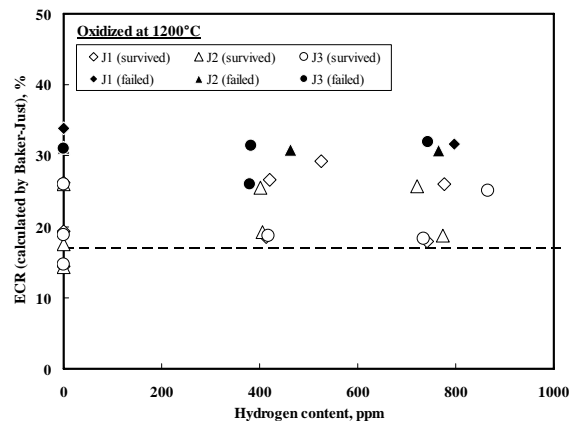


Fig.6 : Result of integral thermal shock test

3. Summary and Conclusion

J-Alloy™ showed some different characteristics from the conventional Zr-Sn alloys under LOCA conditions. First of all, phase transformation temperature of J-Alloy is lower than the conventional Zr-Sn alloys, because J-Alloy contains high niobium (β stabilizing element) content and does not contain tin (α stabilizing element). Secondly, creep property of J-Alloy at high temperature is different from the conventional Zr-Sn alloys due to the difference of phase transformation temperature. Consequently, burst temperature of J-Alloy is generally lower than those of the conventional Zr-Sn alloys. However, the difference between them is small, hypothetically because phase transformation temperature at several °C/sec, simulating LOCA, would have risen compared with that at slow heating (20°C/min) during DTA. Finally, the residual ductility of J-Alloy after oxidation is lower than that of Zircaloy-4. However, it was confirmed that the LOCA criterion in 10 CFR 50.46(b) is applicable to J-Alloy with appropriate tolerance simulating possible LOCA situation. According to these results, it was convinced that J-Alloy was acceptable to the irradiation test in a Spanish commercial reactor from the viewpoint of its performance under LOCA conditions.

Further efforts would be focused on quantitative and mechanistic studies to support appropriate model of J-Alloy cladding behavior under LOCA conditions when it will be utilized as commercial PWR fuel in the future.

Acknowledgements

The authors gratefully acknowledge the assistance and contribution of Spanish utilities, ENUSA, and the other members of the J-Alloy development committee.

References

- [1] N. SEKIMURA et al., "ROADMAP OF CRITERIA RATIONALIZATION AND R&D FOR FUTURE HIGH DUTY USAGE OF FUEL", TopFuel 2006.
- [2] H. TAKABATAKE et al., "DEVELOPMENT PROGRAM OF J-Alloy™, HIGH CORROSION-RESISTANT ALLOY FOR PWR FUEL CLAD", TopFuel2006
- [3] MITSUBISHI HEAVY INDUSTRIES, LTD, "MHI-NES-1021 R8", 2005 (Japanese)
- [4] L.Baker et al., "STUDIES OF METAL-WATER REACTIONS AT HIGH TEMPERATURES III. EXPERIMENTAL AND THEORETICAL STUDIES OF THE ZIRCONIUM-WATER REACTION", ANL-6548 (1962)

MANUFACTURING AND CHARACTERIZATIONS OF J-Alloy™, HIGH CORROSION-RESISTANT ALLOY FOR PWR FUEL CLADDING TUBE

Y.TSUCHIUCHI

*Fuel Engineering and Development Department, Kumatori Works, Nuclear Fuel Industries, Ltd
1-950 Asashiro-nishi, Kumatori-cho, Sennan-gun, Osaka, 590-0481, Japan*

R. WAKAMATSU

*Head Office, Chofu-Kita Division, Zirco Products Co., Ltd.
13-1, Chofu Minatomachi, Shimonoseki-city, Yamaguchi, 752-0953, Japan*

T. ISOBE

*Advanced Materials & Tools Company High Performance Alloy Products Division,
Mitsubishi Materials Corporation
476, Shimoishido-shimo, Kitamoto-city, Saitama, 364-0023, Japan*

S. WATANABE

*Nuclear Fuel & Back-End Systems Designing Department, Mitsubishi Heavy Industries, Ltd.
1-1, Wadasaki-cho 1-Chome, Hyogo-ku, Kobe-city, Hyogo, 652-8585, Japan*

H. TAKABATAKE

*Nuclear Fuel Engineering Group, The Kansai Electric Power Co., Inc.
8 Yokota, 13 Goichi, Mihama-cho, Mikatagun, Fukuiken, 919-1141, Japan*

ABSTRACT

New Zr-Nb alloys (named J-Alloy™) have been considered as candidate cladding alloys for high duty conditions in future PWR operation. As for manufacture, the final annealing temperature was selected for recrystallization of matrix. The quality of the products and producibility are as same as conventional claddings (Zircaloy-4, etc.).

Manufactured J-Alloy™ cladding tubes were provided for a series of out-of-pile tests, in which basic property, mechanical property and corrosion behaviour, etc. have been studied. Thermal conductivity, thermal expansion and microstructure, etc. were examined as basic properties. 0.2% yield strength and tensile strength are lower than those of relieved Zircaloy-4, and ductility is higher. Thermal creep rate is lower than that of stress relieved Zircaloy-4. Long-term autoclave tests at 633K show that J-Alloy™ has higher corrosion resistance than that of low tin Zircaloy-4 in pure water, RCS (3.5ppmLi+950ppmB) conditioned water and high lithiated (10ppm) water.

1. Introduction

The Japanese industry and academic institutes have jointly formed an investigation committee and the committee has developed J-Alloy™ as high performance fuel cladding^[1] Zr-Nb alloys were selected aiming higher corrosion resistance and lower hydrogen absorption than conventional alloys such as low tin Zircaloy-4.

The J-Alloy™ development is conducted in accordance with the roadmap for advanced PWR fuel^[2]. The selection of candidate alloys, manufacture of cladding tube and a series of out-of-pile tests are to

be carried out in the “Stage I” of the roadmap. At a holdpoint of this Stage, the prospect for utilization is considered based on evaluation of the out-of-pile tests results.

2. Manufacture of J-Alloy™ cladding tubes

Three types of alloys, as J-Alloy™, are shown in Table 1. Zr-Nb alloys have higher corrosion and lower hydrogen absorption performance than Zr-Sn alloys represented by Zircaloy-4.^{[3][4][5]} In addition, increasing niobium content would reduce hydrogen absorption. On the other hand, highly addition of niobium hardens the material. J1 is selected from a viewpoint of corrosion resistance, hydrogen pickup and producibility of cladding tube, J2 contains a small amount of chromium for high corrosion performance under also highly lithiated environment, and J3 is aiming at the highest corrosion resistance with high niobium content. As for final annealing condition, recrystallization annealing was applied to reduce creep deformation and irradiation growth.^[6]

Alloy	Composition (wt%)			
	Nb	Cr	O	Zr
J1	1.8	-	0.1	balance
J2	1.6	0.1	0.1	balance
J3	2.5	-	0.1	balance

Table 1 Composition of J-Alloy™

Three types of J-Alloy™ cladding tubes were manufactured based on the specification. There was no problem concerning producibility and the almost same quality of products as conventional one was confirmed, as the microstructure of J1 is shown in Figure 1 and 2.

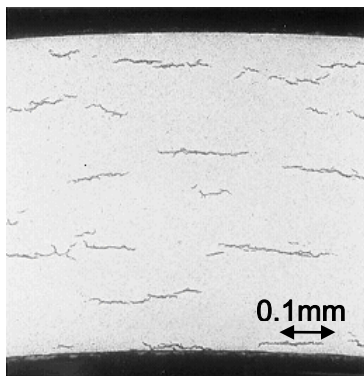


Figure 1 Microstructure (1)
(Hydride orientation)

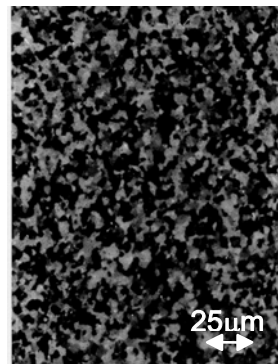


Figure 2 Microstructure (2)
(Grain size)

3. Out-of-pile tests

It is shown that a series of out-of-pile performance of J-Alloy™ comparing between three types of J-Alloy™ and stress relieved low tin Zircaloy-4.

3.1 Basic property

J1, J2 and J3 show almost the same basic properties.

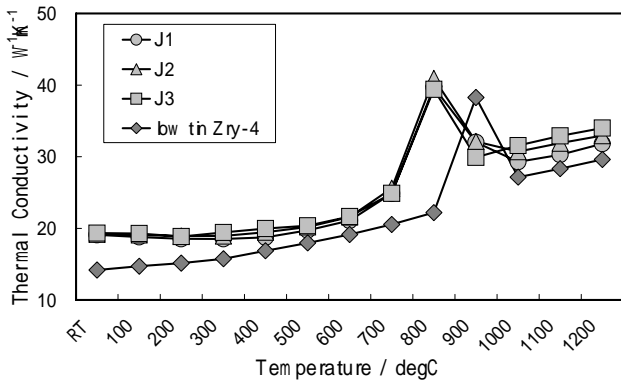


Figure 3 Thermal conductivity

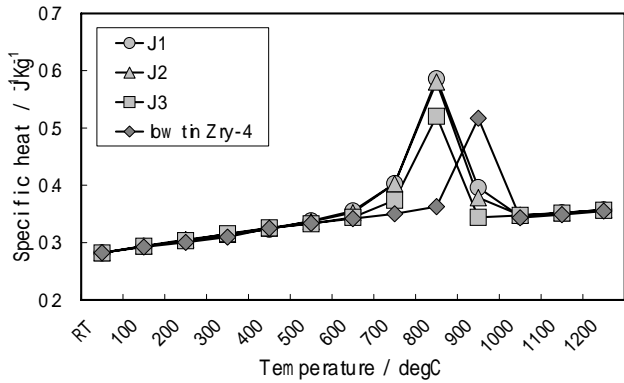


Figure 4 Specific heat

Specific heat and thermal conductivity were measured from room temperature to ~1000°C by laser-flash method, as shown in Figure 3 and 4, respectively. Discontinuity due to phase transformation is shown around 800°C which is lower than that of Zircaloy-4 (~900°C). Specific heat is the same as Zircaloy-4 and thermal conductivity is ~10% higher than Zircaloy-4.

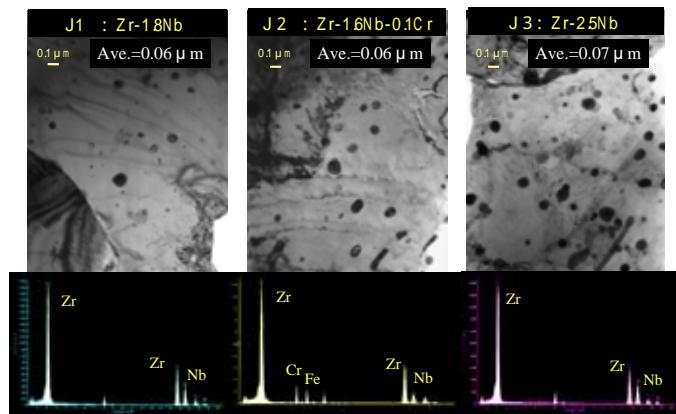


Figure 5 Microstructure of J-Alloy™

Thermal expansion behaviour is almost the same as Zircaloy-4.

Figure 5 is microstructure of J-Alloy™ by Transmission Electron Microscope (TEM). β-Nb particles are dispersing in the matrix. Density and size of particles depend upon the niobium content. A lot of particles are observed and averaged size of the particles is relatively large in J3 alloy with highest niobium content.

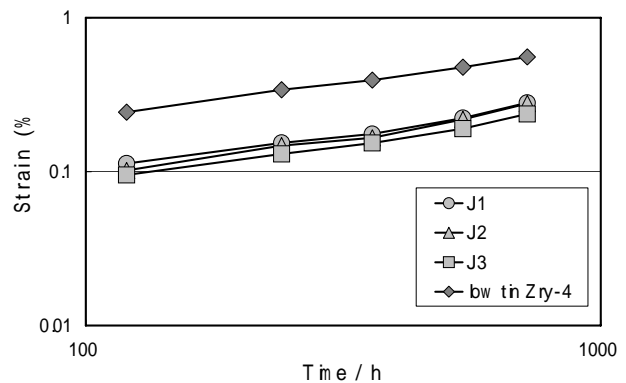


Figure 6 Creep test results (633K, 117.6MPa)

3.2 Mechanical property

J1, J2 and J3 show similar mechanical properties.

Young modulus and Poisson ratio are the same as those of Zircaloy-4. Axial tensile test of cladding tube show lower 0.2% yield strength, lower tensile strength and higher elongation than

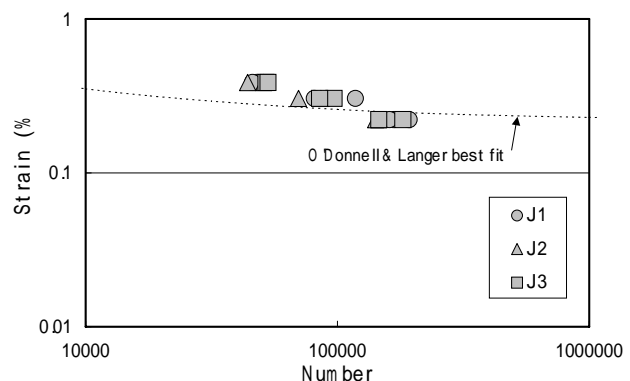


Figure 7 Fatigue test results (589K, 2Hz)

Zircaloy-4. This is peculiar to recrystallized material. J3 shows slightly higher strength and slightly lower ductility than J1 and J2 in both RT and 385°C tensile tests. Additionally, the influence of hundreds ppm of hydrogen absorption on the ductility is relatively small.^[1]

Internal pressurizing creep test results are shown in Figure 6. J1, J2 and J3 show no significant difference. It is seemed that the lower creep rate than Zircaloy-4 is influence of recrystallization.

As for fatigue behaviour of J-AlloyTM, as shown in Figure 7, although fatigue life (total number of cyclic stress) is higher than the best fit curve by O'Donnell and Langer^[7] in high stress condition, it is same or a little lower than the curve.

3.3 Corrosion behaviour

Long-term autoclave tests are performed under RCS(3.5ppmLi+950ppmB) conditioned water, pure water and high lithiated (10ppm) water at 633K. The results of these tests are shown in Figure 8, 9 and 10, respectively. J-AlloyTM shows lower weight gain than Zircaloy-4. Although Zircaloy-4 shows cyclic transition with pitch of $\sim 30 \text{ mg/dm}^2(\sim 2 \mu\text{m})$, the first transition of J-AlloyTM is not observed by the weight gain up to $\sim 50 \text{ mg/dm}^2(\sim 3 \mu\text{m})$. It is suggested that the long cycle period of transition relates to excellent corrosion resistance in the long term. Although J3 shows slightly lower weight gain than J1 and J2 under some conditions, it is not clear at the moment.

4. Summary and conclusions

Three types of J-AlloyTM cladding tubes have been manufactured and the quality of the products and producibility are the same level as conventional claddings (Zircaloy-4, etc.). A series of out-of-pile tests for J-AlloyTM have been conducted about basic properties, mechanical properties and corrosion behaviour. Some performance of J-AlloyTM are better (such as corrosion

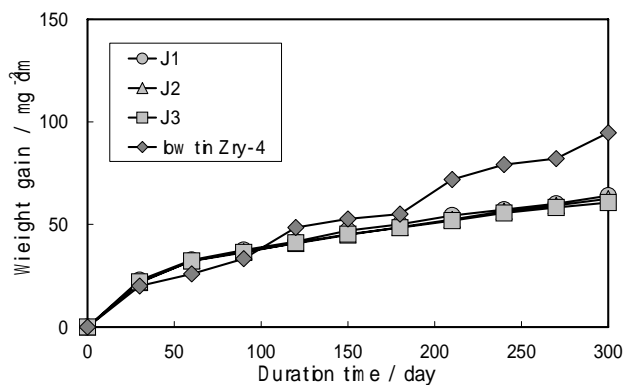


Figure 8 Autoclave test results (1)
(RCS water(3.5ppmLi+950ppmB))

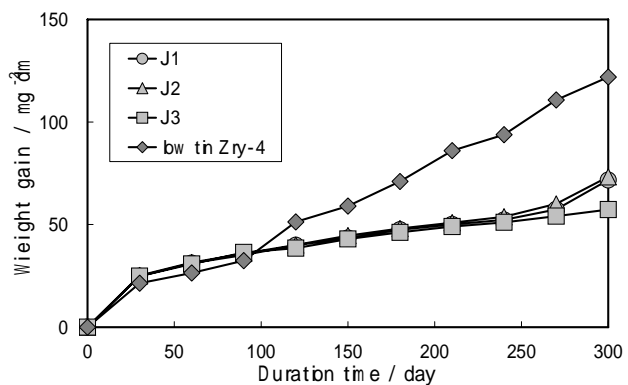


Figure 9 Autoclave test results (2)
(Pure water)

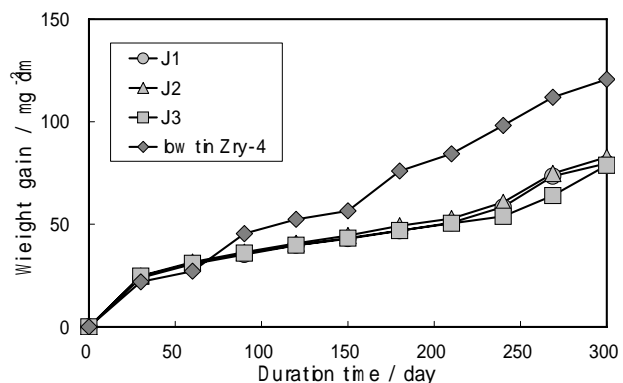


Figure 10 Autoclave test results (3)
(High Li water(10ppmLi))

behavior) and some performance are almost the same as those of Zircaloy-4. Some performance, such as mechanical property, are different from Zircaloy-4, which is expected as characteristics of Zr-Nb alloy or recrystallized material.

Based on the out-of-pile test results, it is suggested that J-Alloy™ is prosperous for utilization. In the near future, additional out-of-pile tests, PIE after an LTA irradiation program in Spanish commercial reactor and feasibility study of the fuel design are to be carried out.

5. Acknowledgement

The authors gratefully acknowledge the assistance and contributions of Spanish utilities, ENUSA and the other members of the J-Alloy development committee.

6. References

- [1] H. Takabatake, et al., TOP FUEL 2006
- [2] N. Sekimura, et al., TOP FUEL 2006.
- [3] F. Garzarolli, et.al., ASTM STP 1295(1995)
- [4] A. Frichet, et.al., HPR-349/32, Vol.II(1998)
- [5] A. Seibold et al., ANS Topical Meeting(2000)
- [6] P. Ivon, et.al., HPR-351/30(1999)
- [7] W. J. O'Donnell et al., Nuclear Science and Engineering.20(1964).



European Nuclear Society

Rue de la Loi 57
1040 Brussels, Belgium
Telephone +32 2 505 3 50
Fax + 32 2 502 39 02
ens@euronuclear.org
www.euronuclear.org

Layout and Design: Marion Brüninghaus, ENS